THE UNIVERSITY OF SHEFFIELD

FACULTY OF ENGINEERING

DEPARTMENT OF MECHANICAL ENGINEERING

Processing of NdFeB for Electric Motor Applications Using Selective Laser Melting

A thesis submitted in fulfilment of the requirements for the degree of Doctor of Philosophy

by

Kubra Genc

NOVEMBER 2022

Abstract

The production of complex/intricate shaped NdFeB magnets can be challenging when using conventional manufacturing techniques due to their inherent brittle structure. The additive manufacturing technique selective laser melting (SLM) may offer an opportunity to produce NdFeB magnets with high geometric complexity and expand the range of applications and magnet capabilities. Nevertheless, some SLM processing challenges exist for the processing of this material, including the generation of the internal porosity due to the intermetallic structure of NdFeB, the creation of residual thermal stresses and crack formation due to the fast-cooling rate of the SLM process. The main objective of this work is to explore SLM process parameter effects on the formation of NdFeB, with the aim of reducing part porosity, internal cracks using process parameter optimization. This study for the first time will also explore the effect of using a heated powder during processing. In addition, this thesis is the first study which investigates the effect of heat treatment, Ni infiltration and HIPping on magnetic properties.

During this investigation, it was found that low laser energy densities, between 50 to 100 J/mm^3 enabled the fabrication of samples with up to 95.72 % density. Pores and crack defects were observed mainly on the edge of the samples. It was found that density is improved by lowering hatch distance and layer thickness, while the former has higher impact on sample density. Regarding the magnetic properties, magnets with a maximum energy product of 81 kJ/m^3 could be produced without any post-treatment. Furthermore, there is no entirely linear relationship observed between the remanence and the density of the samples. Magnetic properties increase with the increasing volume fraction of the strong magnetic phase, $Nd_2Fe_{14}B$, in the samples.

The density of the samples and remanence, B_r can be improved with use of the heated bed while the coercivity, H_c decreases. The maximum energy product improved up to 84 kJ/m^3. The B_r improvement is related to density improvement, and H_c drops related to the bigger /or dendritic grains as a result of slowing cooling rates in heated bed. However, the integrity of the samples is less better than at room temperature fabrication. However, there is an improvement in the sample density, B_r ,and H_c until 580 °C annealing temperature, then H_c starts to decrease while B_r and density increases. The B_r increment

in heat treatment was not as expected according to the literature ofthe sintered magnets. It was found that Ni infiltration and HIPping did not improve the magnetic properties of the samples as the former was applied at very high temperatures (1400 °C), resulting in larger grains, reducing the coercivity. In addition, the amount of hard magnetic phase reduced after infiltration causing a reduction in B_r.HIPping, causes loss of Nd rich phases with the application of heat and inert gas pressure on the samples during the process. Therefore, with the lack of isolating Nd rich grain boundaries, coercivity drops significantly.

In summary, this study found that processing of NdFeB by SLM is very challenging. The brittle structure of the material with the combination of high cooling rates of the SLM, and the low strength of the material, makes it difficult to process without cracks and porosities. Additionally, the high oxygen sensitivity of the material compromises the phases for high magnetic properties, and the oxide layers on top of some samples make it difficult to get high-quality SEM images. However, the contributions of this study to literature are valuable.

This study is the first which examines the effect of the heated bed. It was found that the heated bed has a potential to improve both the magnetic properties (remanence B_r and maximum energy product BH_{max}) and the density of the magnets, in addition to improvement in surface quality. Also, it is the first study that examines the effect of heat treatment on magnetic properties. In addition, the relationship between the magnetic properties and printing parameters are valuable findings for literature. No other study in the literature discusses the Φ phase- a-Fe phase and printing parameter relationships. The SEM images and discussions are also valuable in an academic context since they clearly show the grain formation and morphology in the melt pool, and no discussion is found in the literature about them. Finally, the most important contribution is that the magnetic properties, B_r and BH_{max}, are the highest properties that have improved so far, by parameter optimisation, without any post-processing or element doping, 0.72 T and 81 kJ/mm^3, respectively.

Acknowledgements

This dissertation is submitted for the degree Doctor of Philosophy in Mechanical Engineering at University of Sheffield.

Firstly, I would like to thank my supervisor, Dr Kamran Mumtaz, who guided me so positively and who always made me feel confident in my abilities. His quality advices and support greatly affect my work and meant a lot, especially during the uncertain days of the COVID-19 pandemic. I would also like to thank my second supervisor Professor Iain Todd for his guidance on additive manufacturing and providing equipment access.

Secondly, I would like to thank to Dr Enrique Galindo-Nava and Sirapob Toyting from University College London and Cambridge University, for their valuable contribution in quantitative phase analyse and TEM analyse. I am very thankful to help of Justin Mitchell and Doug Walston from Arnold Magnetic Technologies for magnetic testing of my samples.

I would also like to thank my colleagues; Dr Cheryl Shaw, for the helping me with the SEM analyses, Dr Idris Tugrul Gulenc for his always supportive attitude and his thoughtful recommendations, and Mohammed T Alsaddah for his enormous helps whenever I need.

I would greatly appreciate the scholarship from the Turkish Government for my PhD studies. I am thankful to HiETA Technologies and Equipmake, who jointly funded this project, in addition to special thanks to Henry Greenhalgh from HiETA and James Baker from Equipmake. This work would not be possible without their support.

Above all, I want to thank my parents for always being there for me. Thank you for your endless and unconditional support during my entire life.

Table of Content

List of Figures

List of Tables

Table of Abbreviations

AM	Additive manufacturing
ABS	Acrylonitrile butadiene styrene
Am^{-1}	Amper per meter
AC	Alternating Current
BAAM	Big Area Additive Manufacturing
Bcc	Body centered cubic
Cgs	centimeters-grams-seconds
H_c	Coercivity
CCT	Continuous cooling transformation
DC	Direct current
Emu	Electromagnetic unit
EMF	Electromotive force
e-beam	Electron beam
EBM	Electron Beam Melting
ED	Energy Density
EDX	Electron Dispersive X-Ray
ET	Exposure Time
Fcc	Face centered cubic
FDM	Fused Deposition Modelling
G	Gauss
GBDP	Grain Boundary Diffusion Process
HD	Hatch Distance
H m^{-1}	Henries per meter

IM	Injection moulding
SI	International system
H_{ci}	Intrinsic coercivity
K	Kelvin
LENS	Laser Engineered Net Shaping
LF	Laser Focus
LP	Laser Power
LS	Laser Speed
Y	Laser Velocity
LT	Layer Thickness
H	Magnetic field
M-PSL	Magnetic field -assisted projection stereolithography
B	Magnetic induction
J	Magnetic polarization
MRI	Magnetic resonance imaging
M_S	Magnetic saturation
M	Magnetization
BH_{max}	Maximum Energy Product
Mks	metres-kilograms –seconds
T_2	$Nd_{1+e}\,Fe_4B_4$
T_1	$Nd_2Fe_{14}B$
Φ	$Nd_2Fe_{14}B$ phase, hard magnetic phase
T_3	$Nd_2Fe_3B_4$
Oe	Oersted
PM	Permanent magnets
μ_o	Permeability
PD	Point distance
PA11	Polyamid 11
PLA	Polylactic acid
PMAC	Permanent Magnet AC motors
PMSM	Permanent Magnet Synchronous Motors

W	Power
RE	Rare Earth
B_r	Remanence
SLM	Selective laser melting
α-Fe	Soft phase
STRC	Sports Tech Research Center
SEM	Scanning Electron Microscopy
SS316	Stainless steel 316
SS430	Stainless steel 430
SLA	Stereolithography
SQUID	Superconducting Quantum Interference Device
χ_m	Susceptibility
T	Tesla
XRD	X-ray powder diffraction
VSM	Vibrating sample magnetometer

Chapter 1: Introduction

1.1. Project Background

The NdFeB magnet is one of the most common permanent magnets used in electric motors. Thanks to their high coercivity, *Hc*, high remanence, *Br*, and high energy product, *BHmax*, NdFeB magnets are highly desirable in motor applications as they can keep their magnetism for long periods. However, eddy currents occur in the magnetic core during the working of magnetic devices, which heats the magnets. If the temperature increases above the curie temperature of NdFeB magnets, they might lose their magnetism, reducing their magnetic performance. Therefore, it is important to reduce eddy currents in magnetic devices in order to avoid reductions in magnetic properties.

Isolated-segmented permanent magnets have been designed in order to avoid or reduce these eddy current losses by decreasing the eddy current path with the help of isolation layers[1].The other suggested solution is to design cooling channels in the motor structure. Cooling channels can be placed around the rotor body or embedded between two coils/permanent magnets in rotor. However, more efficient cooling would be achieved by internal cooling channels in magnets by flowing cooling agents through them, which is not possible with the traditional production methods. However, it was confirmed that they can be printed by selective laser melting (SLM) [2].

On the other hand, it is also known that the shape of magnets effects the performance of the magnets/motors [3]–[5]. Toyota found out that the performance of the motor increases by 50% with “V” shape permanent magnet arrangement in rotors rather than flat shaped arrangement. Moreover, efficiency can be increased more if V-shaped magnets are replaced by a single magnetic body with a curved shape. The curved-shaped magnets can be produced by polymer bonded magnets [1]. The most common production method for polymer bonded magnets is the injection moulding (IM). Despite the relatively design freedom in the injection moulding (IM) it reduces the magnetic properties due to the polymer in the feedstock materials. The most common production method for the magnets without polymer blending is sintering. Sintered magnets are superior to IM produced magnets in terms of the magnetic properties

however, it has design limitations for the fabricated product. Additionally, the machining of sintered NdFeB magnets is difficult due to brittle structure of NdFeB.

Therefore, Selective Laser Melting (SLM) is a promising technique to produce NdFeB magnets, which enables complex part geometry without tooling costs and material waste.

In this project Selective Laser Melting (SLM) was used to produce NdFeB magnets. This method is one of the common AM techniques for metal powders. However, limited research has been conducted on SLM-printed NdFeB magnets. The main objective of this project is to improve the density of SLM-printed magnets and their magnetic properties. From this perspective, parameter optimization becomes the mostimportant focus to obtain high densities. Laser power, laser speed, hatch distance and layer thickness affect the powder melting and overlapping mechanism, they all should be investigated in detail. It is important to determine the correct sets of parameters which prevent lack of fusion, delamination, cracks and keyhole porosities.

Additionally, these parameters also affect the cooling rates, which directly affect the microstructure and phase. It is therefore important to determine the optimum sets of parameters to produce a desired microstructure, which are fine $Nd_2Fe_{14}B$ grains isolated by a Nd-rich phase.

Moreover, there are many techniques to improve the magnetic properties of sintered magnets, which can be applied to SLM-printed magnets. Heat treatment, infiltration of low-melting eutectic alloys, grain boundary diffusion, element doping, or element intergranular addition are the common solutions to improve magnetic properties. Nevertheless, these approaches have a number of drawbacks and benefits.

1.2. Project Aim and Objectives

The aim of this project is to manufacture NdFeB components using Selective Laser Melting with magnetic properties suitable for electric motor applications by:

- Undertaking parameter optimisation for density improvement of SLM-printed NdFeB magnets; Undertaking parameter optimization for density improvement of SLM-printedNdFeB magnets to improve the magnetic properties;
- Reducing production based residual stresses and cracks by using a preheated powder bed to improve the density of the samples and subsequently improve the magnetic properties;
- Improving the magnetic properties, coercivity and remanence by adjusting the scan parameters;
- Investigating the effect of the preheated bed on the density and magnetic properties of the samples; and
- Improving the density and magnetic properties of the samples with post treatments, including heat treatment, infiltration and HIPping.

The targeted magnetic properties are B_r 1.2 T , H_{ci} 1592 kA/m , suggested by HiETA Technologies. (Target was taken by Arnold magnetic technologies, the properties belong the N42SH NdFeB magnet).

1.3. Project Novelty

The common production methods for NdFeB magnets have design limitations. The brittle structure of NdFeB magnets makes their being machined difficult. Therefore, Selective Laser Melting, which is one of the promising AM methods for production of complex metallic structures, was used to produce NdFeB magnets. SLM can be used to produce NdFeB magnets alongside the other AM techniques. Using the pure metallic alloy is more favourable compared to AM techniques that include a polymer within the feedstock as it increases the magnetic properties by increasing the volume percentage of the magnetic structure in the magnets. However, SLM itself has challenges, including the extreme sensitivity of NdFeB to oxidation, the brittle structure of the hard magnetic phase which makes the material difficult to process, the residual stresses

occurring during processing due to the thermal gradient and fast cooling of the process. This causes cracks and delamination, and only the specific phase and microstructure will generate high magnetic properties. Therefore, it is necessary to investigate the effects of the parameters in detail. Within literature, studies present a brief overview of processing parameters when using SLM. This study investigates the effects of the printing parameters in more detail and to date has produced the highest magnetic properties for state-of-the-art SLM. In addition, this study is the first to investigate the effect of the heated bed, Ni infiltration and HIPping on the density and magnetic properties of SLM-NdFeB magnets.

1.4. Thesis Outline

This project consists of eight chapters.

Chapter 2 presents some basic information about magnetic materials and a literature review on the additive manufacturing of magnets, and a detailed review on AM-printed NdFeB magnets. The drawbacks of the techniques in addition to comparisons of the magnetic properties of AM-NdFeB magnets are discussed. Finally, pre- and post-processing techniques are discussed in terms of improvement in the magnetic properties of NdFeB magnets.

Chapter 3 presents the materials in this study and explains the methodology followed in the project.

Chapter 4 investigates the feasibility of Selective Laser Melting printed NdFeB magnets. A continuous wave Selective Laser Melting system is used in this chapter. The effects of the processing parameters on density and magnetic properties are examined.

Additionally, the microstructure formation mechanism and phases in the magnets are discussed and the high parameter range is examined.

Chapter 5 explores the effect of the heated bed on the density and magnetic properties of SLM-NdFeB magnets. In addition to analysing the influences of bed temperature, the various processing parameters are examined. Furthermore, the microstructure formation mechanism in heated bed samples is examined.

Chapter 6 examines the heat treatment of SLM-printed NdFeB magnets. The porosity and crack formations in the magnets before and after the treatment are studied. In addition, the change in the magnetic properties in the samples are discussed.

Chapter 7 investigates and discusses the influences of Ni infiltration and HIPping after printing. The application of Ni infiltration was studied in addition to its effect on the density, microstructure and magnetic properties of the SLM-printed samples.

Chapter 8 explores the HIPping of SLM printed samples. The sample density and the magnetic properties changes by HIPping were discussed.

Chapter 9 presents summaries of the conclusions of each chapter and provides recommendations for future studies.

Chapter 2: Literature Review

2.1. Basics of Magnets

In this chapter, basic knowledge of magnets including magnetic units, magnet types, properties and their applications are firstly covered. Crucial information of NdFeB magnet, microstructure and phase diagrams are later discussed. In addition, additive manufacturing of magnets, including SLM printing of NdFeB magnet are also included. Lastly, improving the magnetic properties in processing and post processing methods, which some of them later used in this research, are covered in detail.

2.1.1. Magnetic Units

Before discussing magnetic materials in the additive manufacturing process, some basic definitions will be given to understand magnetic materials. There are two complementary perspectives to define the basic concepts of magnetism. One has been developed by physicists based on circulating currents, and the other has been developed by engineers based on the magnetic poles. The two perspectives have two different systems of units, namely SI (the International System of Units) or MKS (metre-kilogram-second), and the Gaussian system or CGS (centimetre-gram- second) [6].

When a magnetic field, H, is applied to a material, it produces a magnetic field which is called magnetization (M) [7], which is the magnetic moment per unit volume [8]. B is the magnetic induction or magnetic flux density, the total flux of magnetic field linesacross the unit cross-sectional area of the material [7]. The relationship between B, H and M can be seen from Equations 2.1 (in the SI system) and 2.2 (in the CGS system), where μ_O is the permeability of the free space found by B/H in a vacuum [7].

$$\boldsymbol{B} = \mu(\boldsymbol{H} + \boldsymbol{M}) \qquad \textbf{Equation 2.1}$$

$$B = H + \boldsymbol{M} \qquad \textbf{Equation 2.2}$$

The permeability, μ, is the other parameter showing the type and strength of the magnet, found by B/H [7]. The other parameter is magnetic susceptibility, χ_m, which is the material's response to the applied field, found by M/H [8]. The final parameter is the magnetic polarization, J, which is the intensity of the magnetization (in SI units). It is calculated according to the following equation [7]:

$$J = \mu_0 M \qquad \textbf{Equation 2.3}$$

All units explained above can be seen in Appendix 1.

2.1.2. History of Hard Magnetic Materials

The scientific history of the magnet started in the 1600s with the book "*On The Magnet*" published by William Gilbert. After then, electromagnets were discovered in 1825 by Hans Christian Oersted, who found that electric currents produce a magnetic field [9]. With the discovery of electromagnets, simple electric motors were being produced by the end of the 1800s.

At the beginning of the 1900s, magnets were mostly Fe-based [10] Between 1935 and 1939, studies focused on iron-palladium and cobalt-platinum magnets, which have quite poor magnetic properties, such that H_c = 390 kA/m (coercivity), B_r = 1.04 T (remanence), and BH_{max} = 160 kJ/m^3 (maximum energy product).

Then Alnico magnets were developed in 1932. These consisted mainlyof aluminium, nickel and cobalt, but in the following years, they were developed by adding elements such as copper and titanium [9], [11]. Alnico magnets are popular in high-temperature applications due to their high curie temperatures, around 850℃.
However, their low intrinsic coercivity at H_c = 50 kA/m is a problem when the magnets work under a high demagnetization field [11].

In the 1950s, cobalt-platinum, which has a higher corrosion resistance than an Alnico magnet, was produced with properties of H_c = 125 kA/m, B_r = 0.58 T and BH_{max} = 24.4 kJ/m^3 [9], [12]. Then hard hexagonal ferrites such as $BaO_6Fe_2O_3$ and $SrO_6Fe_2O_3$ were developed. These ferrites have lower energy products than Alnico magnets; however, they have higher coercivity than Alnicos [9] at H_c = 250 kA/m andBH_{max} = 40kJ/m^3 [12].

The next step in magnet development is the SmCo type magnet. These magnets were fabricated by the U.S. Air Force Research Laboratory in 1968 [13]. The SmCo type magnet was the first commercial magnet in which rare earth (RE) and transition metals were used. Rare earth elements improve the anisotropy of the phase, and transition elements provide a high curie temperature and magnetization. It was recorded that the maximum energy product of the SmCo type magnets can be increased to 240 kJ/m^3 [11]. Additionally, SmCo type magnets have good thermal stability at around 500°C, which makes them a good candidate for high-temperature applications [12].

In 1983, anisotropic neodymium magnets were developed by sintering. The compound consisted of neodymium (Nd), iron (Fe) and boron (B). The energy productwas nearly 290 kJ/m^3. Subsequently, General Motors produced the isotropic neodymium magnet by rapid solidification with BH_{max} at around 114 kJ/m^3 [14] In the following years, the maximum energy product was improved to around 450 kJ/m^3 withheat treatments [11].

In addition, recently NdFeB magnets were improved by element doping (element adding during powder production), intergranular addition (mechanically blended into powder) and low melting point alloy infiltration (post processing method). Dysporosium (Dy), cobalt (Co), gallium (Ga) are the most common doping elements [15]. Dy [16], Nickel (Ni)[17], Nd-Co [18], praseodim-Cobalt (Pr-Co)[19] , Tantalium (Ta)[20] are used for intergranular additions for coercivity enhancement. Low melting point alloys such as NdCuCo [21] , PrCuCo [21], NdCu [22] are used for infiltration to improve coercivity. More details are given in section 2.6.

2.1.3. Background of Electric Motors

An electric motor is a device that converts to electrical energy to mechanical energy. The working principle of the electric motor based on Faraday`s Law, which means current carrying conductor generates a magnetic field [9]. On the other hand, any change in a flux density, *B*, produces a voltage, the electromotive force (EMF), on a coil (Faraday's Law) [23]. The fundamental principle of all electric motors involves the rotation of the rotor, which is driven by the interaction between two magnetic fields, as shown in Figure 2.1.a. Typically, these magnetic fields are generated in the stationary stator and the rotating rotor, either through energized windings, the use of permanent magnets, or induced

currents. This interaction produces a torque on the rotor, causing it to turn. However, some motors, such as the reluctance motor, rely on the interaction between a magnetic field and a magnetic material, such as iron, which limits their torque output, as shown in Figure 2.1.b. The majority of motors used in modern commercial applications, including DC, induction, and synchronous motors, utilize the interaction between two magnetic fields to generate a greater amount of torque [18].

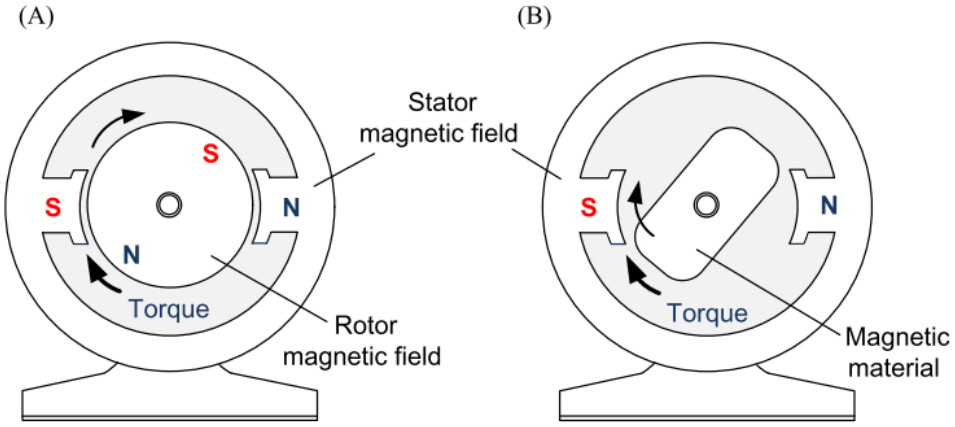

Figure 2-1 Schematic view of the rotation of electric motors (a) Two magnetic fields and (b) one magnetic field and magnetic material [24]

An electric motor consists of a stator, a rotor, winding, bearings, and commutator, as Shown in Figure 2.2. The electric motor's rotor is responsible for generating the mechanical power by rotating the shaft. It is typically composed of conductors that carry currents, which then interact with the magnetic field of the stationary stator to produce the forces that drive the rotation. However, some rotors contain permanent magnets, while the conductors are housed in the stator. The stator is the fixed component of the motor's electromagnetic circuit and typically contains either windings or permanent magnets. To minimize energy losses, the stator core is constructed from numerous thin metal sheets known as laminations. The windings, which are wires coiled around a laminated soft iron magnetic core, are used to create magnetic poles when current is applied. To maintain a repulsive force between the rotor and stator poles, it is necessary to reverse the direction of current in the rotor, which is achieved through the use of commutators [25]–[27].

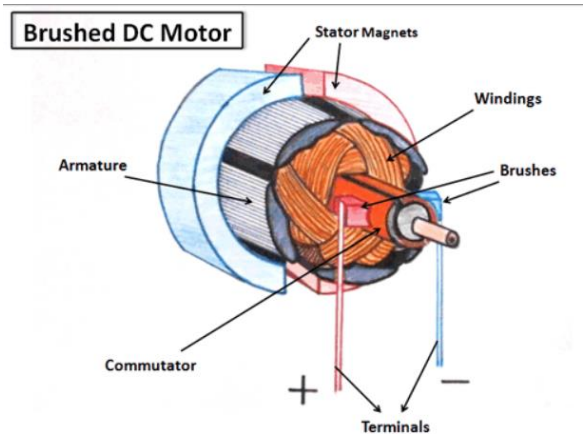

Figure 2-2 Schematic view of the electric motor showing main components of the electric motor[28].

Several motor types uses permanent magnets for field excitation. For instance, in Permanent Magnet Synchronous Motors (PMSM), the rotor contains permanent magnets to establish alignment and produce torque with the rotating Magnetic Field (MMF) generated by the stator winding. Similarly, in PMDC motors, permanent magnets are also used to establish a magnetic field, but instead of a rotating MMF, the net torque is generated by an alternating current created at the armature via the commutator. Permanent Magnet AC motors (PMAC) are similar to regular induction AC motors, but they differ in that they feature permanent rare-earth magnets affixed to their rotors - the component that rotates. Instead of inducing a magnetic field in the rotor, PMACs leverage the rotor's inherent magnetic field to generate motion. The permanent magnets used in motors are classified into three namely Alnico magnets, Ceramic (ferrite) magnets, and Rare-earth magnets.[27], [29], [30].

There is also ongoing research in the electric motor field to improve motor efficiency, reduce costs, and enhance performance, and additive manufacturing technology is being increasingly used in the production of electric motors. Prototyping is one of the way to use AM for electric motors. It is used to create rapid prototypes of motor components. This allows engineers to quickly test and refine designs before moving on to full-scale production. Small batch production is the other reason of using AM; AM can be used to produce small batches of motor components with complex geometries that would be difficult or expensive to produce using traditional manufacturing methods. The other reason of AM usage in electric motors is that AM enables the customization of motor components to fit specific applications or customer needs. For example, a motor manufacturer could print a custom rotor with a unique geometry or material composition

for a particular customer. Additionally, AM can produce lightweight motor components that can improve overall motor efficiency. For example, a motor manufacturer could print a lightweight stator with optimized cooling channels that reduces the motor's weight and improves its heat dissipation. Moreover, AM can be used to develop and test new materials for use in electric motors. For example, researchers are exploring the use of carbon fiber composites to produce lightweight and high-strength motor components [31].

Overall, additive manufacturing is a promising technology for the electric motor industry, as it enables the production of complex geometries, customization, and lightweighting that can improve motor performance, efficiency and cost-effectiveness.

2.1.4. Magnet Types

Magnetic materials are classified into five groups in terms of their alignment with or without a magnetic field as diamagnetic, paramagnetic and ferromagnetic magnets, antiferromagnetic, ferrimagnetic.

Diamagnetic materials have magnetism only under an external magnetic field. When an external field is applied, magnetic domains are aligned in the opposite direction of the external field, and once the external magnetic field is removed, magnetism disappears [32]. Paramagnetic materials do not have magnetism because they have randomly aligned magnetic domains which cancel each other's moments. They only have magnetism once an external field is applied. Although the magnetic moments are aligned in the same direction as the applied field, a paramagnetic material cannot maintain its magnetism after the external magnetic field is removed [32]. Ferromagnetic materials have permanent magnetism without an external field [33]. Domains are aligned parallel to an external magnetic field, and they keep their magnetism after the magnetic field is removed [33].

Ferrimagnetism is seen only in compounds which have more complex magnetic orders. They have two types of magnetic sublattices and the net magnetic moments of these different sub-lattices are not equal. Therefore, they do not cancel each other's moments, thereby causing magnetism [34]. Antiferromagnets have structures similar to ferrimagnets such that they have two different sub-lattices. However, in antiferromagnets, different types of sub-lattices are aligned in the opposite direction and cancel each other's moments, making the net momentum zero [34].

Every type of magnetic material in terms of magnetic moments can be seen in Figure 2.3.

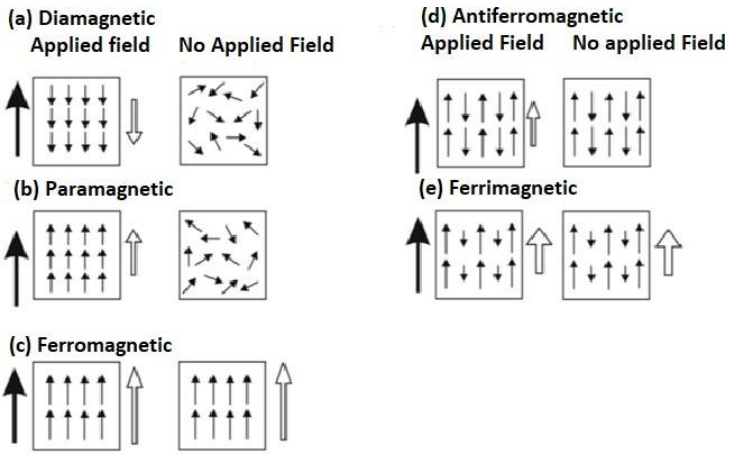

Figure 2-3 Magnetic moment alignment in different types of magnetic material in an external magnetic field and without an external magnetic field, where solid arrows represent the external field, and hollow arrows represent the net magnetic moment in the material, adapted from ref [35].

2.1.5. Hard and Soft Magnets

Ferro and ferrimagnetic materials are named soft or hard magnets depending on the strength of the magnetic field needs to align their domains. The magnetically soft means easy to magnetize and demagnetize and the magnetically hard means hard to magnetize and demagnetize. It is because the domain wall movement of the hard magnetic materials is not easy it requires high value of magnetizing force however, they move easily in soft magnets. Hence hard magnets have high coercivity and low permeability and soft magnets have low coercivity and high permeability. The magnetism of the hard magnetic materials is constant on the other hand it is temporary in soft magnets. On the other hand, eddy current losses are high on hard magnetic materials, due to their low electrical resistance, and they are lower on soft magnetic materials due to the their high electrical resistance [11], [36]–[38]. The use of soft and hard magnetic materials in electric motor applications is very common. Electromagnets which are the soft magnets were common in electric motors until permanent magnets (hard magnets) are invested. However, recently, they both have application area in electric motors. Electromagnets can be turned off and temporarily keep their magnetism, in addition to magnet poles can be altered. On the other hand, permanent magnets (PM) keep their magnetism permanently and they can`t be turned off, in addition to magnet poles can`t be altered.

In electric motors PM magnets are embedded in the motor's stator, or the stator is made of PM. PM magnets, such as neodymium magnets, have high magnetic energy density and provide a strong magnetic field. They are commonly used in motors that require high power and high efficiency, such as those used in electric vehicles or wind turbines. However, they can be brittle and prone to demagnetization under certain conditions, such as high temperatures or strong magnetic fields. Soft magnets, such as iron or iron alloys, have low magnetic energy density but exhibit good magnetic properties when subjected to alternating magnetic fields. They are commonly used in motors that require high torque at low speeds, such as those used in household appliances or power tools. Soft magnets are also less prone to demagnetization and have better thermal stability compared to hard magnets. However, they may require higher currents to achieve the same level of magnetic field strength as hard magnets. In some cases, a combination of hard and soft magnets may be used in electric motors

to optimize their performance and efficiency. For example, soft magnetic materials may be used in the stator, while hard magnetic materials may be used in the rotor.

2.1.6. Hysteresis Loops

When magnets are placed in a strong magnetic field, they reach their saturation magnetization, M_s [35]. If the magnetic field is reduced by the magnetic reversal, a hysteresis loop develops, as shown in Figure 2.4. Two hysteresis loops exist, *B* versus *H*, and *M* versus *H*, called a normal curve and intrinsic curve, respectively [38]. While physicists focus on the *M-H* curve, engineers usually focus on the *B-H* loop [39]. We can determine number of magnetic properties from the hysteresis loop, such as remanence, M_r, B_r, and coercivity, H_c. Remanence is the residual magnetism in the magnets after the applied external magnetic field is removed, which is the state of a number of domains that are still aligned in the direction of the magnetic field without an external magnetic field [23]. Coercivity is the reversed magnetic field to make magnetization zero [39], [40]. The intrinsic coercivity H_{ci} is the reversed magnetic field needed to demagnetize the *M-H* loop magnet completely.

It can be seen from Figure 2.4 that after the saturation point, *M* is constant while *B* still increases with the increase of *H* because *B* depends on *H* (see Equations 2.1 and 2.2) [8].

On the *B-H* curve, every point has *B* and *H* values. The maximum *B-H* value in the second quadrant of the hysteresis is called BH_{max}, which is one of the most important values to evaluate the performance of a magnet [38].

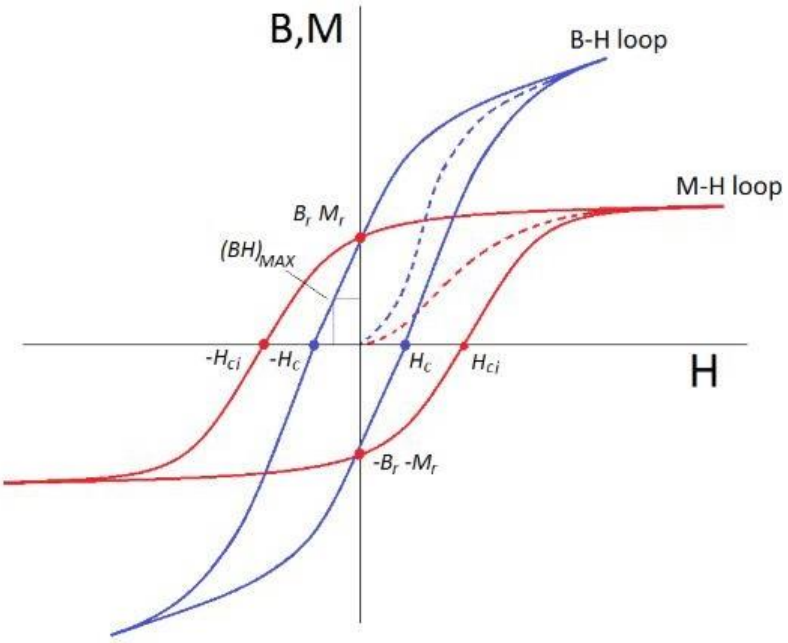

Figure 2-4 Normal and intrinsic magnetic hysteresis loops representation [39].

The hysteresis loops of soft magnets are narrower than those of hard magnetic materials, meaning that the reverse magnetic field to demagnetize the magnet is low, *Hc* or *Hci* [39].

2.1.7. Applications of Magnets

Magnets have been used for many purposes in various fields. Some typical application areas of magnets include generators [10] (such as wind turbines [41] and water turbines [42]), transducers (such as loudspeakers and microphones [11]), transformers [43], sensors [44], alternators [45], DC motors [46], magnetic storage applications [11], and biosurgical applications (such as MRI [47] [11], drug delivery [48] and magnetomotive artificial hearts [49].

The NdFeB magnets are used in various field such as satellite communications, radar technology, electronic tracking, and microphones, hearing aids, stereo headphones, magnetic locks, magnetic pumps, magnetic gears, in refrigerator motors, electric bicycle, in magnetic separation technologies, and even in magnetic therapy machines [50].

2.2. The NdFeB Rare Earth Magnets

In this section the principal phases of NdFeB magnets and their importance for magnetic properties are introduced. The origin of the high magnetic properties of the NdFeB magnet is the highly anisotropic 2:14:1 tetragonal phase, which is called the hard magnetic phase and represented by Φ. It has a high saturation magnetization and anisotropy constant, which gives high magnetic performance [51]. $Nd_2Fe_{14}B$ has a tetragonal structure with lattice parameters a = 0.8792 nm and c = 1.2177 nm, as shown in Figure 2.5. The microstructure of this phase is varied based on the production method and processing conditions. However, the crystal structure is still the same.

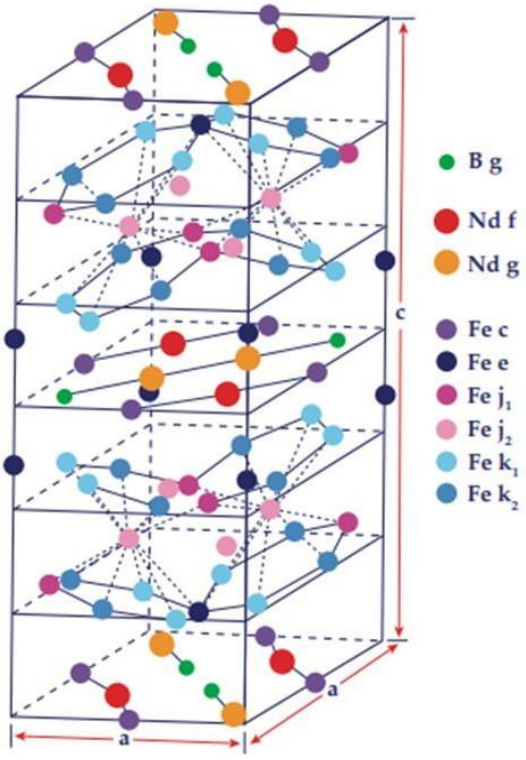

Figure 2-5 Unit cell of the Nd2Fe14B [52].

The other phase is the *a-Fe* (BCC) phase, typically observed phase besides the $Nd_2Fe_{14}B$ phase [52]. It is typically in dendritic structure and the presence of *a-Fe* phase relate to poor magnetic properties since it reduces the volume percentage of $Nd_2Fe_{14}B$ phase [53]. Nd rich phase is the other common phase seen in the NdFeB magnets. The Nd rich phase in the grain boundaries is the most important phase which increases the coercivity by isolating the magnetic grains and inhibiting the demagnetization [54]. The non-isolated $Nd_2Fe_{14}B$ phase grains in stoichiometric magnets and fine and homogeneously distributed $Nd_2Fe_{14}B$ phases surrounded by Nd rich phase are shown in Figure 2.6.a and 2.6.b. The former one can't keep their magnetization due to the exchange coupling between them while the latter can. In addition, if the start alloy composition is selected from the left side of the stoichiometric line, nanocomposites consist of *a-Fe* and $Nd_2Fe_{14}B$ phase can be obtained, as can be seen in Figure 2.6.c.

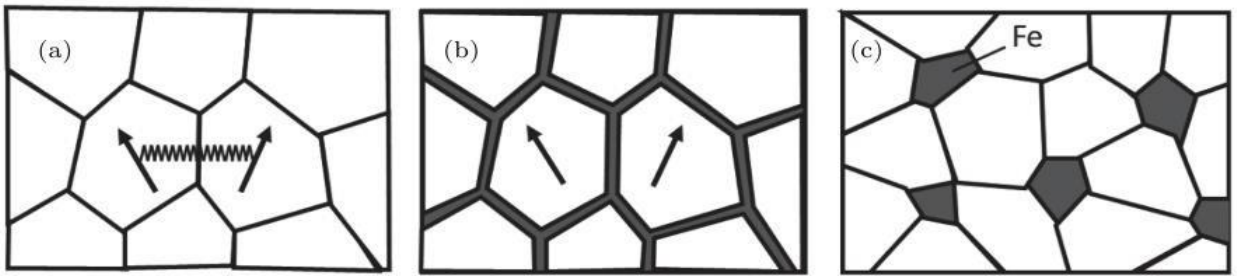

Figure 2-6 Schematic view of the microstructure for (a) stoichiometric 2:14:1, (b) isolated 2:14:1 based nanocrystalline magnets. The exchange coupling (represented by a zigzag) in stoichiometric 2:14:1 lowers the coercivity while there are increases in the remanence. The RE-rich phase in nanocrystalline magnets inhibits the exchange coupling between the 2:14:1phase, hence it increases the coercivity but decreases the remanence and (c) nanocomposite magnets with a-Fe in addition to $Nd_2Fe_{14}B$ phases [51].

2.3. Nd-Fe-B phase diagram and phase reactions

The phase diagrams of NdFeB systems are important to identify the possible solidification reactions taking place in the Nd-Fe-B system. Figure 2.7 shows the vertical section of the Nd-Fe-B phase diagram. The low content Nd alloy is used hence,the Figure 2.7.b is added to investigate the main phase. The first solidification is the liquid transforming into γ-Fe fcc at 1370˚C. Then The $Nd_2Fe_{14}B$ (T1) phase forms at 1180˚C by a peritectic reaction p5, indicated in Table 2.1. Then the following reaction is E1, which is a ternary eutectic reaction producing γ-Fe, T1 and T2 ($Nd_2Fe_7B_6$). Theγ-Fe later transforms into α-Fe at temperatures around 870˚C. In Nd-rich regions, Nd,T1 and T2 are produced by the ternary

eutectic reaction E2 at a temperature of 665 ˚C.Table 2.1 shows other possible invariant and monovariant solidification reactions in Nd-Fe-B [55].

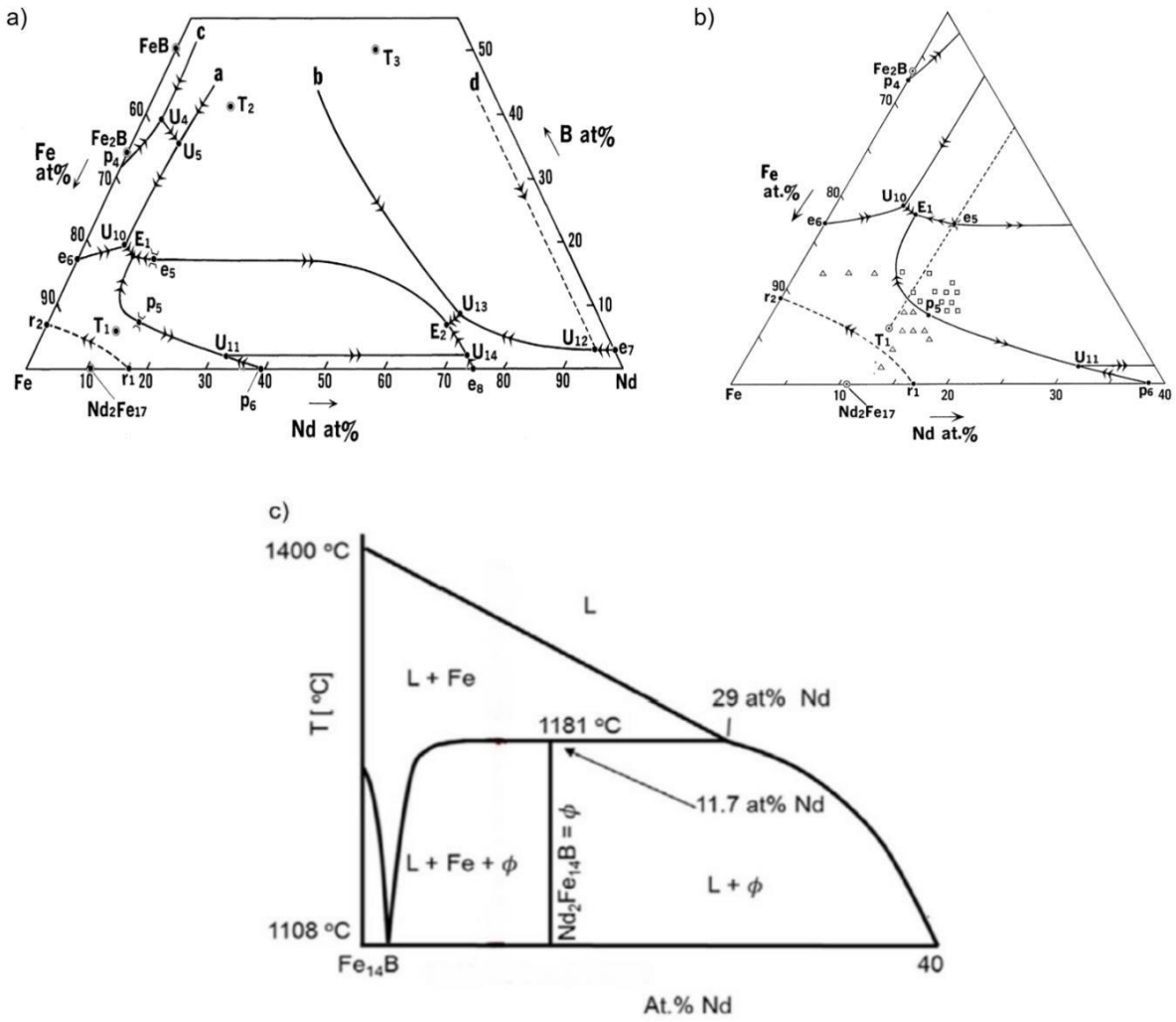

Figure 2-7 Nd-Fe-B phase diagram [2], [51].

Table 2-1 Invariant and monovariant reactions in Nd-Fe-B ternary system reproducedfrom [55].

Symbol	Type of reaction	Reaction	Composition (at%)			Temperature (K)
			Nd	Fe	B	
p_4	peritectic	$L+FeB \leftrightarrow Fe_2B$	0	68	32	1680
p_5	peritectic	$L+\gamma Fe \leftrightarrow T_1$	14	79	7	1428
p_6	peritectic	$L+\gamma Fe \leftrightarrow Nd_2Fe_{17}$	39	61	0	1458
r_1	remelting	$\delta Fe \leftrightarrow \gamma Fe+L$	17	83	0	1665
r_2	remelting	$\delta Fe \leftrightarrow \gamma Fe+L$	0	93	7	1654
e_5	eutectic	$L \leftrightarrow T_1+T_2$	12	71	17	1368
e_6	eutectic	$L \leftrightarrow \gamma Fe+ Fe_2B$	0	83	17	1450
e_7	eutectic	$L \leftrightarrow Nd+Nd_2B_5$	97	0	3	1275
e_8	eutectic	$L \leftrightarrow Nd+Nd_2Fe_{17}$	75	25	0	963
U_4	transition	$L+FeB \leftrightarrow NdB_4+Fe_2B$	3	58	39	-
U_5	transition	$L+ NdB_4 \leftrightarrow Fe_2B+T_2$	6	57	37	-
U_{10}	transition	$L+ Fe_2B \leftrightarrow T_2 +\gamma Fe$	7	74	19	1403
U_{11}	transition	$L+ \gamma Fe \leftrightarrow Nd_2Fe_{17}+T_1$	32	66	2	-
U_{12}	transition	$L+ Nd_2B_5 \leftrightarrow T_3+Nd$	94	3	3	1393
U_{13}	transition	$L+ T_3 \leftrightarrow Nd+ T_2$	68	24	8	-
U_{14}	transition	$L+ Nd_2Fe_{17} \leftrightarrow T_1+Nd$	73	25	2	958
E_1	Ternary eutectic	$L \leftrightarrow Fe +T_1+T_2$	8	74	18	1363
E_2	Ternary eutectic	$L \leftrightarrow Nd +T_1+T_2$	67	26	7	938

2.4. Additive Manufacturing of Magnets

The additive manufacturing techniques used for processing magnetic materials include Laser Engineered Net Shaping (LENS), Fused Deposition Modelling (FDM), Big Area Additive Manufacturing (BAAM), Stereolithography (SLA), Selective LaserMelting (SLM), Electron Beam Melting (EBM) and Binder Jetting Additive Manufacturing.

2.4.1. Laser Engineered Net Shaping (LENS)

2.4.1.1. Fe-30- %Ni

LENS AM was studied to produce homogenous bulk material with good magnetic properties. The results showed that lower travel speeds provide a metastable FCC phase with columnar grains while the higher speeds provide a BCC phase, possibly a martensitic phase. The BCC phase dominated microstructure shows higher saturation magnetization (M_s) than the FCC phase dominated samples [56].

2.4.1.2. Fe-Si-B-Cu-Nb

The Fe-Si-B-Cu-Nb alloy was studied using LENS with nine different processing conditions by [57]. The results show that the effect of travel speed on grain sizeis greater than the effect of laser power on the grain size [57], [58]

2.4.1.3. Ni-Fe-Mo and Ni-Fe-V

Production of Ni-Fe-V and Ni-Fe-Mo based permalloys by LENS was studied by [59] The results show that the saturation magnetization of the LENS produced permalloys are comparable with conventional permalloys, while LENS permalloys have higher coercivity [59]

2.4.1.4. Non-magnetic austenitic stainless steel 316 to magnetic ferritic stainless steel 430

Compositionally graded steel, from non-magnetic austenitic stainless steel 316 (SS316) to magnetic ferritic stainless steel 430 (SS430) in a single structure, was printed by LENS [60].

2.4.1.5. Al-Ni-Co

Alnico 8 type magnets were produced successfully with LENS. It was found that the magnetic properties were affected by magnetic annealing time and annealing temperature. Furthermore, results show that the magnetic properties of AM alnico magnets are superior to their sintered counterparts [61].

2.4.2. Fused Deposition Modelling (FDM)

2.4.2.1. Polylactic acid (PLA)-Iron

A transformer core was printed using FDM by [62]. In the study, 40 wt % iron and polylactic acid (PLA) were mixed and used as a filament for FDM. Various percentages of the fill patterns and different types of fill patterns were analysed. It was found that the fill pattern does not have a great effect on performance, while the highest performance is obtained with the largest percentage fill pattern.

2.4.2.2. NdFeB powder-PA11

Prefabricated NdFeB particles with polyamide 11 (PA11) was mixed to produce a filament for FDM [63]. Printed samples were compared with injection moulded magnets. Results showed that printed magnets have lower remanence due to their lower density. Results included remanence: 310 mT and 387 mT, density: 3.57 g/cm^3 and 4.35 g/cm^3, for 3D printed and injection moulded samples, respectively [63].

2.4.2.3. Magnetite particles – polycaprolactone

Flow sensor by FDM printed by [64].In the study, the main body of the sensorwas printed with acrylonitrile butadiene styrene (ABS) and the functional areas were printed with a mixture of magnetic particles and polycaprolactone. Results showed that complex parts can be printed with FDM. Additionally, less magnetic material wasused compared to conventional ferrous sensors [64].

2.4.3. Stereolithography (SLA)

Magnetic field responsive smart materials were printed with magnetic field-assisted projection stereolithography (M-PSL). In that project, ferromagnetic particles were deposited on the liquid polymer in the feedstock bed by the precisely controlled pumping system. Magnetic particles were aligned in the desired pattern by the external magnetic field. Three cases were studied, namely an impeller, a two-wheel roller and a switch. Magnetic particles were added to locations where they needed to be on the feedstock. Results showed that all three cases were successful and that all printings responded to the external magnetic field changes [65].

2.4.4. Electron Beam Melting (EBM)

The Sports Tech Research Center (STRC Sweden) printed MnAl(C) magnets using EBM. The fast melting-solidification rate of the EBM provides a particular crystalline microstructure. However, there is a risk to the EBM machine. Loose powder may be charged by the e-beam and rise to the build chamber, and this could damage the machine. In that study, powder layers were semi-sintered by the lower e-beam to avoid rising charged powder up to the chamber [66].

2.4.5. Big Area Additive Manufacturing (BAAM)

Big area additive manufacturing (BAAM) is another technique in which polymers and powders are mixed and extruded from a nozzle. The powders are deposited layer by layer.

65 vol.% NdFeB powder and 35 vol.% Nylon-12 uniformly mixed and extruded to obtain composite pellets, which were then used as a feedstock material for BAAM. The BAAM nozzle deposits the feedstock materials as layers fused in the desired shape. Figure 2.8 shows the schematic view of the production of the feedstock pellets for BAAM [67].

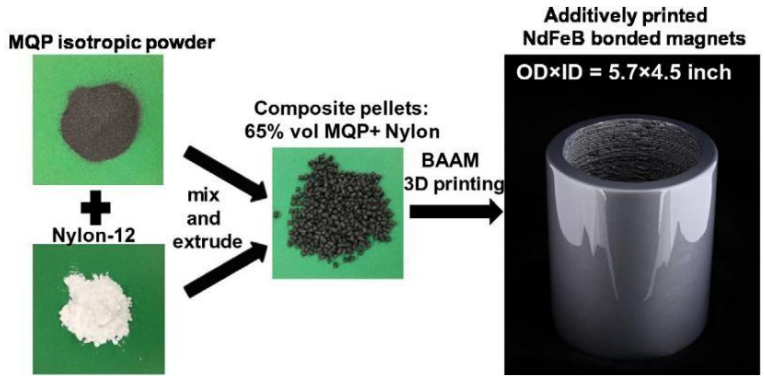

Figure 2-8 Schematic view of mixing the NdFeB powder and Nylon-12 to produce pellets through an extrusion, which are then used in the BAAM [68].

The BAAM-printed magnet was compared with the injection moulded (IM) magnet. The results showed that BAAM magnets are superior to IM magnets. The H_c, B_r and BH_{max} values of the BAAM magnets are better than the IM magnets at all temperatures, as shown in Table 2.2 [67].

Table 2-2 Magnetic properties of BAAM and IM fabricated bonded NdFeB magnetsmeasured at various temperatures (300 K to 400 K) [67].

	Temperature	H_{ci} (kA/m)	H_c (kA/m)	B_r (T)	$(BH)_{max}$ (kJ/m^3)
BAAM	300	688.37	357.31	0.51	43.49
	325	620.72	342.19	0.5	41.02
	350	557.06	323.89	0.48	38.32
	375	502.15	303.99	0.47	35.46
	400	452.01	281.71	0.45	32.2
IM	300	639.82	289.67	0.48	36.17
	325	577.75	274.55	0.47	33.47
	350	525.23	258.63	0.45	30.61
	375	479.87	243.51	0.43	27.59
	400	436.89	226.8	0.41	24.65

2.4.6. Binder Jetting Additive Manufacturing

NdFeB magnets were printed by binder jetting technique [69]. First, resin-coated NdFeB powders were spread on the build plate. Then, the print bed was moved under the heat lamp to bind the powder. Following this, the new powder layer was spread on the previously bonded powder layer by the roller. The same steps were repeated until the entire part was finished. Then the printed green part was placed in the oven to cure the binder.

It was concluded that post-processing of the part is very important to improve the mechanical properties of the magnets. However, the processing temperature has to be kept below 300°C to avoid a decrease in the magnetic properties due to the curie temperature of NdFeB magnets.

XRD results show that there is no significant difference between the starting powder and the printed part in terms of the amount of the $Nd_2Fe_{14}B$ phase, as shown in Figure 2.9. Moreover, the coercivity of the printed part and the starting powder are quite similar: 716.2 kA/m and 692.3-748.0 kA/m, respectively. On the other hand, the remanence value for the binder jet magnet is 0.3 T, which is lower than the injection moulded and compression bonded magnets, 0.5 T and 0.65 T, respectively. The reason for the lower remanence is the lower volume fraction of the $Nd_2Fe_{14}B$ phase in the binder jet magnet, which is 0.45%. The injection moulded magnets contain a 0.65% $Nd_2Fe_{14}B$ phase, and the compression moulded magnets contain a 0.80% $Nd_2Fe_{14}B$ phase. This study suggests that increasing the volume fraction of the magnetic powders would improve the remanence values.

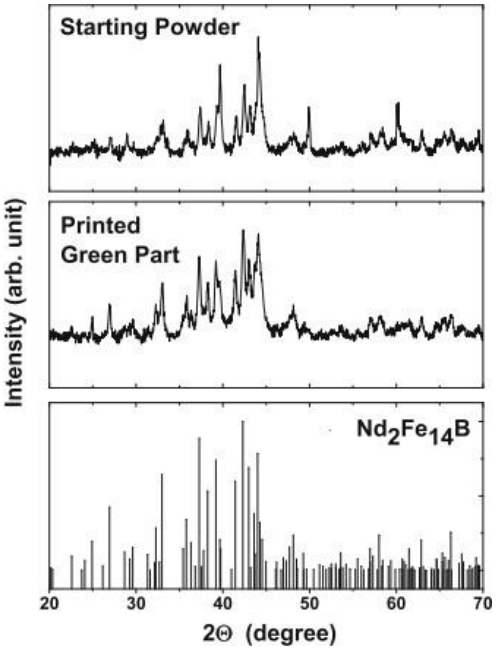

Figure 2-9 XRD results of the starting powder, the printed green part and the XRD peaks of the $Nd_2Fe_{14}B$ phase, from top to bottom, respectively [69]

In addition, isotropic and anisotropic NdFeB powder with a thermosetbinder studied by[68] to print NdFeB magnets. The printing process was similar to the previous study.In that study, different shape magnets were printed, including ring, square and horseshoe shapes. The density of the samples was 43%, compared to the theoretical density of the magnet. Additionally, magnetic alignment was performed by placing thesintered magnet under the binder jet-printed magnets during the post-curing stage inthe oven. The density, remanence and maximum energy product of the magnetically aligned magnets are higher than the non-aligned magnet, while intrinsic coercivity is the same, as seen in Table 2.3 [68]. The reason for the increasing remanence after thealignment is that all domains are aligned in the same direction and do not cancel eachother's momentum. The low density is related to the low volume fraction of the magnetic powder.

Table 2-3 Density, coercivity, remanence and maximum energy product of the binder jetted NdFeB bonded magnets [68].

Sample	Density (g/cm^3)	Hci (kOe)	Br (kG)	BHmax (MGOe)
Without alignment	3.54	14.2	3.3	2.4
Alignment while curing	3.86	14.2	4.2	3.8

2.4.7. Selective Laser Melting (SLM)

Selective laser melting is a powder bed AM method which enables complex part geometry without tooling costs and material waste. It is one of the common AM techniques for metal powders. The working principle of the SLM can be seen in Figure 2.10 below.

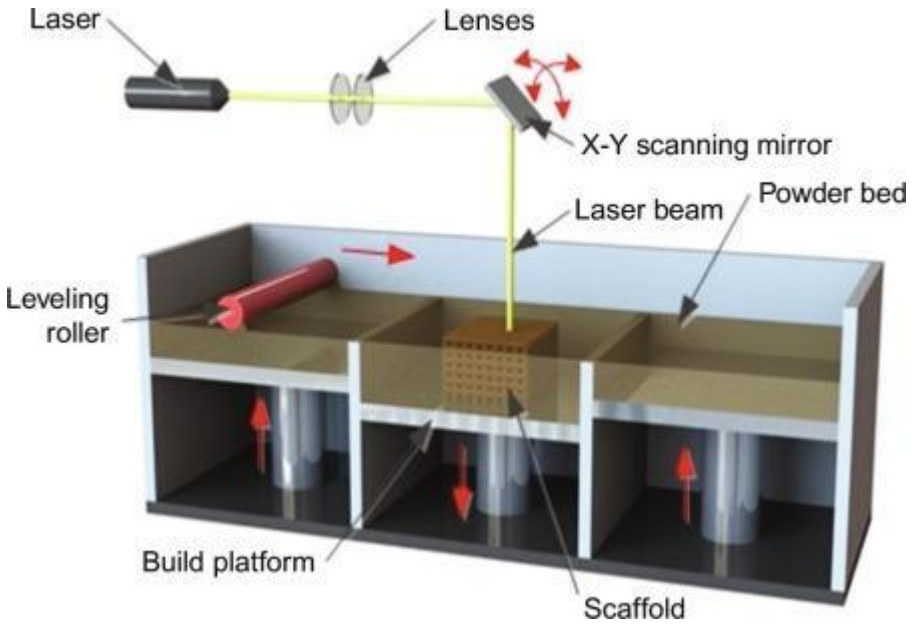

Figure 2-10 Shematic view of the working principle of SLM [70]

For the SLM printing, a CAD design is first converted to an STL file and uploaded to the SLM machine. Then, the feedstock powder is layered on the build platform using the levelling roller. The laser then scans the powder with respect to the desired design geometry and the built platform is lowered by one layer thickness while the powder bed is raised to spread the following layer with the roller [71]. The laser then scans the powder in the desired design as in the previous cycle. The melted layer is fused to the previously solidified layer below. The process repeats the same steps until the entire part is completed [72].

The applied energy density on the powder layer has to be sufficiently high for the powder melting to obtain successful tracks. The applied energy density, *ED,* can be found using Equation 2.4, where *LP* is the laser power, *v* is the laser velocity, *HD* is the hatch distance, and *LT* is the layer thickness [72].

$$ED = LP/(v*HD*LT) \qquad \text{Equation 2.4}$$

2.4.7.1.FeNi alloys

Fe-30%Ni and Fe-80%Ni magnets printed by SLM. In conventional techniques, excessive grain growth could be seen, which would cause the loss of magnetic properties. The fast cooling rate of SLM gives finer grains, which are good for the magnetic properties. Grain refinement was achieved through SLM. The results showed that a grain size reduction to below 100 nm increases magnetization and decreases coercivity [73]–[75]

2.4.7.2. $NiFe_{14}Cu_5Mo_4$

Bauer, Spierings and Wegener (2016) printed a $NiFe_{14}Cu_5Mo_4$ alloy magnet using SLM. They compared single-track and re-scan strategies. Their results showed that re-scanning inhibits grain growth and produces nearly-isotropic magnets, whereas a single scan shows anisotropic properties. Additionally, it was found that Si, O and N are potential risks for crack formation in magnets [76].

2.4.7.3. Fe-Si-Cr

SLM Fe-Si-Cr magnets produced by [77]. They worked with various scan speeds and laser power ranges of 650 mm/s to 1550 mm/s and 140 W to190 W, respectively, with constant layer thickness and constant laser spot size. The most successful magnet was printed at 170 W and 950 mm/s under the 5% oxygen content [77].

2.5. Selective Laser Melting (NdFeB)

As previously mentioned, NdFeB magnets have magnetic properties that are superior to AlNiCo and hard ferrites. NdFeB magnets can be produced using conventional methods; however, the production of complex-shaped magnets is not as easy as the production of traditionally shaped magnets. Moreover, the machining of NdFeB magnets is difficult due to the brittle structure of such magnets. SLM is a solution for both complex shape magnets and machining problems and the waste of material is reduced when applying AM techniques [2].

NdFeB magnets printed by SLM was studied by [2]. In the experiment, $Nd_{7.5}Pr_{0.7}Zr_{2.6}Ti_{2.5}$-$Co_{2.5}Fe_{75}B_{8.8}$ powder alloy was supplied as a feedstock, known as MQP-S, supplied by the Magnequench Corporation.

Various laser parameters were studied, including Laser Power (*LP*), Laser Focus (*LF*), Point Distance (*PD*), Exposure Time (*ET*), and Hatching Distance (*HD*), to produce high-quality printed parts. During the experiment, parts were built on a steel plate connected to a larger copper piece that extracts heat and prevents overheating of the platform.

The results showed that $Nd_2Fe_{14}B$ grain size was reduced to only 1 μm, which is lower than the that of the sintered magnet. The obtained maximum properties were Hc = 695 $kA.m^{-1}$, Br = 0.59 T, and $(BH)_{max}$ = 45 $kJ.m^{-3}$. The density of the produced magnet was 7 g/cm^3, 92% of the theoretical density.In general, magnetic properties increase with an increase in the energy density, E, ($E = LP/(LF*LT*HD*PD/ET)$). However, deeper analyses are required to understand the influences of these parameters.

Figure 2.11 shows the relationship between energy density and magnetic performance. It was reported that low laser velocity, (*PD/ET*), at 0.025 m/s, gives very low BH_{max} even though it provides greater energy density in Region 1. If the laser velocity, *v,* is one order of magnitude higher than the velocity in Region 1, BH_{max} increases *by* two orders of magnitude, represented by Region 2. Layer thickness is the other important parameter discussed in the paper. BH_{max} increases from 15 to 45 kJ.m³ by reducing the layer thickness from 100 to 20 µm. Laser velocity is kept constant, represented by Region 3.

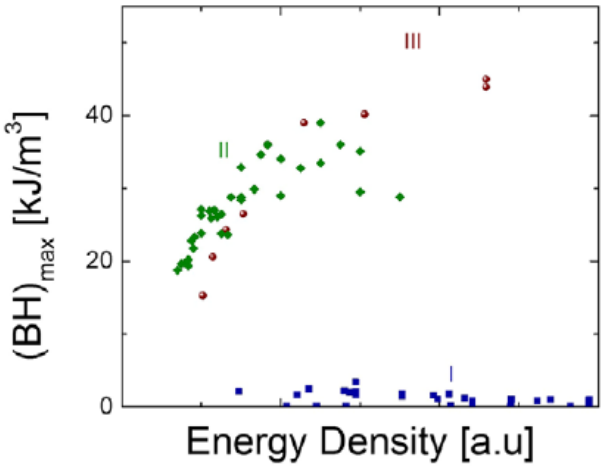

Figure 2-11 Relationship between maximum energy product (BH_{max}) and energy density (anarbitrary unit) [2].

SEM images from Region 1 (BH_{max} = 0.1 kJ/m³) and Region 3 (BH_{max} = 45 kJ/m³) show the slow and the faster solidifications (Figure 2.12). Three different phases are seen: $Nd_2Fe_{14}B$ (hard magnetic phase, Φ1), Fe and Nd-oxide. This oxide phase reverses the magnetic domains resulting in a reduction in coercivity. Moreover, oxides reduce the percentage of the volume of the magnetic phase, which causes a reduction in remanence. Faster cooling rates caused by higher laser velocity provide a high percentage of the Φ phase. Even though some Fe is seen, there is a far lower amount ofit than in the previous slow-cooled sample. XRD patterns of the fast and slow cooling solidifications are shown in Figure 2.13.

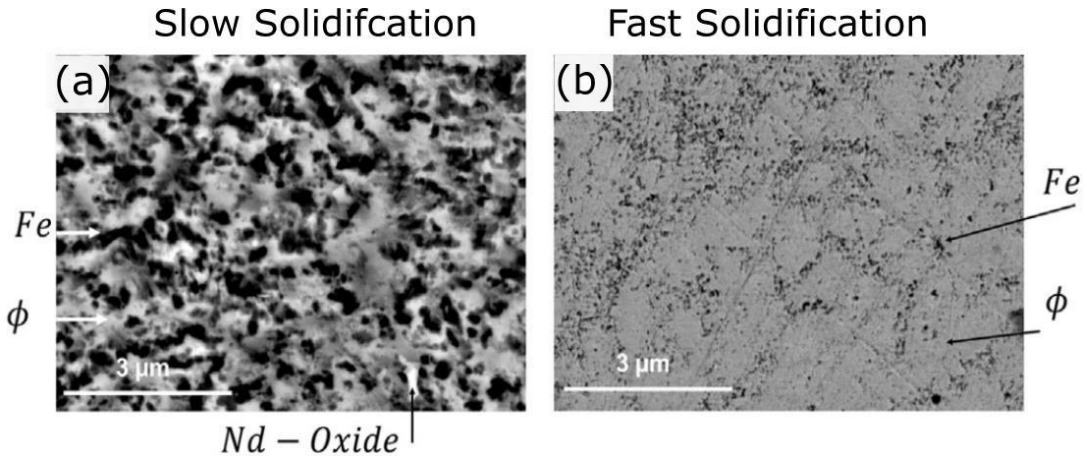

Figure 2-12 a) SEM picture of the printed sample from Region 1, slow solidification; (b) SEM picture of the printed sample from Region 3, fast solidification [2].

It was concluded that faster cooling is essential for direct crystallization of the peritectic $Nd_2Fe_{14}B$ phase. Additionally, it provides a smaller grain size thereby enhancing the coercivity. In contrast, the high presence of the α-Fe phase in the slow cooled part lowers the density of the hard-magnetic phase, thereby reducing the remanence.

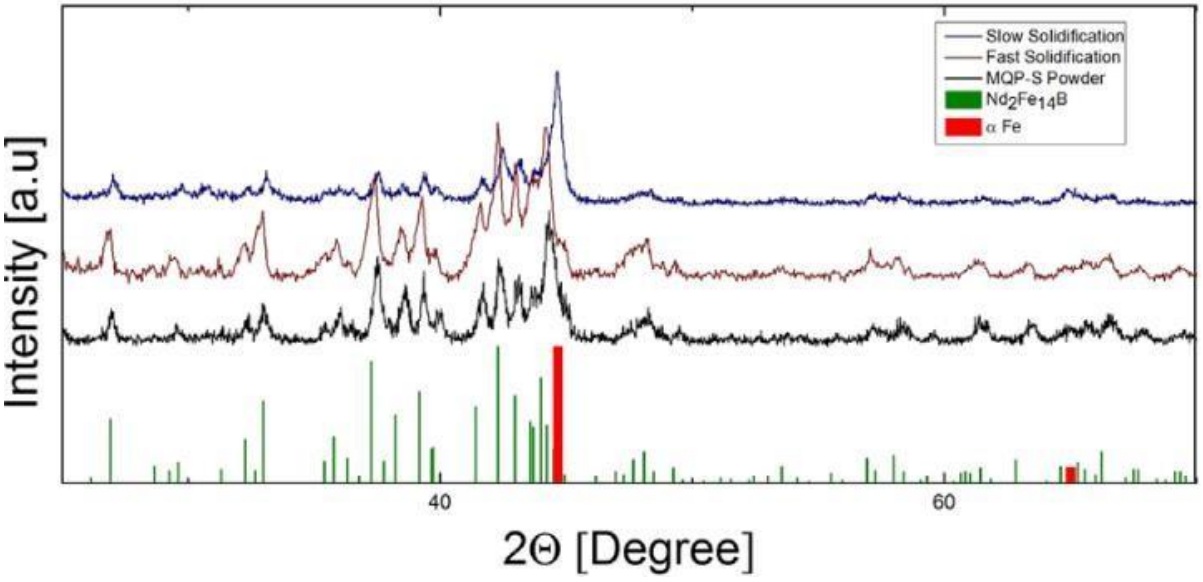

Figure 2-13 XRD patterns of slow and fast cooled samples compared to the starting MQP-S powder. The theoretical spectra of $Nd_2Fe_{14}B$ and α-Fe are added as a guide [2].

The influences of the printing parameters were studied in more detail by [78]. The results showed that the high magnetic properties were obtainedby the energy line between 0.032 and 0.048 Ws/mm, (Energy Line = Laser Power/Laser Speed). A plot showed that both magnetic polarization and the sample densities decrease with the increasing *LT* from 20 to 70 µm (Figure 2.14).

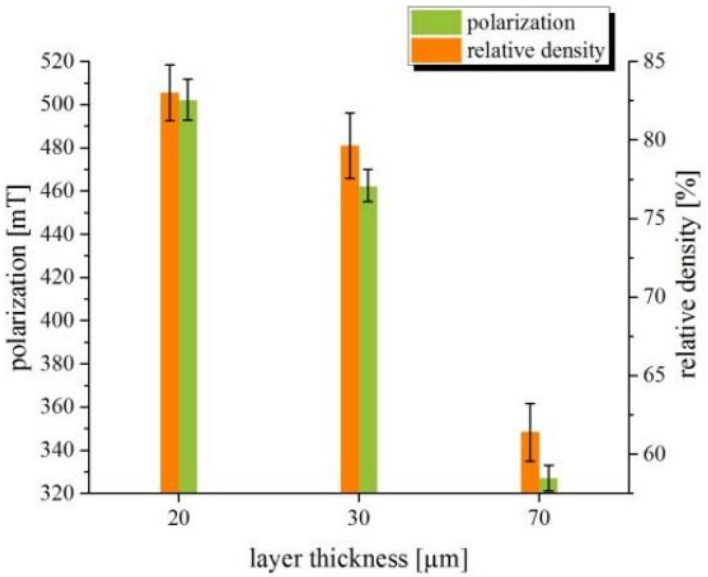

Figure 2-14 Magnetic polarization and the relative density of the samples with respect tolayer thickness [78].

The SLM parameters for NdFeB magnets were studied also by [79]. In their paper, different types of scan strategy and support structures were studied in addition to scan parameters. Their results showed that there is a linearrelationship between density and the polarization of the samples, as shown in Figure 2.15 .

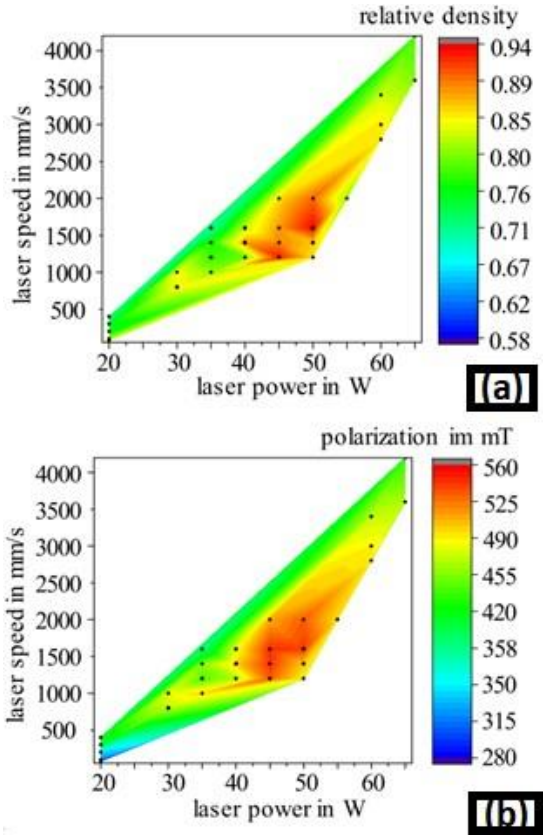

Figure 2-15 (a) Relative density of the specimens and (b) Magnetic polarization of the specimens depending on laser power and laser speed [79].

[80] studied SLM-printed permanent magnets by producing a powder with induction melting, in the composition of Fe_{75}-Nd_{18}-B_7 book mould cast (BMC), following shredding, balling and sieving of the powder. It was found that the faster cooling rates in the SLM printing cause a finer microstructure compared to the BMC magnet, which increases the coercivity, as seen in Figure 2.16. The smaller grains cause better wettability of the Nd-rich phase, hence better decoupling, and subsequently, better coercivity. On the other hand, the *Br* value of the SLM magnets is lower since the amount of the hard magnetic phase is lower than that of the BMC, in addition to the three-times-higher non-ferromagnetic oxides phase in the SLM parts [80] (see Table 2.5).

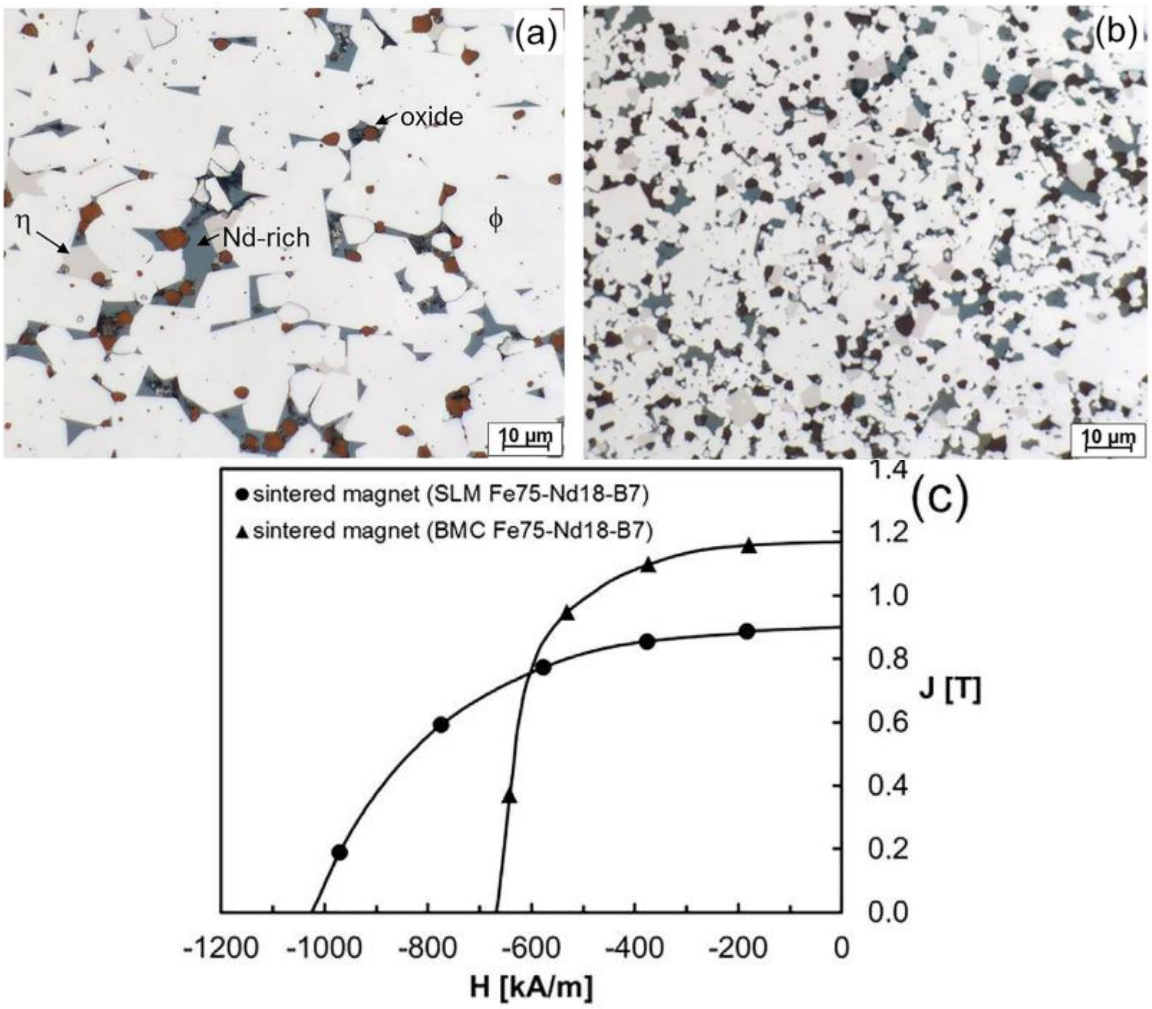

Figure 2-16 Microstructure of a sintered magnet made of (a) BMC Fe_{75}-Nd_{18}-B_7 material and (b) SLM Fe_{75}-Nd_{18}-B_7 material, (η phase=NdFe4B)[80].

Table 2-4 Phases amount on SLM and BMC magnets [80]

	Φ	Nd	Oxides
SLM	76.3	7.6	9.1
BMC	81.88	7.4	3.3

Single tracks to investigate the stability of the melt pool studied by [81]. It was found that layer thickness played a crucial role in melt pool stability. A small layer thickness is required to acquire sufficient magnetic properties, while the remaining parameters had less impact on the magnetic properties. Grain sizes would coarsen with the higher *LT* because of the slower cooling rates compared to the smaller *LT*. The paper suggests

that the finer grains in the smaller *LT* are the reason for the higher coercivity. Because there is no difference in the Φ phase in either sample, it was concluded that the Φ phases are not affected by the process as much as the overall microstructure [81].

Three types of NdFeB alloy with laser powder bed fusion were investigated by [82]: (a) typical sintered magnet/over stoichiometric Nd; (b) close to stoichiometric (14:2:1); and (c) over stoichiometric Fe/composite magnets, by laser powder bed fusion (*L-PBF*). The identified phases in the prepared powders are Φ, Nd-rich phase, fine dispersed boride in (a) and Φ, lower Nd content, *α-Fe*, boride, η phasein (b), and (c), as seen in Figure 2.17.

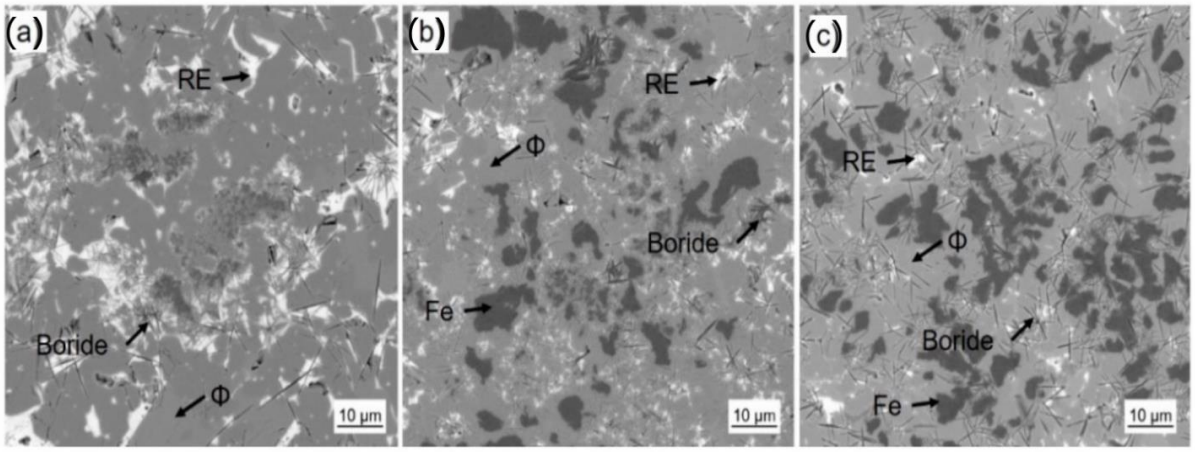

Figure 2-17 Three different types of Nd-Fe-B alloys (a) sintered magnet type/ over stoichiometric Nd,(b) near stoichiometric and (c) composite magnet /over stoichiometric Fe (the η phase cannot be seen due to its close atomic density to the Φ phase) [82].

It was reported that the magnetic properties of the printed "(a) sintered magnet alloy" and "(b) near stoichiometric alloy" were improved with 2 step heat treatment (600°C for 10 min. and 500°C for 60 min.), while the magnetic properties of "composite magnet" could not improve. The other finding is that as the Nd content in the alloy powder decreases, coercivity decreases and B_r increases. Additionally, novel nanocrystalline structures are detected in (a) and (b), which are spherical structures consisting of nanocrystalline Φ phase grains surrounded by an Nd-rich phase, as seen in Figure 2.18 [82].

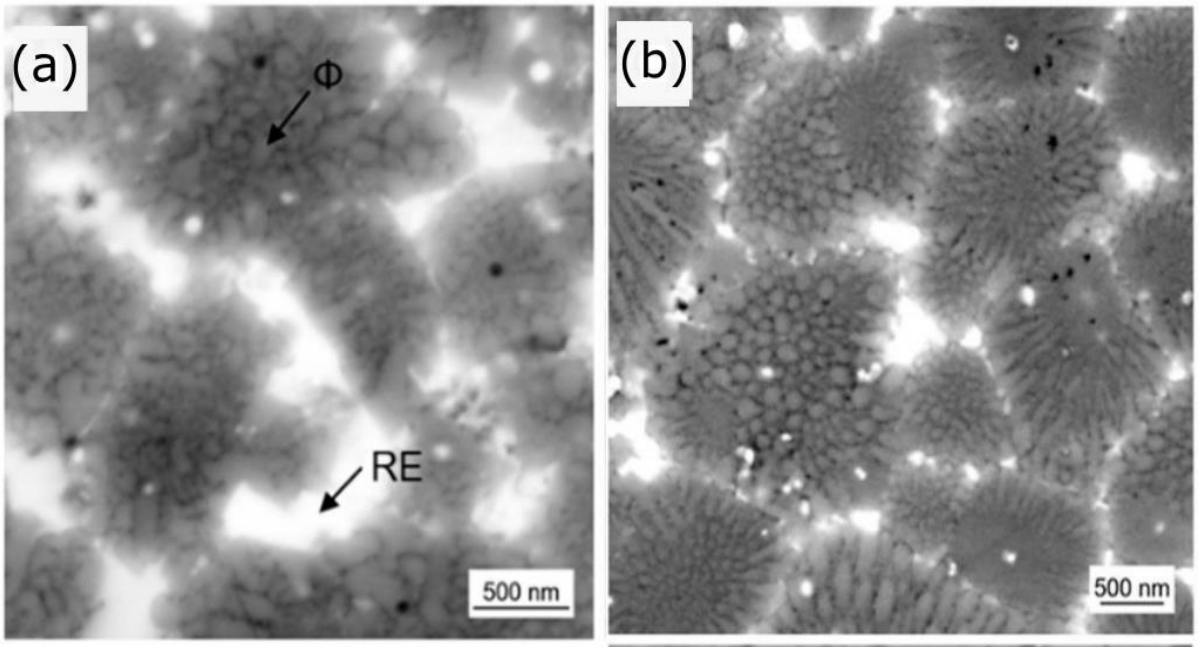

Figure 2-18 SE using backscatter electron detector of the microstructure of L-PBF samples (a) sintered magnet alloy and (b) near stoichiometric alloy [82], [83].

The microstructure and phases of SLM-printed NdFeB magnets were investigated by [83]. It was found that the SLM phases mainly consist of $Nd_2Fe_{14}B$ phases with small amounts of precipitations and cracks in the parts and that the brittle $Nd_2Fe_{14}B$ phases restrict the density and integrity of the parts. It was also found that the residual stresses in a smaller sample are higher since the larger volumes can distribute the heat more efficiently. Hence, smaller samples locally crack where residual stresses are higher than the material strength. Cracks would occur mainly at the interface of the main phase and the precipitated phases due to their different thermal expansion coefficients, and in the heat-affected zone near the boundaries due to the residual and phase transition stresses. Additionally, it was found that the microstructure of the L-PBF NdFeB magnet is different from the sintered magnets since there is a HAZ, cores and boundaries in the L-PBF magnets [83].

The illumination pattern and strategies have an impact on the density and magnetic properties of NdFeB magnets. The scan strategies are shown in Figure 2.19. It was concluded that the scanning strategy without meander promises to be a good compromise in between magnetic properties and density, while the remaining strategies do not [84].

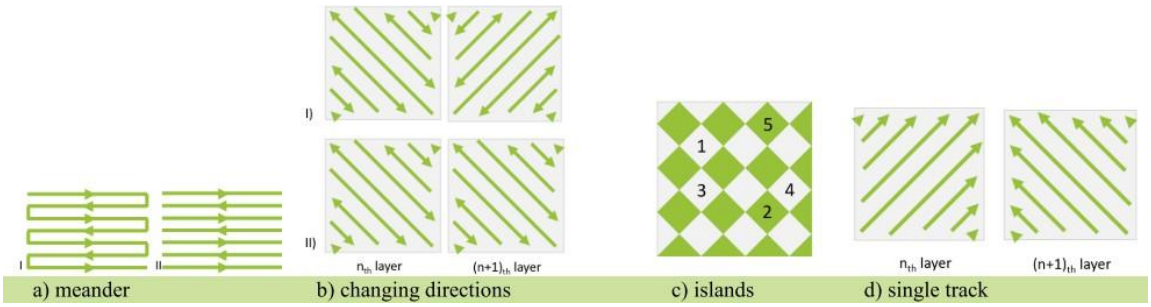

Figure 2-19 *Different illumination patterns (a) with (I) and without (II) meanders; (b) rotation of the scan vectors of 90° with each layer (I) or not (II); (c) Islands are distributed differently for each layer; (d) Single track illumination with no alternation of the scanning direction within one layer* [84].

The maximum magnetic properties of the SLM NdFeB magnet in literature are H_c 885 kA/mm and B_r 0.63 T, which are the highest results obtained so far. It was concluded that the area energy input, E_A, ($EA = \frac{EL}{HD} = \frac{LP}{(LS*HD)}$), is the main parameter that determines stable process parameters. The safe E_A range is between 0.6 and 2.3 J/mm² [85].

2.6. Improving Magnetic Properties in Processing and Post Processing Techniques

Many techniques have been used to improve the magnetic properties of NdFeB magnets. They can be classified into six groups: heat treatment, infiltration, grain boundary diffusion process, grain refinement, doping, and intergranular addition.

2.6.1. Heat Treatment

[86] studied the effect of heat treatments on the microstructure of NdFeB magnets. In the study, magnetic powders were compacted using a cold isostatic press.The magnetic particles were then aligned with a repeated magnetic field followed by post heat treatment at 820°C for one hour after which it was quenched to room temperature. In the final step, several low-temperature annealing treatments were performed at temperatures ranging from 480°C to 580°C. It was found that intrinsic coercivity increases from 439 kA/m to 1,094 kA/m by annealing at 520°C, while annealing does not affect remanence, as seen in Table 2.5.

Table 2-5 Density, remanence, coercivity and the maximum energy product of the as-sintered and annealed parts at 520°C and 560°C [86].

Sample	Unit	As-sintered part	Annealed part at 520°C	Annealed part at 560°C
Density	g/cm^3	7.52	7.54	7.53
B_r	Tesla	1.42	1.42	1.42
H_{cj}	kA/m	439	1094	887
BH_{max}	kJ/m^3	344	381	381

The coercivity increase can be explained by the microstructures of the annealed samples shown in Figure 2.18. The RE-rich phase at the grain boundaries is not well defined in the as-sintered sample, whereas it is much more defined in the annealed sample at 520°C. The RE-rich layer between the RE2Fe14B grains insulates the grains and decouples the exchange interactions. On the other hand, the RE-rich layer is not uniform in the annealed sample at 560°C and shows variations in thickness [86].

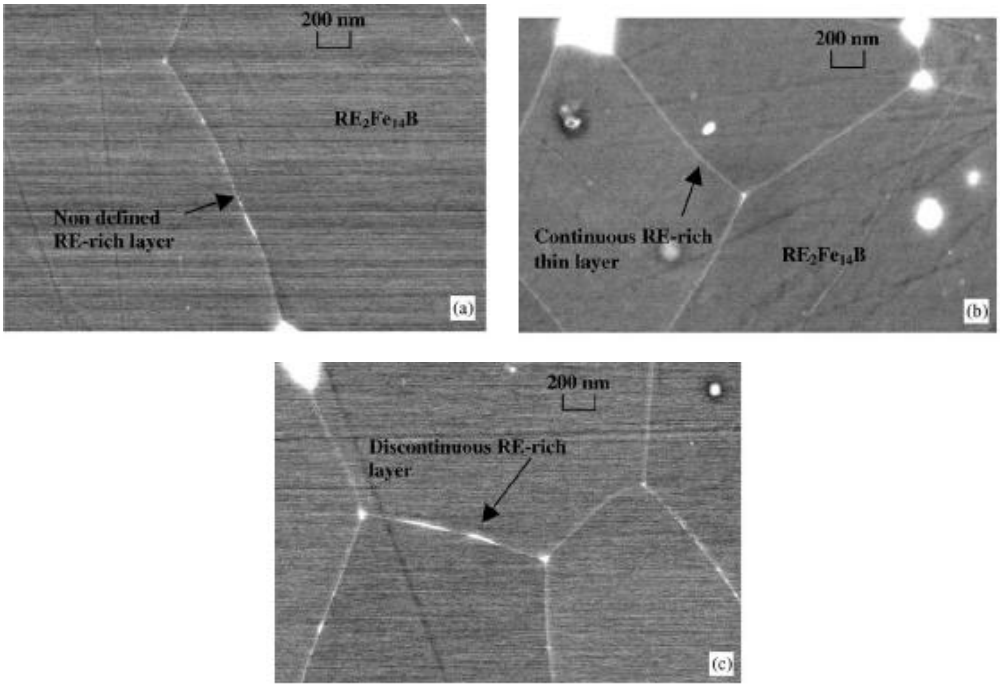

Figure 2-20 *SEM-FEG pictures, (a) as-sintered sample; (b) annealed sample at 520°C; and c) annealed sample at 560°C* [86].

Annealing of sintered magnets studied by [87]. The magnetic propertiesof the annealed samples can be seen in Table 2.6. It is seen that coercivity can be increased from 7.8 to 9.1 kOe by annealing. However, the annealing temperature has to be considered well due to the reduced coercivity after 580°C [87].

Table 2-6 Room temperature magnetic properties of as-sintered magnets and annealed magnets at 480°C, 580°C, 680°C, 780°C and 880°C [87].

Magnet	H_{cj} (kOe)	B_r (kG)	BH_{max} (MGOe)
As-sintered	7.8	12.1	33.5
Annealed at 480°C	8.5	11.9	32.7
Annealed at 580°C	9.1	12.1	33.7
Annealed at 680°C	8.0	12.0	32.9
Annealed at 780°C	7.3	12.2	34.7
Annealed at 880°C	7.2	12.0	33.2

The application of heat treatment on SLM-printed NdFeB magnets was studied by [88]. The study concluded that parameter optimization is more efficient than post-heat treatment in reducing the porosity of laser powder bed- printed NdFeB magnets. Crack formation originating from the internal stresses is the main cause of the sample failure. These are mostly attributed to the high HD causing low energy density, hence insufficient material melting and lack of fusion between thelayers. The other important result is that the porosities are still in the sample, at the same size and geometry, after the heat treatment since the treatment temperature is below the melting point of the material [88].

2.6.2. Infiltration

Infiltration of NdCuCo and PrCuCo into binder jetting printed isotropic NdFeB bonded magnets examined by [21]. Samples were printed with a mix of commercial resin-coated NdFeB powder and diethylene glycol (DEG) as a binder. Theywere then placed in a furnace at 150°C for two hours for binder curing. Afterwards, infiltration alloys NdCuCo and PrCuCo, which are low melting point eutectic alloys, were placed on the top of 2 mm thick samples and treated at 700°C for four hours.

Table 2.7 shows the densities and magnetic properties of the as-printed and infiltrated parts. Mechanically stronger and denser parts with better coercivity can be obtained through infiltration.

Table 2-7 Density and magnetic properties of as-printed and infiltrated parts [21].

Sample	Density (g/cm^3)	H_{ci} (kA/m)	B_r (T)
As-printed	3.3	732	0.35
NdCuCo infiltrated	4.3	1,345	0.31
PrCuCo infiltrated	4.3	1,233	0.25

The non-ferromagnetism of the infiltration alloys can explain the reduction in remanence. The increase in the coercivity can be explained by the non-ferromagnetic phase, which acts as a pin, inhibiting the domain wall motion and blocking reversal domain nucleation and growth [21] The other study was made by [22] ,who combined the Nd-Cu infiltration and post-annealing, increasing coercivity from 19.0 kOe to 26.1 kOe .

2.6.3. Grain Boundary Diffusion

The grain boundary diffusion process (GBDP) is the demanded technique to improve coercivity by isolating hard-magnetic phase grains. NdHx-Cu mixed powder to perform GBDP on NdFeB magnets studied by [89]. In the study, hot deformed NdFeB magnets were dipped into a solution of NdHx-Cu nano powders and ethanol for coating.

The coated magnets were then heat treated at 550°C, 600°C, and 700°C for one hour in a vacuum furnace and rapidly quenched with argon gas. Figure 2.21 shows the increasing coercivity of the hot deformed magnet after heat treatment at 600°C for one hour by removing internal defects or strain. Coercivity can be increased further by applying GBDP, from approximately 16 kOe to approximately 21 kOe. However, remanence decreases from 13.9 kG to 13.0 kG due to the addition of non-magnetic material [89].

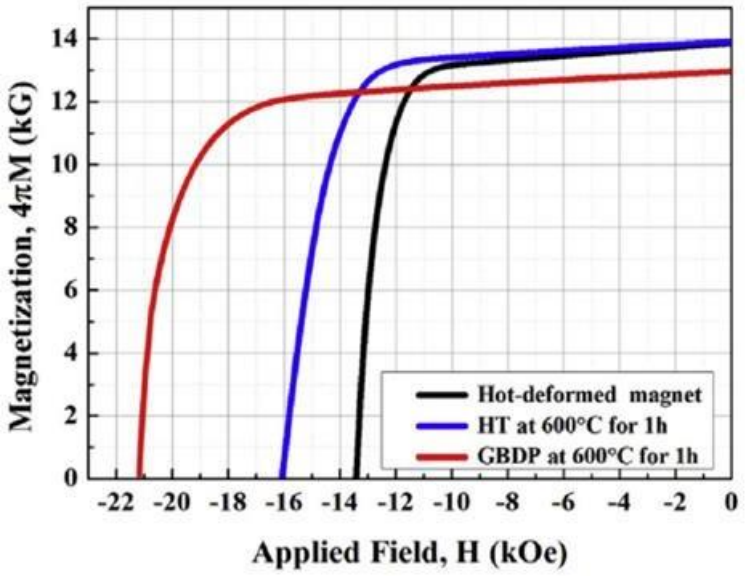

Figure 2-21 Demagnetization curve of the hot-deformed magnet, with heat treatment and GBDP by NdHx-Cu[89] .

In another study, Nd-Dy-Al alloy was used for GBDP. The results showed that following the GBDP, there were Dy-rich shells surrounding the (Nd, Ce)$_2$Fe$_{14}$B grains, which separate the grains and inhibit exchange coupling. Figure 2.22 shows that as the diffusion time is prolonged, coercivity increases while BH_{max} decreases after seven hours due to the decrease in B_r. The excessive Dy diffusion into the matrix grains reduced the B_r; hence it is important to find the optimum diffusion time, in this case seven hours [90].

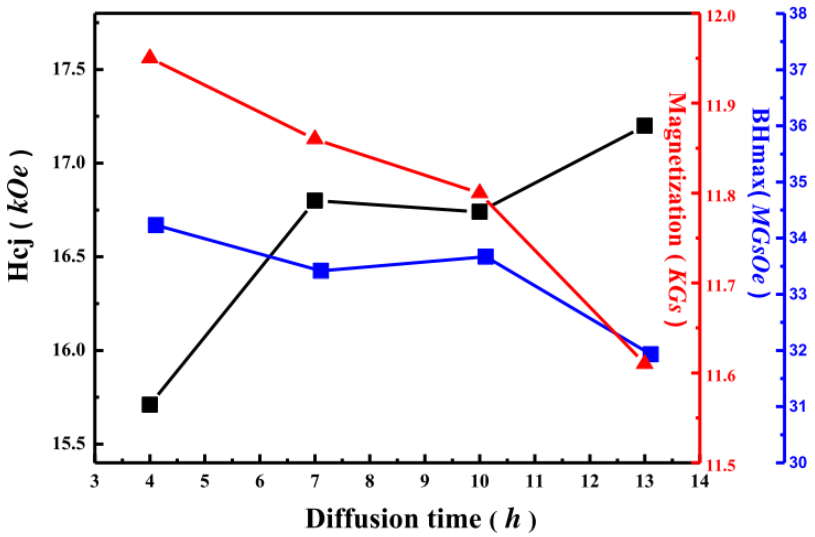

Figure 2-22 Magnetic properties of Nd-Dy-Al diffused samples as a function of the length of diffusion time [90].

The infiltration mentioned previously is one of the common methods used for coercivity improvement; however, it is good only for the thin magnet slices. Therefore, [91]combined chemical bath deposition (CBD) and GBDP to improve the magnetic properties of thick magnets. In the study, magnetic powder was dipped into a solution of alcohol and 0.2% terbium chloride anhydrous ($TbCl_3$) for 10 minutes. The coated powders were then compacted under the 2.25 T magnetic field. The results showed that coercivity increased from 11.89 kOe to 14.72 kOe.

During the infiltration, Tb atoms would enter the $(PrNd)_2Fe_{14}B$ phase on the grain surface, partially substituting to the hard phase and forming $(PrNd, Tb)_2Fe_{14}B$. The higher magneto-crystalline anisotropy field of the $Tb_2Fe_{14}B$ was found to be the reason for the coercivity increment [91].

2.6.4. Grain Size

Effect of grain refinement on coercivity was studied by [92]The relationship between coercivity and grain size is seen in Figure 2.23.a. As grain size decreases, coercivity increases until grain size reaches D = 4.5 μm; then there is a drop in coercivity. SEM analyses were performed for the 4.5 μm and 3 μm grain size samples to investigate the reason for this drop.

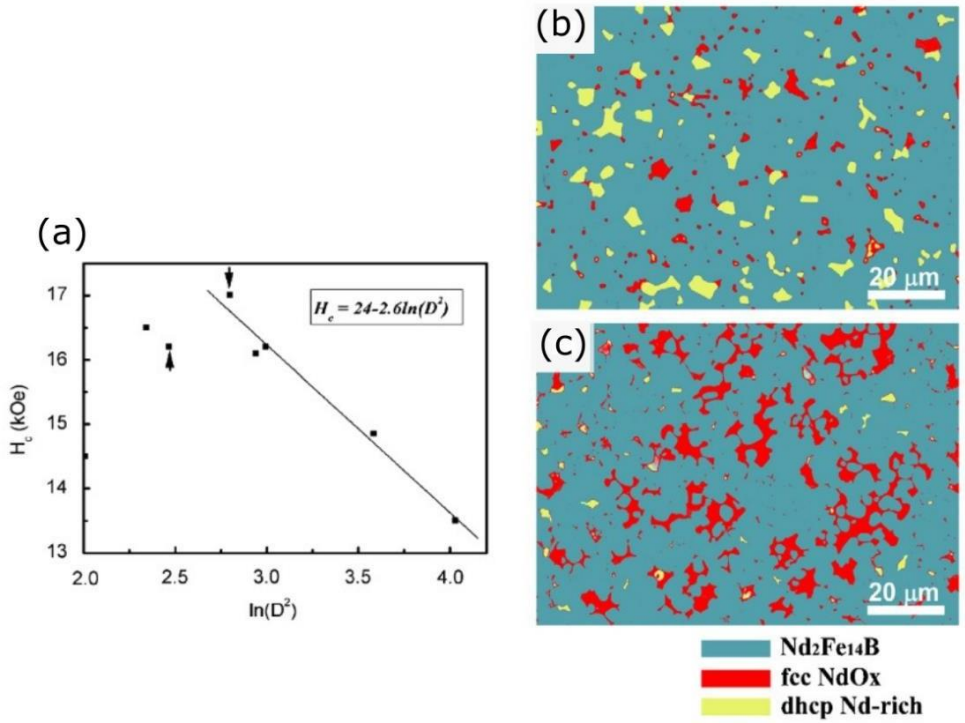

Figure 2-23 *(a) Coercivity and logarithm of the square of grain sizes. The arrows indicate the two samples on the right side; (b) SEM images of the sample grain size 4.5 μm; and (c) 3 μm* [92].

The 4.5 μm grain size sample has a homogenous distribution of an Nd-rich phase with a lower oxygen content than the 3 μm grain size sample. Moreover, the 3 μm grain size sample has some conglomeration of an NdO_x phase with the Nd-rich phase. Furthermore, when the fractured surface of the 4.5 and 3 μm grain size samples were analysed, it was observed that there is a smooth surface in the 4.5 μm grain size sample, which shows that the fracture occurred through the Nd-rich grain boundaries surrounding the $Nd_2Fe_{14}B$. In contrast, a number of sharp edges were observed in the 3 μm grain size sample, indicating the absence of grain boundaries [92], [15] thereby causing a reduction in coercivity through exchange coupling.

2.6.5. Element Doping

Element doping is one of the other techniques used to improve the coercivity of NdFeB magnets. Dy, Ga and Co are three of the most well-known doping elements. [93]conducted a project to understand the effect of Ga and Dy doping on the magnetic properties of sintered NdFeB magnets. In that study, Dy and Ga were added during

the powder production, which includes strip casting, hydrogen decrepitation and jet milling.

The theory behind the increasing coercivity is explained by the high anisotropy field of the Dy entering the hard magnetic phase. Dy enters the hard magnetic phase and replaces the Nd to form $Dy_2Fe_{14}B$, which has a larger anisotropy field than the $Nd_2Fe_{14}B$ of 15.8 T and 7.6 T, respectively. Therefore, coercivity increases with Dy doping. On the other hand, the saturation magnetic polarisation of $Dy_2Fe_{14}B$ is lower than that of $Nd_2Fe_{14}B$, at 0.7 T and 1.6 T, respectively, which causes a reduction in *Br* and the BH_{max}.

In addition to using Dy, coercivity can be increased by doping with Ga. It was found that Ga, including the Nd rich phase, separates the magnetic grains and inhibits or weakens the exchange coupling between them. Moreover, Ga doping improves temperature stability. However, it reduces B_r and BH_{max} due to the non-magnetic structure of Ga [93].

Doping with Ce is another coercivity enhancement method for NdFeB magnets. Coercivity increases significantly with the addition of Ce while the B_r and the BH_{max} values decrease. Ce prefers to be distributedat the grain boundaries instead of diffusing into the hard 2:14:1 phase. The Ce in the grain boundaries decreases the Fe content and provides a pinning effect which improves coercivity. Moreover, Ce doping refines the grains, thus enhancing coercivity [93].

2.6.6. Intergranular Addition

The other coercivity improvement technique is the intergranular addition of elements, which improves coercivity significantly with small decreases in remanence and maximum energy product. An additional element is mechanically blended with the magnet powder during that process.

Nickel as an intergranular addition to the NdFeB alloy was studied by [17] Various amounts of Ni powders were blended with NdFeB powder to understand the effect of Ni on magnetic properties. Then Ni blended NdFeB powders were aligned in the

magnetic field and pressed in the green compact through the perpendicular direction of the alignment. In the final stage, the green compacts were sintered at 1065℃ for four hours followed by quenching to room temperature under Ar gas.

Ni enters the hard magnetic phases of Nd2Fe14B, replaces the Fe atoms, and forms the Nd2(Fe, Ni)14B phase, as shown in Figure 2.24.

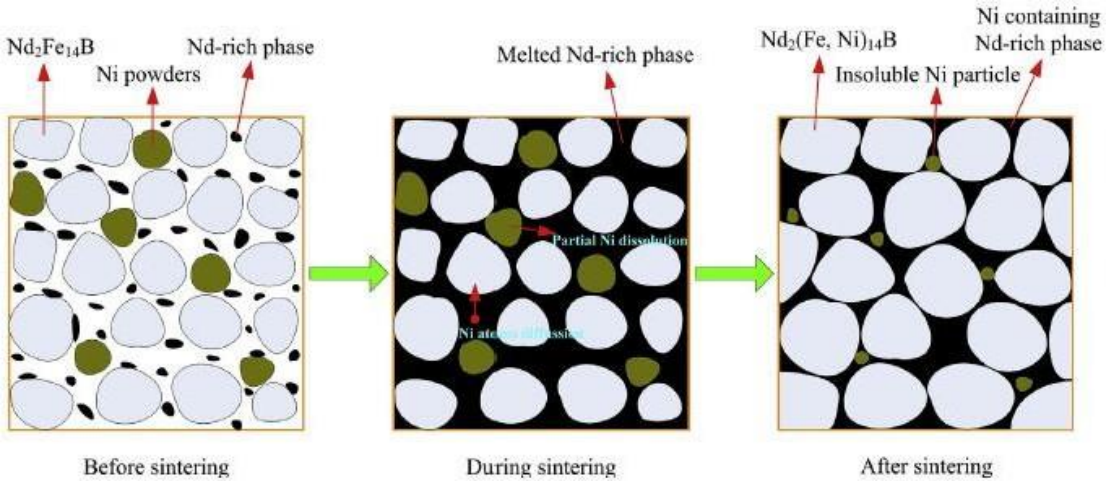

Figure 2-24 Schematic view of the sintering mechanism with the intergranular addition ofNi powders [17].

Moreover, the average grain size in the magnets decreases from 9.19 μm to 8.54 μm by adding 0.3 wt% Ni. The refractory Ni particles are believed to aggregate at the grain boundaries and inhibit grain growth during the sintering. Additionally, it improves the distribution of the Nd-rich phase resulting in a more homogenous microstructure. It reduces the defects on the grain surface and inhibits reversal domain nucleation. Lastly, clearer and continuous grain boundaries are enhanced. All these factors increase the coercivity of NdFeB magnets [17].

WC nanoparticles [94], Nd-Co[18] ,Pr-Co [19], Ta [20], and Dy-Co [95]are some of the other intergranular additions to NdFeB magnets.

2.7. Summary and Comparison

Previous researchers have developed binder jetting, SLA, FDM and BAAM magnets. However, these magnets have limitations in terms of magnetic properties. Because they have polymer in the feedstock material, the volume fraction of magnetic structure drops, which causes a reduction in remanence.

The density of binder jetting NdFeB magnets is nearly half that of sintered magnets, at 3.54 g/cm^3 [68] and 7.5 g/cm^3, respectively. Additionally, the remanence value of the binder jetting magnets is lower than both IM and compression bonded magnets (binder jet magnet = 0.3 T, IM magnet = 0.5 T, compression bonded magnets = 0.65 T [68]). On the other hand, the remanence of the BAAM printed NdFeB magnet is higher by a narrow margin than IM. However, it is still lower than the remanence of sintered magnets (BAAM magnet B_r = 0.51 T, IM magnet B_r = 0.48 T [67], sintered magnet B_r = 1.2 T by Arnold Magnetic Tech).

In contrast, there is very little literature on SLA magnets. Nevertheless, it can be stated that SLA magnets are not a promising candidate for NdFeB magnets due to the limited magnetic properties of the polymer in them. However, SLA has the advantage of producing graded magnets [65].

FDM is also not a promising AM method due to the low B_r and low density of the samples compared to IM and sintered magnets (B_r =0.31 T, 0.38 T and 1.2 T; density: 3.57 g/cm^3, 4.35 g/cm^3 [62] and 7.5 g/cm^3, in FDM, IM and sintered magnets, respectively).

EBM, LENS and SLM are expected to be more promising than the polymer-based AM methods. However, EBM is not a good candidate for NdFeB since EBM uses an electron beam which charges the powder and raises the powder through the build chamber, which could damage the machine [66].

LENS and SLM are the most promising methods despite SLM magnets not having high density like their sintered counterparts due to their intermetallic structure. The high cooling rate of SLM helps to reduce grain size close to magnetic domain sizes, thereby

improving coercivity. In contrast to SLM, grains are larger in sintered magnets because of the slow cooling rates [92].

For LENS, no study has been found regarding LENS printing of NdFeB in the literature. However, it has an advantage over SLM as it deposits material only where it is required. Moreover, it can add a second material to make functionally graded magnets [92]. In this study, it was decided to produce NdFeB magnets using SLM.

Table 2-8 Summary of the magnetic properties of AM magnets.

	Density (g/cm3)	***Br* (T)**	**Reference**
Binder Jetting	3.54	0.30	[68]
BAAM		0.51	[67]
FDM	3.57	0.31	[63]
Target	7.5	1.2T	Arnold magnet

Table 2-9 Summary of magnetic properties of SLM-printed NdFeB magnets in the literature.

Density percentage of the magnets	***Br* (T)**	***Hci* (kA/m)**	***BHmax.* (kJ/mm³)**	**Reference**
90.9	0.563	516	35.9	[81]
	0.69	99.71	30.4	[82]
92	0.59	695	45	[2]
	0.51			[78]
97	0.55			[79]
	0.65	603	62	[83]
	0.63	885	63	[96]
	0.55	825		[84]
	0.90	1025		[80]

The achieved magnetic properties through SLM are not as high as in sintered magnets. The obtained maximum magnetic properties from SLM with MQP-S-11-9-20001 powder are H_{ci} = 885 kA.m^{-1}, B_r = 0.63 T, and $(BH)_{max}$ = 63 kJ.m^{-3}, Therefore, it was decided to focus on the post and in-built methods to improve the magnetic properties of the SLM printed magnets.

Heat treatment is an effective method to improve coercivity while having no effect on remanence. Basically, grain boundaries become more defined and continuous, which increases coercivity by inhibiting the exchange coupling between hard-magnetic phase grains.

The other two effective methods for coercivity improvement are infiltration and GBDP. However, they reduce remanence due to the non-magnetic structure of the infiltration and the grain boundary diffusion alloys. Additionally, infiltration has a limitation since it is good only for thin magnets, while GBDP can be applied to thick magnets, too.

Grain refinement is the other promising method which increases coercivity without decreasing remanence. However, it is important to achieve optimum grain size to avoid reduction in coercivity.

Dy and Tb doping is another promising technique, despite some of their limitations. The doping elements enter the hard magnetic phases and substituted with the Nd in them. The high magnetocrystalline anisotropy of the Dy and Tb increases the coercivity of the magnets. However, remanence decreases with Dy doping. Because the smaller radii of the Dy atoms closes up the Fe atoms in the crystal structure of hard phase. The closer Fe atoms causes antiferromagnetic coupling between them and decreases saturation magnetization, thus resulting decrease in B_r.

Intergranular addition is the last method mentioned above which increases coercivity by reducing the grain size, improving the microstructure homogeneity and improving the continuity of the grain boundaries with a slight decrease in B_r. The percentage of the intergranular addition is important to achieve high magnetic properties as it was found that the excess amount of intergranular addition causes a reduction in coercivity.

All the methods mentioned here have advantages, disadvantages or limitations. They have to be considered in detail in order to avoid unexpected reductions in magnetic properties. In this project, it is planned to do heat treatment and Ni infiltration.

Table 2-10 Summary of the density and the magnetic properties achieved by the methods mentioned in Section 2.6.

Methods	
Heat Treatment	• *Hc* increases from 439 kA/m to 1094 kA/m [86]. • Annealing does not affect the *Br* [86]. • Density is not affected by the heat treatment [86].
Infiltration by NdCuCo and PrCuCo.	• *Hc* increases from 732 kA/m to 1345 kA/m, with NdCuCo,1233 kA/m, with PrCuCo [21] • Density increases from 3.3 g/cm3 to 4.3 g/cm3 [21]. • *Br* decreases from 0.35 T to 0.31 T, with NdCuCo, 0.25 T, with PrCuCo [21]. • Hc can be increases more by the post annealing after Nd-Cu infiltration, from 19.0 kOe to 26.1 kOe [21].
Grain Boundary Diffusion	• *Hc* increases from 1273 kA/m to 1671 kA/m, with NdCuCo after GBDP by NdHx and Cu [89] • *Br* decreases from 1.39 T to 1.3 T [89]. • *Hc* increases from 946 kA/m to 1171 kA/m, with chemical bath deposition (CBD) and GBDP by Terbium Chloride Anhydrous ($TbCl_3$) [91]
Grain Size	• As the grain size decreases, coercivity increases until grain sizeD = 4.5 μm, then there is a drop seen in coercivity [92]
Element Doping	• *Hc* increases from around 1114 kA/m to around 1591 kA/m, while *Br* decreases from 1.32 T to 1.24 T with the Ce doping [93] • *Hc* increases from around 954 kA/m to around 2785 kA/m, while *Br* decreases from 1.4 T to 1.2 T with the Dy doping [15]
Intergranular Addition of Ni	• *Hc* increases from around 800 kA/m to around 900 kA/m, but after certain percentage of Ni addition, it starts to reduce, while *Br* decreases from 1.37 T to 1.32 T [17]

Chapter 3: Materials and Methodology

3.1. Materials

NdFeB Alloy Powder

The desired powder morphology for SLM printing is spherical in order to obtain good powder deposition on the build platform, which produces highly dense parts. The commercial spherical NdFeB powder, called MQP-S-11-9-20001, from theMagnequench Corporation was used as a feedstock. It is a spherical powder produced for bonded magnets, particularly by injection molding and extrusion. However, this is the most suitable powder for SLM in terms of its spherical morphology.The chemical composition of the powder is summarised in Table 3.1. Nd, Fe and B are the main elements needed to get desired strong magnetic phase $Nd_2Fe_{14}B$. Other elements are also added in purposes. Praseodymium and cobalt are added to improve corrosion resistance[97] . In addition, it is known zirconium is added to powder to act as $Nd_2Fe_{14}B$ grain growth inhibitor [98]. Titanium addition also increases the amount of $Nd_2Fe_{14}B$ phase by suppressing the $Nd_2Fe_{23}B_3$ formation[99].

Figure 3.1 shows the powder morphology and particle size distribution of the powder. The measured particle sizes ared_{10} = 20.1 µm, d_{50} = 41.1 µm and d_{90} = 70.3 µm, measured using the Mastersizer 3000 laser diffraction analyser.

Table 3-1 Concentration weight of MQP-S-11-9-20001 powder from Magnequench.

Substance	Concentration (Weight%)
Neodymium	17.2
Praseodymium	1.9
Boron	1.7
Cobalt	2.8
Copper	0.1
Titanium	2.1
Zirconium	4.3
Carbon	0.1
Iron	69.8

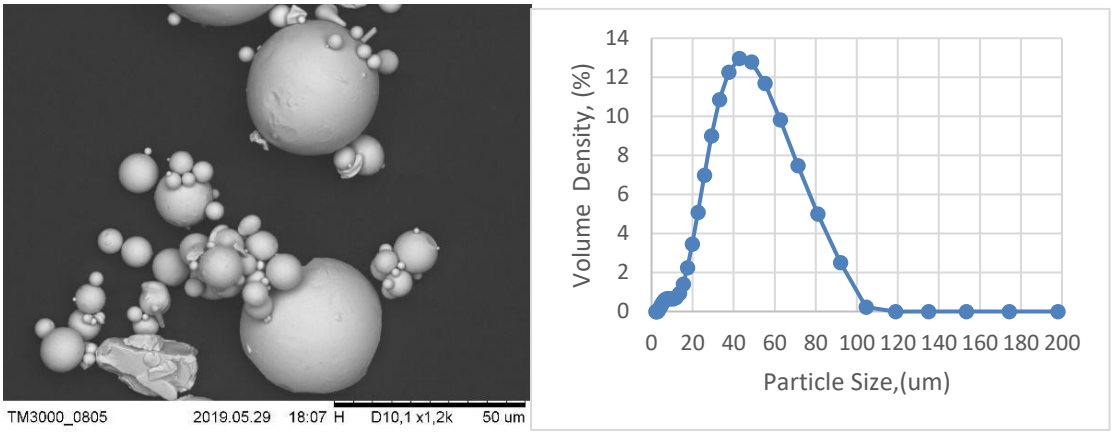

Figure 3-1 (a) SEM results for MQP-S-11-9-20001; (b) particle size- volume distribution of MQP-S-11-9-20001 powder.

3.2. Selective Laser Melting Machine

The powder was processed layer by layer to form cubic specimens with dimensions of 10 mm × 10 mm × 10 mm. Autodesk Netfabb Premium was used for every parameter setting, part positioning, and final data slicing. Samples were placed crosswise, as in Figure 3.2, to avoid any damage originating from the failed samples in the printing. The scanning strategy was rotation of 67 degrees between the layers.

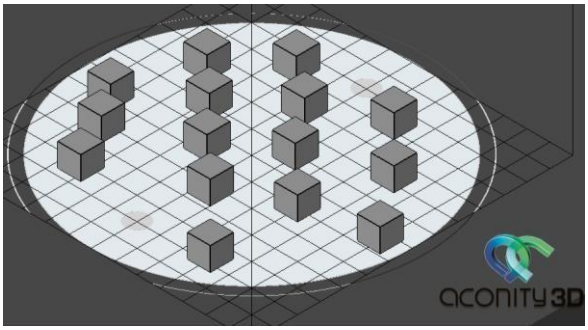

Figure 3-2 Netfabb design file.

Aconity Mini and Aconity Lab selective laser melting machines, consisting of a 1070 nm wavelength, 200 W continuous-wave fibre laser, were used.

The outer view of the Aconity Mini system is seen in Figure 3.3. The Aconity Mini has a Ø 140 mm build platform which can be lowered to a maximum of 150 mm. The powder is fed on the built platform from the powder reservoir fitted in the build chamber using a recoater blade, as seen in Figure 3.4a. The built platform is lowered based on the sample layer thickness in the design file. The powder reservoir rises according to the sample layer thickness and supply factor set in Aconity's software. Then the recoater blade brushes the excess powder from the powder reservoir to the build platform. Finally, the laser scans the freshly layered powder on the build platform according to the design file.

Aconity Lab uses a continuous laser like the Mini, but it has a different powder feeding mechanism. The powder is fed via the hopper at the back of the build chamber area, (as illustrated in Figures 3.4.b and 3.5). The powder flows into the chamber in a controlled manner via the dosing unit. Similarly to the Aconity Mini, the powder is brushed with the recoater blade. The Aconity Lab has a larger build platform, at Ø 170 mm, with a maximum build height of 200 mm.Figure 3.5 shows the outer view of the Aconity Lab system.

Additionally, it has a heated bed capability of up to 1200°C. The size of the heated bed is Ø 70 mm, and it is placed in the centre of the building area where the induction heater unit is found underneath. The oxygen content can be decreased to under 100 ppm using argon gas for both the Aconity Mini and Aconity Lab systems.

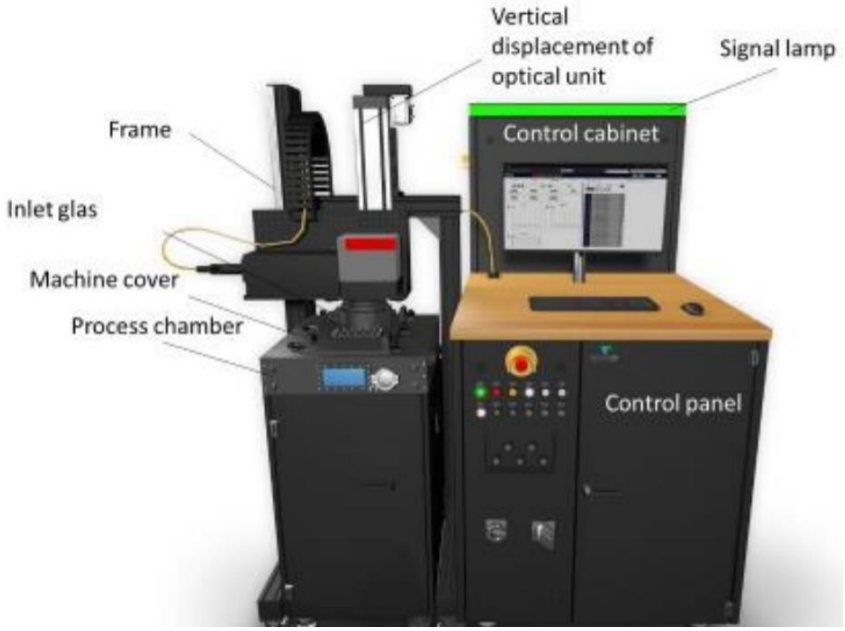

Figure 3-3 Outer view of the Aconity Mini

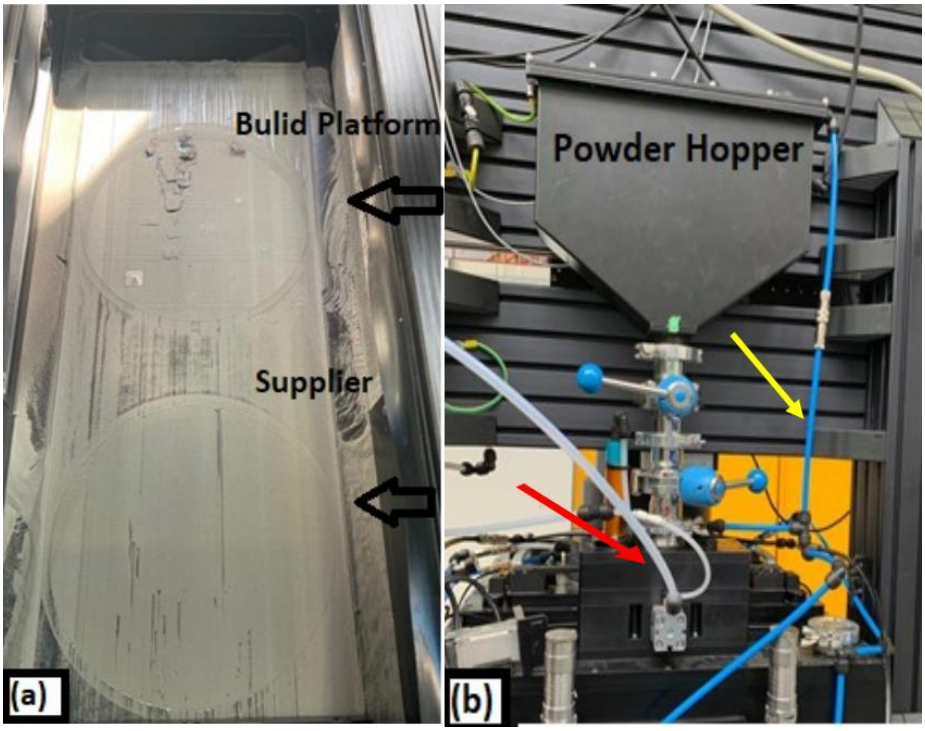

Figure 3-4 (a) The build platform and the supplier powder reservoir of the Aconity Mini;(b) The powder hopper of the Aconity Lab. (Red arrow points the pressurized air pipe connected to dosing unit to supply the powder on build area; yellow arrow points the argon gas pipe connected to the powder hopper and dosing unit).

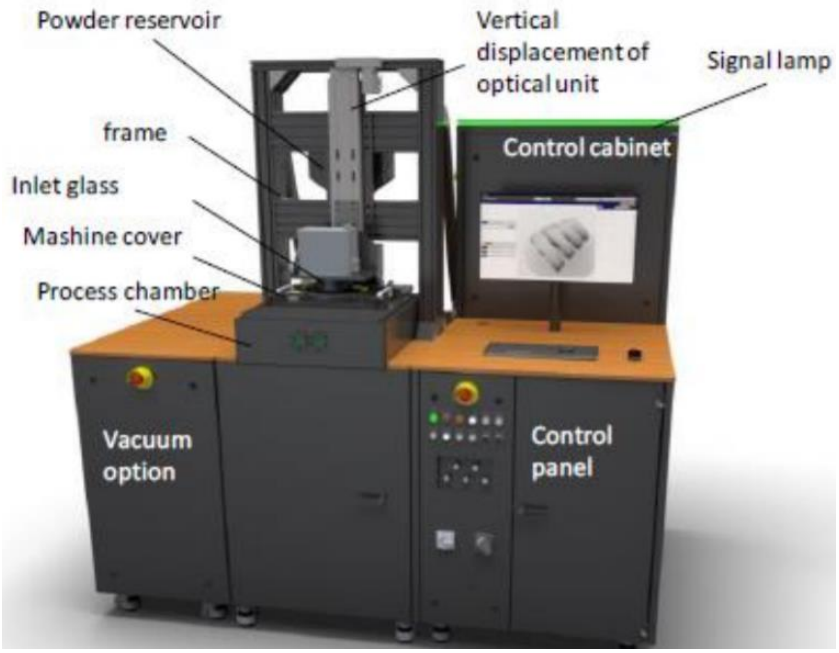

Figure 3-5 Outer view of the Aconity Lab

The printing parameters used in Aconites are as follows: laser velocity or laser speed, v or LS (in mm/s), laser power, LP (in W), hatch distance, HD (in μm), and layer thickness, LT (in μm). The volumetric energy density, ED (in J/mm^3), is calculated using Equation 3.1:

$$ED = LP/(v*HD*LT) \quad \text{Equation 3.1}$$

Samples were built on a stainless steel platform with a diameter of 70 mm for the Aconity Lab and 35 mm for the Aconity Mini. They were removed by hand with the help of a scraper and hammer since the electrical discharge machine with the water- based cooling system caused oxidation of the samples and the building of a support under the samples failed due to their precise design.

3.3. Parameter Design and Optimization

Parameter design was challenging since there was limited literature and paper sharing that detailed the printing parameters. The first trials were run regarding published papers to determine the starting point of the experiments. Then they were optimised regarding the results taken from the first experiments. The heated bed printings were set based on the optimised parameters in Chapter 4.

3.4. Characterisation Equipment

3.4.1. Archimedes Density Test

The densities of the printed samples were checked with an Archimedes test. The samples were measured one by one based on the samples' weights in the air and in the water. Each sample was checked three times, and the average densities were calculated. The density percentages of the samples were calculated based on the density of the commercial NdFeB magnet, 7.5 g/cm^3, taken by Arnold magnets.

3.4.2. Sample Preparation

Samples were cut using a Struers Secotom-50 cutting machine. The samples were mounted in conductive Bakelite in a Buehler SimpliMet hot mounting press. A Buehler AutoMet grinder-polisher was used to grind and polish the samples, which were ground with P600 and P1200 SiC paper for 10-30 minutes. A ChemoMet polishing cloth was used with 0.02-0.06 μm MasterMet colloidal silica for polishing for 10 minutes. A 150 rpm plate speed, 60 rpm head speed, complimentary head rotation direction and a 10-20 N/sample force were applied for grinding and polishing. Afterwards, the samples were dipped in an etching solution of 5% citric acid or 2% Nitalfor 5 to 60 seconds to reveal their grain boundaries. Etching was done for the samples analysed by optical imaging and SEM analyses.

3.4.3. Optical Microscopy

A Nikon optical microscope was used for optical microscopy imaging. It was used to check the continuity of single tracks, microstructural evaluation and crack formation. However, it was not used for the porosity analysis since some parts of the surface were pulled out after the grinding and polishing, causing holes and porosities. These holes affected the porosity analyses in the Image J software.

3.4.4. Scanning Electron Microscopy (SEM) and Energy Dispersive X-Ray Analysis (EDX)

Philips XL30 SEM, Inspect F and Inspect F50 were used to analyse the grain morphology. Images were respectively taken at 10 kV and 15 kV accelerating voltages for the secondary and backscattering imaging. Elemental mapping and quantitative element analyses were performed using Inspect F and Inspect F50.

3.4.5. X-Ray Diffraction Analysis

PANalytical X'Pert^3 powder in reflection mode with Cu-Kα radiation, a 10°-120° scanning window and PANalyticalAeris with Cu-Kα radiation, 10°-90° scanning window were used for the phase analysis. The XRD data were analysed by the International Centre for Diffraction Data's (ICDD) PDF4 software for phase identification. GSAS software was used for the quantitative phase analysis.

3.4.6. Magnetic Testing

The magnetic test was performed following three different methods: permeameter for the hysteresis loop, Helmholtz coil-fluxmeter for remanence and SQUID (Superconducting Quantum Interference Device) magnetometer for the hysteresis loop. The first two tests were performed by Arnold Magnetic Technologies, and the samples were magnetised with a 100 kJ charge and a 5500 kA/mfield to reach their magnetic saturation before the testing.

Complex-shaped magnets can be tested by Helmholtz coil and fluxmeter without sample damage. The original purpose of the Helmholtz coil is to create a very homogeneous magnetic field by two separated circular coils with equal currents flowing in them.The currents create a homogenous magnetic field between two coils. To measure the magnet, it is placed on a flat plane in the magnetic field created between the coils. Then it is removed, and it induces a voltage in a fluxmeter [100]. Figure 3.6 shows the example of Helmholtz coil and Fluxmeter.

Figure 3-6 (a) Helmholtz coil and (b) fluxmeter [101].

On the other hand, SQUID detects the magnetic flux changes originated by mechanically moving the sample through superconducting pick-up coils which are converted to a voltage [102]. SQUID is sensitive enough to measure the small changes in a magnetic field, and it can test only small pieces of magnets. However, not only the remanence but also the coercivity can be tested by it.

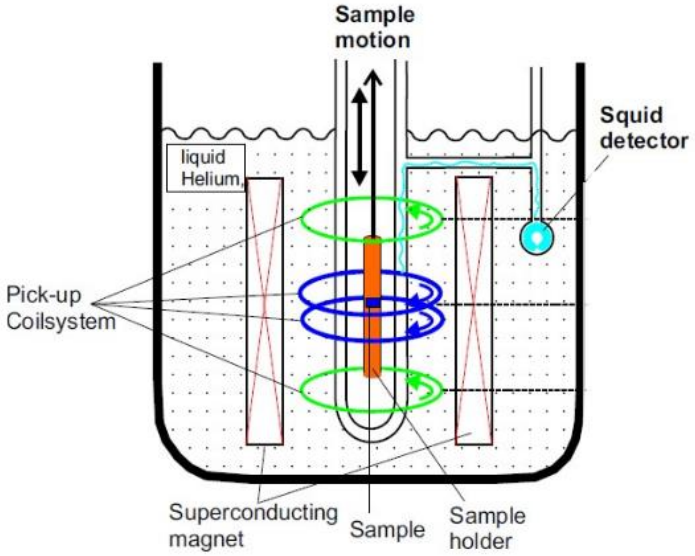

Figure 3-7 Scheme of SQUID set up.

The sample tested by the Squid magnetometer was cut into small pieces since the maximum sample fit in the Squid is 1 mm × 1 mm × 1 mm. Three measurements weretaken from the top, middle and bottom of the sample to find whether the magnetic properties were the same across the sample. Despite the magnetic properties being mostly the same for three of the samples, as seen in Table 3.2, the coercivity results were less than half of the coercivity results taken by permeameter, which was 891 kA/m. This drop is very likely related to the sample cut before the Squid test. The variability in H_{ci} results is much higher, SD: 39.97, than B_r, SD: 0.046. It is because coercivity is most likely related to the material`s external properties and sample cutting might reduce the coercivity. Hence, it was concluded to run the magnetic tests with the Helmholtz coil-fluxmeter and permeameter.

Table 3-2 Squid Results of the pieces taken from the top, middle and bottom of the sample.

Squid Test	***H_{ci},kA/m***	***B_r/T***
Top	*377*	*0.691*
Middle	*328*	*0.61*
Bottom	*300*	*0.61*
Standard Deviation, SD	*39.97*	*0.046*

3.4.7. Micro Computed Tomography

The Micro CT analysis was performed to evaluate the internal cracks and porosity of the samples. Images were taken by Luke Ashton performing Micro CT, using the Nikon Metrology XTH 225/320 LC at the advance manufacturing research centre (AMRC).

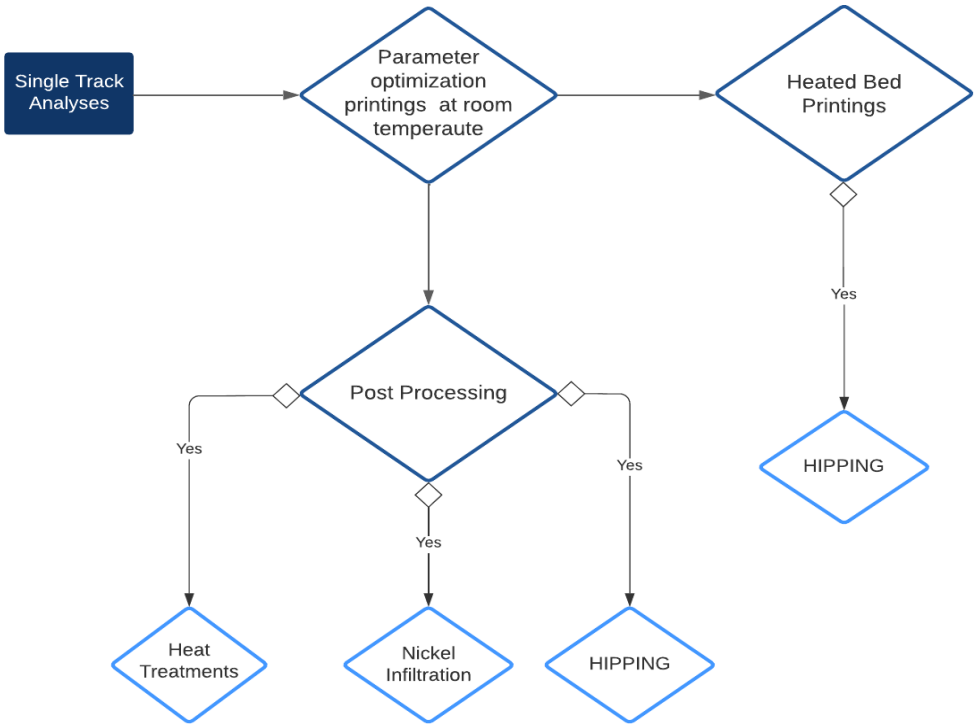

Figure 3-8 Project Flow Chart

Chapter 4: Effect of Parameters on Density and the Magnetic Properties of SLM-Printed NdFeB Magnets

4.1. Introduction

This chapter investigates the influences of the printing parameters on sample density and magnetic properties. Samples were printed using the Aconity Mini and Aconity Lab. The chapter aim to evaluate the feasibility of the selective laser melting of NdFeB magnets. The effects of laser power (*LP*) (W), hatch distance (*HD*) (μm), and layer thickness (*LT*) (μm) were evaluated with respect to the density results taken by the Archimedes density test. Optical images taken by the Nikon, SEM images taken by XL30 SEM and Inspect F, and Micro CT images taken by Nikon Metrology XTH 225/320 LC helped us to understand the density changes with the various scan parameters. Additionally, the relationship between the magnetic properties and the densities of the samples was examined using the Archimedes density test and Helmholtz Coil-Fluxmeter test results.

Finally, further evaluations of the relationship between the magnetic properties and the scan parameters were improved with the *XRD* analysis results. This chapter concludes that low laser energy densities, between 50 and 100 J/mm^3 enabled the fabrication of samples with up to 95.72% density. Pores and crack defects were observed mainly on the edges of the samples. Regarding to the printing parameters it was found that *ED* is important parameters which affects the density and the magnetic properties of the samples, however it is not the only parameter should be considered in terms of the melting ability of the powder. It was found that the *E,(LP/LS),* is also importantwhich should be in between 0.03-0.04 Ws/mm. Moreover, it is found that the effect of *HD* on density of the samples is higher than the *LT*. Regarding the magnetic properties,magnets with a maximum energy product of 81 kJ/m^3 could be produced without any post-treatment. Furthermore, there is no entirely linear relationship observed between the remanence and the density of the samples. Magnetic properties

increase with increasing volume fraction of the strong magnetic phase, $Nd_2Fe_{14}B$, in the samples.

4.2. Printing Parameters

In the study, SLM parameters, laser power (*LP*), laser speed (LS), hatch distance (*HD*), layer thickness (*LT*) and energy density ($ED = LP/(LS*HD*LT)$), were studied to attain high-density defect-free components.

In this study, using DoE tools was impossible due to the limited parameter data in the literature. It was needed to define a relatively safe *ED* range before going through a detailed analysis of individual parameters. Therefore, at first, parameters were set with the help of some of the published parameters. After relatively safe *ED* was defined, Taguchi method in Minitab software was used to narrow down to combinations of parameters, including 4 independent parameters, *LP/LS/HD/LT*, and a dependent parameter, *ED*. However, the combinations of parameters given by the software were not enough to understand the effect of parameters in detail. Because the limited variant (parameter) could fit the software templates, some essential parameter combinations were missed, which are important to understand the parameter effects. Hence parameters were set in respect of published papers in the literature, then developed in respect of the findings in this project. The details of the parameter settings are given in the rest of this section.

Single-track analyses were conducted before 3D printing to understand better the effect of laser power and speed on the melt pool. The Aconity Mini machine was used for single-track analyses. Single track parameters were set in a wide range of laser power and speed, from 50 W to 140 W and from 1000 mm/s to 1400 mm/s, respectively.

Afterwards, preliminary printings were performed to define a relatively safe energy density range based on the [78] , [79] and [2] parameters, as presented in Table 4.1.

Table 4-1 Preliminary sets of parameters, according to the published papers by [78] , [79] *and* [2]

Sample No.	Layer thickness (µm)	Hatch (µm)	Laser power (W)	Laser speed (mm/s)	Energy density (J/mm³)	Energy line (Ws/mm)
1.1	20	20	90	1200	187.5	0.075
1.2	20	20	100	1200	208.333	0.083
1.3	20	20	110	1200	229.166	0.09
1.4	20	20	120	1200	250	0.1
1.5	20	20	90	360	625	0.25
1.6	20	20	100	360	694.444	0.277
1.7	20	20	110	360	763.888	0.305
1.8	20	20	120	360	833.333	0.333
2.3	20	20	50	1200	104.166	0.041
2.5	20	20	50	1750	71.428	0.028
2.6	20	40	40	1200	41.666	0.033
2.7	20	40	50	1200	52.083	0.041
3.1	20	20	60	1200	125	0.05
3.2	20	20	70	1200	145.833	0.058
3.3	20	20	80	1200	166.666	0.066
3.4	20	40	60	1200	62.5	0.05
3.5	20	40	70	1200	72.916	0.058
3.6	20	40	80	1200	83.333	0.066
3.7	20	30	60	1200	83.333	0.05
3.8	20	30	70	1200	97.222	0.058
3.9	20	30	80	1200	111.111	0.066

In addition to single-track analysis and energy density range printing, the effect of each parameter was examined in detail. In the first stage, the printing parameters were set based on the published paper by [79].In the paper, the maximum sample densities were obtained from the laser power from approximately 45 W to 55 W and laser speed from 1000 mm/s to 2000 mm/s, where the layer thickness and the hatch distance were 20 µm. Some parameters were set based on the paper and some were developed with higher laser powers of up to 100 W.

The energy line was the other parameter defined during the parameter setting since [78] found that successful printing was possible with the *EL* between 0.03and 0.05 Ws/mm. Hence, in the second stage, the parameters were varied basedon *EL* = 0.03-0.05 Ws/mm. The second stage examines the effect of *LP* and *ED* and the effect of *LT* and *HD* on the sample density, in addition, examines the relationship between the magnetic properties and the sample density. A summary of the printing parameters is shown in Table 4.2.

Table 4-2 Summary of the printing parameters – first stage and second stage

Parameter	First stage	Second stage
Hatch distance (µm)	20	20-30-40
Layer thickness (µm)	30	20-30-40-50
Laser power (W)	40-100	70-200
Laser speed (mm/s)	1000-3000	1500-5500
Energy density (J/mm^3)	50-83	20-130

Additionally, various *LP* and *LS* giving *ED;* 100 J/mm^3 and *EL;* 0.4 Ws /mm were set by keeping the *LT* and *HD* constant, 20 µm. Table 4.3 gives the detailed parameters for constant *ED* and *EL*.

Table 4-3 Sets of parameters for constant ED and EL

Sample ID	Laser Power (W)	Laser Velocity (mm/s)	Layer Thickness (µm)	Hatch Distance (µm)	Energy Density (J/mm³)	Energy Line (Ws/mm)
53	100	2500	20	20	100	0.04
47	90	2250	20	20	100	0.04
43	80	2000	20	20	100	0.04
35	60	1500	20	20	100	0.04

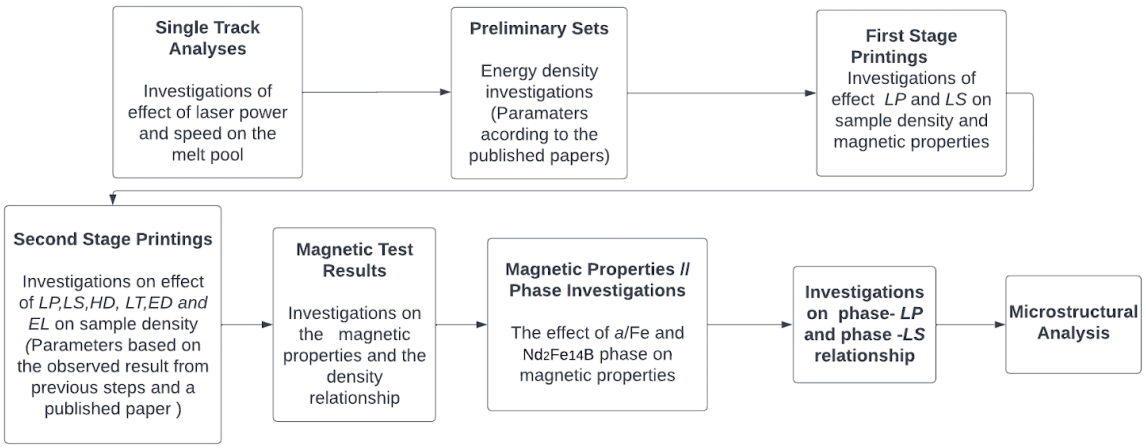

Figure 4-1 *Experimental Flow Chart.*

4.3. Results and Discussion

4.3.1. Single Track Analyses

A single-track analysis is a simple way to obtain a basic idea of the effects of the laser power and speed on scan width. Figure 4.2 shows the track width data of single scans. Despite a number of conflicts in the graph, it helps to understand the general trend. The track width increases with increasing laser power and decreasing laser speed. Figure 4.3 shows optical microscope images of the single tracks. It can be observed that the continuity of the laser track improves as the laser power increases. The 130 WLP tracks are better at all laser speeds from 1000 to 1400 mm/s, meaning high *EL* values gives better track continuity, which is coherent with the published results in [81].

A number of conflicts and some missing data are seen in Figure 4.3 due to the manually layered powder and not a 100% flat build platform. Because the powder could not possibly spread equally, some sides of the build platform have a thicker powder layer than the other sides. In this case, even if the scan parameters are sufficient for powder melting, tracks on the thickly layered powder cannot attach to the build platform well. These tracks clear away when the excess powder is brushed.

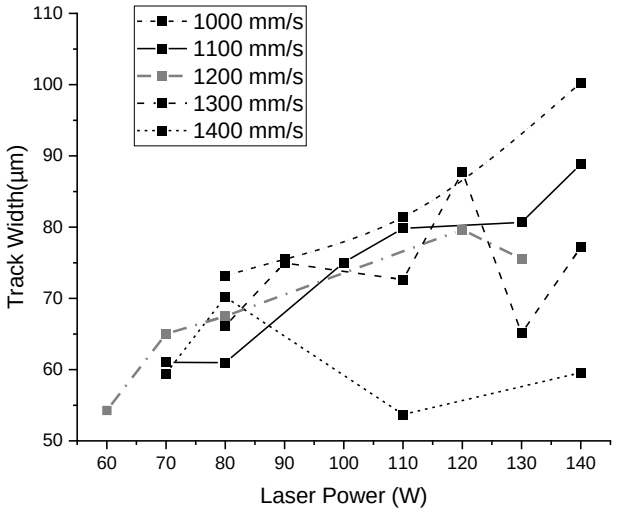

Figure 4-2 Track width relationship between laser power and laser speed.

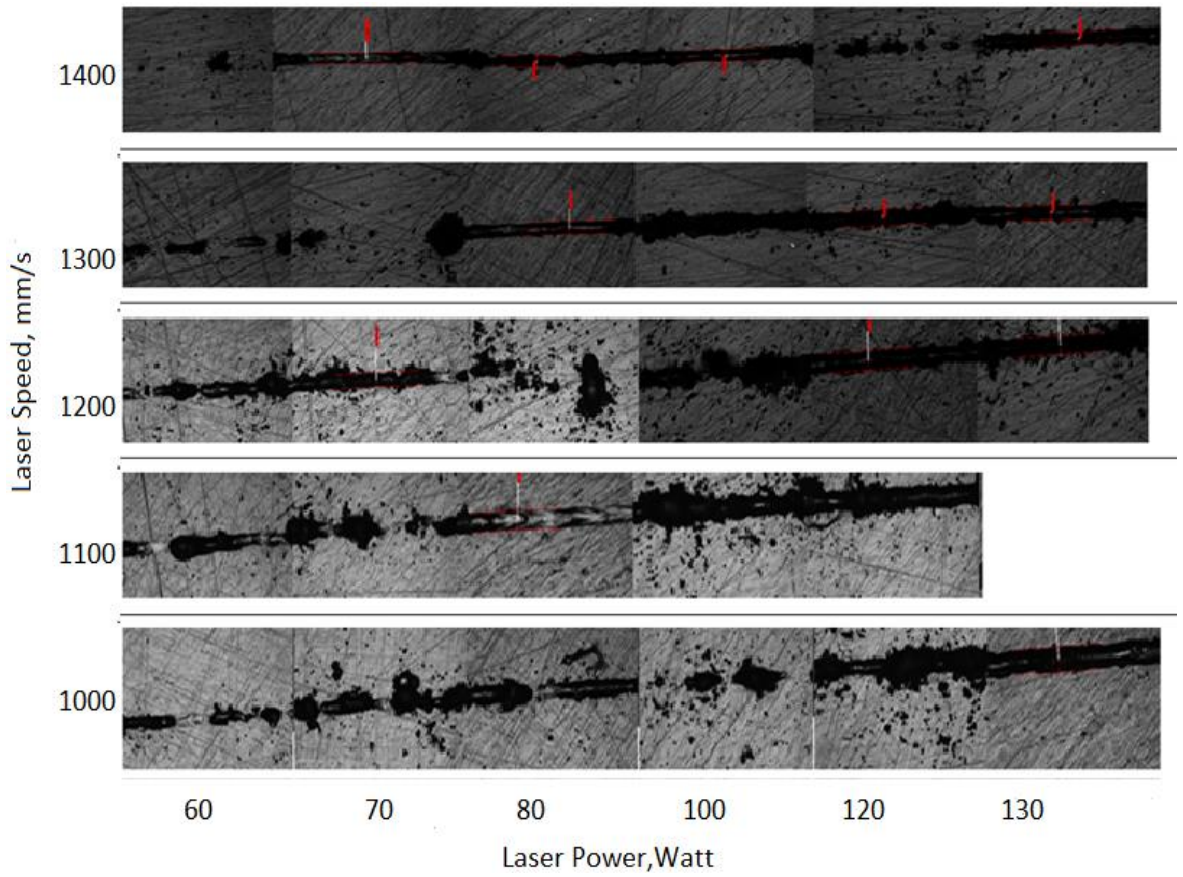

Figure 4-3 Images of the single tracks, laser power from 60 W to 130 W and laser speedfrom 1000 mm/s to 1400 mm/s.

4.3.2. Preliminary Printing – Energy Density Range

The preliminary experiments were conducted to define the successful energy density range. The high *ED* samples, between 187 to 833 J/mm^3 (*EL*: 0.07-0.3 Ws/mm), failed, as seen in Figure 4.4a. It was reported that the high *ED* caused excessive stresseson the lower part of the samples, which caused the crack formation and delamination [83]. Additionally, the high-energy density boils the material, and it causes material evaporation and entrapped gas bubbles in the melt pool, known as keyhole porosity [103].

In contrast, lower *ED* samples are relatively successful, shown in Figures 4.4b and 4.3c, from 52 to 104 J/mm^3 and 62.5 to 125 J/mm^3, respectively. It can be observed that the former are in better condition than the latter. The difference between them is the energy line. The former have *EL* between 0.028 to 0.041 Ws/mm, as published by [78] and the latter have *EL* between 0.050 to 0.066 Ws/mm. It was observed that the high

EDs, above 125 J/mm3, failed, possibly due to high residual stresses caused by a high thermal gradient, which causes cracks and delamination, consequently failing the samples.

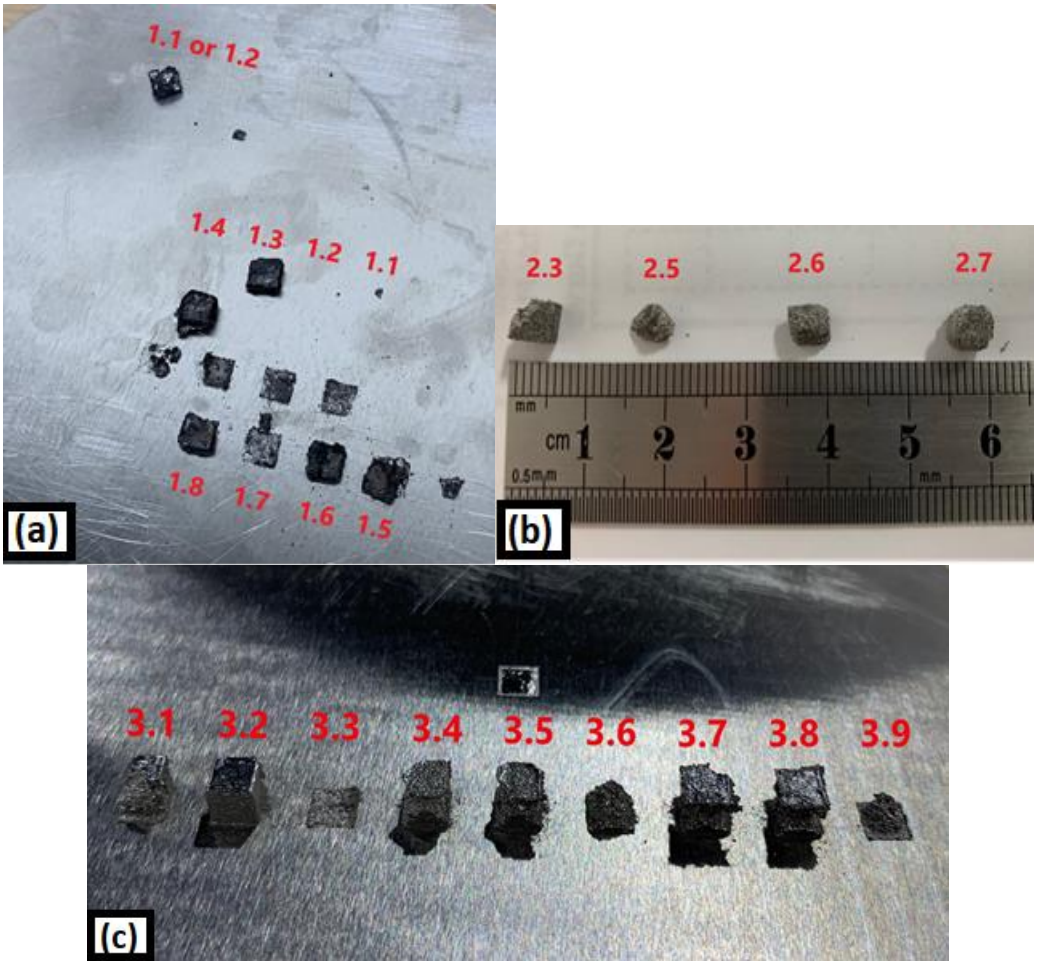

Figure 4-4 Sample images of the parameters given in Table 4.1, (a) ED; from 187 to 833 J/mm³, (b) ED; 52 to 104 J/mm³ , and (c) ED; from 62.5 to 125 J/mm³.

4.3.3. Archimedes Density and Magnetic Test Results of the First Stage Printing

There was no successful printing below laser power 60 W, as shown in Figure 4.5.a (samples 1 to 5). It is assumed that the low laser power (below 60 W) is insufficient tomelt NdFeB powder. What is interesting about the results in Figure 4.5a is that the failed samples from 1 to 5 (*LP*;40-50 W) have the same *ED* as the successfully printedsamples near them. Despite all the *EDs* being between 50 and 83 J/mm³, the only successful

printings were obtained with *LP*:60 W and above. The laser speeds of the failed samples were 1500mm/s and below.

Additionally, samples from 6 to 9 failed due to the failed samples near them. The broken pieces and layers coming from the failed samples (samples 1-5) are carried by the wiper and hit the other samples around them, or they are placed on top of the samples. Hence the laser scans the broken pieces instead of the freshly layered powder. Therefore, Sample 6 and Sample 8 were reprinted successfully, as shown in Figure 4.5.b.

Some defects are seen on the corners and the bottom of the samples (shown by the red arrows in Figure 4.5.a). It is highly likely that the temperature differences between thecold building platform and the hot melted powder cause thermal stresses and subsequently cause these defects and cracks on the bottom of the samples [104]. As the printing progresses, the new layers are melted on the previously melted hot layer. Thetemperature differences between the layers decrease as the building progresses, reducing the thermal stresses on the top part of the samples. Table 4.4 shows the detailed printing parameters in Figure 4.5. The process window is *LP* from 40 W to 100 W in 10 W increments with *HD:*20 μm and *LT*:30 μm.

Figure 4.6.a shows that the density of the samples increases with increasing laser energy densities. The highest density was achieved using 100 W, 95.72%, sample 24, while Sample 6 has about the same energy density as Sample 24 but has 60 W *LP* at 91.52%. Both samples are circled in red in Figure 4.7.a. A similar trend is seen within the remanence values. The higher remanence values were achieved by using higher laser powers/higher scanning speeds. The maximum B_r, 0.658 T, was obtained using 100 W (sample 24, circled in red in Figure 4.6b), while the B_r value of Sample 6 is 0.591 T, circled in red in Figure 4.6.b. Micro CT scans show, in Figure 4.7, Sample 6 processed using 60 W *LP,* containing more porosity inclusion than sample 24, while their *HD* and *LT* processing conditions remain the same (energy densities are close at74 J/mm^3 and 80 J/mm^3). Additionally, two main phases were detected in Sample 6 and Sample 24,soft magnetic *α-Fe* and hard magnetic $Nd_2Fe_{14}B$, as seen in Figure 4.8.It is assumed that the higher amount of *α*-Fe phase in Sample 6 reduces the remanenceby reducing the volume percentage of hard magnetic phase and because of the soft magnetic structure of *α-Fe*, it reverses the magnetic domains of the hard phase [2].

Table 4-4 Scan parameters of the samples shown in Figure 4.5.

Sample ID	Laser Power (W)	Energy Density (J/mm^3)
1-2	40	53-66
3-5	50	55-83
6-9	60	50-80
10-13	70	51-77
14-16	80	53-76
18-22	90	50-75
24-26	100	60-83

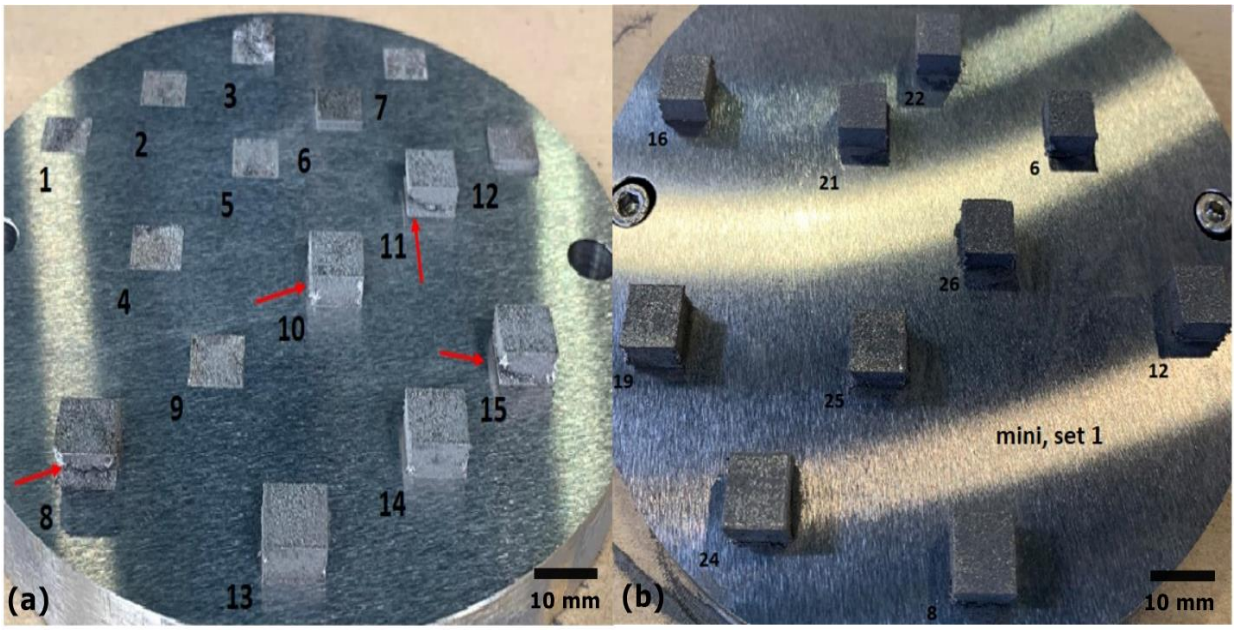

Figure 4-5 Printed samples using the Aconity mini, LP sample 1-2: 40 W, Sample 3-5: 50 W, Sample 6-9: 60 W, sample 10-13: 70 W, Sample 14-16: 80 W, Sample 19-22: 90 W, Sample 24-26: 100 W. ED:50-83 J/mm^3, scan parameters can be seen in Table 4.4.

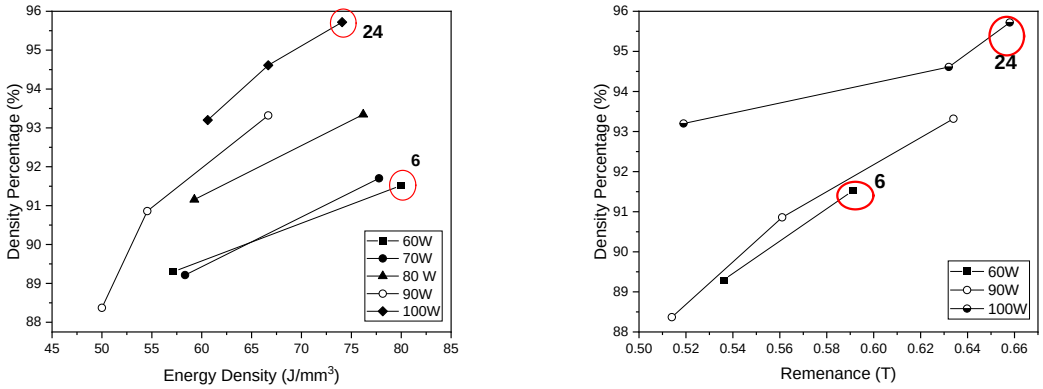

(a) (b)

Figure 4-6 (a) Relationship between energy density and sample density with respect to ED, (b) Relationship between sample density and remanence with respect to varying laser power.

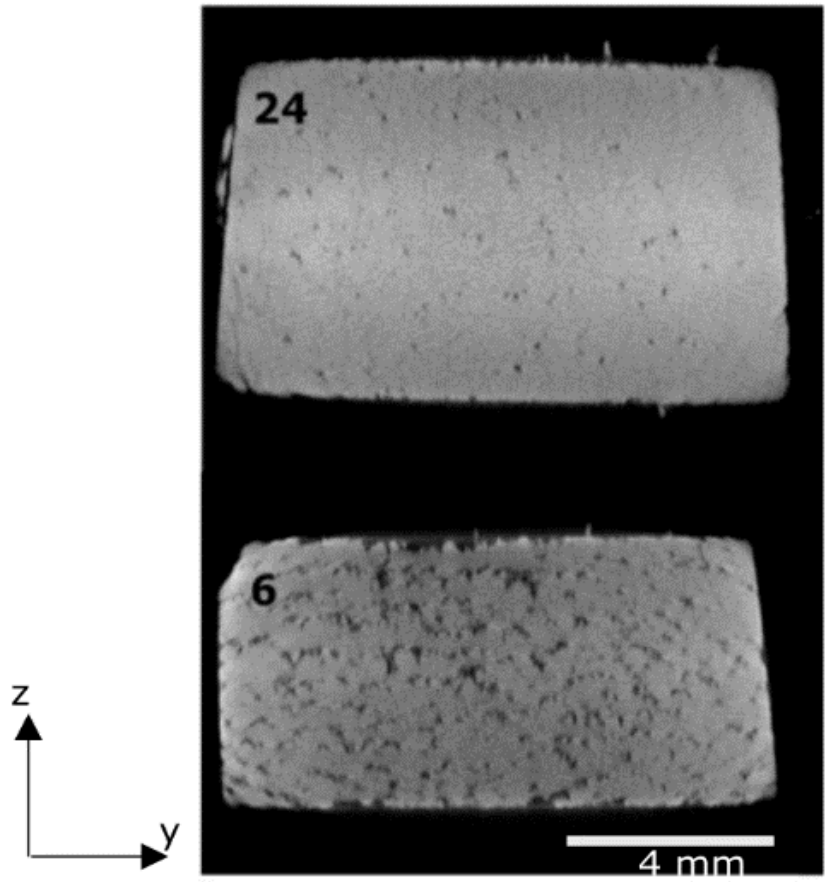

Figure 4-7 Micro CT scan images: sample 24, LP:100 W- ED:74 J/mm³ and sample 6, LP:60 W - ED; 80 J/mm³, side view of the samples.

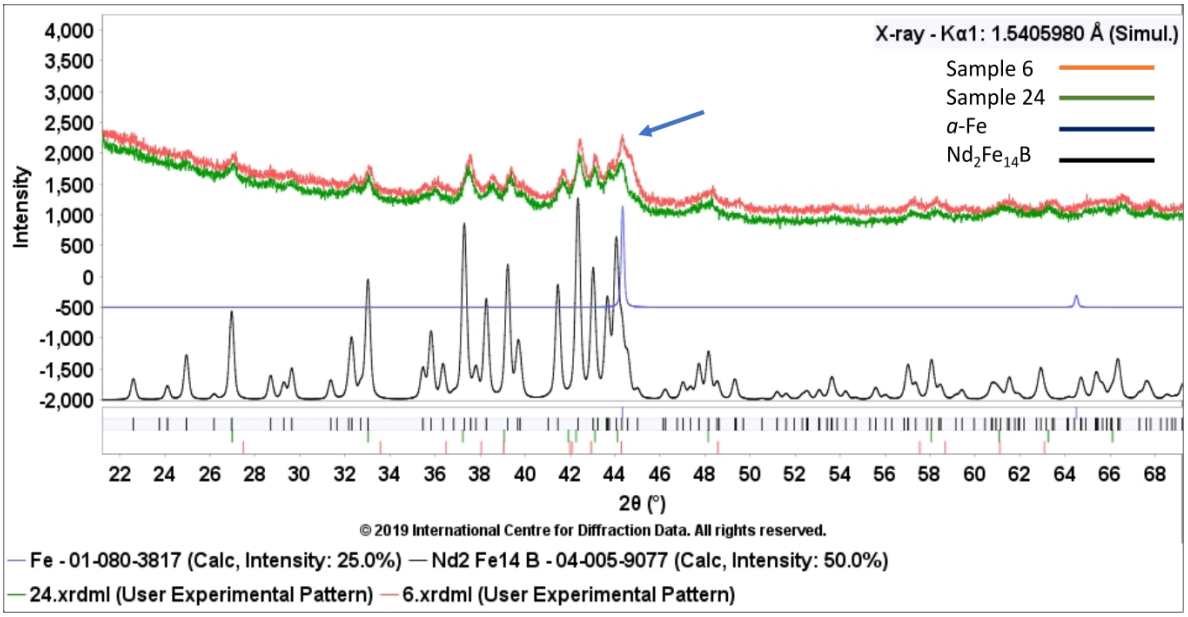

Figure 4-8 XRD patterns of printed samples 6 and 24, blue arrow points to the α-Fe phase

The first stage of the experiments was planned with the narrower process parameters window so as to be able to reduce the risk of failure and to be able to control the effect of the laser power and laser speed on both the density and magnetic properties. In the second stage, printing parameters were widened based on the preliminary and first stage results. To secure the printing quality, *LP* was set from 70 W to 200 W. Furthermore, hatch distances between 20 and 40 μm and layer thicknesses between 20 and 50 μm were studied to examine their effect on sample density and magnetic properties. A summary of the parameters is shown in Table 4.2.

4.3.4. Effect of Laser Power and Energy Density on Sample Density, Second Stage

As the laser power increases to 100 W, density increases, as identified in the first stage experiments. However, further investigations on laser power show that the density of the samples starts to decrease after 120-130 W despite the energy densities being maintained within the same range as the lower laser power samples, as seen in Figure 4.9.

The reason for this reduction might be the higher scan speeds. The combination of high laser speed and high laser power generates unstable melt pools that result in low-density samples. Laser speed should be sufficiently low to allow sufficient melting and

powder consolidation. Moreover, no sample could be processed above 125 J/mm^3 due to the excessive energy density causing material evaporation. High energy densities created keyholes within the melt pool, making the samples extremely brittle. In addition, high *EDs* cause higher residual stresses in part. The combination of tensile stresses occurs on the top of samples due to the material shrinkage caused by the rapid cooling, and the compressive stresses on the bottom of the sample [104] cause cracks [83] and consequently material delamination. It is essential to keep the energy density below the critical maximum *ED* value, in this study 125 J/mm^3, to reduce cracks, delamination and part distortion [65], and keyhole pores. However, it is also necessary to generate sufficient energy density to prevent the lack of fusion pores. Figure 4.10b shows the lack of fusion pores in the low *ED* sample (*ED*:50 J/mm^3, sample density percentage: 88.37%), while Figure 4.10.a shows the high-density sample, 95.72%, with *ED*:74 J/mm^3. Additionally, it was found that the very high *LP*/fast *LS* combinations damage the integrity of the samples, as seen in Figure 4.11. This can be attributed to the high cooling rates caused by fast scanning speeds which cause high temperature gradients, leading to internal stresses and cracks [88].

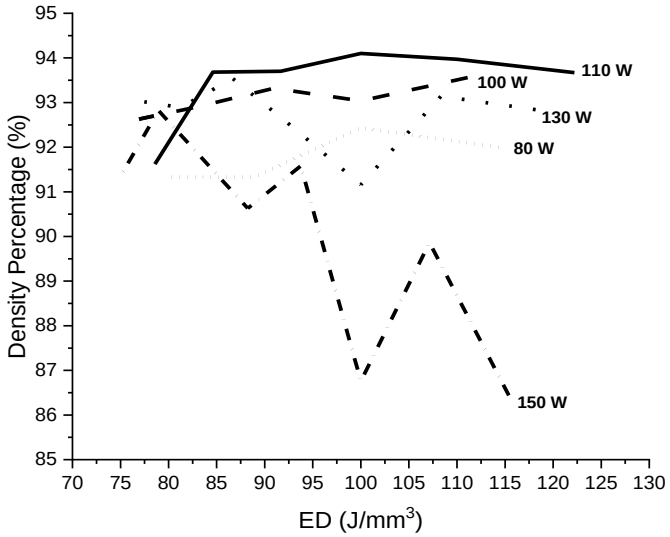

Figure 4-9 Relationship between ED and density of the samples with variation in laser power 80-150 W, HD:20 µm-LT:20 µm.

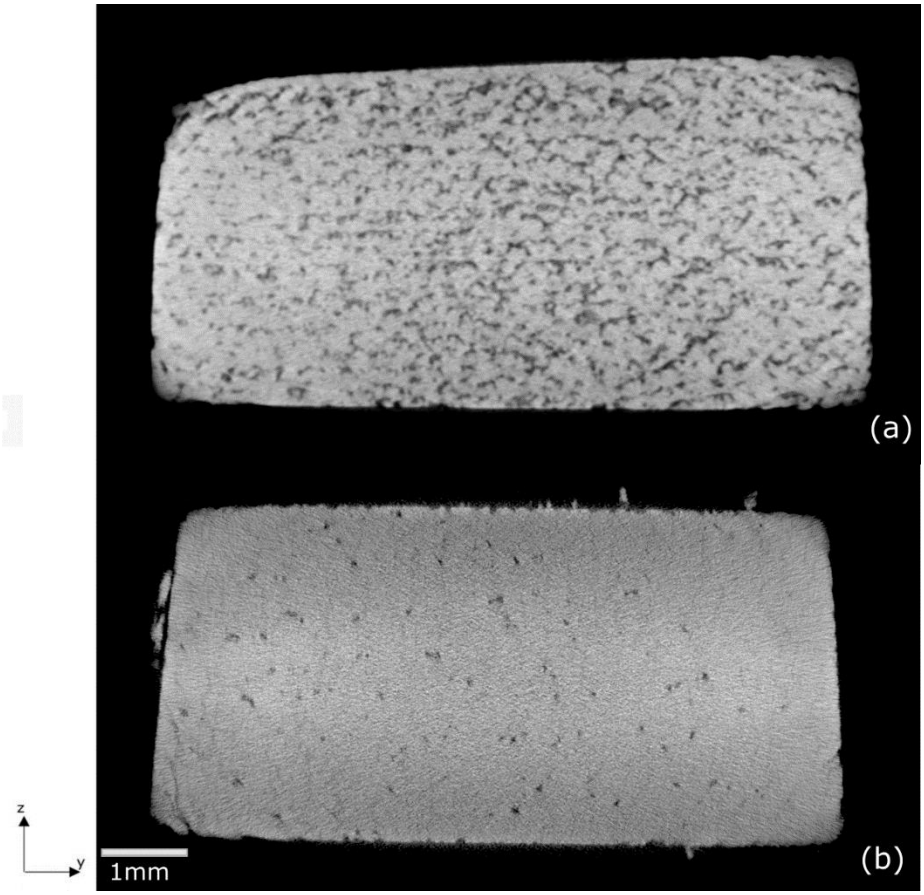

Figure 4-10 Micro CT scans of (a) sample 74 J/mm³ (100 W, 2250 mm/s, 95.72%); (b) sample 50 J/mm³ (90W, 3000 mm/s, 88.37%).

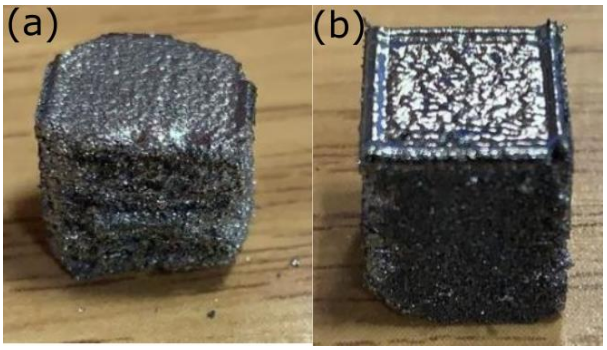

Figure 4-11 (a) 90.9 J/mm³ (200 W, 5500 mm/s, 20 µm HD-20 µm LT) and (b) 92.85 J/mm³(140 W, 3500 mm/s, 20 µm HD 20 µm LT), sample size 10 mm × 10 mm × 10 mm.

4.3.5. Effect of Layer Thickness and Hatch Distance on Density

The density of the samples improved from 50 µm to 20 µm by decreasing *LT*, and by decreasing *HD* from 40 µm to 20 µm, as shown in Figure 4.12. The increasing trend in density is due to the increasing *ED* as the *HD* and *LT* decrease, obtained from the equation *ED = (LP/(LS*HD*LT))*. Moreover, high *HD* causes an insufficient overlap

[88]where the laser is not able to melt all the powder in the layer, causing an un-melted powder gap and, subsequently, an unstable melt pool [103], which in turn causes an increase in the porosity of the SLM samples. The sample densities are mostlyover 90% in the 20 µm *HD* samples (Figure 4.12a), while they are in the range of 84%to 95% in the 30 µm *HD* samples (Figure 4.12b). On the other hand, they are below 88%, down to 76% in the 40 µm *HD* samples (Figure 4.12.c). Figure 4.13 shows the un-melted powders in the high *HD* samples.

In addition, the sample densities increase by decreasing *LT,* as seen in the graphs in Figure 4.12. The increasing density trend from 20 µm *LT* to 50 µm *LT* is clearer in Figures 4.12b and 4.12c, where *HD* is 30 µm and 40 µm compared to *HD* being 20 µm in Figure 4.12a. Figure 4.14 shows the surface porosity of the samples *LT* from 20 µm to 40 µm. The porosities increase by increasing *LT* from 20 µm to 40 µm, where the densities of the samples are 94.21%, 92.63% and 87.34%, respectively.

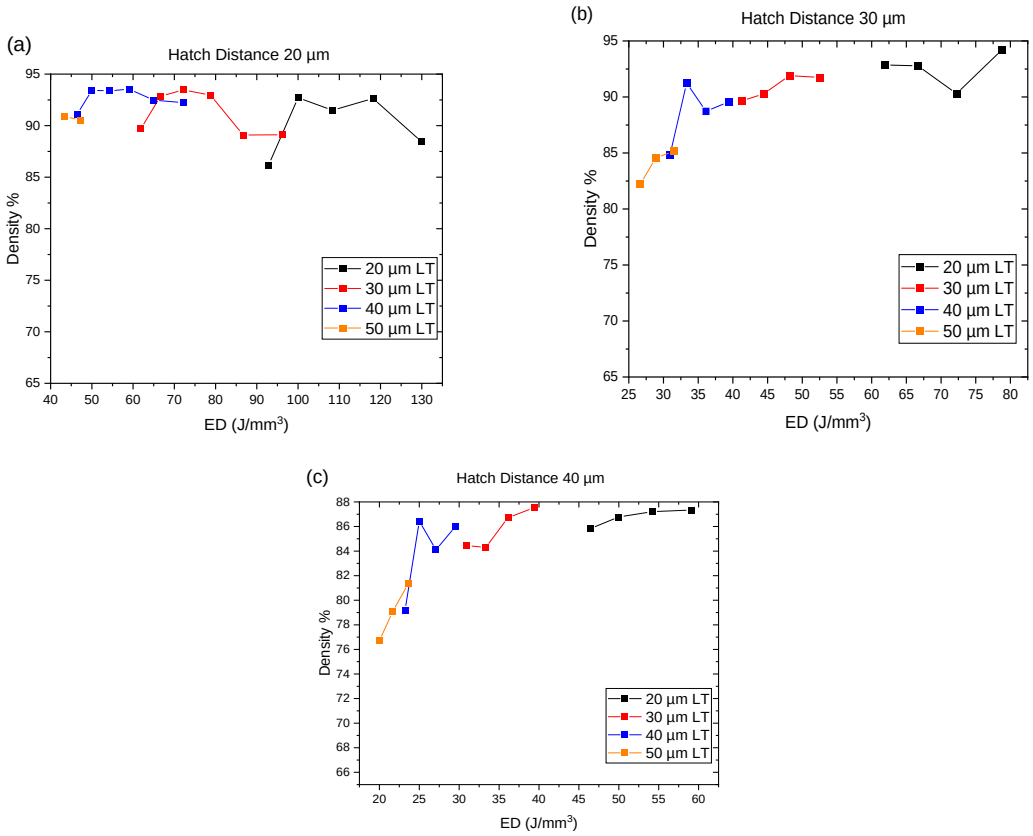

Figure 4-12 (a) Density percentage in dependence of ED and LT (a) 20 µm HD; (b) 30 µm HD; (c) 40 µm HD, LP:130 W, various LS:2250 mm/s to 3500 mm/s.

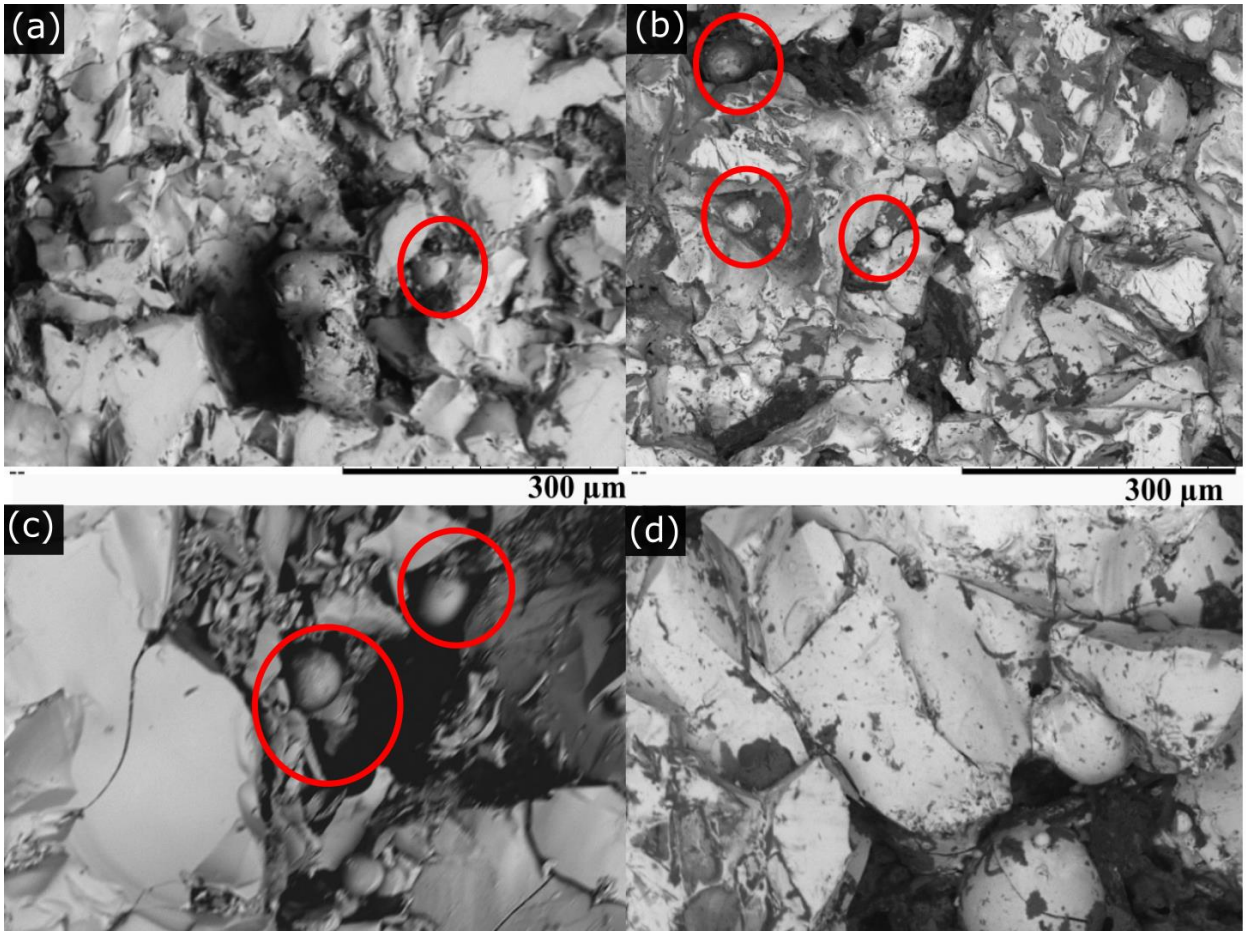

Figure 4-13 SEM images of un-melted powder in HD:40 µm, LT: 20 µm, (a)-(b) cross-section of the samples; and (c)-(d) top view of the samples, red circles indicate un-melted powders.

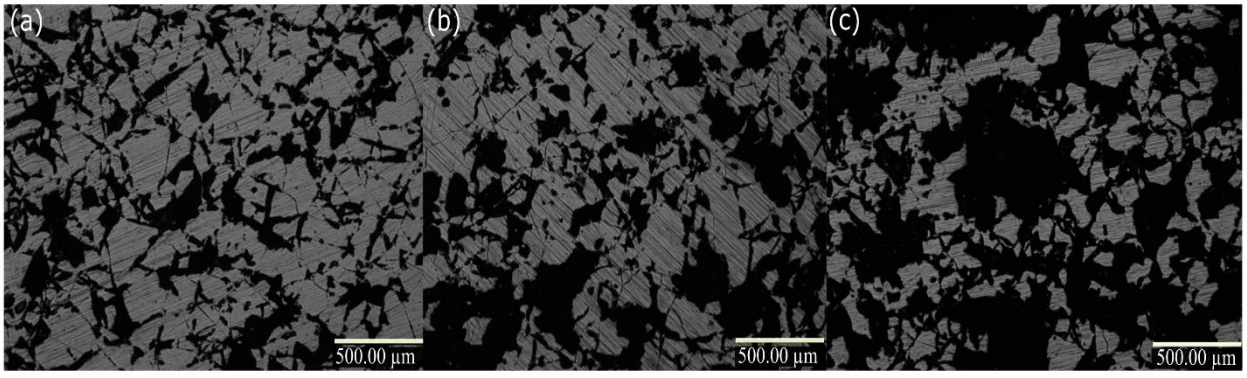

Figure 4-14 Surface porosity in dependence of LT a-20 µm b-30 µm and 40 µm for HD:30 µm LP:130 W LS:3500 mm/s.

Increasing *LT* narrows the melt pool horizontally while increasing the depth,as shown in Figure 4.15. The depth of the melt pool by increasing *LT* is as follows; 33 µm-72 µm -95 µm for 20 µm -30 µm -40 µm, respectively. (Measurements were done from 6 to 8 different points to calculate the average depth of the melt pool using image J software). It

was found that melt pool morphology is affected by *LT* [105] as confirmed in this study. It is also known that sufficient overlap is needed between one after another melt pools to avoid lack of fusion porosities.The *LT* affects the ability of the powder to melt. If the *LT* is not low enough, un-melted defects between the melt pools occur [106]. To get successful melt, the overlap between laterally adjacent melt pools, *L,* must be at least as large as the *LT*, (see Figure 4.14) [107]. Therefore, it can be said that there is a strong relationship between the overlapping quality and the *LT*.

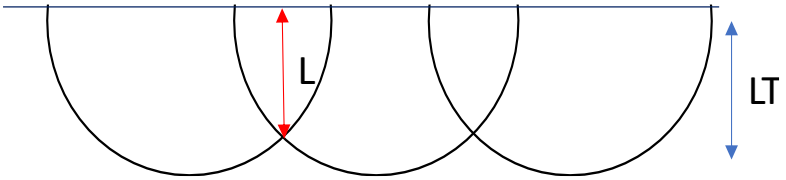

Figure 4-15 Schematic representation of the assumed semi-circular shape of melt pools, L is the depth of the overlap between laterally adjacent melt pools, and LT is the layer thickness., Figure is adapted from [107]

Moreover, it was reported that a shallow melt pool is desired to achieve rapid solidification in AM [82],affecting the resulting microstructure, consequently, the magnetic properties. Hence, in this study, the *LT* and *HD* were set to 20 µm and 30 µm for further experiments to get a shallow melt pool.

Many dark spots are seen on the sample surfaces in Figure 4.16, indicated with red arrows. Additionally, many cracks are observed, mainly in the build direction. The topographic images of the samples show that the dark spots on the surfaces are the holes that occurred after the sample preparation steps, as seen in Figure 4.17. Since thesample is very brittle, some pieces were pulled out while grinding and polishing.

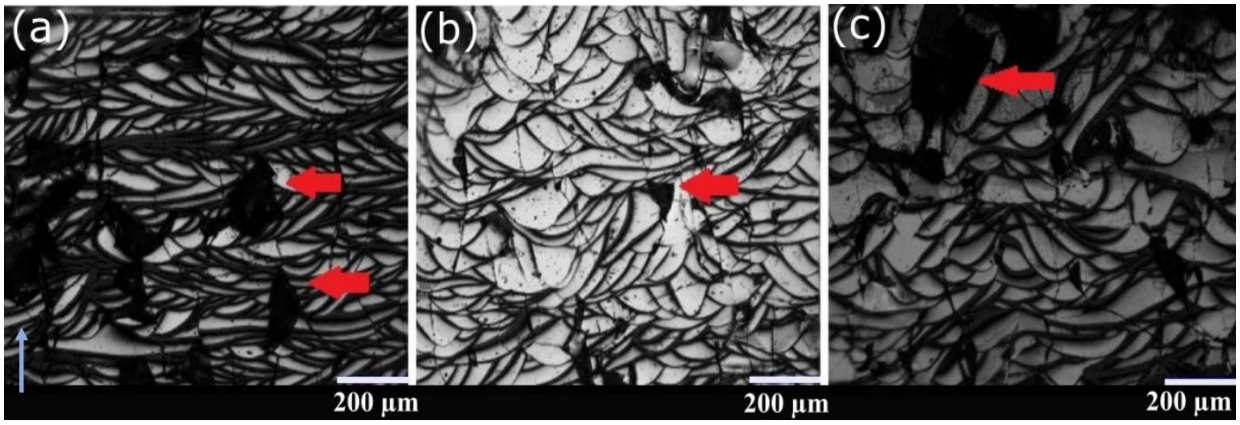

Figure 4-16 (a) LT: 20 µm; (b) 30 µm; (c) 40 µm, (HD:20 µm, LP: 130 W, LS: 3500 mm/s, EL = 0.037 Ws/mm), cross-sections of the samples.

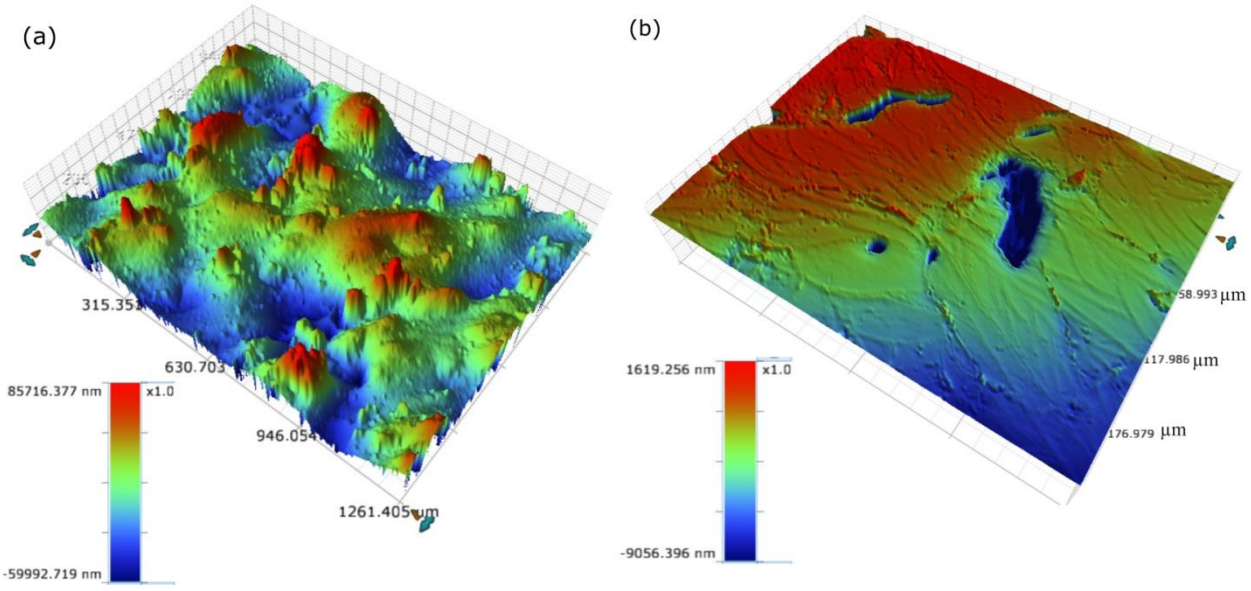

Figure 4-17 (a) Contour GT images of the as-sintered sample, top view; the surface is quite rough; (b) Contour GT images of the ground and polished sample, top view; the surface is smoother after sample preparation.

Further investigations on *HD* and *LT* showed that the effect of *HD* on sample density is higher than the effect of *LT* on sample density. Experiments have been run at a fixedlaser power of 130 W, with various laser speeds from 2750 to 3000 to 3250 mm/s. Multiple combinations of the layer thicknesses and hatch distances were set at 20 µm *HD*-30 µm *LT*, 30 µm *HD*-20 µm *LT*, 20 µm *HD*-40 µm *LT*, 40 µm *HD*-20 µm *LT*, 30 µm *HD*-40 µm *LT*, 40 µm *HD*-30 µm *LT* for all three speeds. The set parameters and the density results are shown in Table 4.5.

It was found that the sample densities improve more when the *HD* is lower and *LT* is higher than when *HD* is higher and *LT* is lower. For instance, when the *LS* is 3000 mm/s, the density percentage of the sample 20 µm *HD*-30 µm *LT* is higher than the density percentage of the sample 30 µm *HD*-20 µm *LT*, 93.46% and 90.26%, respectively, despite both combinations giving the same *ED*, 72.22 J/mm^3, derived by *ED* = (*LP*/(*LS***HD***LT*)). Every result in Table 4.5. shows that the lower *HD*-higher *LT* combinations give higher densities than the higher *HD*-lower *LT* combinations at all three speeds, 2750, 3000 and 3250 mm/s. The only consistency is seen in the 20 µm *HD*-30 µm *LT* and 30 µm *HD*-20 *LT*, highlighted in red in Table 4.5 Additionally, the 20 µm *HD*-40 µm *LT*//40 µm *HD*-20 µm *LT* combinations have the highest density difference between them, at over 6%, compared to the combinations having close *HD/LT* values, e.g., the 20 µm *HD*-30 µm *LT*//30 µm *HD*-20 µm *LT*.

Table 4-5 Archimedes density test results of HD-LT combinations resulting in constant ED.

LP-130 W	20 µm *HD*-30 µm LT	30 µm *HD*-20 µm LT	20 µm *HD*-40 µm LT	40 µm *HD*-20 µm LT	30 µm *HD*-40 µm LT	40 µm *HD*-30 µm LT
LS-2750 mm/s	92.95%	**94.21%**	**93.54%**	87.34%	**89.56%**	87.53%
LS-3000 mm/s	**93.46%**	90.29%	**93.37%**	87.20%	**88.72%**	86.72%
LS-3250 mm/s	**92.86%**	92.78%	**93.44%**	86.77%	**91.26%**	84.30%
	Differences between density percentages of the samples					
LS-2750 mm/s	−1.26%		6.20%		2.03%	
LS-3000 mm/s	3.17%		6.17%		2.00%	
LS-3250 mm/s	0.08%		6.67%		6.96%	

Figure 4.18 shows plots of the main effects for the density percentage of the samples. The lowest level of hatch distance and layer thickness (20 µm) gives the maximum density of the samples. 2750mm/s was found to be the optimum factor level generating the maximum density of the samples. However, since the contribution of this factor is very small compared to the other factors, the difference between the effects is accepted as being negligible.

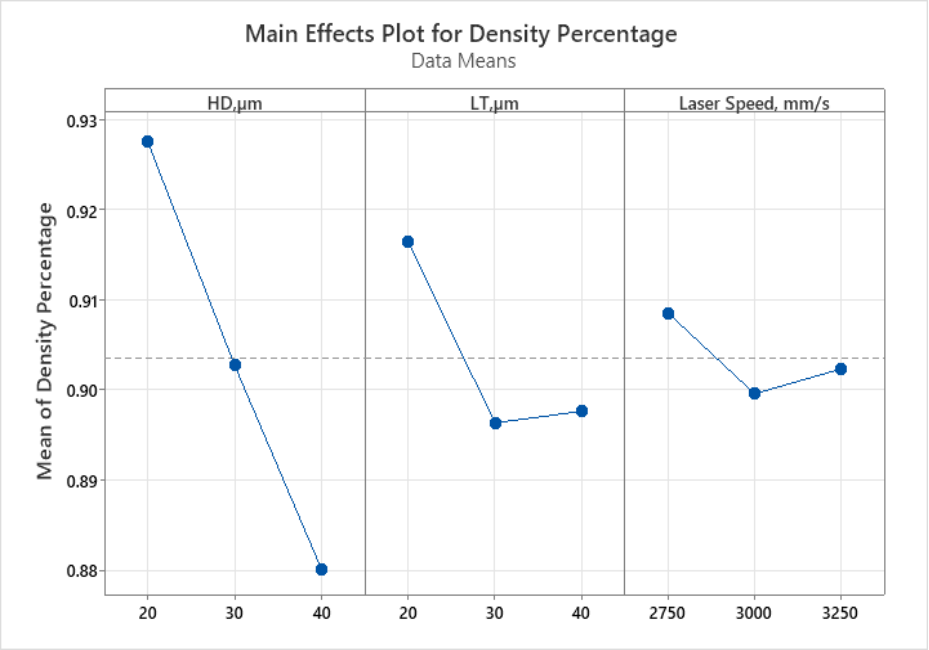

Figure 4-18 Main effects plot for density percentages of the samples.

The smaller *LT* below 20 µm is not investigated since conflicts are seen in the 20 µm *LT* trials in contrast to a clear trend observed in higher *LT* trials, as seen in Figure 4.12. The reason might be that the powder particle size is not small enough to spread a new powder layer whose thickness is below 20 µm. The smaller *HD* is not studied due to the limited time of the project.

4.3.6. Effect of *LS* and *LP* with Constant *ED* and *EL*

It was found that the combinations of *LP*-*LS* giving fixed *ED* and *EL* do not provide the same sample density, while both *HD* and *LT* are fixed at 20 µm. Figure 4.18 shows the sample density difference between the different laser power and laser speed combinations while their *ED* and *EL* are the same, at 100 J/mm^3 and 0.04 Ws/mm, respectively. It was found that **high *LP*/fast scan** combinations would give higher sample densities than the **low *LP*/slow scan** combinations. Densities can be improved from 86% to 90% with an increasing *LP,* from 60 W to 100 W, and an increasing *LS*, from 1500 mm/s to 2500 mm/s.

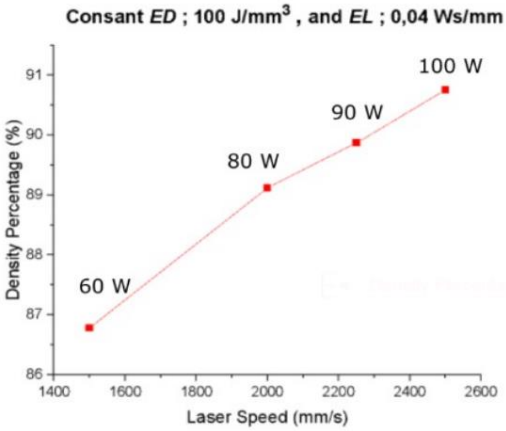

Figure 4-19 Density relationship with the *LP-LS* combinations with fixed *ED* 100 J/mm3 and fixed *EL* 0.4 Ws/mm, with *HD*:20 µm *LT*:20 µm.

4.3.7. Magnetic Test Results/Relationship Between Densityand Remanence

The densities of the 78 samples in the second stage printing, *LP* from 70 W to 200 W and *LS* from 1500 mm/s to 5000 mm/s, are plotted in Figure 4.20a. Since the energy density takes into account four independent printing parameters (E*D* = *LP/(LS*HD*LT)*), hatch distance and layer thickness were kept constant. The red areas represent regions of high density within the samples. The results show that the maximum obtained density is 7.066 g/cm3, 94%, based on the theoretical density of NdFeB magnets (7.5 g/cm3). Furthermore, the remanence values of the 57 samples, selected among 78 samples were tested with the Helmholtz coil and fluxmeter, and the results can be seen plotted in Figure 4.20.b, showing that the high B_r samples are in the direction of faster scans, as indicated by the red arrow. The increasing scan speed causes faster solidification, which in turn results in higher remanences. These results correspond to the results published by [2]. The general trend is that the remanence improves as the density of the samples increases, as shown in Figure 4.20.c.

On the other hand, it was observed that all the highly magnetic samples contained a high density; however, not all the high-density samples are highly magnetic, which is coherent with [81]. Figure 4.20.d shows that the higher B_r samples are obtained by the *EL* between 0.03 and 0.04 Ws/mm with *ED* between 75 and 100 J/mm3. The B_r values decrease by increasing *EL*=0.04-0.05 Ws/mm and *ED* from 100 to 125 J/mm3.

Hence, it can be concluded that the magnetic properties are not only related to the density of the samples but also related to the cooling rates. The following section discusses a more detailed analysis of the specific parameter contribution to the phase and magnetic properties.

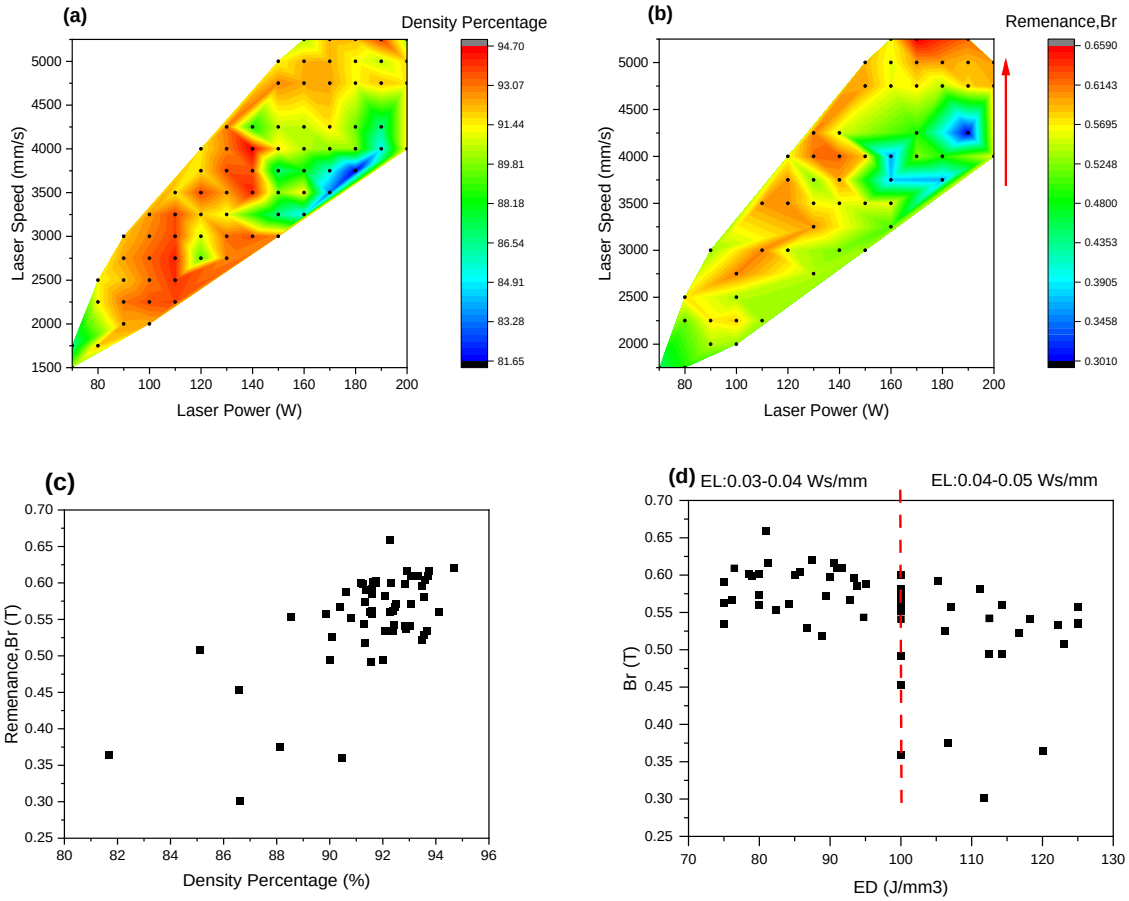

Figure 4-20 (a) Archimedes density results of the samples independent of the laser speed and laser power for 20 µm hatch and layer thickness; (b) Remanence of the samples, tested using Helmholtz coil and fluxmeter, independent of the laser speed and laser power for 20 µm hatch and 20 µm layer thickness; (c) Dependency of the remanence on the density percentage of the samples; (d) Dependences of the remanence on the energy density.

4.3.8. The Relationship between Phase-Magnetic Properties

The maximum energy product, BH_{max}, is one of the essential magnetic properties to evaluate the performance of permanent magnetic materials. It is the maximum *BH* value in the second quadrant of the hysteresis loop [38]. Thus, remanence, B_r, needs to be considered in order to improve magnetic performance. In our case, the XRD analyses show that remanence, B_r, increases as the volume fraction of the $Nd_2Fe_{14}B$ phase increases, as shown in Figure 4.21.a. The reason for this increase is the high saturation magnetisation of the $Nd_2Fe_{14}B$ phase, which improves the remanence [108]. On the other hand, coercivity is resistance against demagnetising the magnet, and thus it is the other important magnetic property to produce high-performance magnets [40].High magnetocrystalline anisotropy is one of the requirements for high coercivity. Low magnetocrystalline anisotropy that is seen in high symmetry systems such as Fe means that there are many easy axes in the structure, and the magnetic domains can be easily aligned in many different directions by an external field. However, in less symmetrical systems with high magnetocrystalline anisotropy, such as the tetragonal $Nd_2Fe_{14}B$ phase, there are only two axes whose domains can easily align. In that phase, more energy is needed to change the domain structure. Therefore,magnetic domain motion is restricted, preventing decoupling between domains and demagnetisation, and improving the coercivity [108]. Graph (a) in Figure 4.21.b showsthe increase in the coercivity, H_{ci} value, with the increasing volume fraction of the $Nd_2Fe_{14}B$ phase, possibly resulting from the high magnetocrystalline anisotropy of the$Nd_2Fe_{14}B$ phase. There is a clear increasing trend in the B_r and H_{ci} values with the increasing volume fraction of the $Nd_2Fe_{14}B$ phase, while there is a decreasing trend in the B_r and H_{ci} values with the increasing volume fraction of the *α-Fe* phase, as shown in Figures 4.22.c and 4.22.d. That decrease is due to the magnetically soft α-Fe phase reducing the magnitude of the hard magnetic phase, $Nd_2Fe_{14}B$, and reducing the remanence. Furthermore, since *α-Fe* is a soft magnetic phase and easily demagnetised,it acts as the centre of reversed magnetic domains, lowering the coercivity [2].

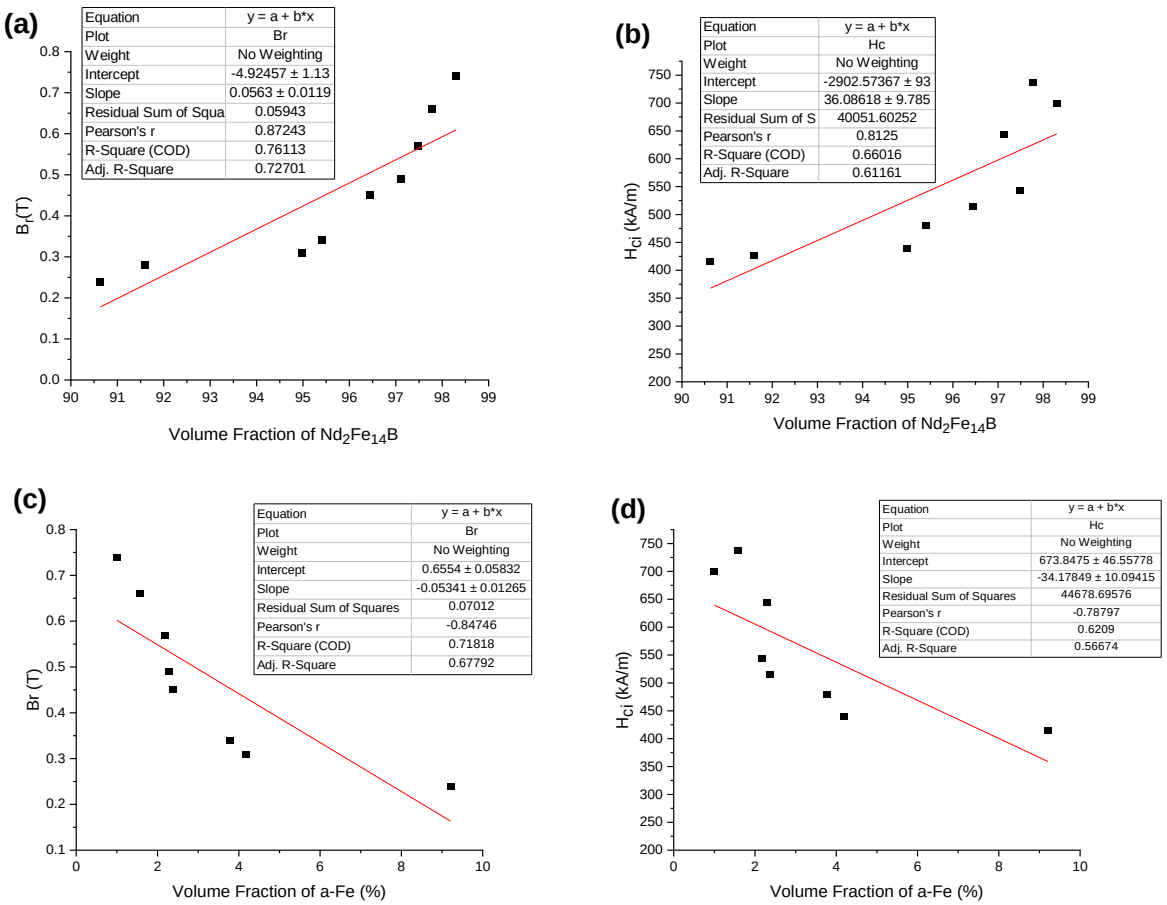

Figure 4-21 Relationship between (a) the volume fraction of $Nd_2Fe_{14}B$ and B_r, (b) the volume fraction of $Nd_2Fe_{14}B$ and H_{ci}, (c) the volume fraction of α-Fe and B_r, and (d) the volume fraction of α-Fe and H_{ci}. (Volume fraction of the phases are taken from the XRD patterns, rietveld analyses done by Sirapob Toyting at Cambridge University)

Table 4-6 error factors of the graphs in Figure 4.21

	Intercept-Standard Error	Slope-Standard Error	Sum of Squares- Error
H_{ci}/α-fe	46.55778	10.09415	44678.69576
H_{ci}/$Nd_2Fe_{14}B$	935.13856	9.78596	40051.60252
B_r/$Nd_2Fe_{14}B$	1.13912	0.01192	0.05943
B_r/α-fe	0.05832	0.01265	0.07012

The smaller the residual sum of squares means the better fitting of the data and the greater the residual sum of squares means the poorer fitting of the data. It is seen that the errors of H_{ci}/a-Fe and $H_{ci}/Nd_2Fe_{14}B$ are high. Even the generally decreasing coercivity trend seen by increasing *a-Fe* phase and decreasing $Nd_2Fe_{14}B$ phase, the relationship between them is not linear. Therefore, it is confirmed that H_{ci} is not only related to phase but also the microstructure [81]. On the other hand, even the fitting is greater in the $B_r/Nd_2Fe_{14}B$ and B_r/a-fe graphs, the errors values are not 0. This is possibly because of the cracks and porosities in them, which effects the amount of magnetic phase- $Nd_2Fe_{14}B$ in the samples. The printing parameters of the plotted results in Figure 4.21 are shown in Table 4.7.

Table 4-7 Effect of laser power on phases -Scan parameters samples from C1 to C9, HD;20 µm, LT; 20 µm.(tested by VSM).

Sample ID	**Laser Power (W)**	**Laser speed (mm/s)**
c1	100	3500
c2	110	3500
c3	120	3500
c4	130	3500
c5	140	3500
c6	150	3500
c7	160	3500
c8	170	3500
c9	180	3500

4.3.9. The Relationship between the Phase/Laser Power and Phase Laser Speed

The relationship between laser power and magnetic properties are investigated with the samples given in Table 4.7. Results are shown in Figure 4.22. The maximum B_r value, 0.74 T, was obtained at *LP:*130 W, and the highest H_{ci} value, 737 kA/m, was obtained at *LP:*120 W, as shown in Figure 4.22a and Figure 4.22b. The decrease in B_r and H_{ci} values after 130 W and 120 W, respectively, is similar to that found in the reduction in density of the samples after 120 W-130 W. The reason behind the decreasing B_r and H_{ci} is the decreasing density of the samples due to the high *EL*.. The samples having 140 W laser power and above have *EL* = 0.04Ws/mm and above, and they have *ED* = 100 J/mm^3 and above, which reduces B_r, which supports the results in Figure 4.20.d. The trend in the laser power $B_r$and laser power H_{ci} graphs is related to the volume fraction of $Nd_2Fe_{14}B$ and *α-Fe* phases. The increases in B_r is directly proportional to the increasing volume fraction of the $Nd_2Fe_{14}B$ phase and decreasing *α-Fe* phase, as seen in Figures 4.22.c and 4.22d.

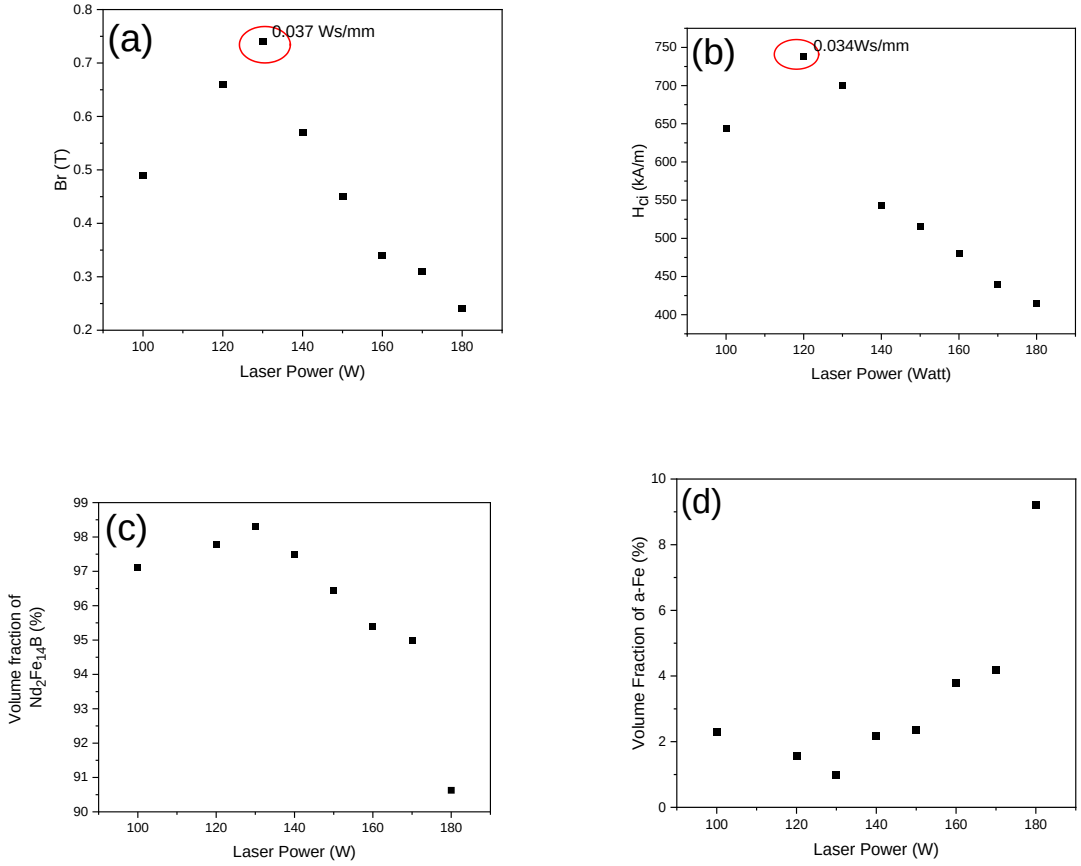

Figure 4-22 The relationship between (a) LP and B_r, (b) LP and H_{ci}, (c) LP and the volume fraction of $Nd_2Fe_{14}B$, and (d) LP and volume fraction of α-Fe, LS:3500 mm/s, LT:20 µm, and HD:20 µm.

Figure 4.23 shows the effect of laser speed on the B_r value. *Br* improves from 0.389 T to 0.622 T with a decrease in *LS* from 3250 mm/s to 2000 mm/s. These results conflict with previously indicated results in this paper and [2]; however, they are coherent with the results published in [85]. An increase in *LS* was expected to improve the *Br* value since it increases the cooling rates. However, it was noticed that the ED is far below the critical *ED* needed to fully melt the powder. The low *EDs* cause poor fusion,hence there is a lack of fusion porosity [83]. Thus, in Figure 4.23, B_r improves from 0.389 T to 0.622 T by decreasing laser speed due to the increasing *ED* from 38 J/mm^3 to 62 J/mm^3. It is also noticed that the *EL* is above 0.04 Ws/mm for the samples having higher B_r, 0.52 T and above. However, they are not affected poorly by the high *EL* rates, which was expected based on the previously discussed result. It is because the hatch distance of the samples plotted in Figure 4.23 is 40 µm, while it is 20 µm in the samples

discussed previously. High *HD* here causes poor melting ability and therefore requiring a lower scan speed, causing higher *EL* to be able to melt the powder.

It was found that the volume fraction of the $Nd_2Fe_{14}B$ phase is 92% in sample V/3-B_r:0.527 T, 90% in sample V/5-B_r:0.432 T, and 88.12% in sample V/6- B_r:0.389 T, while the volume fractions of *α-Fe* are 5.28%, 8.08%, 10.63%, respectively. The higher amount of $Nd_2Fe_{14}B$ phase in high B_r samples is seen from the XRD patterns in Figure 4.24. It is known that high B_r mainly originated from the hard phase [80]. The density of the samples fluctuates between 90.53% and 93.33%. The maximum B_r sample also has the maximum density of 93.33%. The parameters of the analysed samples are shown in Table 4.8. *LP* was kept constant at 100 W; *LS* was set from 2000 mm/s to 3250 mm/s; *HD* to 40 μm, and *LT* to 20 μm.

Table 4-8 Scan parameters of the samples from V/1 to V6.

Sample ID	Laser Power (W)	Laser Speed (mm/s)	EL (Ws/mm)	ED (J/mm^3)	Density Percentage (%)
V/1	100	2000	0.05	62.5	93.39
V/2	100	2250	0.044	55.55	90.53
V/3	100	2500	0.04	50	91.33
V/4	100	2750	0.036	45.45	91.2
V/5	100	3000	0.033	41.66	91.66
V/6	100	3250	0.03	38.46	90.94

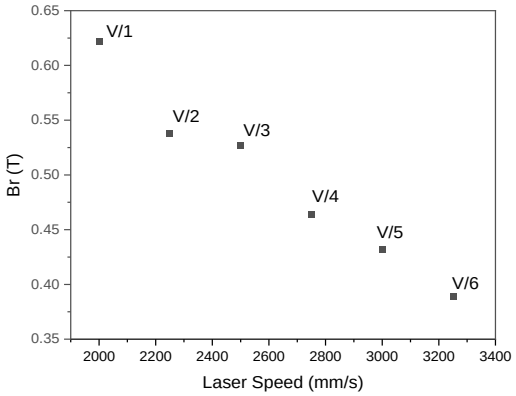

Figure 4-23 Br and density of the sample relationship with respect to laser speed, HD: 40 µm and LT: 20 µm, taken with Helmholtz coil and fluxmeter.

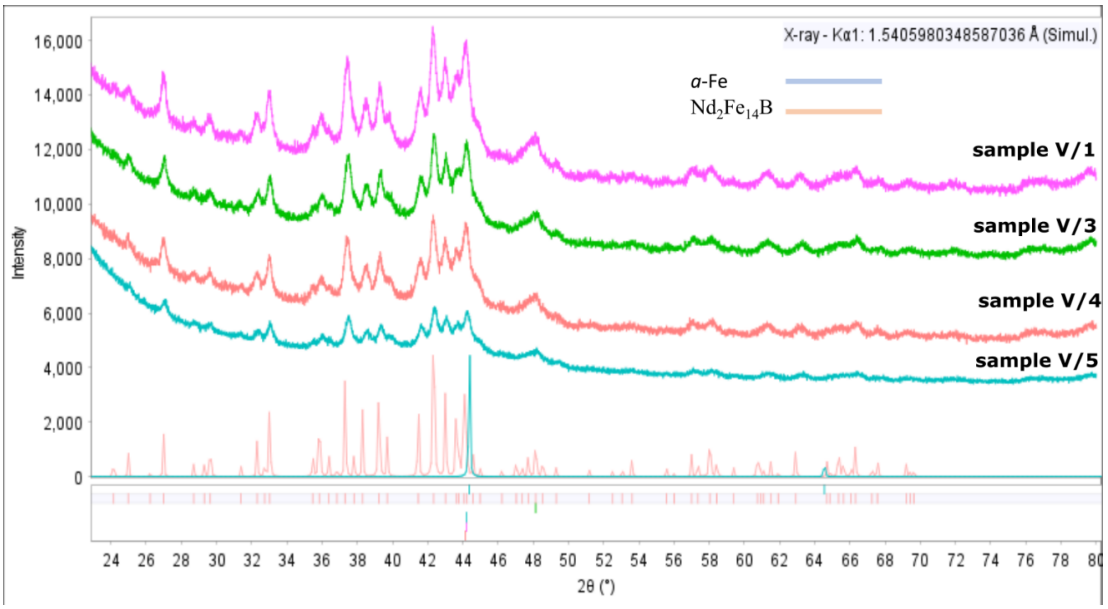

*Figure 4-24 X*RD pattern of the sample V/1-V/3-V/4-V/5, plotted in Figure 4.23.

The *ED* and the volume fraction of hard phase relationship is plotted, in Figure 4.25, in respect of samples plotted Figure 4.22 and 4.23. The hard phase, Φ, starts to decrease after *ED* 98 J/mm^3, which suits the results plotted in Figure 4.20.d, where the B_r startsto reduce nearly around the same *ED*.

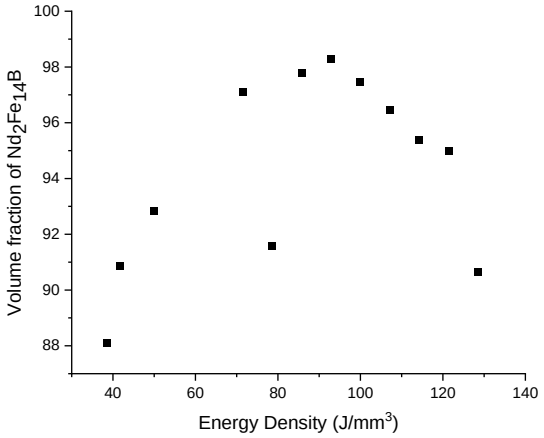

Figure 4-25 Volume fraction of $Nd_2Fe_{14}B$ versus ED, J/mm³.

4.3.10. Microstructural Analyses

The solidification process of the melt pool causes variations in grain size and shape, as seen in Figures 4.26.b and 4.26.c. This can be explained as follows: as the laser scans the powder on the top layer, it melts where T > T liquidus, 1370°C [2]. Since the scan speeds are fast, above 1000 mm/s, the powder cools rapidly, forming fine grains in the melt pool. When the laser scans the upper layer, the previously solidified layer also experiences heat. (T is lower than liquidus 1370°C and higher than T solidus 1180°C). The lower cooling rates in the heat-affected zone (HAZ) cause grain growth. The grains grow in a dendritic shape parallel to the build direction (as seen in Figure 4.26c, between the purple dot line). The grains above the HAZ are coarse and decrease in size in the build direction as the rate of cooling is higher. In addition, it was observed that the grain morphology is cubic just under the HAZ, where they are globular/near equiaxed through to the melt pool.

The XRD results, presented in Figure 4.24, show two main phases in the room temperature printed samples: $Nd_2Fe_{14}B$ and the *α-Fe* phase, in addition to the presence of oxides and the Nd-rich phases. (Confirming the Nd-rich phases was challenging since their peaks crossed $Nd_2Fe_{14}B$ peaks) (see the oxides on the surface in Figure 4.26.d).

Based on the XRD results and reported results in [109] it is deduced that the black areas in the band (marked between the red dotted lines in Figure 4.26.b), just under the HAZ, are *α-Fe*, and the bright areas are the Nd-rich phase.

The melt pool consists of $Nd_2Fe_{14}B$ phase grains (light grey areas), *α-Fe* phases (black areas), and the grey phase between the Φ grains. The TEM-EDX results confirmthat the phase between the Φ grains includes less Nd but more Fe, Ti and Zr, shown inFigure 4.27.b (These results match with the heated bed sample's EDX-SEM results in Table 5.1). It is understandable since the Zr at the grain boundaries acts as grain growth inhibitor by providing nucleation sites for $Nd_2Fe_{14}B$ precipitation [98].

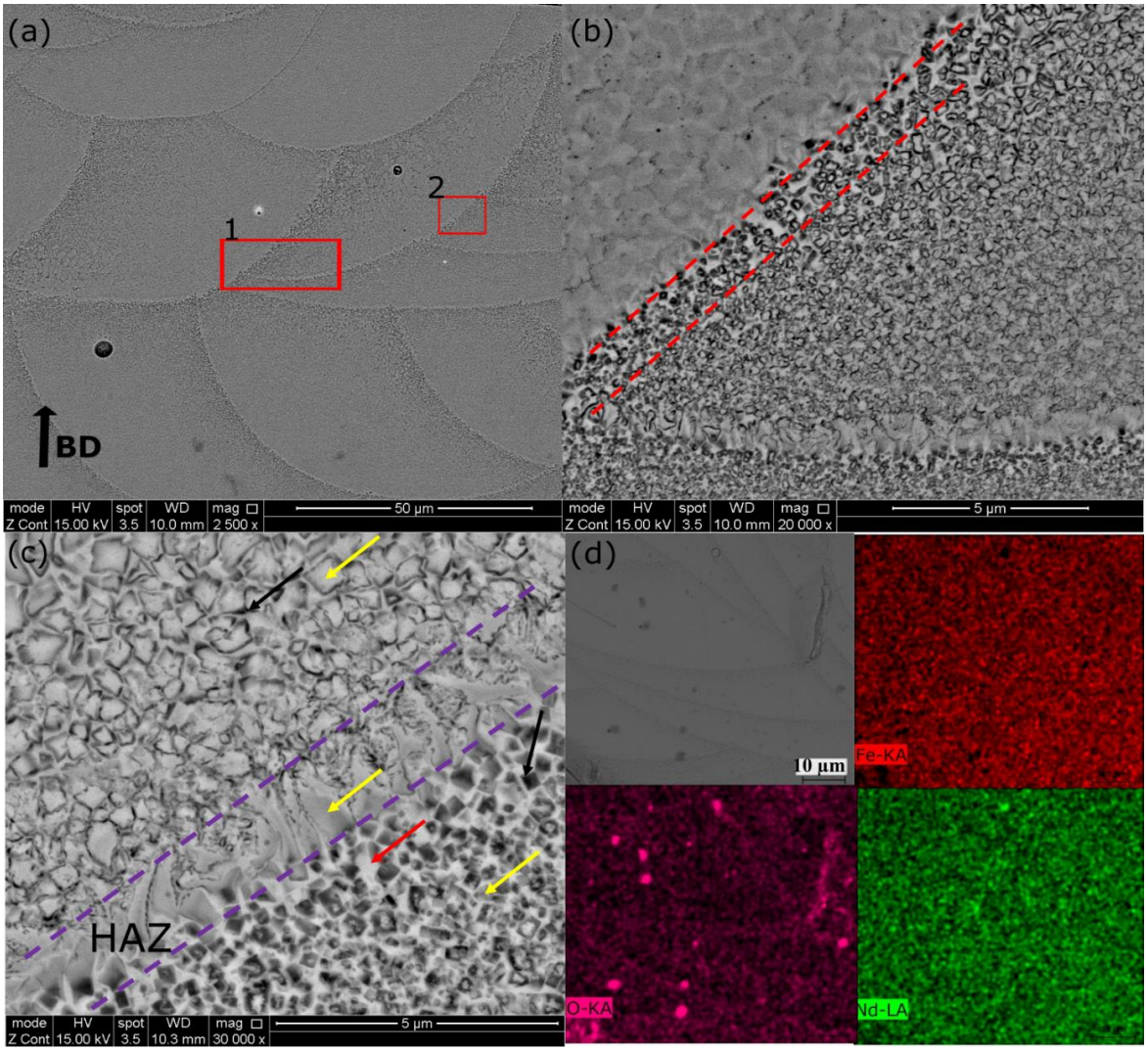

Figure 4-26 SEM images of the SLM-printed NdFeB, (a) a high-scale image showing the melt pools; (b) grain size variations in the melt pool;(c) phases in the melt pool (HAZ) and just under the HAZ (black arrows point to α-Fe, red arrow points to Nd-rich phases and yellow arrows point to Φ; (d) EDX-SEM colour map showing O, Fe and Nd content on the sample surface.

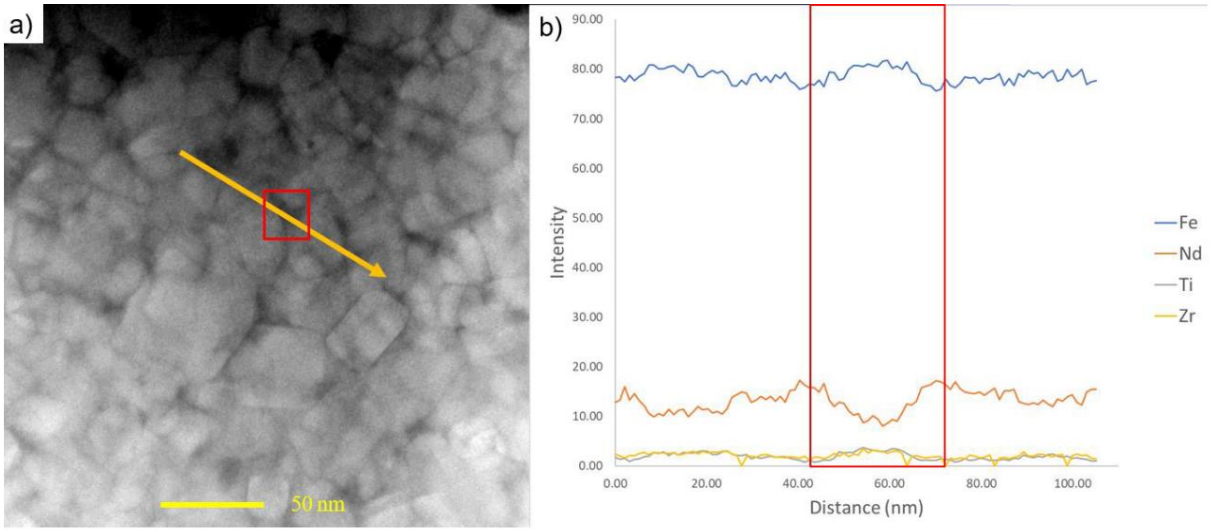

Figure 4-27 TEM-EDX line scan of the main phase; b) Corresponding elemental signal.

4.4. Discussion

4.4.1. Effect of LP and ED on Density of the Sample

Single track analyses show better continuity of the tracks obtained by increasing linear energy, *EL=LP/LS*. *EL* is increased by increasing laser power and decreasing laser speed, which results in a higher level of energy absorption by powder, then melts better the powder layer on the build platform. However, in 3d printing, high *LP*/ low *LS* combinations were found to cause unsuccessful printing since they cause high *ED* and excessive energy exposure on powder. It was found that *ED* needs to be below a critical value, in that case, 125 J/mm^3, to avoid overheating; hence the printing fails. On the other hand, it needs to be above the minimum level of *ED* to melt the powder and avoid lack of fusion porosities. In that study, there is no minimum level of *ED* defined. However, a minimum level of laser power is defined as 60 W. It was found that the samples having laser power 40 W and 50 W cannot be printed; their *ED* is between 50 -83 J/mm^3. The laser power is quite low here; however, the laser scan speed is also kept low. Hence it was expected that the *ED* would be enough to melt the powder, but the energy of laser power was not sufficient to melt the powder. There was no successful printing obtained. (Failed samples can be seen in Figure 4.5). On the other hand, samples having laser power 60 W and above could be printed since the laser power was enough to melt the powder. Their *ED* is between 50-83 J/mm^3 , as same as the sample having *LP* 40 W and 50 W. Furthermore, laser power from 60 W to 100 W in the same *ED* range, 50-83 J/mm^3, shows that the higher *LP* results in higher densities, as shown

in Figure 4.6. It is because even though the *EDs* of the samples are in the same range, the ability to melt powder reduces with the reducing *LP*. The micro-CT images presented in Figure 4.7 proves this statement; there are many LoF porosities in the low *LP* sample, 60W, while the higher *LP*,100 W, melts the powder better.

Another important aspect worth noting is the pronounced effect of power on part density. Varying the laser power level affects the minimum Energy Density required for achieving 91 % dense NdFeB SLM parts. Figure 4.6 shows an inverse correlation between power and the minimum Energy Density required for good melting of NdFeB powder in the SLM process. It can be seen that for a power of 60 W the minimum Energy Density required is 80 Jmm^3, while for a power of 80 W the minimum Energy Density required for achieving 91% dense parts is reduced to 59 J/mm^3 only. Therefore, it can be concluded from this analysis that power has a more pronounced effect on NdFeB melting in the SLM process. The printing quality is more likely depending on the laser power however the increasing *ED* also increases the density of the samples, seen in Figure 4.6. It is also worth noting that the increasing laser power above 130W reduces the sample density (as can be seen in Figure 4.9), which is possibly due to the excessive energy causing overheating of powder and creating keyholes in the melt pool. In addition, very high laser power/ very high scan combinations do not help to improve printing quality since they cause larger cracks in the sample [88] .The damaged integrity of the sample can be seen in Figure 4.11, *LP*: 200 W/ *LS*: 5500 mm/s.

4.4.2. Effect of *LP* and *ED* on Magnetic properties

The remanence, B_r, of the samples decreases with the decreasing *LP* and *ED* since the LoF porosities reduce the percentage of magnetic structure in the components. In addition, XRD findings, as seen in Figure 4.6, prove that the low *LP* -low *LS* reduces the amount of Φ phase and increases the α-Fe phase, possibly caused by lower cooling rates resulting from lower laser power with lower laser scan combinations. These results are confirmed by the results in Figure 4.20, showing that the increasing laser speed results in higher B_r, since it increases the cooling rates.

4.4.3. Effect of *HD* and *LT* on Density

It is found that the decreasing *LT* and *HD* increase the density, as can be seen in Figure 4.12. Because high *HD* causes insufficient overlap between the laser tracks, and the laser cannot melt all powder in the layer, reducing the density. On the other side, if the layer thickness is very high, the laser source can only melt some of the powder in the layer [110], which causes insufficient overlap between the layers. In addition, the melt pool morphology is affected by *LT*. Low *LT* values give shallow melt pool morphology, as seen in Figure 4.16, which increases the cooling rates [82]. It is favourable since the previous section concluded that higher cooling rates result in a higher amount of Φ phase. Both *HD* and *LT* are important; however, the results in Table 4.5 shows that the impact of *HD* on density is higher than the impact of *LT* on density.

4.4.4. Effect of Cooling Rates on Magnetic Properties

It was found that the magnetic properties are not only related to density of the samples, but also related to the cooling rates. Figure 4.20.a and 4.20.b proves that statement since it is obvious that all highly dense samples are not highly magnetic. The highly magnetic samples are in the direction of faster cooling rates, where the laser speed increases. It was confirmed that the faster scans result in high Φ phase – low *a-Fe* phase, while slow scans result in low Φ phase – high *a- Fe* phase [2] . The cooling rates are important to control the magnetic phase, so *EL, (LP/LS),* is another important parameter needed to be considered. This study found that the *EL* between 0.03-0.04 Ws/mm, gives higher remanence. In contrast, the remanence tends to decrease by increasing *EL* to 0.05 Ws/mm, as shown in Figure 4.20.d. This confirms the conclusion in the "Effect of *LP* and *ED* on Magnetic properties" section; the higher cooling rates give higher B_r.

4.4.5. The Relationship Between *LP-EL* and Magnetic Properties/ Phase

Figure 4.21 shows an improvement in B_r until *LP* 130 W; then, it starts to decrease as the *LP* increases from 130 W to 170 W. The decrease in the B_r is related to decreases in the amount of Φ phase after 130W. Figures 4.21.c and 4.21.d show that Φ phase reduces and the amount of *a*- Fe phase increases after 130 W. The laser speed is kept constant here; hence the increasing laser power applies more energy to the powder, causing

slower cooling. The *EL* is 0.037 Ws/mm for the 130 W sample; then it increases up to 0.048 Ws/mm with the increasing *LP* to 170 W. Therefore, it can be concluded that the cooling rates above *EL*, 0.37 Ws/mm need to be avoided to get a high percentage of Φ phases. This finding is almost same with the finding in previous section; *EL* between 0.03-0.04 Ws/mm, gives higher remanence.

On the other hand, H_c is not directly proportional to the percentage of a-Fe phase and Φ phase, as seen in Figure 4.21 and Figure 4.22. It is because the coercivity is not only related to the phase amount but also the phase distribution, homogeneity, and composition of the grain boundaries [81].

4.4.6. Overall Analysis of SLM-NdFeB Printed Magnets and Comparison with the State- of- the- Art

Parameter optimisation in this study improved the magnetic properties more than the published results in the literature, up to B_r;0.72 T H_{ci} ; 947 ka/M. However, the magnetic properties of the selective laser-melted NdFeB magnets are still low compared to their sintered counterparts. High quality magnets using traditional method typically have magnetic properties are between B_r:1-1.3T and H_{ci} : 870 -2700 kA/m (data is taken from Arnold Magnetic Technologies). SLM-printed samples need to be improved to reach these magnetic properties. The element doping might increase the coercivity, while there is a risk of remanence reduction. Dy substitutes the Nd in the $Nd_2Fe_{14}B$ phase, creating $Dy_2Fe_{14}B$, which has a larger anisotropic field, 7.6 T, than $Nd_2Fe_{14}B$,15.8 T. Additionally, it makes grains fine and uniform. Both improve coercivity. In contrast, the saturation magnetisation of the $Dy_2Fe_{14}B$ is lower than $Nd_2Fe_{14}B$, 0.7 T to 1.6 T, respectively. So, remanence decreases by Dy addition. Even though the risk of remanence reduction, Dy addition is worth trying. Because the improvement of magnetic properties by optimising processing parameters is limited due to the intermetallic structure of NdFeB, the high thermal stresses caused by high cooling rates of SLM, and the brittle structure of the material cause porosities, cracks and delamination [15].

4.5. Conclusions

The SLM printing of NdFeB has many challenges because the material's low thermal conductivity causes high thermal gradients during the cooling, generating high residual stresses. In addition, the brittle nature of the hard magnetic phase reduces the fracture toughness of NdFeB. Consequently, the residual stresses cause cracks easily, in addition to delamination.

The cracks on the sample surfaces make it difficult to get a smooth surface with grinding and polishing, which is needed to get high-quality microscope images. Most of the melt pools were cracked, and some pieces were pulled out after the sample preparation. Moreover, there is a risk of misleading the magnetic test results due to the poor surface quality of the samples, and extreme oxidation sensitivity of Nd-Fe-B. Oxidation on the surface also affects the EDX and XRD results.

The experimental conclusions are as follows;

- The higher laser power gives wider track width. In addition, higher *EL* values result in better track continuity.
- High *ED* causes high residual stresses during the cooling of the samples, causing cracks, material delamination and possible keyholes due to the entrapped air bubbles in the sample. All cause sample failure during or after the printing with the brittle nature of the material.
- The high *LP*/high *LS* combinations (up to 100 W *LP*/3000 mm/s *LS)* give higher sample density and remanence values than the low *LP*/low *LS* combinations (below 60 W *LP*/1250 mm/s *LS*). The higher amount of *α-Fe*phases detected in the low *LP*/Low *LS* combination can be attributed to the lowB_r. Moreover, the printing quality is more likely depending on the laser power however the increasing *ED* also increases the density of the samples.
- The density of the samples starts to reduce after *LP* 120-130 W (*ED* and *EL* are kept in the safe *ED* range). The combination of very high laser speed and high laser power generates unstable melt pools that result in low-density samples. Laser speed should be sufficiently low to allow sufficient melting and powder consolidation. The very high *LP/LS* (200 W/5500 mm/s) combinations also

destroy the sample's integrity. In addition, no successful sample obtained *ED* above 125 kJ/mm3.

- Variable layer thicknesses and hatch distances from 20 to 50 μm and 20 to 40 μm, respectively, were set in order to be able to understand how it would affect the density. The decreasing *LT* and *HD* increase the density of the samples, and increasing *LT* narrows the melt pool horizontally while it increases the melt pool depth. There are un-melted powders in the high *HD samples* since high *HD* causes insufficient overlap between the scan lines, thereby reducing the density of the samples. Furthermore, the effect of layer thickness and hatch distance on density was compared. It was found that the effect of *HD* on sample density is higher than that of *LT* on sample density. In addition, many cracks were observed in the samples, mostly parallel to the build direction.

- There is no linear relationship between the remanence and the density values. It was noticed that all the high magnetism samples are high density, but all the high density samples were not high magnetism. It can therefore be concluded that the cooling rates, hence the phases, are the other vital points that should be considered in order to understand the background of magnetic properties. The higher *Br* samples are obtained by the *EL* between 0.03-0.04 Ws/mm with the *ED* between 75 to 100 J/mm3 while the *Br* values reduce with the increasing *EL* to 0.05 Ws/mm and *ED* to 125 J/mm3. It is also concluded that the high B_r samples are result of faster scans.

- The results of the XRD analyses show that there are two main phases in the $Nd_2Fe_{14}B$ samples, which is the strong magnetic phase and the α-Fe phase. It was found that the magnetic properties are highly dependent on these phases. The higher magnetic phase ($Nd_2Fe_{14}B$) was detected in the samples with higher B_r and H_{ci} values. In contrast, the lower *α-Fe* phase found in the samples has higher B_r and H_{ci} values.

The state of the art of this chapter is it that the improving the magnetic properties B_r and the BH_{max}, 0.72 T and 81 kJ/mm3, respectively, by processing parameters. (The printing parameters are *LP*:100 W-*LS:* 2250mm/s, *LT*:20 μm- *HD*: 30 μm). They are the highest properties obtained with *MQP-S-11-9-20001* by SLM without post-processing or element doping. The coercivity value is 947 ka/M, which is much better

than most of the works in the literature. However, the magnetic properties are lower than the desired properties for industrial applications, which are around B_r 1.2 T, H_{ci} 1592 kA/m and BH_{max} 310 kJ/m^3.

On the other hand, there is an improvement in understanding parameter effects on density and magnetic properties, which are not discussed detailed in the published papers. The SEM images in this chapter are also valuable in an academic context since they clearly show the grain formation and morphology in the melt pool. In addition, the phase analysis in this chapter is also significant since there is no study in the literature showing the relationship between the phase and printing parameters.

Chapter 5: Influence of the Heated Bed in SLM on Density and the Magnetic Properties of NdFeB

5.1. Introduction

In this chapter, the effect of the heated bed on the magnetic properties and densities of the samples will be analysed. This chapter discusses the goal of reducing the porosity of the samples and the cracks originating from thermal stress. It is expected that the magnetic properties could improve by increasing the density of the samples.

NdFeB magnets are the most common permanent magnets due to their high coercivity (*Hc*), high remanence (*Br*), and high energy product (BH_{max}). Selective lasermelting is one of the production methods that helps to overcome the design limitationsof common production methods (e.g., sintering). However, SLM-printed magnets have lower magnetic properties compared to sintered magnets mostlyrelated to cracks, (caused by residual stresses originated fast cooling) and the high porosity in SLM-printed samples. It is reported that the preheating and re-scanning reduces the residual stresses in SLM -stainless steel efficiently [111]. Also, bonding abilityof the magnesium powder improved by preheating [112]. Therefore, it was considered that the heated bed has a potential to decrease residual stresses in SLM NdFeB.

This chapter will focus on the effects of the heated bed on the density and magnetic properties of SLM-printed NdFeB magnets. In addition, the influences of printing parameters will be examined at 300℃, 400℃ and 500℃ bed temperatures. The expectation is a reduction in cracks and porosities in the samples by reducing the thermal stresses that occur during the printing process, thus improving the magnetic properties.

The heated bed trials are affected by the instability of the built platform. However, there are a number of important findings discussed in the chapter. The results show that, compared to a room temperature printed sample, both sample density and B_r increased with the heated bed while coercivity decreased. The increase in the B_r is

related to increase in density and the drop in H_c is related to the change in microstructure. The larger non-uniform grains, (compared to room temperature printing), with the dendritic shape grains reduces coercivity. In addition, the surface quality is improved.

5.2. Materials and Methods

Heated bed temperatures were set from 300℃ to 550℃ in 50℃ increments. The samples were printed in 10 mm × 10 mm × 10 mm sizes in an argon atmosphere with oxygen levels below 50 ppm. The temperatures of the samples were checked at the end of the printings using a gun pyrometer. SEM images were taken with an Inspect F 50 and Inspect F machine. The magnetic properties were tested with a permeameter in Arnold Magnetic Technologies.

5.3. Working Principle of the Heated Bed and Preliminary Observations

Initially, the heated bed platform was replaced with a room temperature platform. The steps of the heated bed fitting are shown in Figure 5.1. The heated bed is placed in the centre of the build area on the induction heater. The diameter of the heated bed build platform is smaller than the diameter of the regular/room temperature build platform, at 35 mm and 70 mm, respectively, (the diameter of the induction heater is 35 mm).

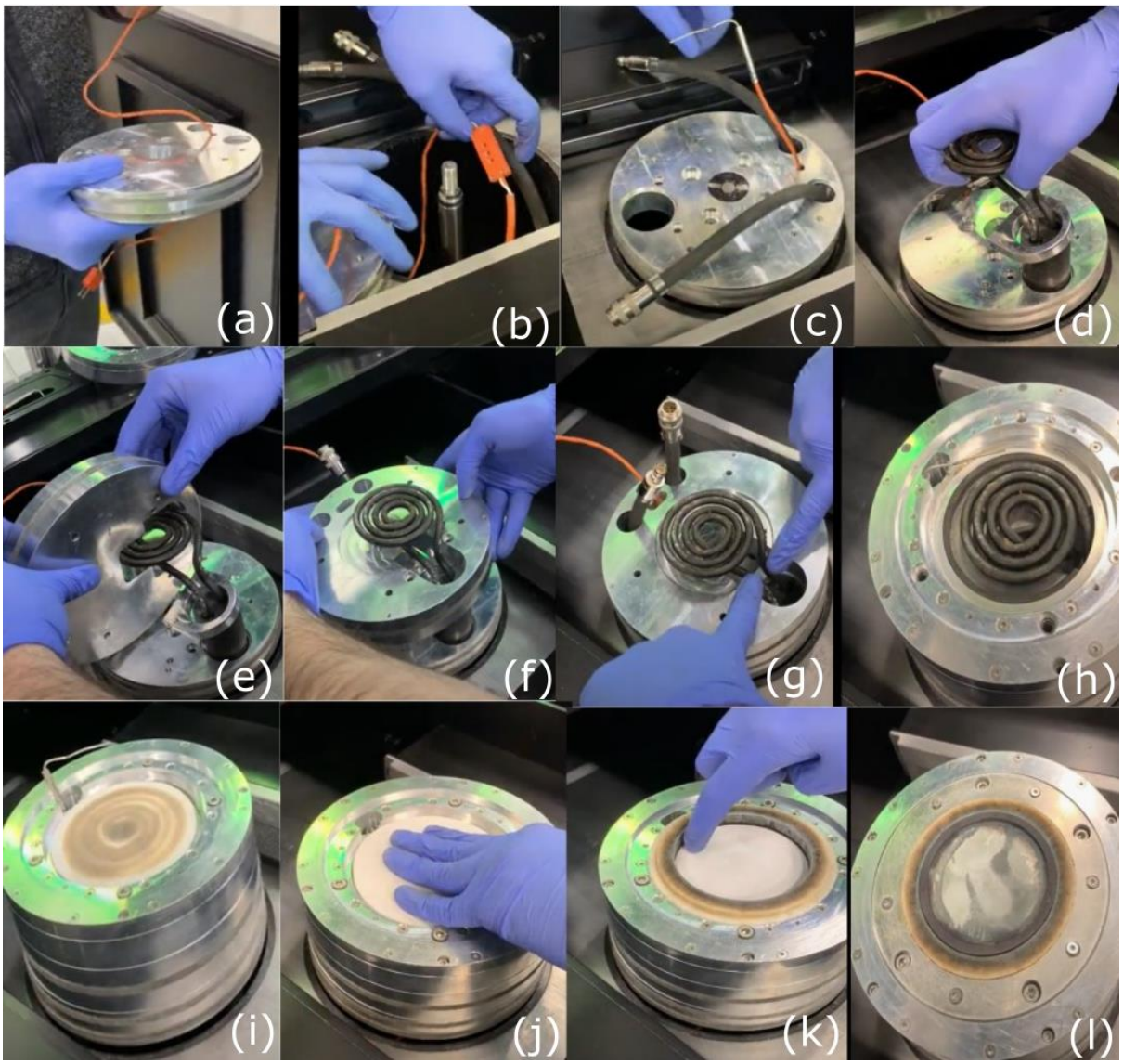

Figure 5-1 Heated bed fitting steps, (a)-(b) thermocouple attachment ;(c) fittings of cooling water pipes and thermocouple; (d)-(e)-(f)- (g)-(h) fitting of induction heater; (i)-(j) placement of insulation on top of induction heater; (k)-(l) placement of insulation circle.

Once the heated bed is fitted, the build platform is placed on it. Then an external thermocouple is connected on the build platform, while there is another thermocouple is fitted under the heated bed, schematic view of thermocouple connections can be seen in Figure 5.2.

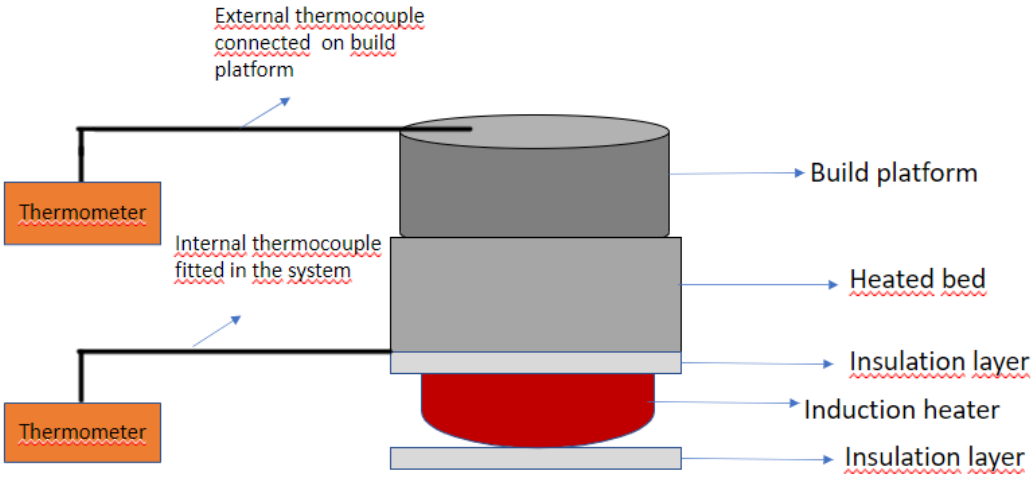

Figure 5-2 Schematic view of the thermocouple connections to heated bed system.

There is a temperature difference measured between the software (data collected from the thermocouple fitted under the heated bed) and the temperature on the build platform (data collected by the thermocouple connected on the build platform). The temperature tests were done without powder. The results were plotted and can be seen in Figure 5.3.a. The difference is small until 380°C after which it increases to 160°C until cooling down starting at 75 minutes.

In the third step, the first heated bed trials were performed at 200°C and 400°C with the following printing process parameters: 130 W 3500 mm/s 20 µm *LT* 30 µm *HD*. Both trials failed, due to the extremely brittle samples and also due to the sample attachment problem on the build platform. The temperatures of the samples were checked by a gun pyrometer after the printing stopped, and it was observed that 200°C sample was 400°C and the temperature of the sampleprinted at 400°C was 600°C. Before any further heated bed printing trials, it was decided to check the temperature differences in more detail. Therefore, in the next trialthe heated bed was turned off and the printing completed without heating. Then it wasturned on again while the samples were still waiting in the closed chamber. The bed was heated to 600°C. Figure5.3.b shows that the temperature difference between the samples and the software was 100°C at the beginning of heating; then it increased to 280°C after 45 minutes. It was concluded that the temperature difference increases with the increasing set temperature.

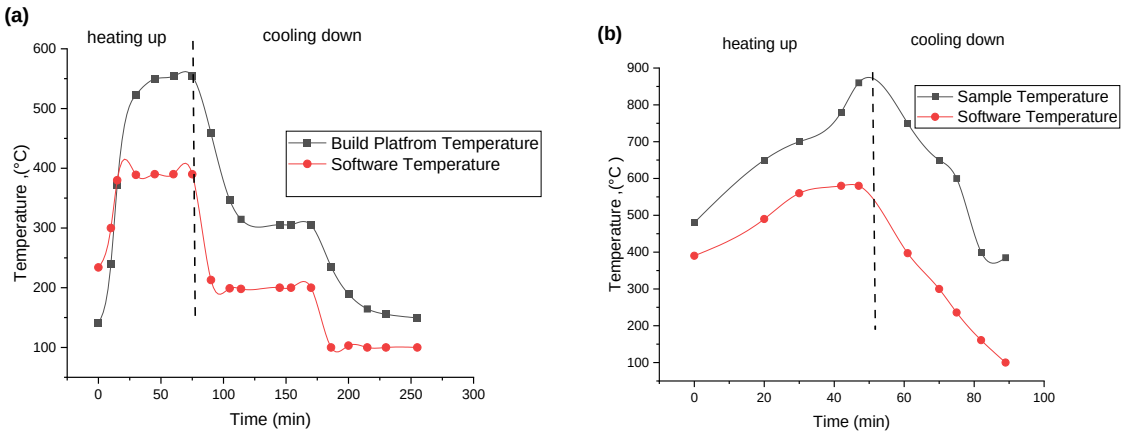

Figure 5-3 (a) Build Platform temperature - time versus software temperature-time; (b) Sample temperature-time versus software temperature-time.

The excessive heat on the build platform with the combination of the heated bed and laser scan makes it difficult to produce successful prints as the first couple of layers cannot attach to the build platform. A possible explanation for this might be that the material evaporation is caused by the excessive heating. Therefore, in the following step, it was decided to turn off the heater until the first half of the printing completes to ensure that the samples attached to build platform well and they do not break due to the wiper movement. Then the heater was turned on for the second half of the printing. A gun pyrometer was used to check the temperature of the samples in the closed chamber after the end of each heated bed trial.

The heated bed printing is challenging not only because of the excessive temperature but also because of the unstable build platform. The build platform of the heated bed is smaller than the room temperature build platform. During the heated bed printing, the build platform is placed on the induction heaters in the middle of the room temperature building area and fixed by the filled powder around it, as shown in Figure 5.4.a. This creates a relatively stable platform. Directional printing because of the unstable build platform can be seen in Figure 5.4.b. In this study, set/software temperatures were used to avoid confusion. Figure 5.5 shows the schematic view of the fixed heated bed build platform by surrounding powder around it.

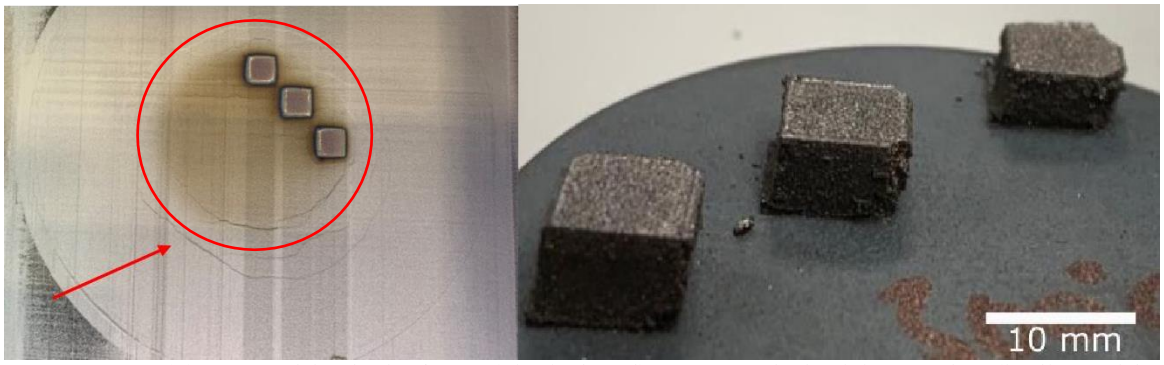

Figure 5-4 (a) Heated bed platform (circled red) surrounded with powder (indicated by the red arrow); (b) Heated bed samples with directional printing at 300°C.

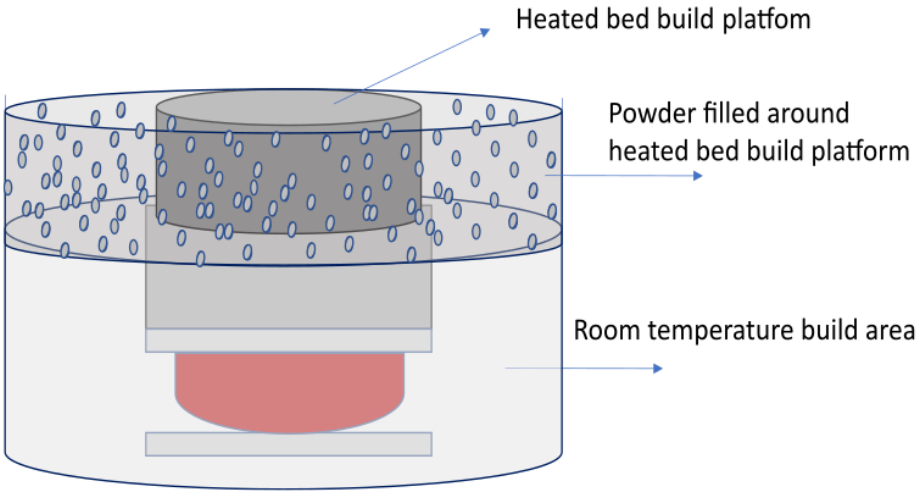

Figure 5-5 Schematic view of fitted heated bed by surrounding powder around.

5.4. Results and Discussion

5.4.1. Effect of the Heated Bed on Density and the Magnetic Properties of the Samples

The heated bed could improve the density of the room-temperature printed sample from 90% to over 96%. Despite this improvement in density, there is no increasing trend between the rising bed temperature and the sample density. The average density of the samples is 93.93% at 300°C, 96.66% at 350°C, 93.80% at 400°C, 94.60% at 450°C, 96.4% at 500°C and 96.3% at 550°C (Figure 5.6). The fluctuations in the densities of the three samples at every bed temperature from 300 to 550°C are likely related to the instability of the building platform. Figure 5.7 shows the printed samples at 300°C, 350°C, 400°C and 500°C. It is deduced that the delamination near the top

surfaces and the corners indicated by red arrows are related to the faster cooling rates on the top of the samples and excessive energy input.

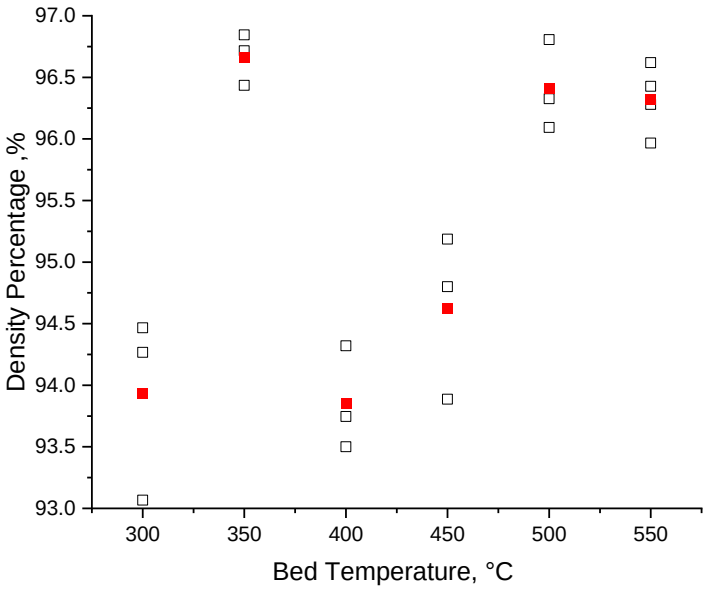

Figure 5-6 Relationship between bed temperature and sample density; the red points are the average density of the samples.

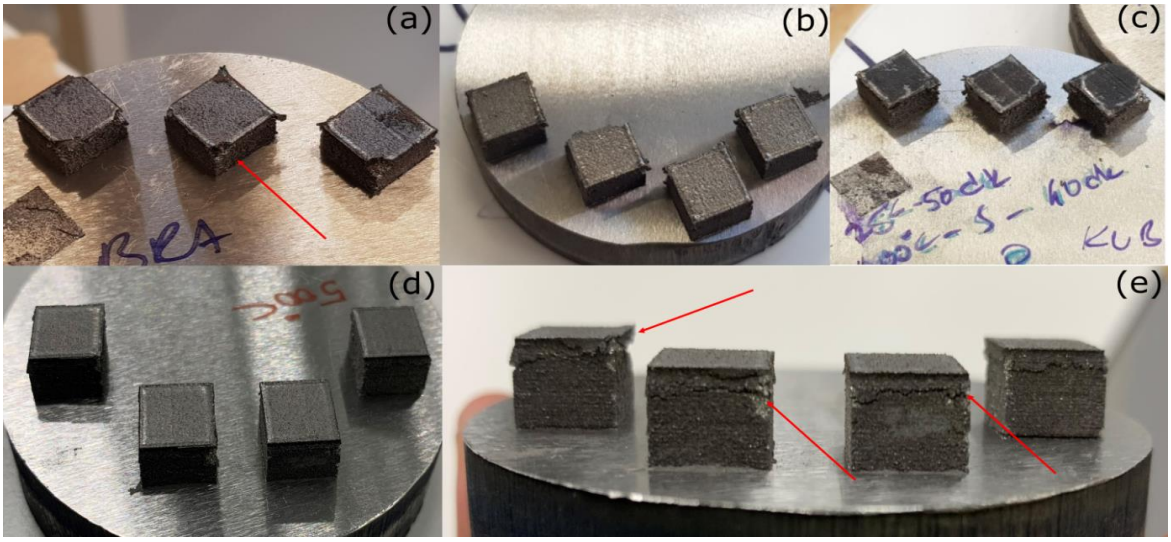

Figure 5-7 Heated bed printed samples; bed temperature at (a) 300℃ (410℃); (b) 350℃(520℃); (c) 400℃ (580℃); (d) 500℃; and (e) 500℃. The temperatures in the parentheses were checked with a gun pyrometer after the printings finished. (Sample size: 10 mm × 10 mm × 10 mm).

5.4.2. Magnetic Properties

The printed magnets were magnetized by a pulsed magnetic field. It was found that the easy axes of the samples are on the print build direction. The fluctuations seen on the density results are also seen in the magnetic properties. Figure 5.8 shows the B_r *and* H_{ci} values of the samples at 300℃, 350℃ and 400℃. The remanences of the samples printed at 300℃ range from 0.57 T to 0.72 T, and those printed at 350℃ range from 0.64 T to 0.75 T, while those samples printed at 400℃ are almost the same, at 0.65 and 0.67 T. On the other hand,the coercivities of the 300℃ samples range from 320 kA/m to 913 kA/m, the 350℃ samples range from 509 kA/m to 871 kA/m, while the 400℃ samples are nearly the same. The B_r and H_{ci} values of the 300℃ and 350℃ samples fluctuate, while the 400℃ B_r *and* H_c values of the samples are nearly the same as like their density results are nearly the same.

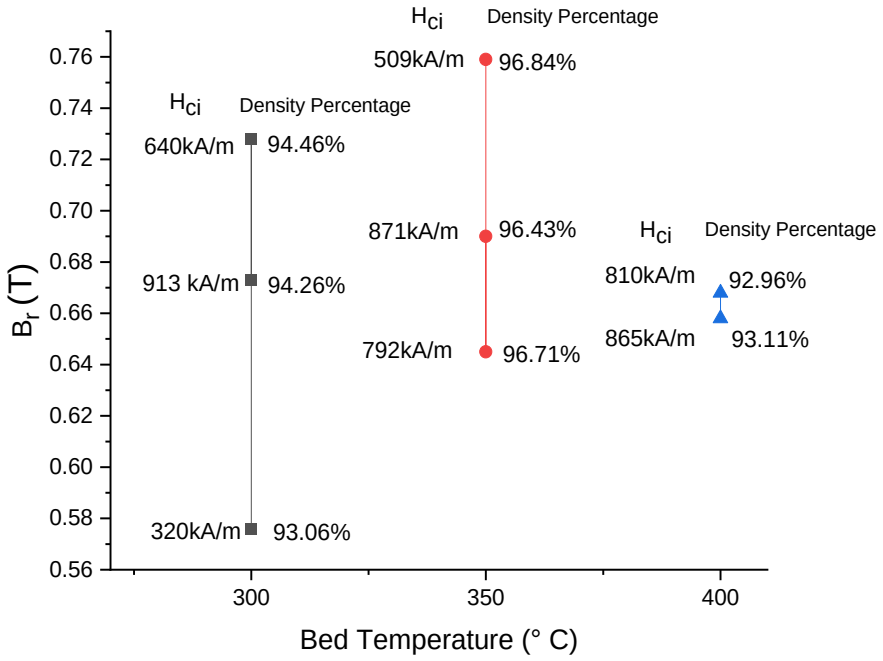

Figure 5-8 B_r-H_{ci} – density of the sample relationship with the heated bed temperatures of 300℃, 350℃ and 400℃.

On the other hand, a clear improvement is seen in the density of the samples with the heated bed, as seen in Figure 5.9.a. Despite the B_r increments not following the density increment trend, the heated bed improves the B_r and BH_{max} values, as shown in Figures 5.9.b and 5.9.c. B_r increases from 0.61 T to 0.76 T, while BH_{max} increases from 55 kJ/m^3 to 84 kJ/m^3. Moreover, there is a remarkable trend in the BH_{max}. Despite the fluctuations in the B_r and H_{ci} values, the BH_{max} has a remarkable decreasing trend regarding increasing the heated bed temperature from 400°C to 550°C. Regardless of the decreasing trend in the BH_{max}, it is still superior to the room-temperature printed sample. In contrast, the H_{ci} value drops dramatically with the heated bed, from 1000 kA/m to below 850 kA/m, as shown in Figure 5.9.d. In summary, the increasing heated bed temperature shows no trend in both the B_r and H_{ci} values, while the BH_{max} decreases with the increasing heated bed temperature. In addition, it is concluded that the heated bed increases the density of the sample hence increases the remanence, by increasing the percentage of the magnetic content in the entire structure. On the other hand, the increasing bed temperature decreases the cooling rates, which was expected to result in lower percentage of Φ phase in the samples. However, Figure 5.9 shows improvements in the B_r values; hence it is concluded that the effect of density improvement is greater than the effect of cooling rates on B_r. Even though the heated bed reduces the cooling rates with an extra energy input from the bed heating, the cooling rates are still much higher than the cooling rate required for Φ phase. (Φ is confirmed in section 5.4.5. by XRD results).

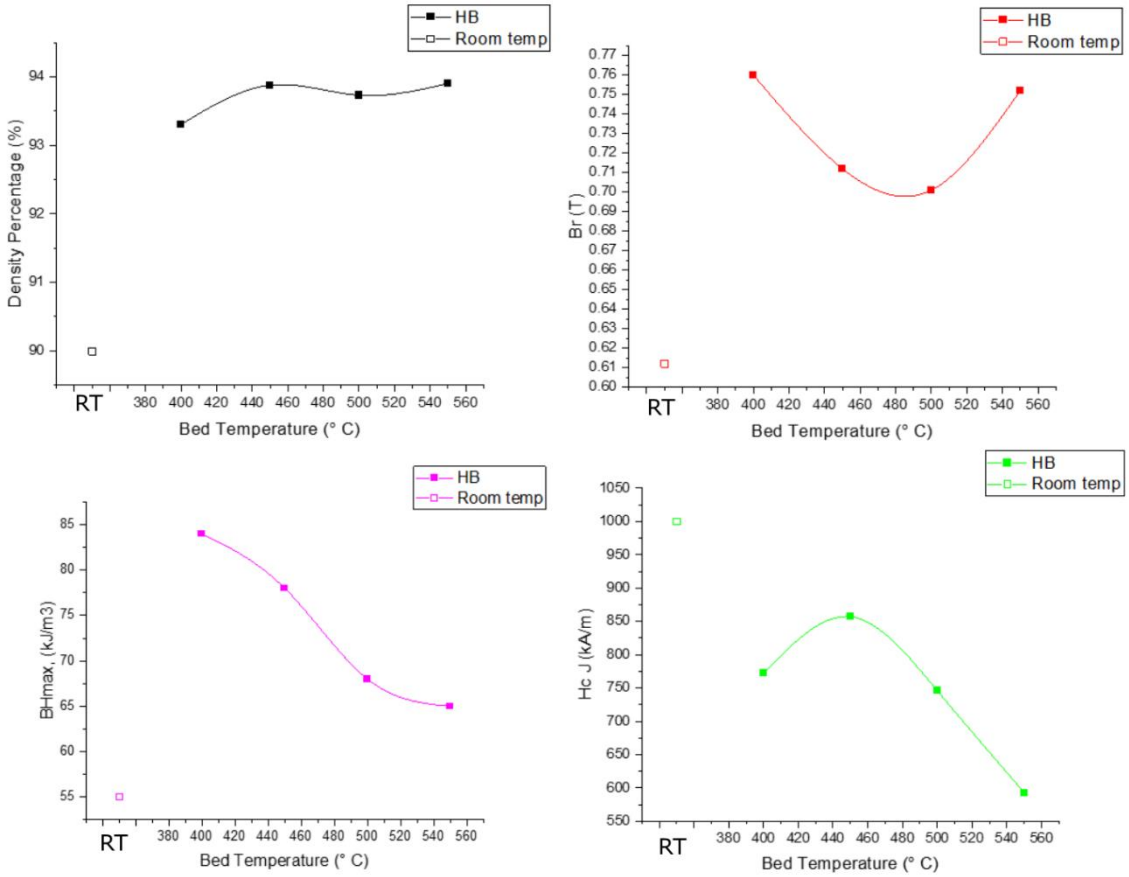

Figure 5-9 Relationship between (a) the density percentage of the sample and heated bed temperature; (b) B_r and heated bed temperature; (c) BH_{max} and heated bed temperature; and (d) H_c and heated bed temperature. (Magnetic tests were done with a permeameter by Arnold Magnetic Technologies) – (RT: room temperature).

5.4.3. Microstructural Evaluation

The microstructure occurring in the heated bed samples are different from the room temperature printed samples. The grain morphology in the room-temperature printed samples is globular homogenous compared to the heated bed samples, as seen in Figure 5.10.d. In comparison, the dendritic grains observed in the heated bed printed samples are mostly oriented in the direction of the building, seen in Figures 5.10.a, 5.10.b and 5.10.c. The drop in coercivity in the heated bed samples might be related to the dendritic grain formation. The lower cooling rates of the heated bed cause in situ heattreatment during and after the printing, allowing grains to grow larger, while high cooling rates in the room temperature printing results in finer grains. It is known that the smaller grains in room temperature printed samples leads to better wettability Nd, which improves the decoupling between the grains, which consequently increases the coercivity [80]. It is known from the literature that grain size is lowered to below 1 μm through SLM printing, which helps to improve coercivity [2]. Thus, it can be deduced that the larger and more dendritic grains in the heated bed samples might be the reason for the drop in coercivity in the heated bed. On the other hand, B_r improved with the heated bed, possibly due to the lower porosity in the heated bed samples, giving higher magnetic structure.

The grain size of the heated bed samples and the room temperature printed samples are shown in Figure 5.11.

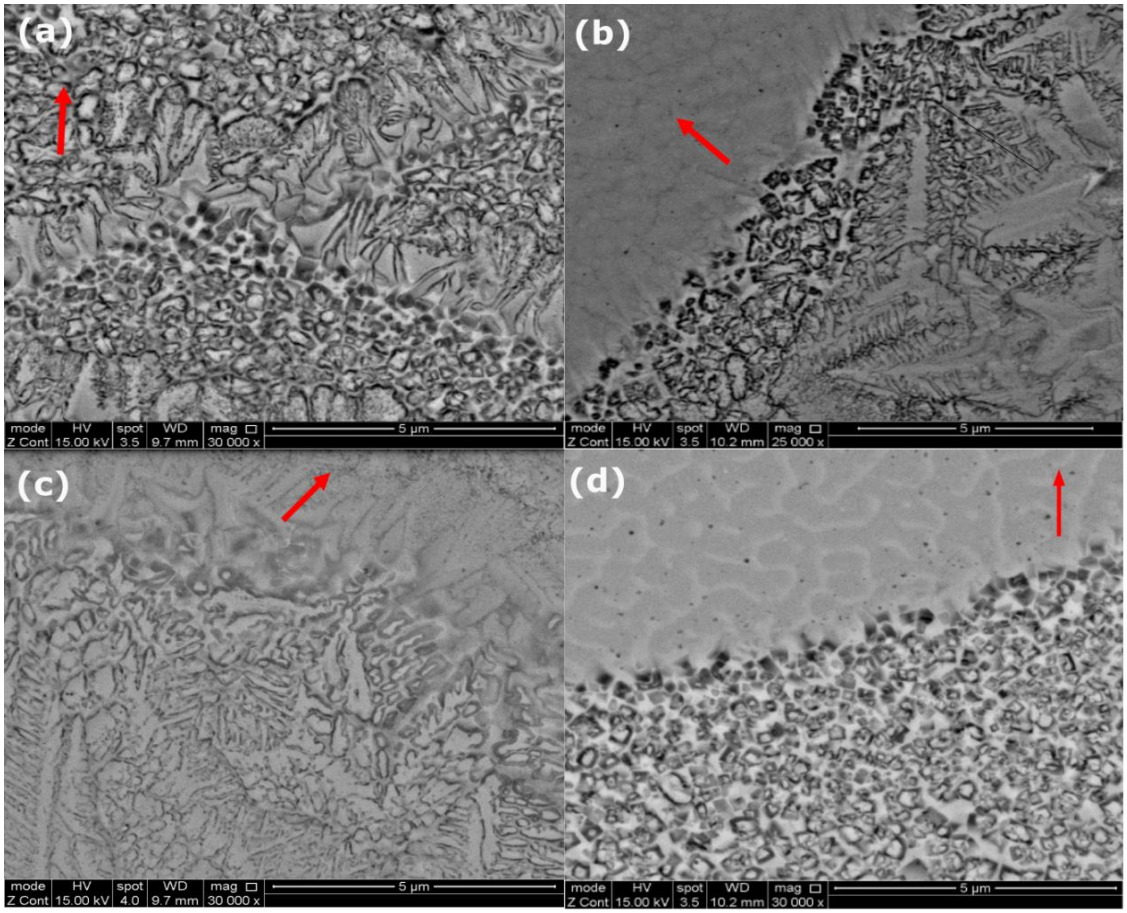

Figure 5-10 SEM images of the heated bed printed samples (a) at 400°C; (b) at 450°C; and (c) at 500°C; (d) room temperature printed sample; red arrows indicate the build direction.

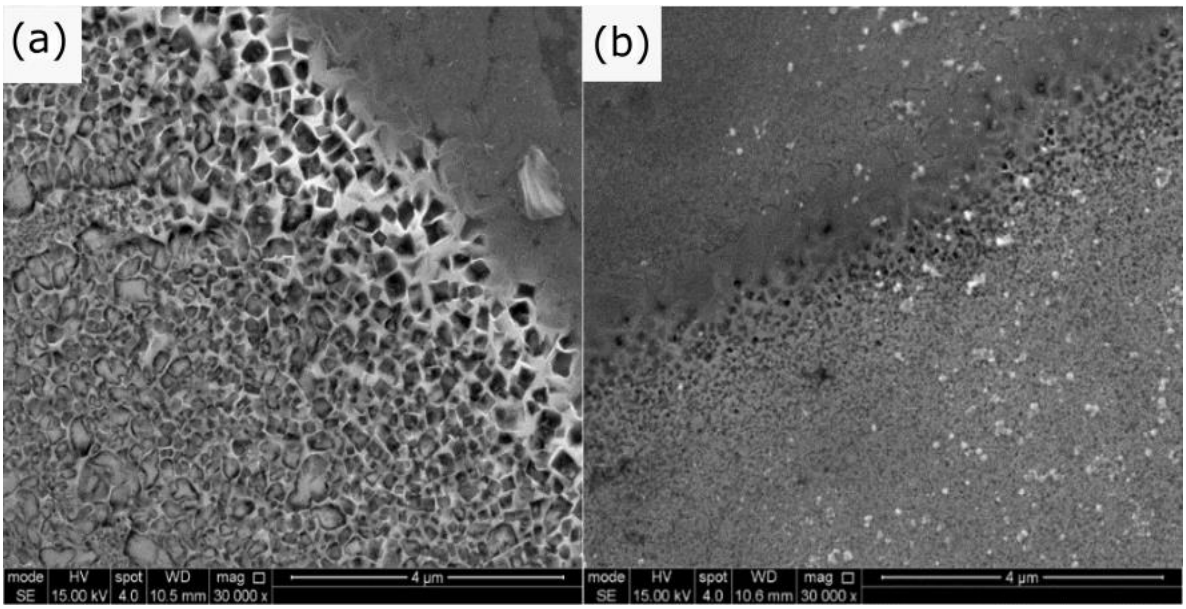

Figure 5-11 (a) SEM image of the 400°C heated bed printed sample; (b) SEM image of the room temperature printed sample.

The microstructural evolution of the NdFeB heated bed printed sample is complicated by the different cooling rates in the melt pool zone (MPZ) and the heat-affected zone (HAZ). Two different grain morphologies were observed in the MPZ and HAZ. Figure 5.12 shows the top view of the printed sample at 400℃. The grain sizes are more spherical and smaller in the MPZ compared to the HAZ. Since the grains in the HAZ were exposed to heating by the previously scanned powder, they found time to grow. Hence, grain sizes gradually decrease from the bottom of the MPZ to the top of the MPZ.

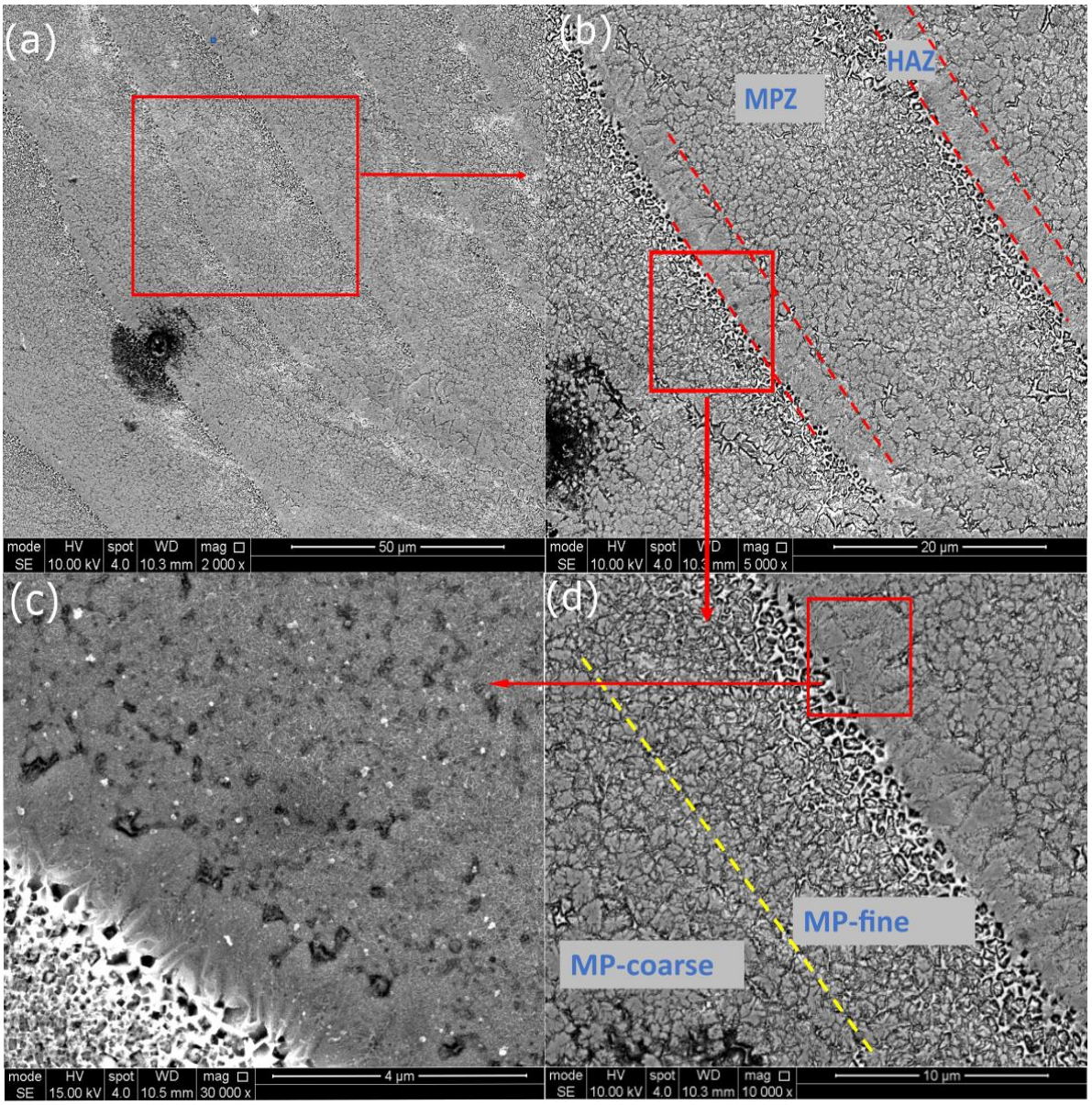

Figure 5-12 SEM micrographs of the SLM heated bed printed samples (a) laser scan tracks on the microstructure; (b) melt pool zone (MPZ) and heat affected zone (HAZ); (c) a closer look at the HAZ; and (d) coarse and fine grain areas in the MPZ.

Figure 5.13 shows the cross-section of the 400℃ printed sample. The melt pool lines can be seen in Figure 5.13.a. A closer look at the HAZ and MPZ shows that the equiaxed grains are seen in the MPZ, while columnar grains are seen in the HAZ/melt pool line, shown in Figures 5.13.c and 5.13.d, respectively.

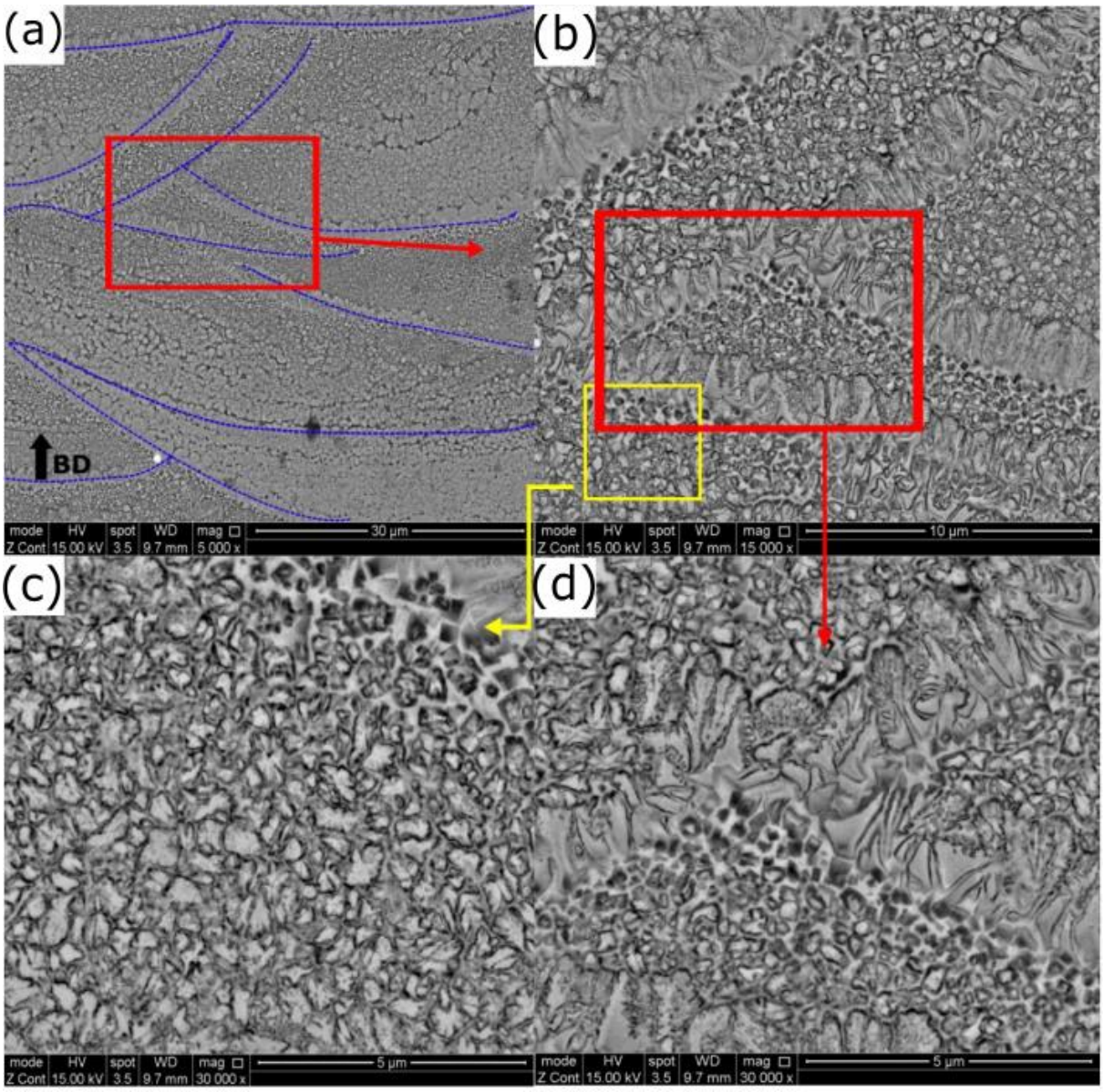

Figure 5-13 SEM micrographs of SLM-heated bed printed samples at 400℃ cross-section (a) melt pool lines; (b) closer look at melt pool line (HAZ) and melt pool zone (MPZ); (c) closer look at the HAZ and MPZ; and (d) fine grains in the MPZ.

In printed samples at 400℃, the columnar dendritic grains are seen only at the melt pool line (HAZ), and globular and equiaxed grains are seen in the MPZ. A different microstructure is seen in the 500℃ printed samples. The higher temperatures in them cause the columnar dendritic grains to be not only in the melt pool line but also in the melt pool zones, since the heat affecting area expands into the melt pool zone, as seen in Figures 5.14.a and 5.14.b. The grains are mostly columnar dendritic in the MPZs, where they narrow and cross each other and cause slower cooling rates which allows dendritic growth. However, there are still globular/equiaxed grains in the middle of the larger MPZ where the cooling rates are faster, as seen in Figures 5.14.c and 5.14.d.

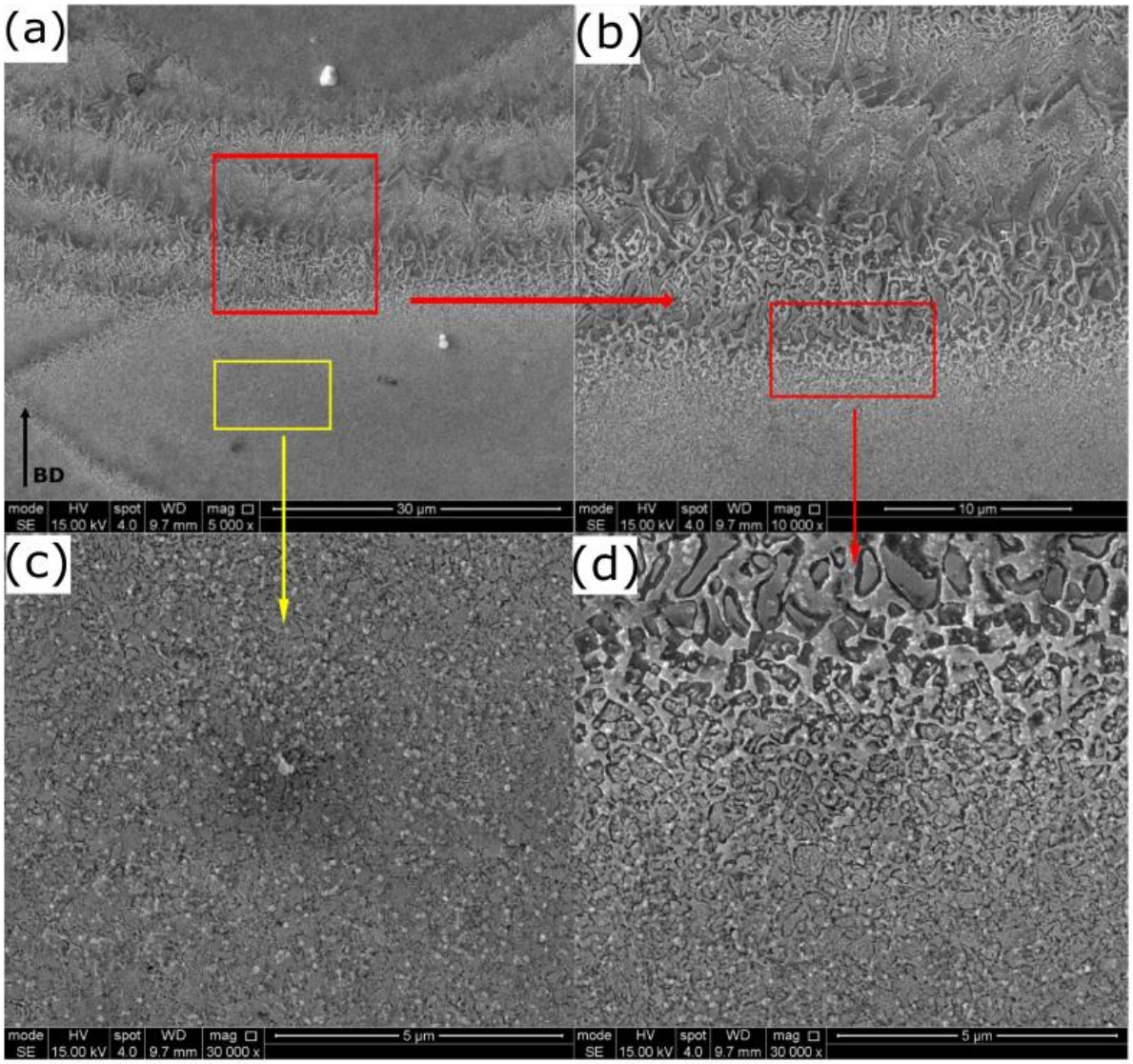

Figure 5-14 SEM micrographs of SLM heated bed printed samples at 500℃ cross-section (a) laser scan tracks/melt pool lines on the sample; (b) closer look at the overlapped melt pool zones (MPZ); (c) middle of the MPZ with finer grains; and (d) closer look at the HAZ and MPZ.

5.4.4. Surface Quality of the Heated Bed Samples

Surface quality improves with the heated bed. The samples have a smoother top surface quality than the room temperature samples, as shown in Figures 5.15.a and 5.15.b. The cross-section of the heated bed sample shows fewer cracks at the top layers, approximately 1 mm below the surface, which are better sintered. Furthermore, it is observed that the melt pool depth decreases through the building direction, as seen in Figure 5.15.c.

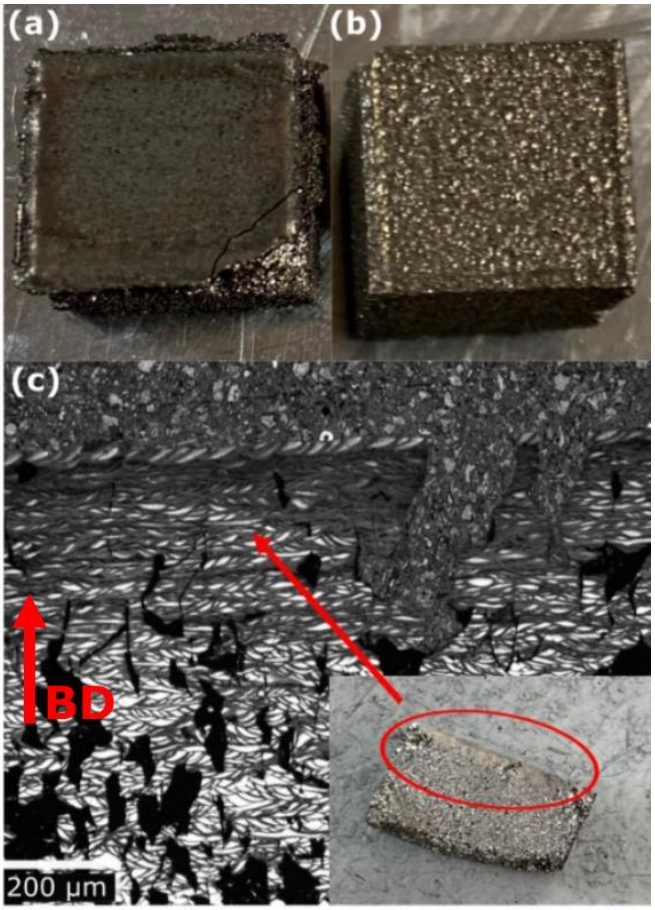

Figure 5-15 (a) Sample surface printed at 400°C; (b) Sample surface printed at room temperature; and (c) Optic image of the cross-sectioned heated bed sample.

Figure 5.16 shows the optic images of room temperature, 400℃ and 550℃ printed samples. Surfaces that are almost crack-free are seen in the heated bed samples. The melt lines are combined and become continuous at 550℃.

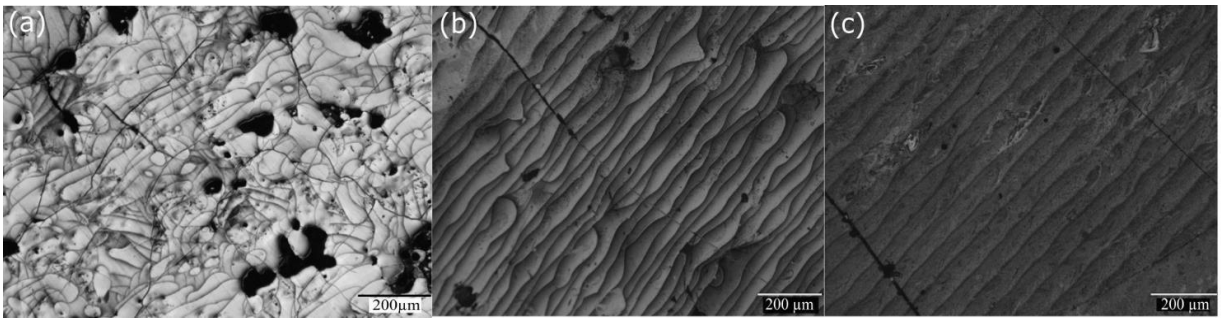

Figure 5-16 Top surface of the (a) room temperature printed sample; (b) 400℃ printed samples; and (c) 550℃ printed sample

5.4.5. SEM-EDX and XRD Results

The heated bed samples were investigated with an SEM-EDX microscope. The results show that the weight percentage of the Nd is higher in the grains (16.97%) than the Nd at the grain boundaries (13.48%). In contrast, the percentage of the Zr and Ti are higher at the grain boundaries. In addition, the Fe percentage is almost the same in terms of the grains and at the grain boundaries, at 69.98% and 71.02%, respectively. There is no significant difference in the remaining elements (Al, Si, Ti, Co, and Pr) (see Table 5.1). These results match with the TEM-EDX results in Chapter 4. Also, it is known that the Nd-rich grain boundaries consist of mostly metallic Nd and intermetallic Nd-rich compounds, in addition to transition metals such as Fe, Co, Zr, Ti, and Cu [113].

Table 5-1 The average of the EDX results of spectrums from 11 to 20.

Weight%	Al%	Si%	Ti%	Fe%	Co%	Zr%	Pr%	Nd%
In grains	0.14	0.25	2.28	69.98	3.11	5.42	1.9	16.97
Grain boundaries	0.12	0.195	3.53	71.02	3.14	7.14	1.57	13.48

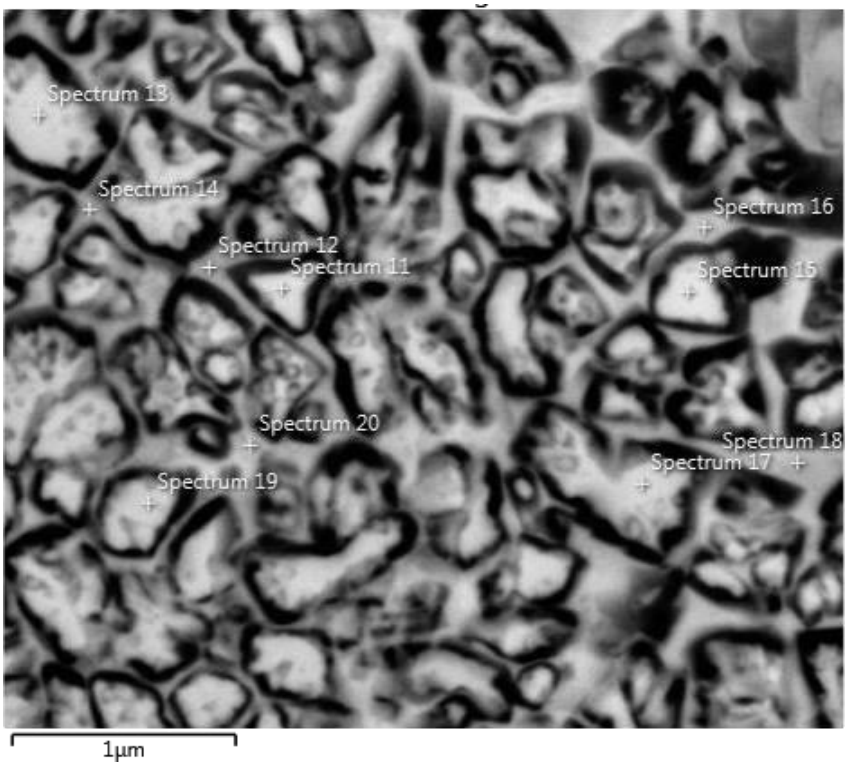

Figure 5-17 EDX spectrums in Table 5.1 - heated bed printed samples at 400°C.

Figure 5-18 shows the XRD patterns of the 300°C-350°C-400°C heated bed printed samples. There is no difference seen in the peak intensity however, there is also C detected in the heated bed samples, different than the room temperature printed samples. In contrast the heated bed sample has sharp and higher intensity $Nd_2Fe_{14}B$ phase peaks than the room temperature printed sample, as shown in Figure 5.19. Which consisted with their B_r values, room temperature printed B_r:0.53T, and 400°C heated bed printed sample, B_r: 0.76T.

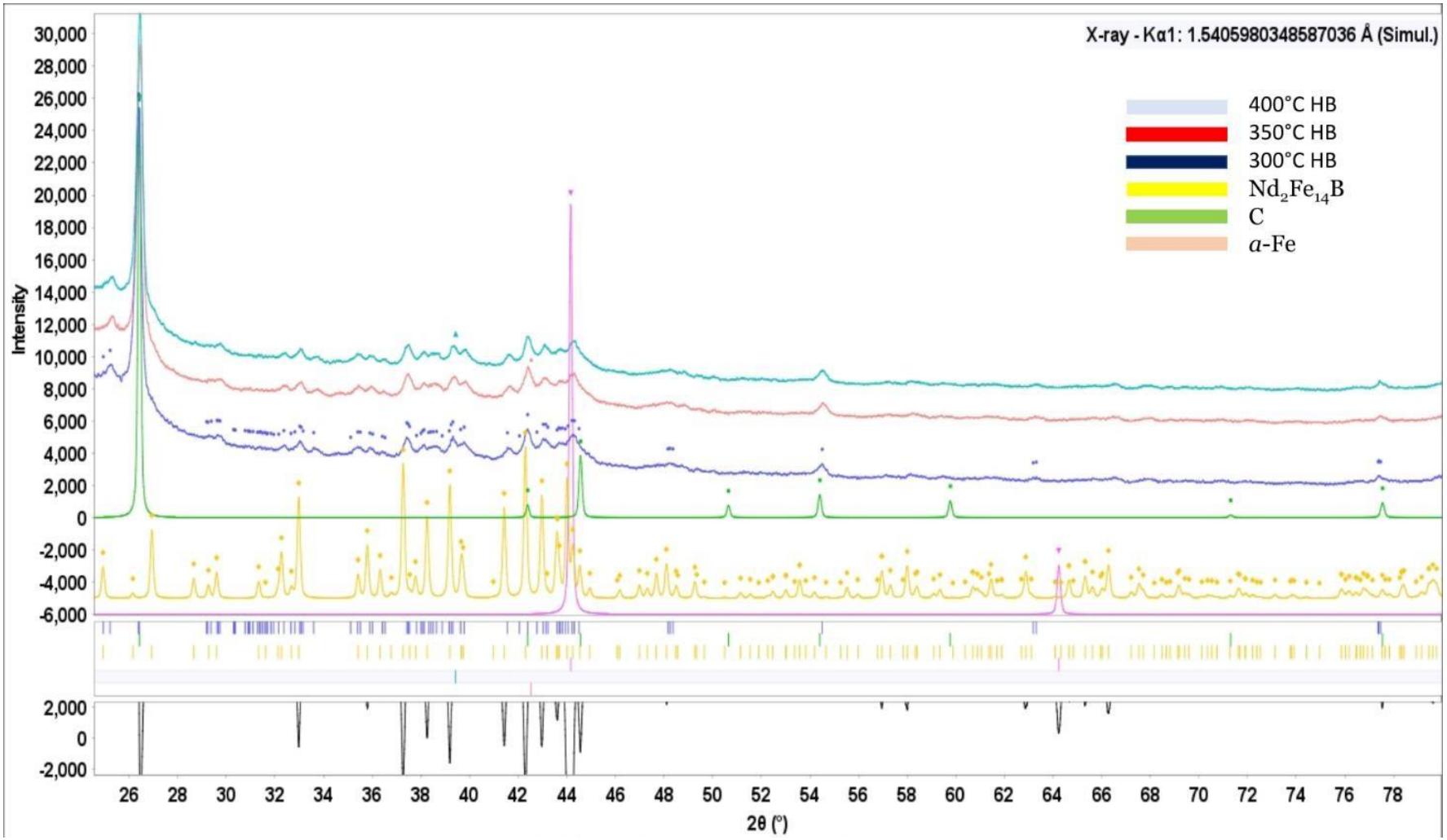

Figure 5-18 XRD patterns of 300°C-350°C-400°C heated bed printed sample.

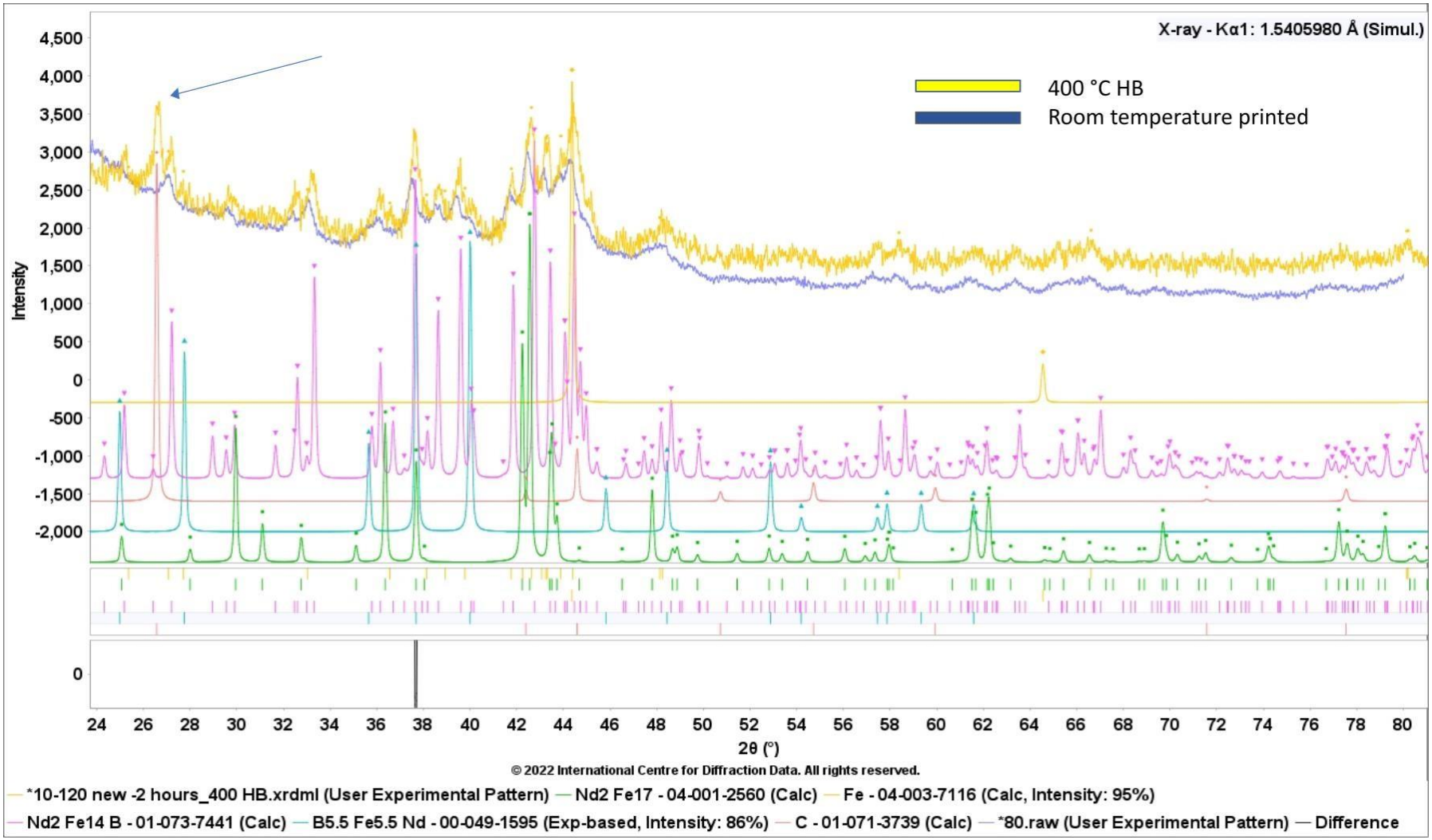

Figure 5-19 XRD patterns of room temperature printed sample, *Br*:0.53T, and 400°C heated bed printed sample, *Br*: 0.76T, arrow shows the carbon peak in heated bed sample.

5.4.6. Effect of the Printing Parameters on the Magnetic Properties at 300°C, 400°C and 500°C

The printing parameters affect not only the density of the samples but also the magnetic properties of the samples. They need to be selected carefully so as to control the cooling rates and the phases. The temperature of the heated bed involves the cooling phenomena in heated bed printings. Hence, the parameter effects were examined with respect to bed temperature. The magnetic properties of the heated bed printed magnets at 300°C, 400°C and 500°C both for 30 µm *HD* and 40 µm *HD* samples with 3000 mm/s and 3500 mm/s laser speeds are shown in Figure 5.20. The detailed parameters are presented in Table 5.2.

Table 5-2 Printing parameters

SET 1	3000 mm/s *LS*	300°C-30 µm *HD*	400°C-30 µm *HD*	500°C-30 µm *HD*
SET 2	3000 mm/s *LS*	300°C-40 µm *HD*	400°C-40 µm *HD*	500°C-40 µm *HD*
SET 3	3500 mm/s *LS*	300°C-30 µm *HD*	400°C-30 µm *HD*	500°C-30 µm *HD*
SET 4	3500 mm/s *LS*	300°C-40 µm *HD*	400°C-40 µm *HD*	500°C-40 µm *HD*

The remanence increases with the increasing *HD* from 30 µm to 40 µm at all bed temperatures. Changing the *HD* from 30 µm to 40 µm has not altered the *Br* range between the bed temperatures at 3000 mm/s laser speed. The highest remanence was obtained at 400°C and the lowest at 500°C for both *HDs*. 3500 mm/s *LS* samples follow the same trend, except for the 30 µm *HD*, 500°C printed sample, indicated by the arrow in Figure 5.20.

The B_r increase is higher at 300°C and 500°C samples at 3000 mm/s when the *HD* is increased from 30 µm to 40 µm compared to the printed samples at 400°C. The B_r increase with increasing *HD* is lower when the laser speed is 3500 mm/s. Moreover, the effect of laser speed on remanence in a heated bed is not remarkable. Except for the difference between the 30 µm *HD* - 500°C - 3000 mm/s *LS* and the 30 µm *HD* - 500°C - 3500 mm/s *LS* samples, the B_r difference between the 3000 mm/s and 3500 mm/s *LS* is not higher than 0.01 T.

Figure 5.21 shows the coercivity results. The coercivity decreases with the increasing *HD* from 30 µm to 40 µm at all temperatures. The results of the 3000 mm/s *LS*- 40 µm *HD*, show that H_{ci} is the highest at 400℃, followed by 300℃ and the lowest at 500℃, 585 kA/m, 516 kA/m and 503 kA/m, respectively. The H_{ci} of the 3000 mm/s *LS*- 30 µm*HD* is the same at 300℃ and 400℃, and it is the lowest for the 30 µm *HD*-500℃.

The samples with 3500 mm/s *LS* have the same H_c trend between all bed temperatures. H_{ci} is the highest at 400℃, lower at 300℃ and the lowest at 500℃, 478 kA/m-420 kA/m for 40 µm *HD* and 647 kA/m-571 kA/m-522 kA/m for 30 µm *HD*.

It was observed that H_{ci} drops by increasing laser speed from 3000 mm/s to 3500 mm/s for both 40 µm *HD* and 30 µm *HD* samples for all bed temperatures, except for the 400℃-30 µm *HD*, indicated by the black arrow in Figure 5.21. The drops in the 40 µm *HDs* are larger than the drops in the 30 µm *HDs,* up to 107 kA/m and 63 kA/m, respectively.

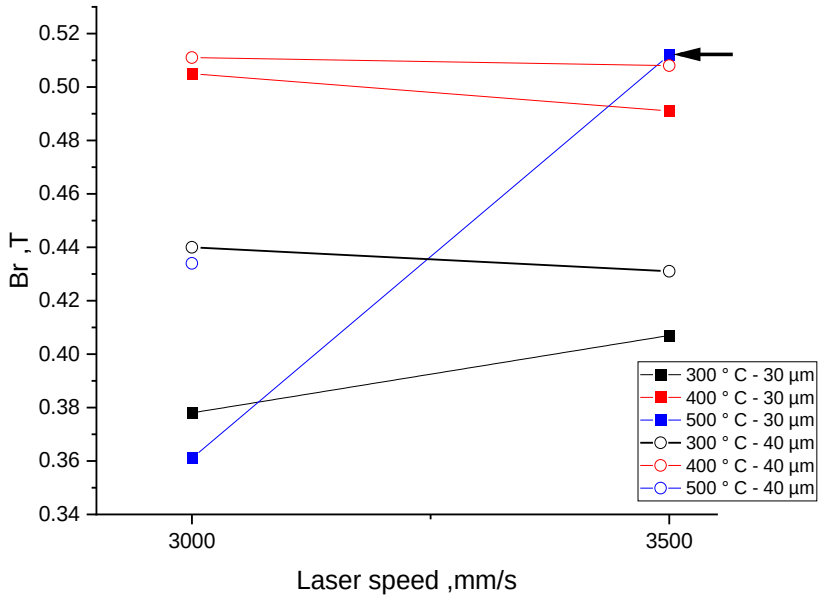

Figure 5-20 Br-laser speed relationship with respect to the heated bed temperatures and hatchdistance (40 µm HD sample printed at 500℃ broken during the permeameter test)

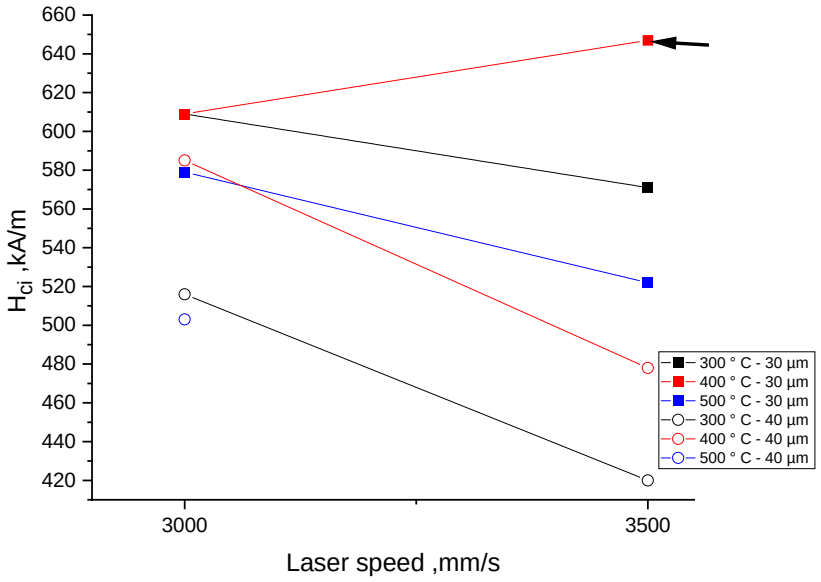

Figure 5-21 Hci-laser speed relationship with respect to the bed temperatures and hatch distance.

5.4.7. ANOVA Results

The results in Figure 5.20 and Figure 5.21 were analysed by ANOVA to investigate the influences of the bed temperature, *LS,* and *HD* on density percentage, H_{ci} and B_r of the samples, factor information presented in Table 5.3. Table 5.4 shows the analysis of variance (ANOVA) table for the coercivity (H_{ci}) outputs.The *LS* and *HD* factors have been found to be significantly influential since they are lower than 0.05 (95% confidence interval). The most significant factor that affects the coercivity of the magnets has been found to be the *HD* with the lowest p-value (0.004)and the highest contribution (59.07%). While the bed temperature does not have a meaningful impact on H_{ci}, it does have an effect on B_r with the highest contribution (55.34%) (see Table 5.5). (For all the factors, the p-values in Table 5.5 are higher than0.05; however, the bed temperature is 0.056, which is the closest p-value to 0.05).

F is the variation between group means to variation within group variances. The larger F means greater the variation between sample means to the variation within sample. Thus, the larger F means there is a difference between the group means. The F value is used to calculate P value to determine if the F values is significant or not depends on

the degrees of freedom. If the p-value is more than 0.05, then the result is not significant. If the p-value is less than 0.05, then the result is significant.

Table 5-3 ANOVA Factor Information

Factor	Type	Levels	Values
Bed Temperature (℃)	Fixed	3	300, 400, 500
Laser speed (mm/s)	Fixed	2	3,000, 3,500
Hatch distance (μm)	Fixed	2	30, 40

Table 5-4 ANOVA for Coercivity (H_{ci})

Source	DF	Contribution	Adj SS	Adj MS	F-Value	P-Value
Bed Temperature (℃)	2	13.30%	9,489	4,744	3.76	0.087
Laser speed (mm/s)	1	10.84%	8,058	8,058	6.38	0.045
Hatch distance (μm)	1	59.07%	26,639	26,639	21.1	0.004

Table 5-5 ANOVA for Remenance (B_r)

Source	DF	Contribution	Adj SS	Adj MS	F-Value	p-Value
Bed Temperature (℃)	2	55.34%	0.016509	0.008255	4.86	0.056
Laser speed (mm/s)	1	7.27%	0.002716	0.002716	1.6	0.253
Hatch distance (μm)	1	4.77%	0.001491	0.001491	0.88	0.385

Figure 5.22 and Figure 5.23 show the main effects plots for H_{ci} and B_r, respectively. The lowest level of *LS* (3000 mm/s) and *HD* (30 µm) give the maximum H_{ci}, while the medium level bed temperature (400°C) gives the highest H_{ci}. In contrast, the highest *LS* (3500 mm/s) and *HD* (40 µm) gives the highest value of the B_r. The medium level bed temperature, 400°C, gives the optimum H_{ci} and B_r.

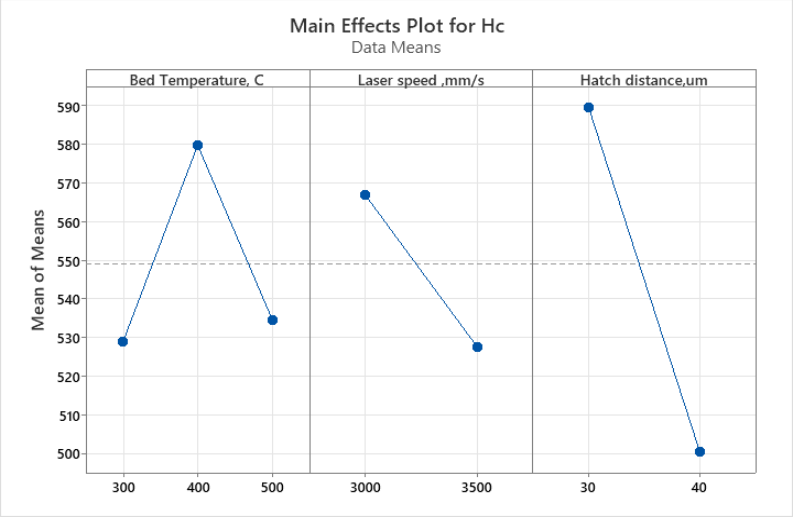

Figure 5-22 Main effects plot for H_{ci}.

Figure 5-23 Main effects plot for B_r.

5.5. Conclusions

- The density percentage of the samples is improved with the heated bed from 90% to 96%. However, no linear relationship is observed between the bed temperature and density increment. The instability of the heated bed is one of the reasons for the fluctuations in the density of the samples.
- The surface quality of the samples improved. Smoother surfaces are obtained with the heated bed, can be seen in Figure 5.15. However, delamination is seen in the layers near the top ofthe samples.
- The remanence of the samples increased with the heated bed, while the coercivity decreased. The former is related to the sample density increment and a possibly higher Φ phase in them, and the latter is related to the larger and more dendritic grains in the heated bed printed samples. B_r is related to the Φ phase in the samples, while coercivity is related to the phase distribution and homogeneity and the composition of the grain boundary phases [61]. The non-uniform and irregular Nd-rich phases reduces the coercivity [91].
- It was observed that the dendritic shape grains are larger and higher in number in the high-temperature heated bed printed samples, due to the slower cooling rates in them.
- The amount of Nd between the grains reduces while the amount of Fe, Zr and Ti increases. These results matched with the TEM-EDX results in Chapter 4.
- The effect of the parameters on the magnetic properties in combination with the bed temperature was studied. The effect of *HD* on coercivity is higher than laser speed and bed temperature. Coercivity can be improved by lowering the *HD* to a lower setting than that of the bed temperature or by lowering the laser speed. On the other hand, the setting of the bed temperature highly affects B_r, while the change in *HD* and *LS* does not affect it too much. It was concluded that the

heated bed temperature, 400°C, gives the highest B_r and H_{ci}, and 30 μm *HD* increases the H_{ci} with a small decrease in the B_r value.

- The heated bed printing quality and consequently the density and magnetic results mostly depend on the built plate stability. Therefore, in the later trials, the sample with higher magnetic properties could be obtained with relatively stable plate.
- The maximum properties are obtained by the heated bed is B_r: 0.76 T, H_{ci}:750 kA/m, BH_{max} :84 kJ/m^3, by 400° C.

This is the only study that examines the effect of using a heated bed during the SLM printing of the NdFeB magnet. This chapter investigates the influences of heated bed temperature and the parameter effect in respect of various heated bed temperatures. In addition, it was discovered that the grain growths in the melt pool differ from the room temperature printings. All finding in this chapter creates a potential base for further studies in SLM printing of NdFeB magnets. Despite the significant impact on literature, the improving magnetic properties are still lower than their sintered counterparts in the industry.

Chapter 6: Heat Treatment of the SLM-Printed NdFeB Magnets

6.1. Introduction

SLM-printed NdFeB magnets can be improved with parameter optimization. However, their magnetic properties are still lower than their sintered counterparts.

In this chapter, the effect of heat treatment on the magnetic properties and density of the samples will be analysed. The goal of this chapter is to present an improvement of the coercivity by defining the Nd-rich grain boundaries with the help of heat treatments. In contrast, there is no increase expected in B_r.

Effects of processing parameters and post-heat treatment on porosity/crack formation and microstructure were studied by [88]. The researchers found that cracks in the heat-treated samples are lighter and have smaller diameters than those in as-printed samples. Moreover, energy input calculated using the varying parameterscan be used to reduce the porosity of SLM-NdFeB magnets, and it is more effective than the post-heat treatment [88].

However, magnetic properties were not studied. This study is the first study which investigates the magnetic properties of SLM-NdFeB magnets after post heat treatment.

6.2. Experimental Materials and Equipment

As in Chapters 4 and 5, the samples for the heat treatment experiment were printed with MQP-S-11-9-20001 powder supplied by the Magnequench Corporation. The experiments were executed on the Aconity Lab SLM industrial machine, which is equipped with a 1070 nm wavelength-200 W continuous wave fibre laser with an 80 μm spot size. Especially when working with materials that are highly oxygen-sensitive, filling the processing chamber with argon gas is necessary to prevent oxidation. Therefore, the mentioned machine reduces the 100-ppm oxygen level. For the subsequent heat treatment, the CarboliteGero STF160180-230SN tube furnace with a maximum temperature of 1300°C was used.

6.3. Experimental Methods

For the investigations, 10 mm × 10 mm × 10 mm cube samples were built. The printing parameters were 130 W *LP*, 1300 mm/s *LS*, 20 μm *LT* and 30 μm *HD*. The subsequent heat treatment followed the published heat treatment for conventionally produced NdFeB magnets [87]. The samples were annealed for 4.5 hours at 480°C, 580°C, 680°C, 780°C and 880°C, under an inert gas atmosphere. Every magnet was furnace-cooled to room temperature in an Ar atmosphere since they are extremely oxidation sensitive. Since the samples were oxidized after the inert gas annealing, the vacuum atmosphere treatment with the same annealing conditions was also attempted. However, they were also oxidised, as can be seen in Figure 6.1. This may be due to insufficient Ar gas flow and an insufficient vacuum level.

It was decided to run the experiment with an inert gas atmosphere since there is no remarkable density difference found between the vacuum samples and inert gas annealed samples, as can be seen in Table 6.1.

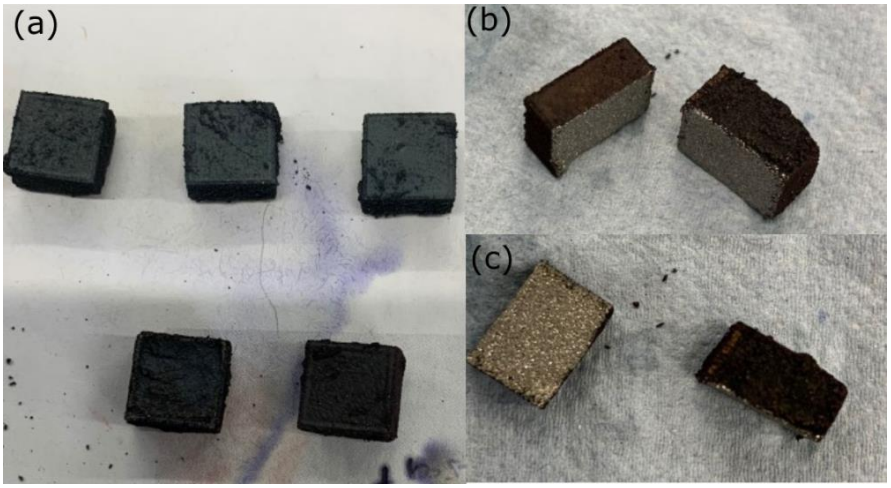

Figure 6-1 Oxidised samples after heat treatment (a) under vacuum (b)-(c) under an inertgas atmosphere (the oxide layer on the surface is seen brownish on the surface of the sample)

Table 6-1 Archimedes density results of the as printed sample, annealed sample at 580 and680°C, in inert gas and vacuum atmosphere.

Sample	Density, g/cm³	Density, g/cm³, annealed at 580 °C	Density, g/cm³, annealed at 680°C
As printed sample	6.822		
Inert gas atmosphere		7.363	7.251
Vacuum atmosphere		7.353	7.312

6.4. Methods for Analysis

After the printing samples were removed from the platform manually, their densities were tested using the Archimedes density test in water. Then they annealed in a furnace under an inert gas atmosphere. Four samples were annealed for each annealing temperature. The samples for characterization of porosity and cracks were embedded in Bakelite with the following grinding/polishing and etching, and they were analysed using an optical microscope and SEM/EDX. The samples for the magnetic test were ground and polished since the oxide layer on the surface might have mislead the magnetictest. Magnetic tests were run with the Permeameter by Arnold Magnetic Technologiesafter samples were magnetized.

6.5. Results and Discussion

6.5.1 Density Test Results

The Archimedes density of the samples shows that the heat treatment improves density by up to 5%, as shown in Figure 6.2. The optical image of the heat-treated samples from 480-780-880-980°C supports the Archimedes density results with less porosity on the sample surfaces than the as-printed sample, as shown in Figure 6.3.

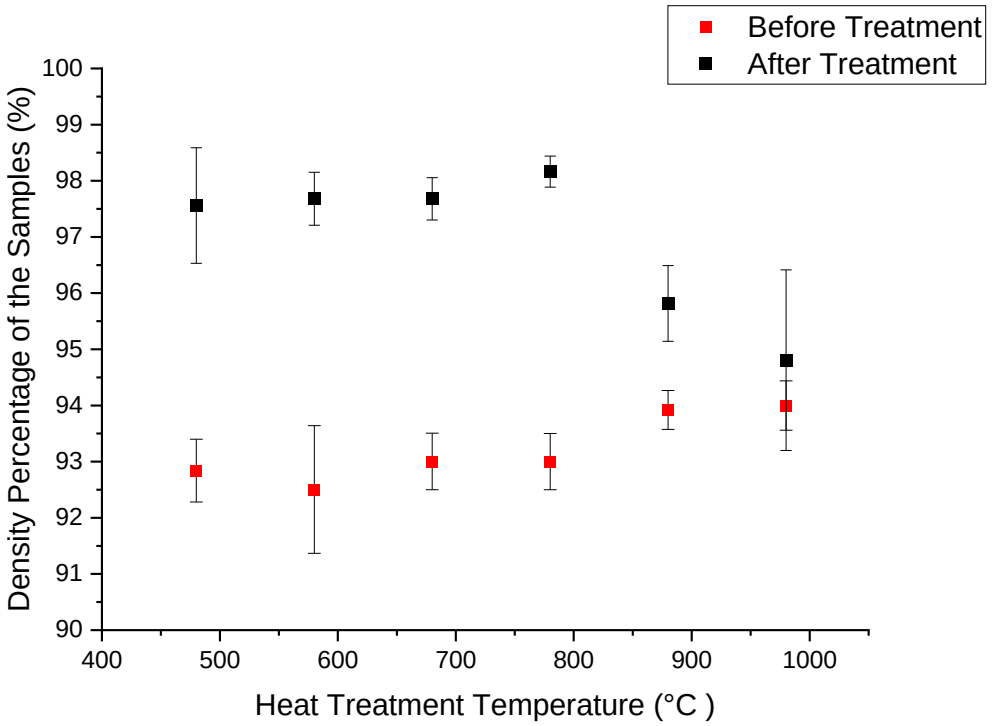

Figure 6-2 Archimedes density test results in respect of heat treatment temperature

The Archimedes method results depend on the nature and temperature of the fluid, but also depend on sample volume and its surface roughness. Therefore, all samples were in the same size 10*10*10 mm, and they were measured in water at room temperature. On the other hand, the surface roughness depends on the printing parameters and post processing techniques.

Figure 6.2 shows the increases after the heat treatment. However, samples plotted here are not ground and polished. The as sintered parts are quite rough as can be seen clearly in Figure 4.17. The rough surface might provide air pocket formation, so, water cannot wet the entire surface, it only interact with the peaks of the roughness [114].

The reducing wettability reduces the water penetration and it would lead the overestimation of measured volume [114], reduction of densities. On the other hand, the oxide layer formed on the heat-treated samples might seal the surface porosities [115] ,inhibits the water penetration through the porosities and distort the results, especially for the samples treated at high temperatures. The oxide layer on the surface creatates a buoyancy effect that leads to an overestimation of the material's density. The Archimedes method involves measuring the weight of a material both in air and when submerged in a liquid, typically water. The difference in weight between the two measurements is used to calculate the volume of the material, which is then divided by its mass to obtain the density. However, if the surface of the material has an oxide layer, this layer can trap air bubbles or pockets when the material is submerged in water. This trapped air can cause the material to appear more buoyant than it actually is, leading to an overestimation of its density. Additionally, the oxide layer itself may have a different density than the underlying material, further complicating the measurement"

Therefore, to make sure the density results were not distorted by oxide formation on the surfaces and surface roughness, the density of the 2 of the as printed sample and 2 of the heat-treated samples were measured before and after grinding / polishing. There is no huge difference observed in the density results after grinding /polishing, as can be seen from Table 6.2.

Table 6-2 Archimedes density test results of the as printed, 680°C HT, and 880°C HT samples, before and after grinding- polishing

Sample	Density g/cm^3	Density g/cm^3	Before	After
as - printed	7.142	7.13	95.22667	95.06
as - printed	7.066	7.142	94.21333	95.22
680°C HT	7.22	7.22	96.26667	96.26
880°C HT	7.22	7.23	96.26667	96.4

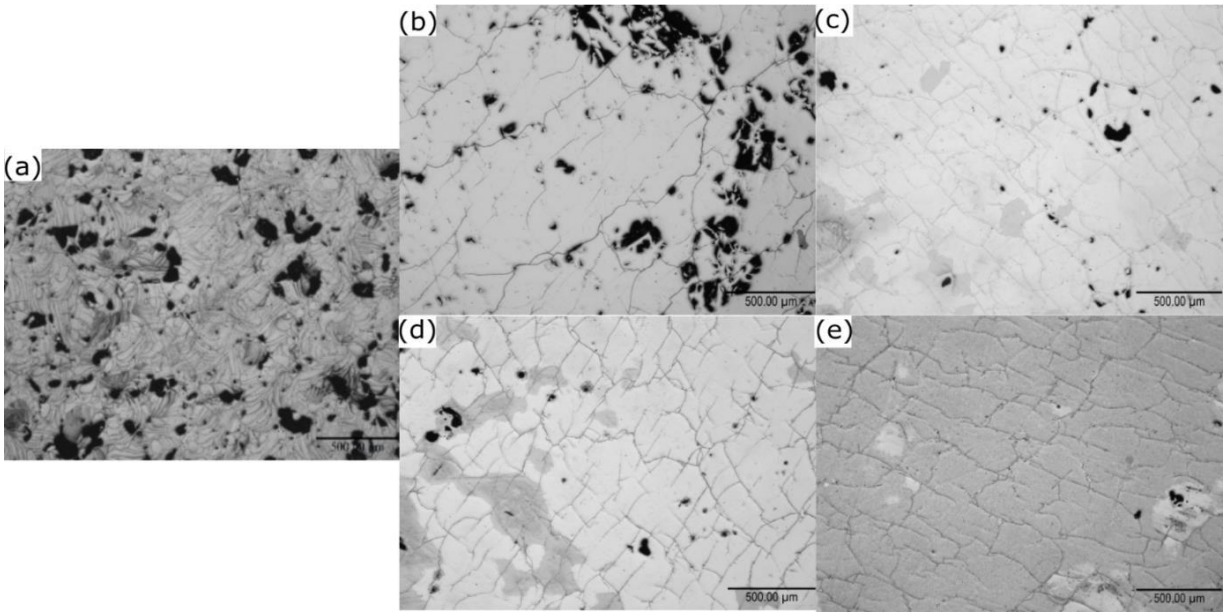

Figure 6-3 Optical images of top view of the sample (a) as printed (etched), heat treated at (b)480 °C, (c) 780°C, (d) 880°C, (e) 980°C (before etching)

Despite an improvement in the density, many cracks were observed in the cross section of the annealed samples at 580°C and 680°C, as seen in Figure 6.4. They are mainly in the direction of building, which was also reported that they are sensitive to oxidation [88].

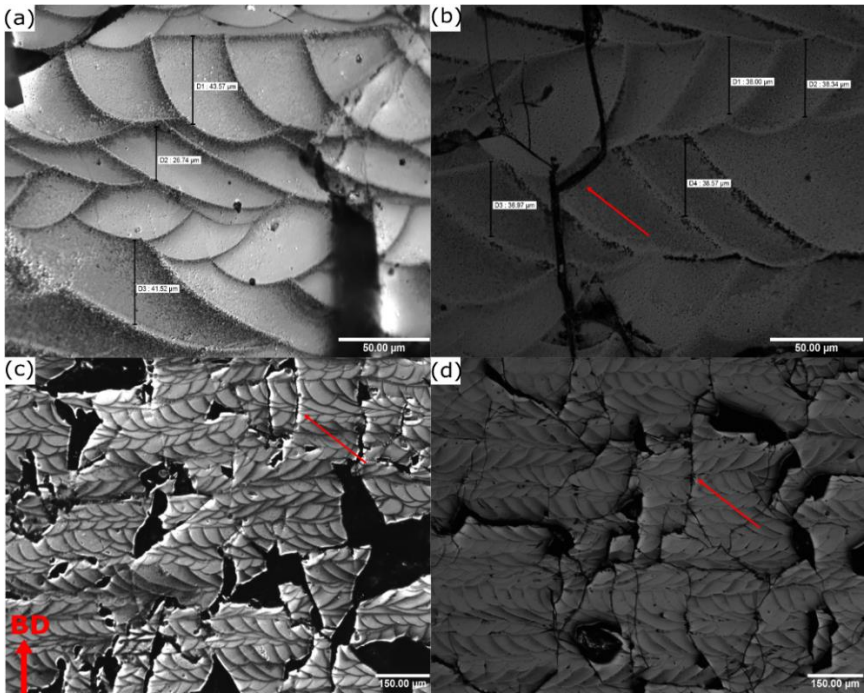

Figure 6-4 The cracks across the melt pool in the direction of building, (a) annealed at 580 °C and (b) annealed at 680°C. Red arrows point the cracks in the direction of the building.

6.5.2. Magnetic Properties

The key role of the annealing is the formation of a continuous Nd-rich layer between the Φ grains by heating the magnets over the melting point of the Nd-rich phase, at 655℃, but below the melting point of the Φ phase, at 1180℃ [83], [87]. The well-defined Nd-rich layers between the hard magnetic grains inhibit the exchange interactions between them. Hence, the heat treatment increases the coercivity of the sintered NdFeB magnets with no remarkable difference in the B_r [86], [87]. However, the results of this study show the improvement in the B_r while decreasing in H_{ci}. The B_r values of the printed sample improved from 0.61 T to 0.69 T at 580℃ and 0.75 T at 680℃. Then it starts to decrease as the annealing temperature increases to 980°C. The drop might be related to oxidation seen on the high temperature treated samples. (*EDX* results of the 880 ℃ 980 ℃ treated samples are shown in Appendix 2). While the H_{ci} decreased from 1000 kA/mm to 844 kA/mm at 680℃ (H_{ci} is slightly the same for 580℃, 1020 kA/mm), and it keeps decreases as the annealing temperature increases, (H_{ci} drops to 15kA/mm at 980°C), as shown in Figure 6.5

According to the literature, heat treatment does not affect the density of the sintered magnets too much (as-sintered magnet 7.52 heat treated magnets: 7.53 and 7.54 [86]). However, in this study, there is a notable increase in density of up to 5%. Despite the B_r being mainly related to the hard magnetic phase [80], the improvement in B_r might be explained by the improvement in sample density since less porosities and cracks decreases the magnetism loss.

On the other hand, coercivity is mainly related to the phase distribution, homogeneity and the composition of the grain boundary phases [81]. The microstructural evolution in the following parts provides further discussion on it.

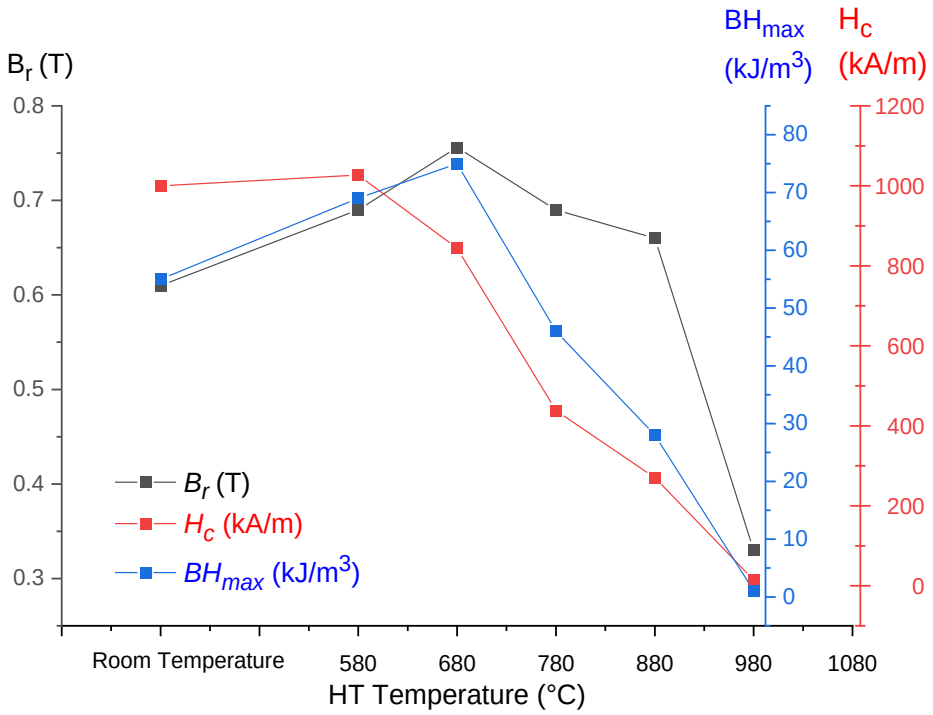

Figure 6-5 Remanence, Coercivity and Maximum Energy Product of as-printed and heat-treated samples at 580°C -680°C -780°C -880°C -980°C, tested by permeameter.

6.5.3. Microstructural Evaluation

The variations in the grain sizes and the grain morphology are seen in the melt pool, (as shown in Figure 6.6). The grains are dendritic in the HAZ. They are coarse and near equiaxed in the bottom of the melt pool. Then they are gettingcoarser grains in the middle of the melt pool; and finally, they are small and in a cubicshape at the top of the melt pool (under the following layer's HAZ), as seen inFigure 6.7. Even the EDX results do not show the elemental difference on the surface, as seen in Figure 6.8, (since the elements are smaller than the possible lateral resolution), the back scattering images show that the colour difference originated from the elemental difference. From the phase diagram of the Nd-Fe-B ternary system in theslow cooling, at first is the Fe nuclei directly from the liquid phase, then Φ crystallizes at 1181°C. These results show a high amount of α-Fe with the Φ phases in addition to iron boride and Nd_xFe_yB, (they occur in very small amounts and are difficult to detect). However, the high cooling rates cause the non-equilibrium cooling, which directly solidifies the Φ phase and suppresses the α-Fe phase, which still exists but at a lower amount compared to the

slow cooling [2], in addition to the Nd content being lower than the sintered magnets [80].

Hence, it was deduced that the light grey grains are the Φ phase with surrounding black *α*-Fe phases and the Nd-rich phase (grey) in the back scattering images presentedin Figure 6.7. The more *α*-Fe phase is seen below the HAZ, compared to middle of the meltpool.

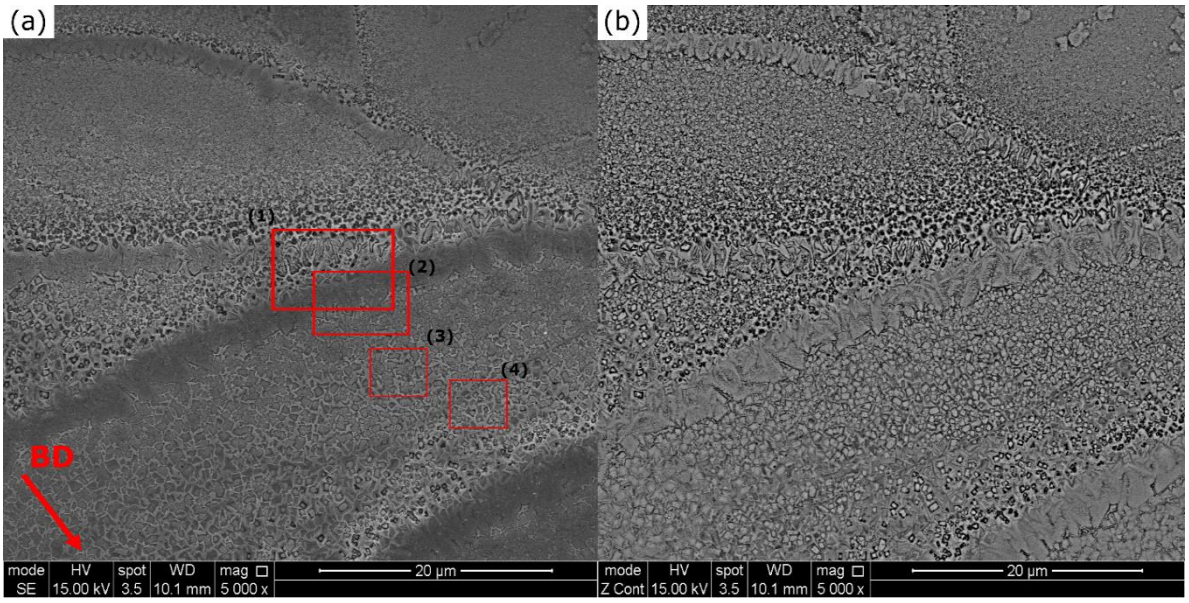

Figure 6-6 Sample annealed at 580 °C , showing the grain size distribution in the melt pool, red squares are 1- the HAZ and the top of the melt pool above it,2- HAZ and the bottom of the melt pool, 3- middle of the melt pool, 4- upper middle of the melt pool.

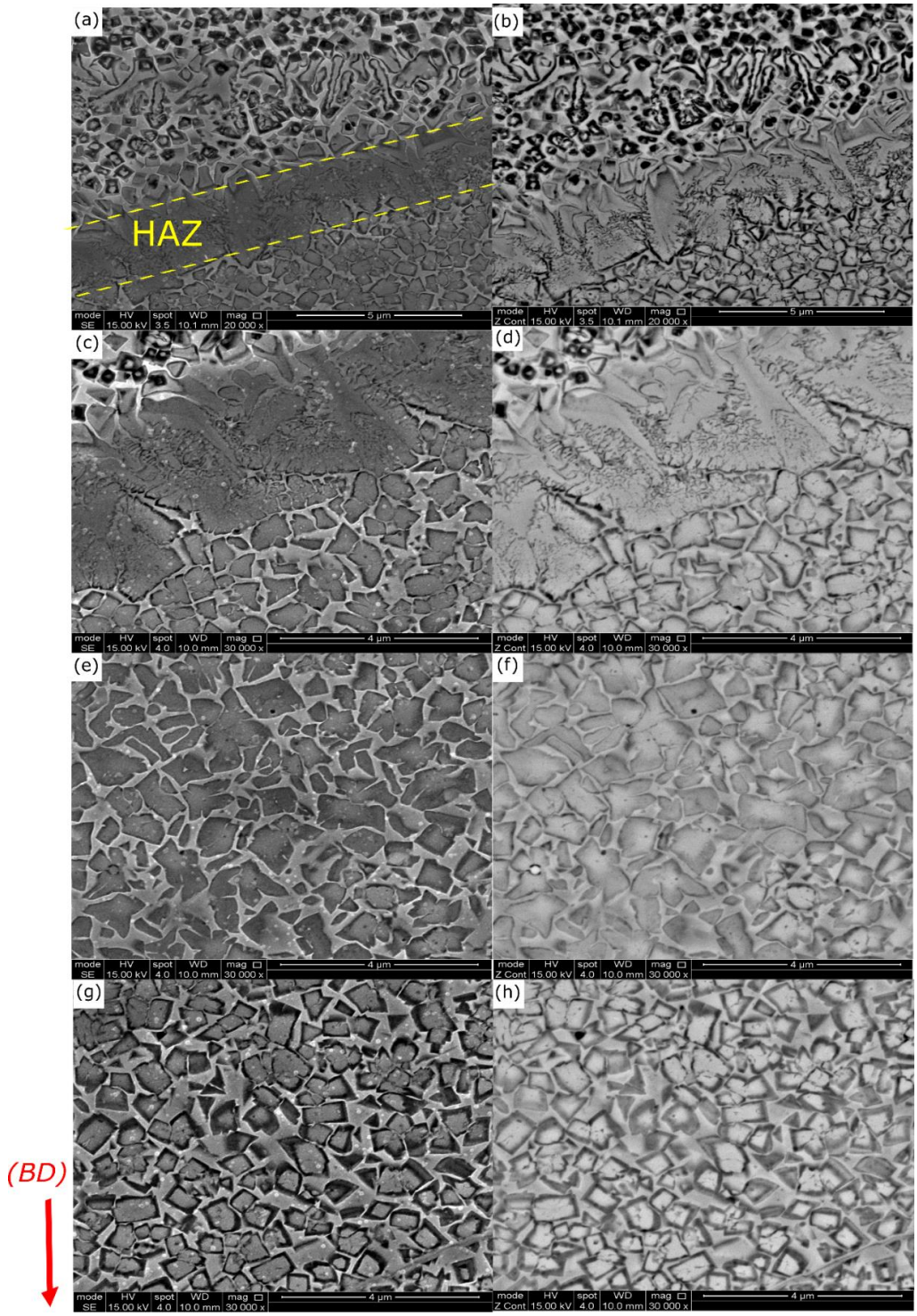

Figure 6-7 Sample annealed at 580°C (a-b) HAZ with the large dendritic grains in the direction of building (between the yellow dot lines) and below the HAZ top of the previously melted layer with the cubic grains(upper side of the dot lines) - (c-d)the bottom of the melt pool with near equiaxed grains), (e-f) the middle of the melt pool(near equiaxed Φ grains) (g-h) the upper side of the melt pool (cubic Φ grains with clear a-Fe surrounding) // light grey areas are the Φ phase, black areas are the a-Fe phase, and the grey areas between grains are Nd Rich phase.

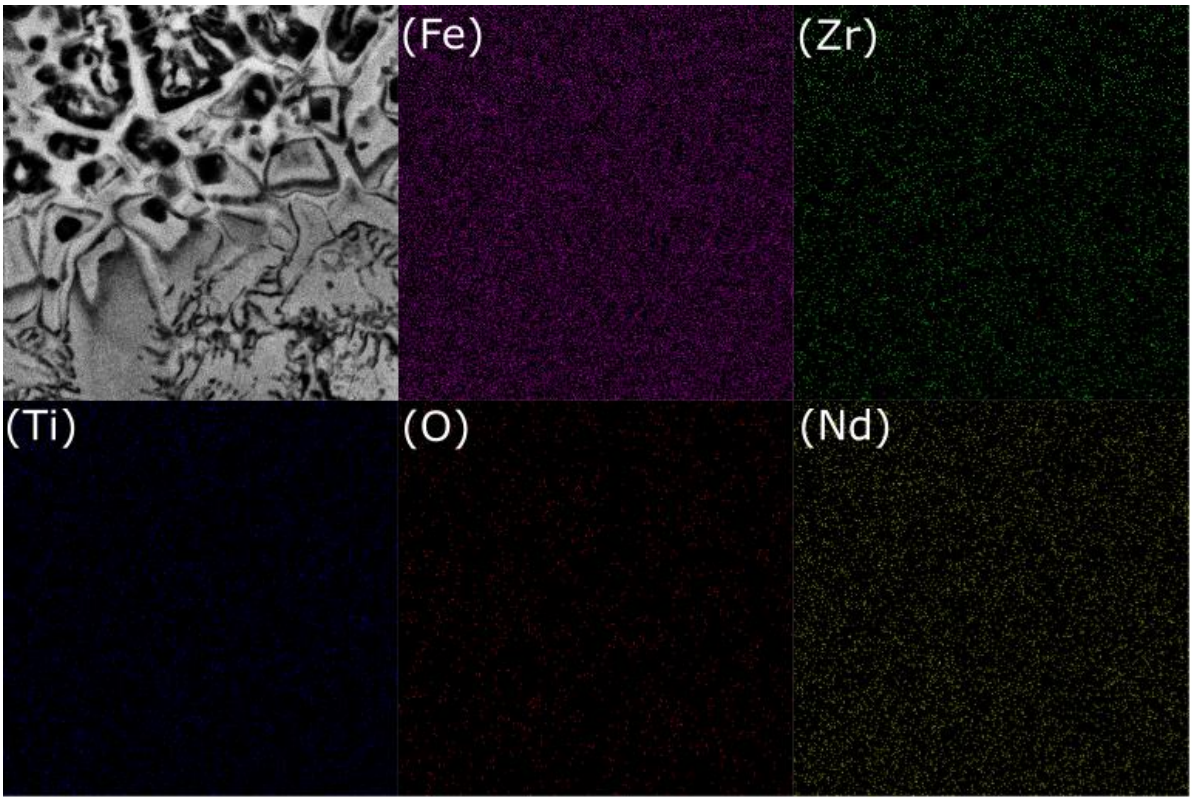

Figure 6-8 The EDX results of the annealed samples at 580 °.

The sample annealed at 680℃ shows variations in grain size. In addition, smaller grains are observed in the narrow melt pools, (as seen in Figure 6.9, square area 1), while larger grains are above the HAZ, (square area 2). It is also seen that the grain boundaries are not continuous in the 680℃ sample as they are in the 580℃ sample (see Figure 6.7). It is concluded that the very well-defined grain boundaries are the reason for the high coercivity at 580℃, while the discontinuous grain boundaries are the reason for the coercivity drop in the 680℃ sample.

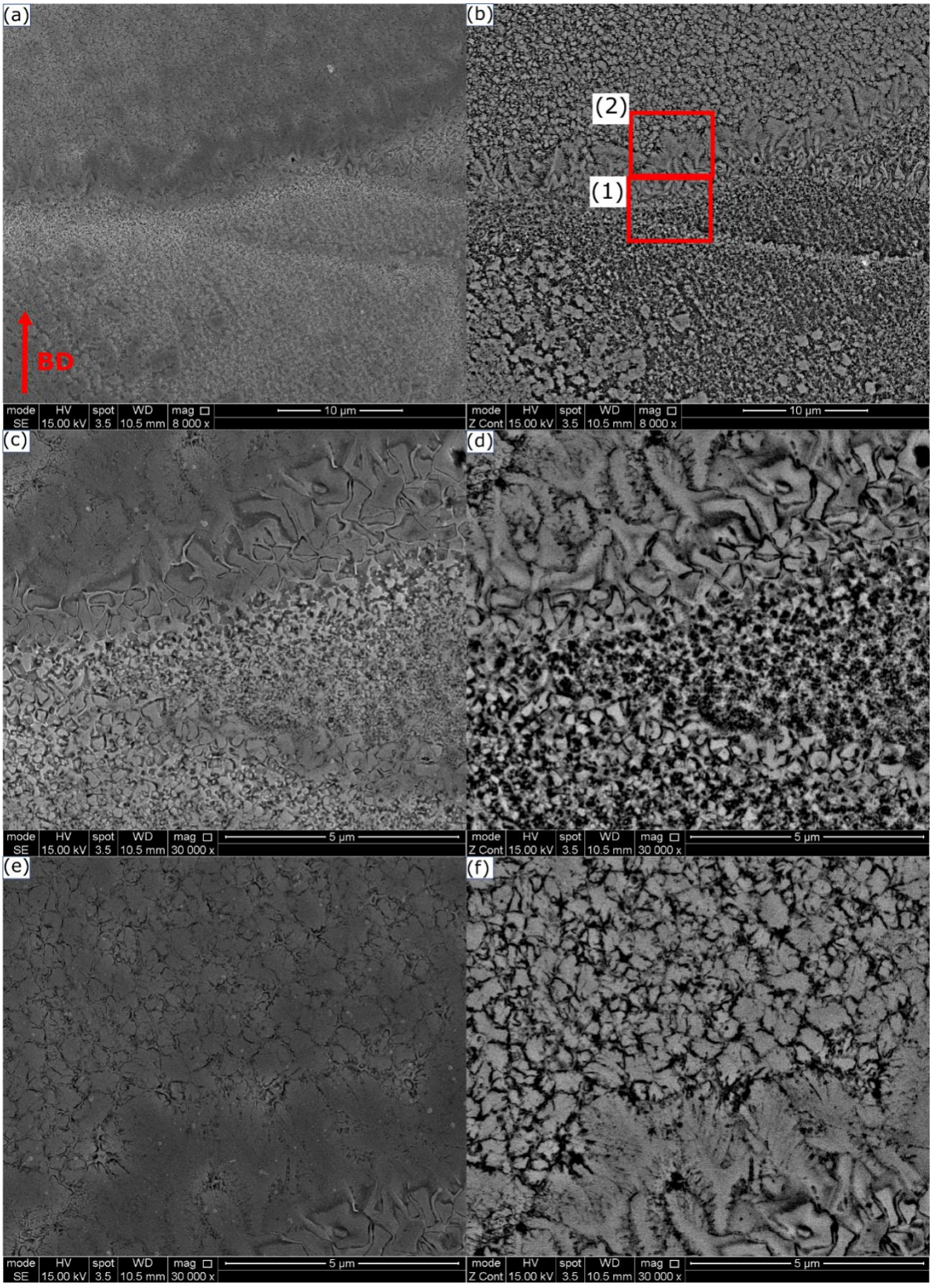

Figure 6-9 SEM images of the sample annealed at 680 °C (a-b) the melt pool lines,(c-d) closer look the narrow melt pool where the grains are finer, square box 1 and (e-f) bottom of the melt pool just above the HAZ, square box 2.

Figure 6.10 shows that the room temperature grains are small and more globular , in addition more homogenous, comparing to heat treated samples in Figure 6.9.

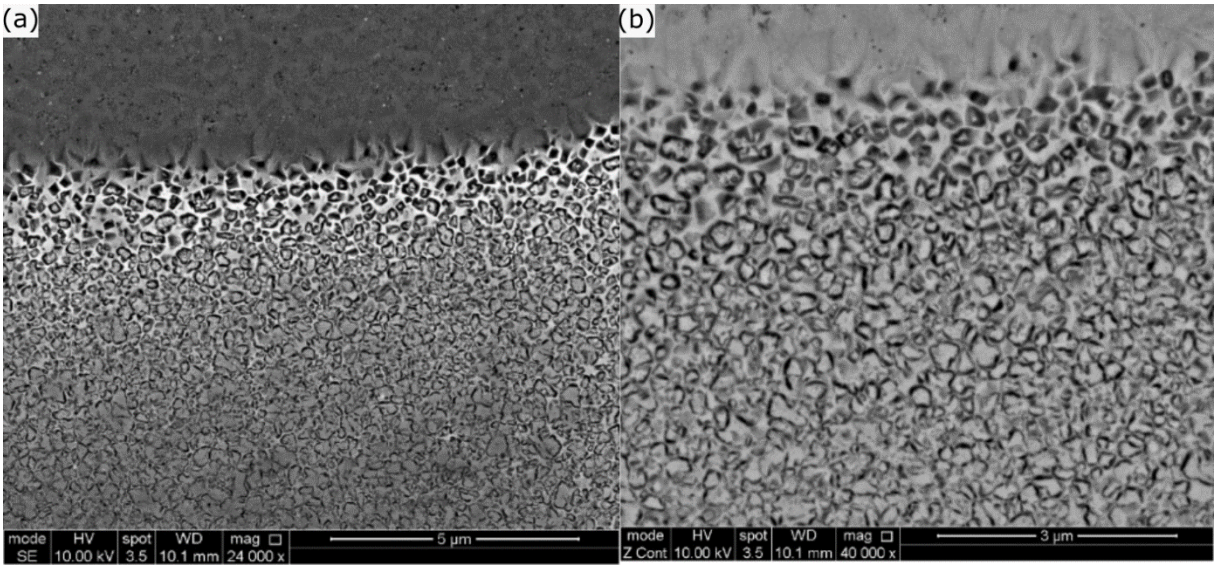

Figure 6-10 SEM images of the room temperature printed sample

The samples treated at temperatures above 680°C were extremely sensitive to etching. Despite the etching solution being diluted and the etching time reduced, no clear images were obtained. Figure 6.11 shows the SEM images of the annealed samples from 480°C to 980°C. The EDX analyses were performed; however, there were no elemental differences found in the low-temperature treated samples at 480°C, 580°C and 680°C, while oxygen was the main element on the 880°C and 980 °C heat treated samples. The EDX analysis results can be checked in Appendix 2.

.

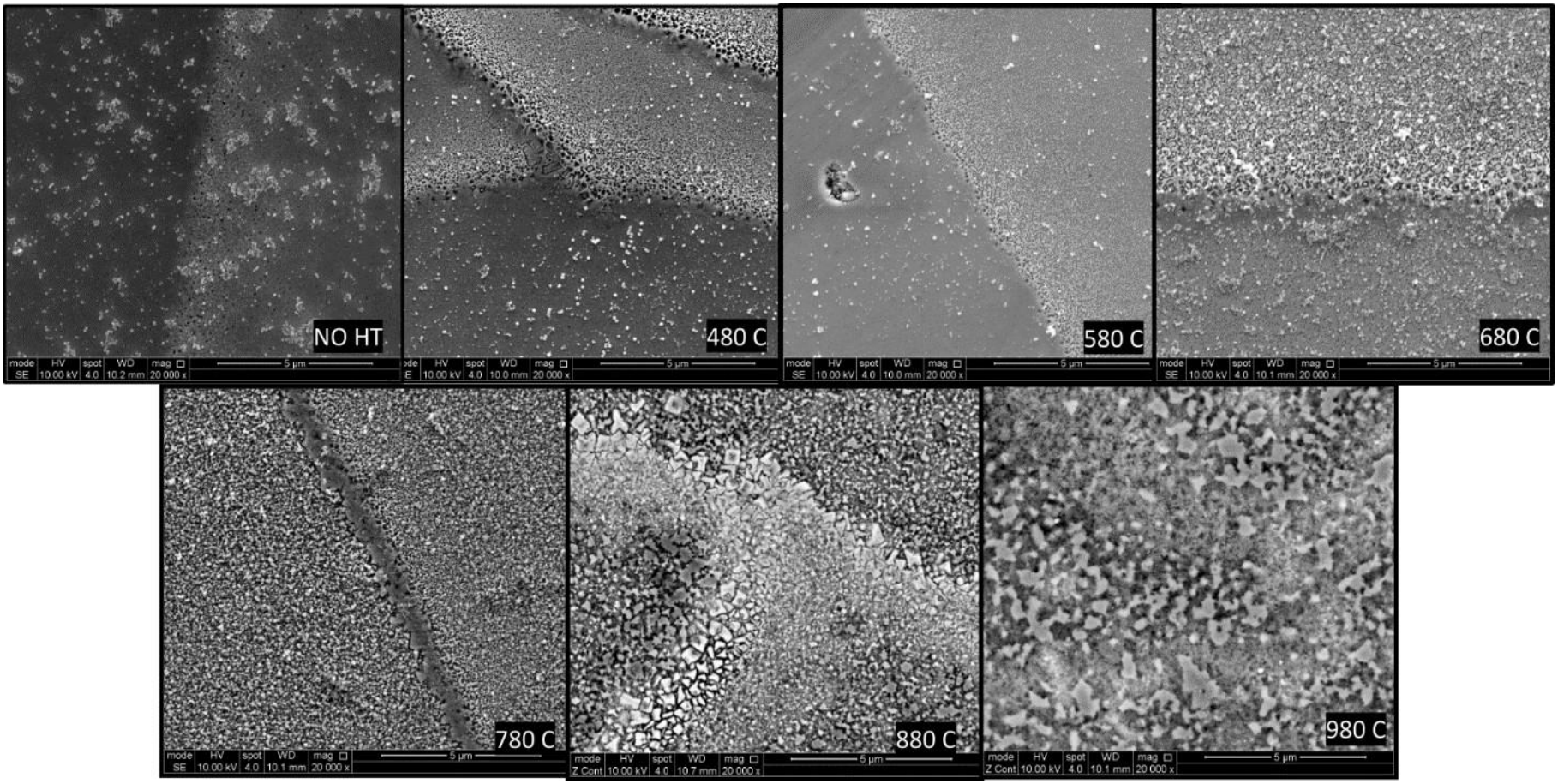

Figure 6-11 SEM images of the samples annealed at 480-580-680-780-880 °C, the surface of them contaminated due the extreme oxygen sensitivity of the samples.

6.6. Conclusions

The density of the samples was improved to up to 5% with the help of the heat treatment, in contrast to the heat treated sintered magnets. The samples were oxidized after the heat treatment. Both Ar and vacuum atmosphere treatment did not inhibit the oxide formation. Despite the improvement seen at the top of the surfaces, there were still cracks observed in the samples, mostly in the direction of building.

The B_r improved more than the H_{ci}, in contrast to the results in literature. The B_r increased from 0.61 T to 0.68 T and 0.75 T, by annealing at 580°C and 680°C, respectively. There is no remarkable density and B_r increase in the literature, while both density and B_r improved in this study. Hence, it was deduced that the B_r increase is related to the increase in the density. On the other hand, coercivity increased from 1000 kA/m to 1027 kA/m with the 580°C treatment, and then decreased to 15 kA/m as the heat treatment temperature increases.

It was observed that the grain boundaries are more continuous and well defined in the 580°C annealed samples, and then become discontinuous at 680°C. It is known that the continuous grain boundaries improve coercivity, while discontinuous grain boundaries decrease.

Finally, the analysis of the high-temperature treated samples was challenging due to their extreme oxygen sensitivity and their extreme sensitivity to etching. These samples were over etched immediately just after dipping the samples into the etching solutions. Moreover, oxide layers form on the surfaces very easily, which reduces the SEM imaging and EDX analysis qualities. Hence, it was challenging to investigate the microstructure and elemental distribution on the sample surfaces. Moreover, there was an oxide layer detected in the 880°C and 980 °C annealed sample.

Chapter 7: Infiltration

7.1. Introduction

Many techniques have been used to improve the magnetic properties of NdFeB magnets. They are mentioned in section 2.6. Infiltration is one of the post-processing methodwhich improves the coercivity of the magnets [21], [22] . It is reported that coercivity of SLM-NdFeB magnets can be improved by infiltration with low-melting Nd-Cu, Nd-Al-Ni-Cu, and Nd-Tb-Cu alloys. In this study, the infiltration alloy ribbons are crushed, and the sample surfaces are covered with flakes. Then they are annealed at 650℃ for 3 hours in a vacuum. It was reported that the coercivity increased from 0.65 T to 1.5 T [116]. Moreover, the coercivity increased to 1.7 T with the intergranular addition of $(Pr_{0.5}Nd_{0.5})_3(Cu_{0.25}Co_{0.75})$ low-melting eutectic alloy. The alloy is added to the magnetic feedstock powder before the printing [117], which is not a post-processing method.

It is known that the Ni intergranular addition improves coercivity [17]. Therefore, nickel was used as an infiltration element in this study. In addition, nickel is relatively cheap and easy to acquire. On the other hand, post-processing method infiltration was used instead of the powder blending before the SLM printing, as it is easier to apply. The aim of this chapter is to improve the coercivity of the printed magnets and investigatethe possible nickel infiltration process.

7.2. Materials and Experimental Procedure

The infiltration method was developed through the following steps. Initially, paraffin is melted and mixed with Inconel 718 powder. Inconel is used as a preliminary powder instead of nickel powder itself to examine whether the paraffin coating works for infiltration. Then, samples are dipped into the mixture and taken out to dry at room temperature. Infiltration occurred using a heat treatment furnace at 900℃ for 2.5 hours, then at 490℃ for 2.5 hours in an argon gas atmosphere. The XRD result shows no nickel-related phase in the paraffin/Inconel coated samples, as seen in Figure 7.1. The only phases are the usual phases in the as-printed samples, $Nd_2Fe_{14}B$ and *α*-Fe phase. The infiltration failed due to the very low melting temperature of the paraffin of ~300℃. The coated powder could not stand on the surfaces at higher temperatures above 300℃. A sample is shown in Figure 7.2.a.

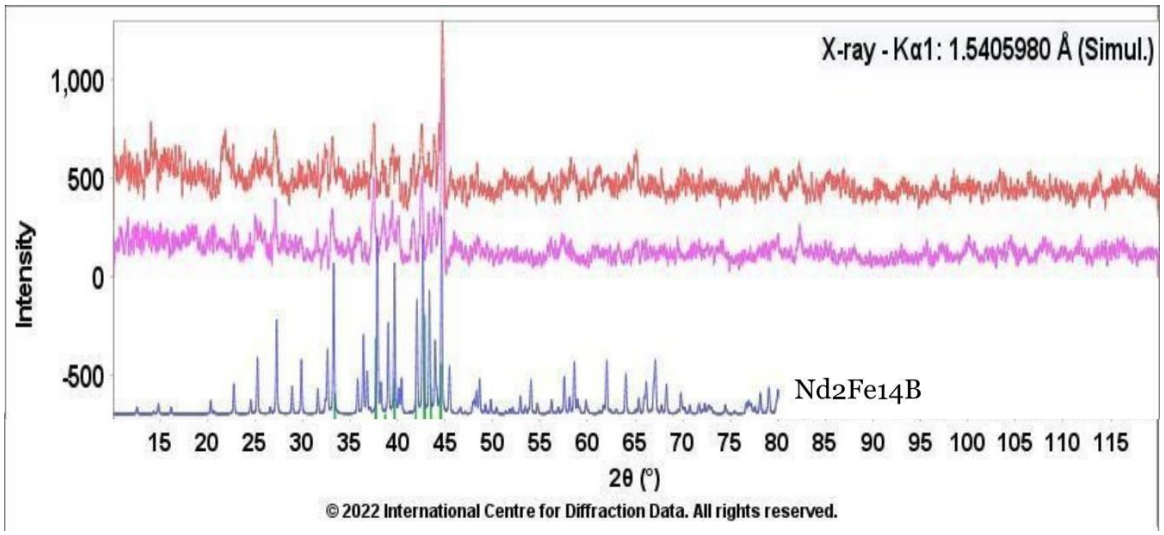

Figure 7-1 XRD patterns of the Inconel/paraffin infiltrated samples

Therefore, the second attempt was made with a nickel foil. The details of theinfiltration process are as follows: in the first trial, the samples were first wrapped in 0.125 mm nickel foil, and then wrapped in tantalum foil to avoid oxidation on the samples. The samples were treated at 1400℃, close to the melting point of nickel, for 2.5 hours. Then the temperature dropped to 490℃; the treatment temperature was taken from reference [93] and kept there for another 2.5 hours, then cooled down in the furnace to

room temperature, all in an argon gas atmosphere. The samples were melted, as seen in Figure 7.2.c, possibly due to excessive temperature increase caused by the tantalum foil sealing.

In the second trial, samples were wrapped in only Nickel foil and treated at 750°C for 2.5 hours by the following annealing at 490°C for 2.5 hours, then cooled down to room temperature, all under an Argon gas atmosphere. However, Nickel could not melt and diffuse in the samples at 750°C, as shown in Figure 7.2.d.

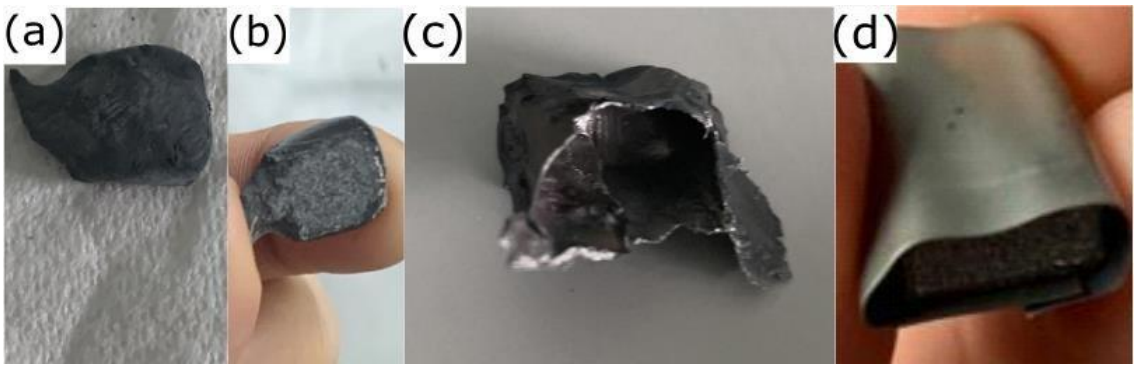

Figure 7-2 (a)- (b) Paraffin /Inconel coated sample, (c) Ni/Ta wrapped sample and (d) Niwrapped sample at 750 °C.

In the third trial, the cycles of the first treatment were followed, but the samples were wrapped in only nickel foil. The preliminary results showed dendritic structures in the samples, which differed from the previously printed samples, as seen in Figure 7.3.

There are melt pool lines seen in the Inconel/paraffin coated samples and in the second trial sample. In contrast, no melt pool lines are seen in the third trial samples (see Figure 7.3), which might be due to the unsuccessful etching or the high treatment temperature of 1400°C, which melts the melt pool lines and makes them disappear

7.3. Results and Discussions

7.3.1. SEM/EDX Results

The SEM-EDX result of the third trial shows nickel in the samples in addition to Nd and Fe, shown in Figure 7.3, which confirms that nickel infiltration was successful. In addition, the cross-section images in Figures 7.4 (g), (h) and (i) show the same dendritic structure in the entire sample from top to bottom, which confirms that infiltration is successful for the entire sample.

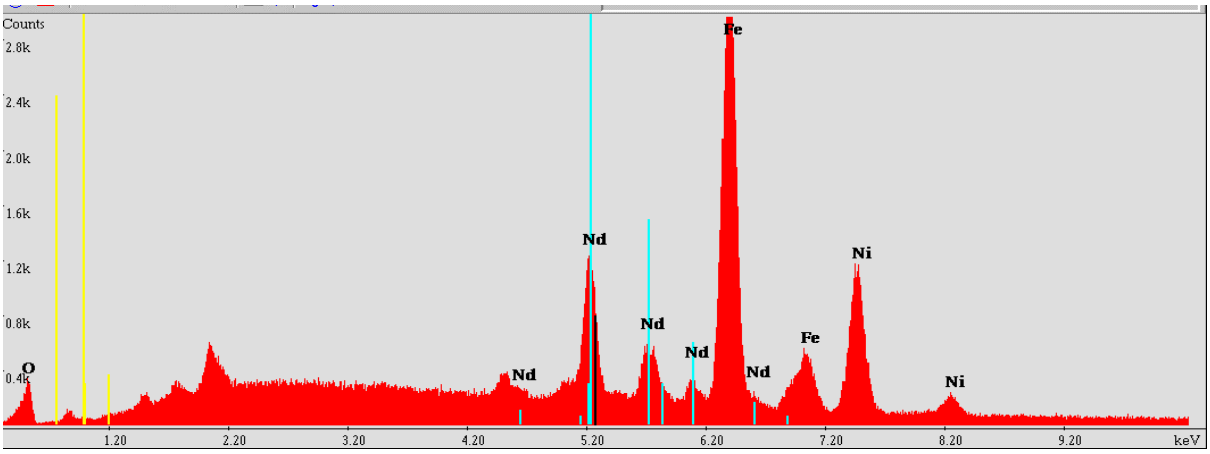

Figure 7-3 EDX result of the Ni infiltrated sample at 1400 °C

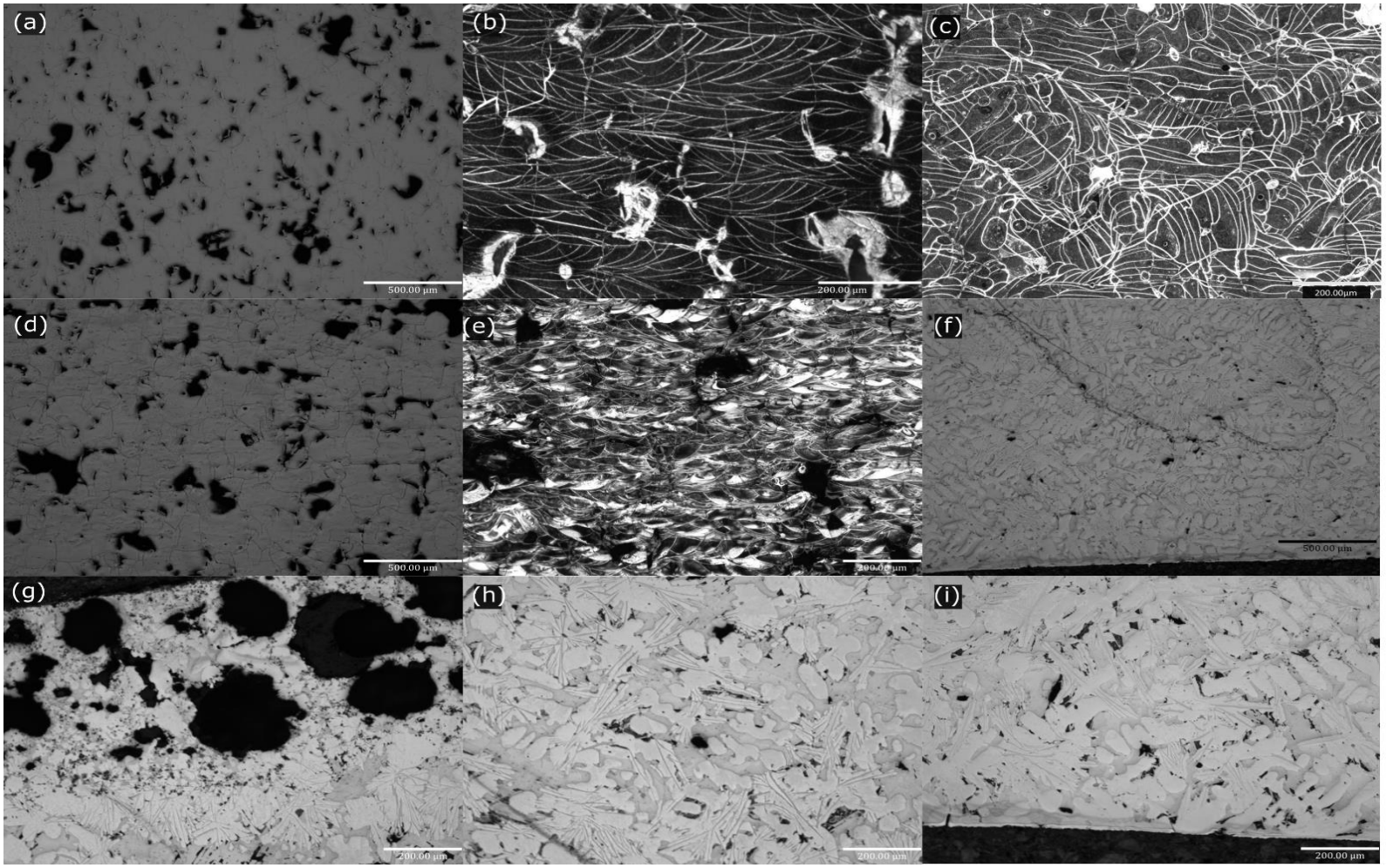

Figure 7-4 (a) Inconel/paraffin coated sample before etching, (b) cross-section of the Inconel paraffin coated sample after etching, (c) top view of the Inconel/paraffin coated sample after etching, (d)Ni foil wrapped sample at 750°C before etching, (e) cross-section of the Ni foilwrapped sample at 750°C after etching,(f) Ni foil wrapped sample at 1400° C before etching, Ni foil wrapped sample at 1400° C after etching (g) top (h)middle (i) bottom of the cross-section of the sample.

Further elemental investigation confirms that the dendritic structures in the samples are Fe-rich areas. The SEM image taken in backscattering mode in Figure 7.5 shows a closer look at the samples. There are different colours seen in the samples; the dark phase shown in square 1 is the Fe-rich phase (61% Fe rich-23% Zr-8% Ni), the brightest phase shown in square 2 is the Nd-Ni rich phase (42% Nd-37% Ni), and the bright phase in square 3 is the almost equally blended NdFeBNi phase. In addition, the dark needles indicated by the orange arrows are Fe-Zr rich areas (56% Fe-29% Zr), and thecubical shapes indicated by the blue arrows are Zr-rich areas (85% Zr) (which can be seen more clearly in Figure 7.6). Finally, the bright dots indicated by the yellow arrowsare Nd-oxides. Figure 7.6 shows a closer look at the sample. The EDX results of the almost equally blended NdFeBNi phase, cubical shaped Zr-rich areas and the bright Nd-oxides points are shown in Figure 7.7. (Quantitative EDX results can be seen in Appendix 3).

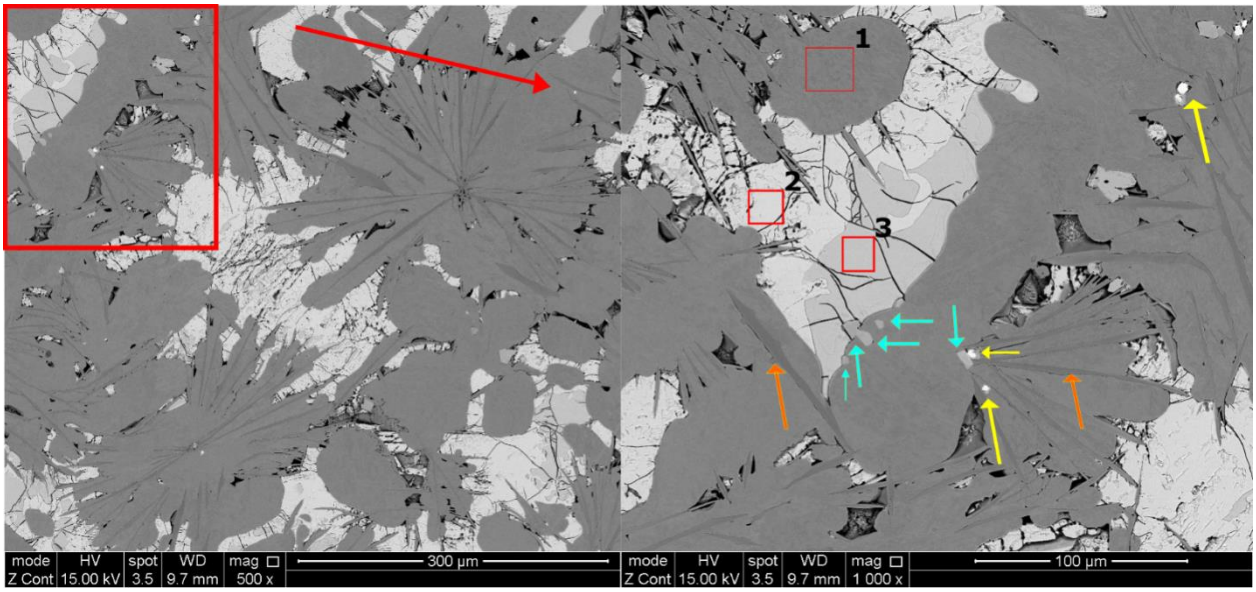

Figure 7-5 SEM-EDX images of the Nickel infiltrated sample at 1400 °C

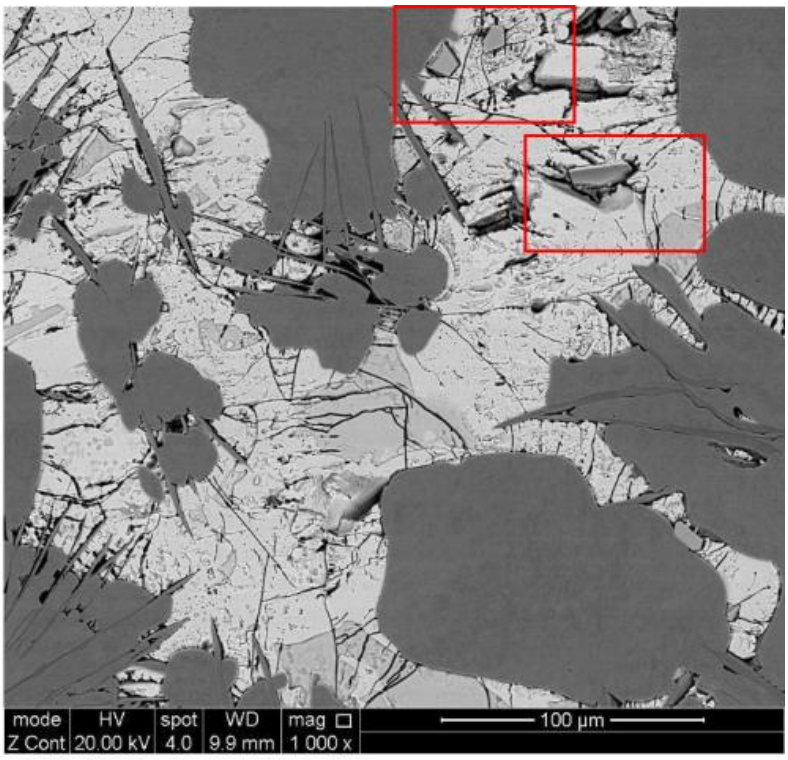

Figure 7-6 SEM-EDX images of the nickel infiltrated sample at 1400 °C, red square-Zr rich cubical areas.

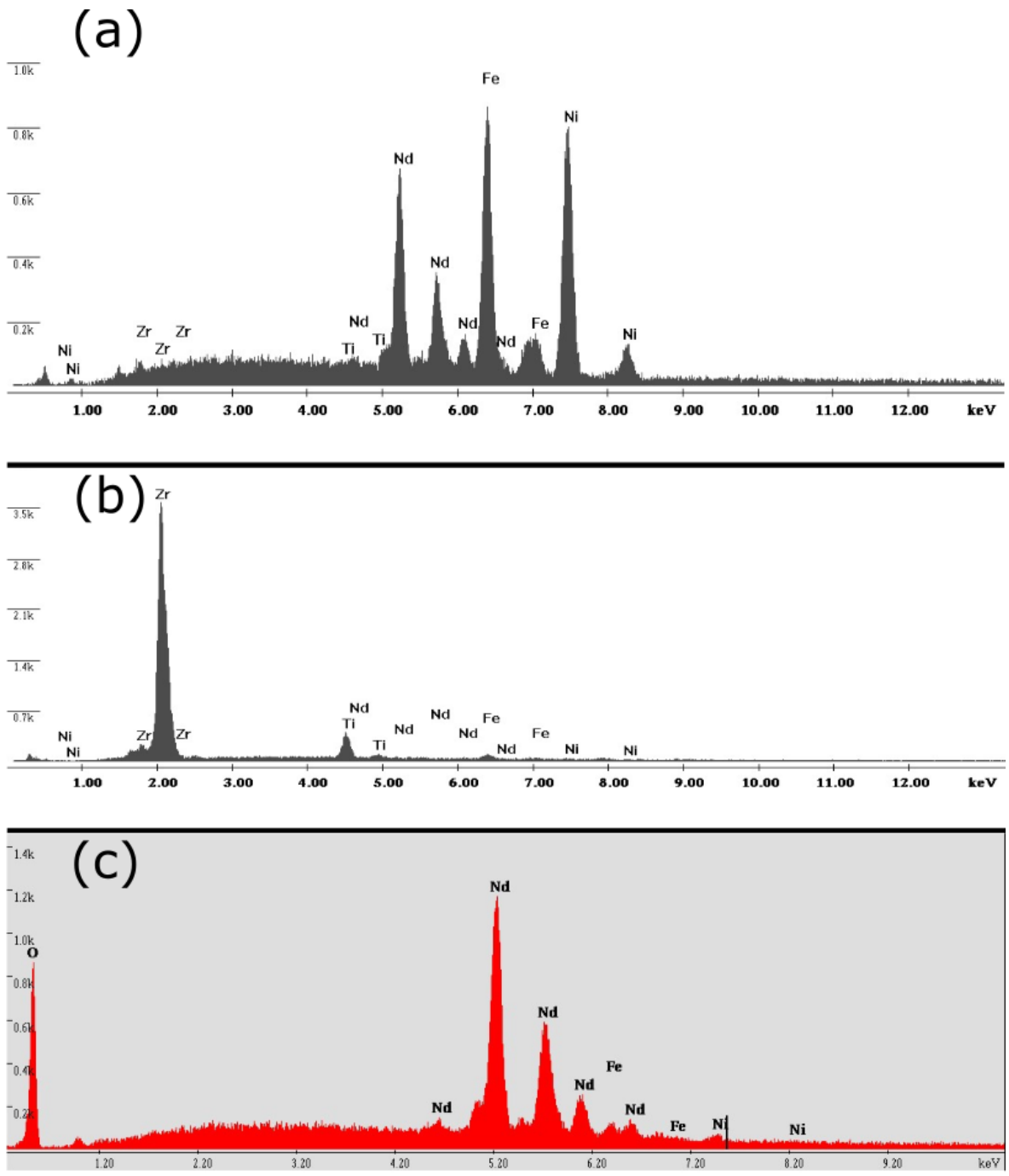

Figure 7-7 EDX results of (a) the NdFeBNi phase, (b) the cubical Zr rich areas, (c) the bright Nd-oxide spots

7.3.2. Magnetic Test Results

Ni intergranular addition (before the sintering) improves the coercivity of sintered NdFeB magnets by compromising the B_r, and magnet density reduction [77]. Hence, it aims to improve coercivity of the SLM magnets with a slight drop in *Br* by adjusting the Ni content.

Two samples were prepared for the magnetic test: (i) 10 mm × 10 mm × 10 mm (full size) Ni-infiltrated sample; and (ii) 5 mm × 5 mm × 5 mm (half size) Ni-infiltrated sample (samples wrapped in 0.125 mm Ni foil). In the furnace treatment cycle, samples were kept at 1400°C for 2.5 hours, then temperature dropped to the annealing temperature of 490°C for 2.5 hours followed by cooling down in the furnace to room temperature in an inert gas atmosphere.

The density of samples improved with Ni infiltration from 6.90 g/cm^3 as-printed to 7.156-full size and 7.45 g/cm^3-half size samples. The Ni content in the half-size sample was higher than the full-size sample, hence the density was higher.

On the other hand, the magnetic properties would reduce with Ni infiltration. The H_{ci} values dramatically drop from 1000 kA/m to 11 kA/m and 10.6 kA/m, while the B_r reduction is lower, from 0.61 T to 0.41 T and 0.20 T, from as-printed samples to full-size and half-size infiltrated samples, respectively (as shown in Figure 7.8).

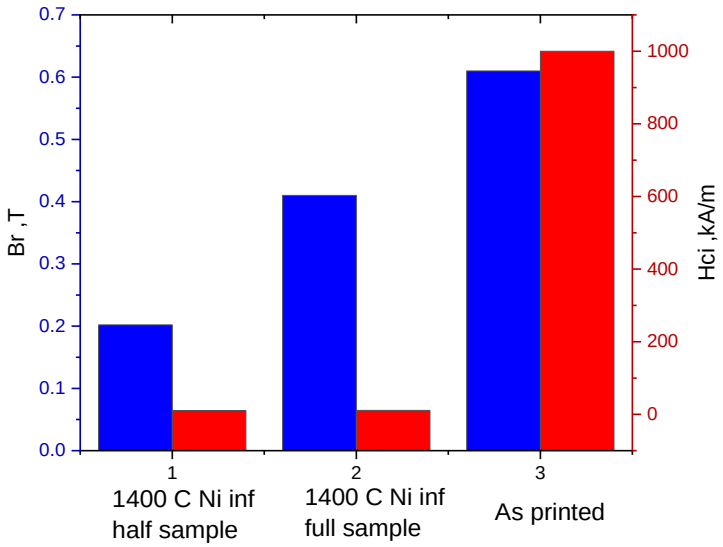

Figure 7-8 B_r -H_{ci} results of half size, full size nickel infiltrated samples and as printed sample.

It was deduced that the Br reduction is related to Ni content in the sample. Because the remanence of the half size sample is almost half of the full-size sample, coherent the Ni content in them.

The SEM images, presented in Figures 7.5 and 7.6, show microstructures that are completely different from the printed samples. There are larger dendritic structures in the infiltrated samples, up to 300 μm width dendrites having 100 μm dendritic arms. It was deduced that the coercivity decreases due to the very large dendritic grains compared to the room-temperature printed samples (nanograins are in the room-temperature printed sample).

Figure 7.9 shows the XRD patterns of the as printed -1400°C treated and Ni infiltrated samples. It is difficult to match the peaks with the possible phases since there are more than one matches for some of the peaks.

However, it is assumed that as-printed sample includes Fe where $Fe_{0.6}Ni_{0.4}$ is in the Ni infiltrated sample. It is also seen that there are no patterns for Φ phase, which likely be the reason for B_r drop. Other possible phases are Nd_2Fe_{17}, $FeBO_3$ and $Fe_{0.8947}Nd_{0.1053}$..Hence, the B_r reduction can be explained by the reduction in the strong magnetic phase in the presence Nd-oxides [94], confirmed in the EDX analysis in Figure 7.7.c.

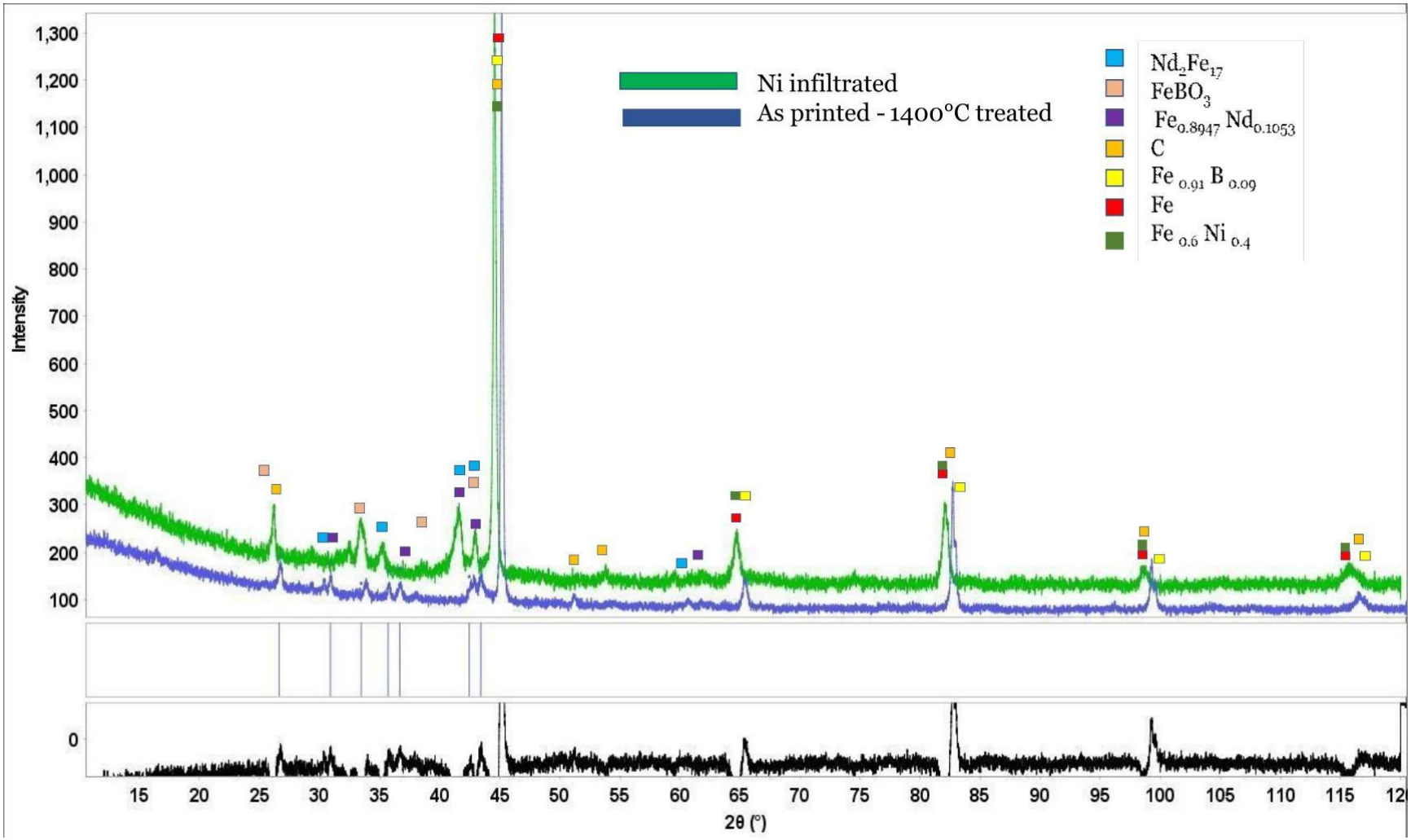

Figure 7-9 XRD patterns of as printed and -full size Ni infiltrated sample.

It was also found that the as printed sample treated at 1400°C has needle shape microstructure, consisting of Zr,B,Ti, as shown in Figure 7.10, reducing the coercivity to 20.2 kA/m.

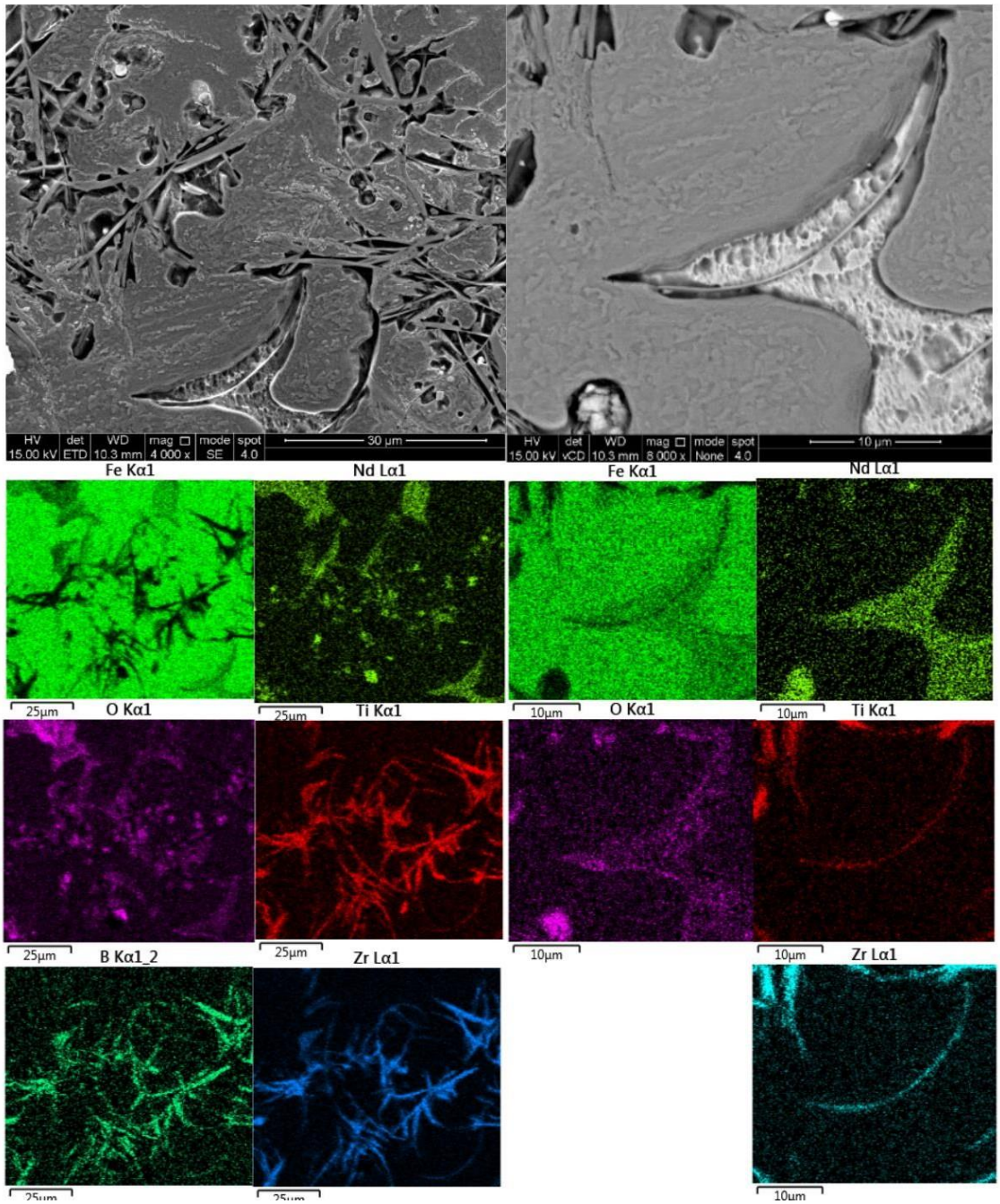

Figure 7-10 EDX elemental mapping of the as printed sample, treated with the infiltration cycle.

7.4. Conclusions

The density of the samples can be improved through Ni infiltration; however, it does not help to improve either the coercivity or remanence of the samples. The coercivity drop is very sharp as the infiltration causes very large dendritic grains. Furthermore, the infiltration temperature, 1400°C, is higher than the crystallization temperature of the hard phase, 1181°C; hence, the hard phase nanograins in the as-printed samples are destroyed during the infiltration. Then slow cooling in the furnace causes fewer hard phases, with the Nd_2Fe_{17}, FeNi/Fe and FeB phases, in addition to Nd-oxides. All reduces the percentage of hard phase, $Nd_2Fe_{14}B$ consequently the B_r.

Chapter 8: Hipping

8.1. Introduction

Hipping is one of the methods used for density improvement through the application of high pressures and high temperatures on samples [118], [119]. To date, there are only a few study reports on HIP-NdFeB sintered magnets, and no reports on HIP-SLM-NdFeB magnets. The density of sintered magnets is improved with hipping. However, the magnetic properties are more complicated. It was reported that H_c can be improved with a small amount of deterioration in B_r [120]. In contrast, [121] reported an improvement in the BH_{max} value with a drop in coercivity. Coercivity is highly dependent upon grain size [92], [122] and if the hipping temperature is sufficiently high for grain growth, it might reduce the coercivity [120]. This study is a pioneer in the application of hipping on SLM-NdFeB magnets. It is expected to improve the density and maximum energy product of the magnets.

8.2. Experimental Procedure

Samples were printed with the following parameters by Aconity Lab: 130 W *LP*, 1300 mm/s *LS*, 20 μm *LT* and 30 μm *HD*. Then hipping was performed at 800℃, 900℃ and 1200℃ at 150 MPa with a 30-minute hold time at each of those temperatures. The HIP cycle details are as follows: temperature increase of 5℃/min and pressure increase of 1 MPa/min. (Hipping was done at RTC (Royce Discovery Centre)). Three different types of printed magnets were analysed, heated bed (HB) printed samples (at 350℃ and 500℃), heat treated (HT) samples at 580℃, and room-temperature printed samples.

The density of the samples was tested following the Archimedes density method in water. The top surface quality and the melt pools in the cross sections of the samples were examined with an optical microscope. SEM/EDX analyses were performed to check grain morphologies and the elemental dispersion. Phases in the samples were checked with XRD. Magnetic tests were run with a permeameter by Arnold Magnetic Technologies.

8.3. Results and Discussion

8.3.1. Density Results

The density of the room temperature printed samples was around 7.1 g/cm^3, nearly 95% dense compared to the theoretical density of 7.5 g/cm^3. The expectation was to see density improvement; however, they dropped 1% to 4% after the hipping at 800℃and 900℃ (as shown in Figure 8.1). In contrast, the density of the HT and HB samples increased after 800℃ hipping, from around 6% to 12%, respectively. The density increase is lower in the 900℃ hipped samples; 5% in the 580℃- HT sample, and it is nearly the same for the 500℃ HB sample. In contrast, density is decreased 1% by 900℃ hippıng for the 350℃ HB sample. (This may be attributable to the error factor in the Archimedes density test; hence, it is ignored in the discussion).

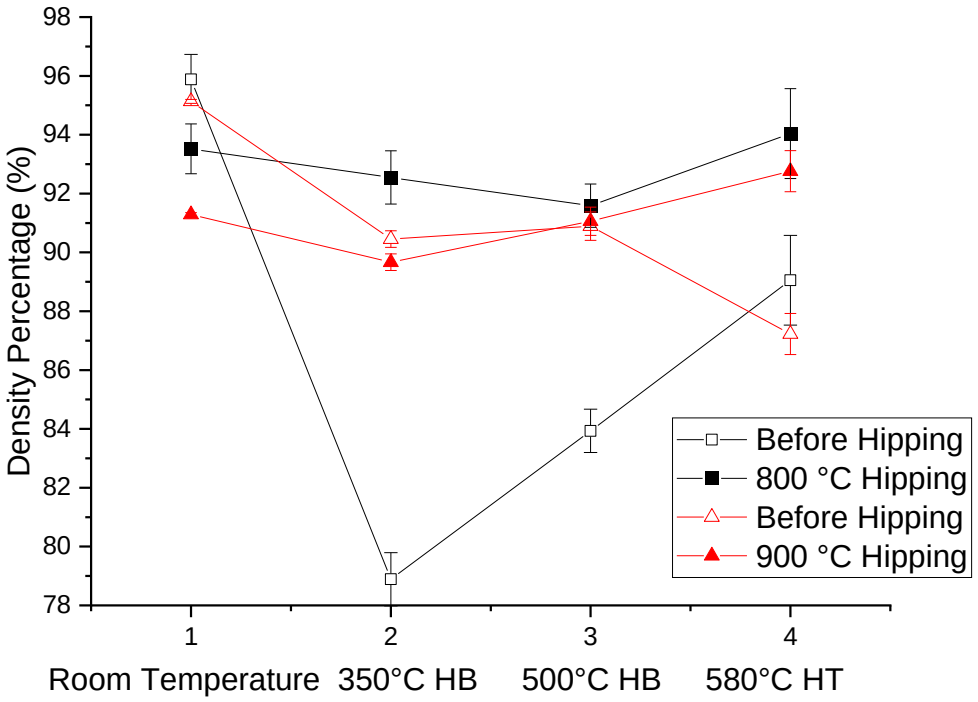

Figure 8-1 Archimedes density test results of the room temperature; heated bed printed samples at 350°C and 500°C; and annealed sample at 580°C.

The density decreases in the room-temperature printed samples can be explained with by crack propagation as the pressure is applied. Figure 8.2 shows the cracks and porosity in the cross section of the room-printed and hipped samples at 800℃ and 900℃. The cracks are mainly in the build direction of the samples while they have a higher occurrence in the hipped samples. In addition, there is a possibility of a flowing out of the low melting point Nd-rich phase through the porosities and cracks with the high pressure application.

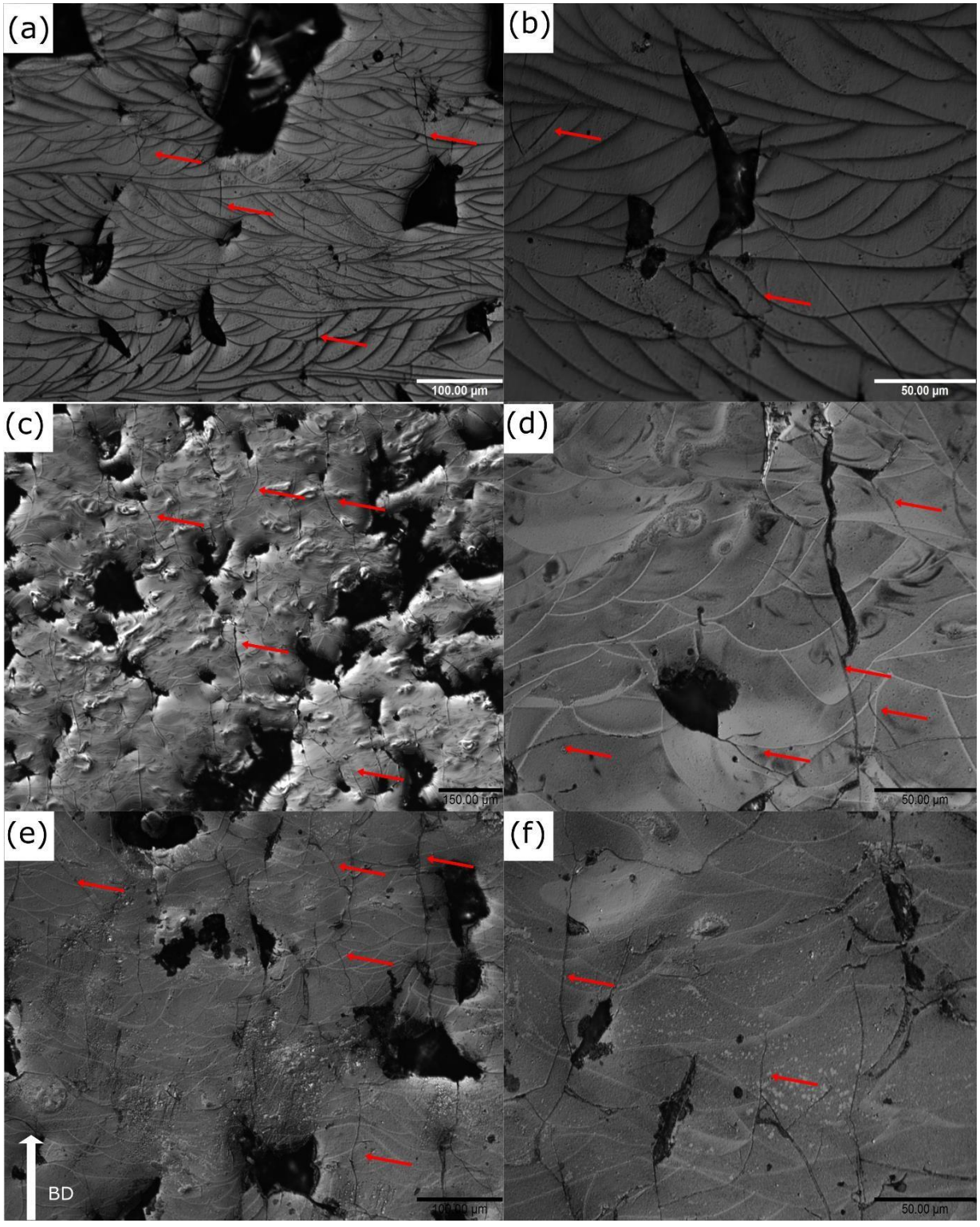

Figure 8-2 The cross section of the (a)-(b) room temperature printed sample ,(c)-(d) room temperature printed then hipped at 800°C and (d)- (e)room temperature printed then hippedat 900°C. (The red arrows point the cracks)

However, in the heated bed and heat treatment samples, there is a better sintering, causing fewer porosities and cracks; hence, crack propagation might be inhibited or lower than in the room temperature printing. In addition, the fewer porosities might keep the Nd-rich phase in the build during the hipping. Hence, the density improves or remains the same.

The hipping samples at 1200℃ were not plotted in Figure 8.1 as their label mixed by mistake after the hipping. However, the average percentage of the room-temperature printed samples were 96%, then they reduced to 90% after hipping at 1200℃.

Figure 8.3 shows shape distortions in the 1200℃ sample. In contrast, there is no distortion in the 800℃ and 900℃ hipped samples. This supports to loss of Nd-rich theory by hipping. The high-temperature hipping causes a high amount of Nd-rich loss, and the HIP pressure distorts the sample.

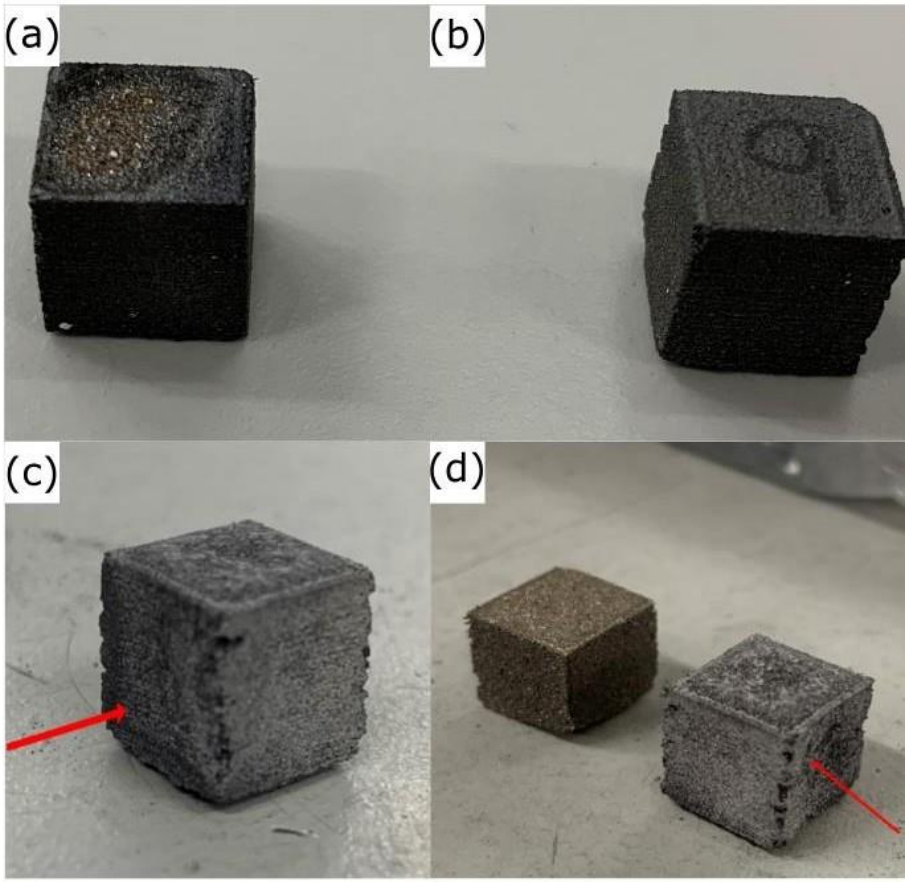

Figure 8-3 The images of the (a) 800°C, (b) 900°C, (c) 1200°C, (d) as printed and 1200°C hipped samples, red arrows point the distortion as in the direction of isostatic pressure.

8.3.2. Magnetic Test Results

Table 8.1 shows the magnetic test results before and after hipping. It can be seen that the coercivity values of all the samples decrease due to hipping. The coercivity of the room-temperature printed sample decreases from 1000 kA/m to 480 kA/m then to 60.1 kA/m. The 350℃-HB samples drop from 871 kA/m and 792 kA/m to 422 kA/m and 279 kA/m, respectively, by hipping. The 500℃-HB samples drop from 750 kA/m and 547 kA/m to 361 kA/m and 62.6 kA/m, respectively, and the annealed samples drop from 1027 kA/m to 430 kA/m and 171 kA/m, by 800℃ and 900℃, respectively for allsamples.

On the other hand, the change in the remanence values is not as great as the change in the coercivity values. B_r increases for room-temperature and 350℃-HB printed samples at 800℃ hipping, while they decrease for 500℃ HB printed samples. Additionally, a small drop can be seen in the annealed sample, from 0.69 T to 0.68 T. That drop may be the error factor in the magnetic test. In contrast, B_r has a decreasing trend for all 900℃ hipped samples.

Table 8-1 Magnetic properties of the hipped samples

HIP	**B_r (T)**	**H_{ci} (kA/m)**	**B_r (T)**	**H_{ci} (kA/m)**	**B_r (T)**	**H_{ci} (kA/m)**	**B_r (T)**	**H_{ci} (kA/m)**	**B_r (T)**	**H_{ci} (kA/m)**	**B_r (T)**	**H_{ci} (kA/m)**
Sample Detail	Room temperature	Room temperature	Heated Bed at 350℃	Heated Bed at 350℃	Heated Bed at 350℃	Heated Bed at 350℃	Heated Bed at 500℃	Heated Bed at 500℃	Heated Bed at 500℃	Heated Bed at 500℃	Annealed at 580℃	Annealed at 580℃
Before HIP	0.61	1000	0.69	871	0.64	792	0.71	750	0.771	547	0.69	1027
HIP-800℃	0.65	481	0.809	422			0.63	361			0.68	430
HIP-900℃	0.541	60.1			0.63	279			0.507	62.6	0.59	171

It is suggested that high-temperature hipping causes grain growth which can lead to magnetic coupling that consequently decreases the coercivity. In addition, the loss of the Nd-rich phase is a potential reason for a drop in coercivity. A lack of Nd-rich phases decreases the isolation of grain boundaries; hence, the magnetic grains have exchange interactions and can easily be demagnetised under an external field. The B_r and H_{ci} values given in Table 8.1 are plotted in Figure 8.4.

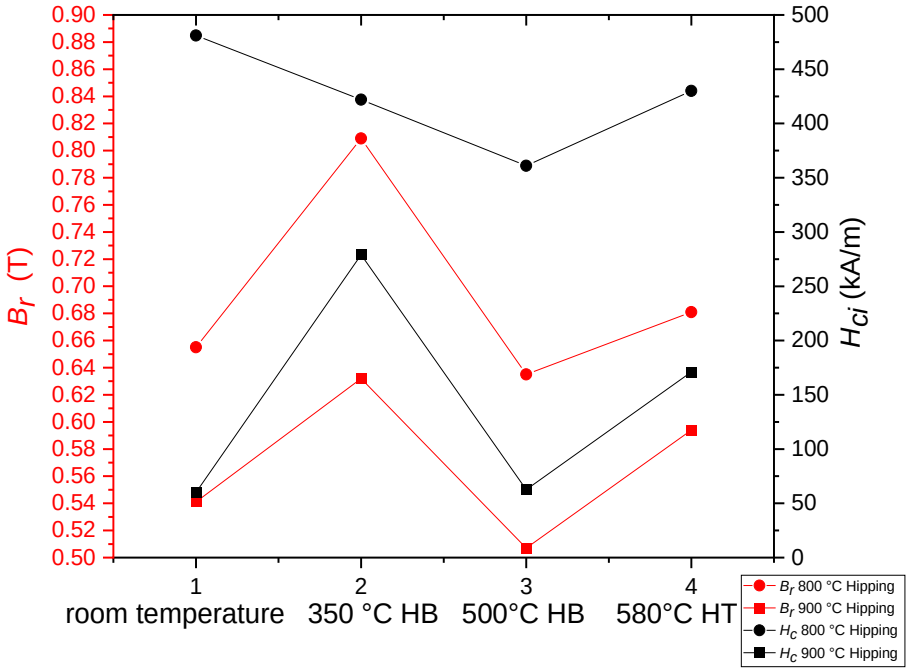

Figure 8-4 B_r and H_{ci} values of the room temperature, and heated bed printed samples at 350°C and 500°C, and annealed sample at 580°C.

Figure 8.5 shows white layers surrounding the cracks and porosities at the top of the hipped samples. They are likely to be oxide layers since it has been reported that sintered HIP NdFeB magnets oxidise [120] and it is known that cracks that are sensitive to oxidation [88]. The oxide form on the hipped samples might reduce the B_r. *EDX* mapping shows the oxide layer on sample surface, as shownin Figure 8.6.

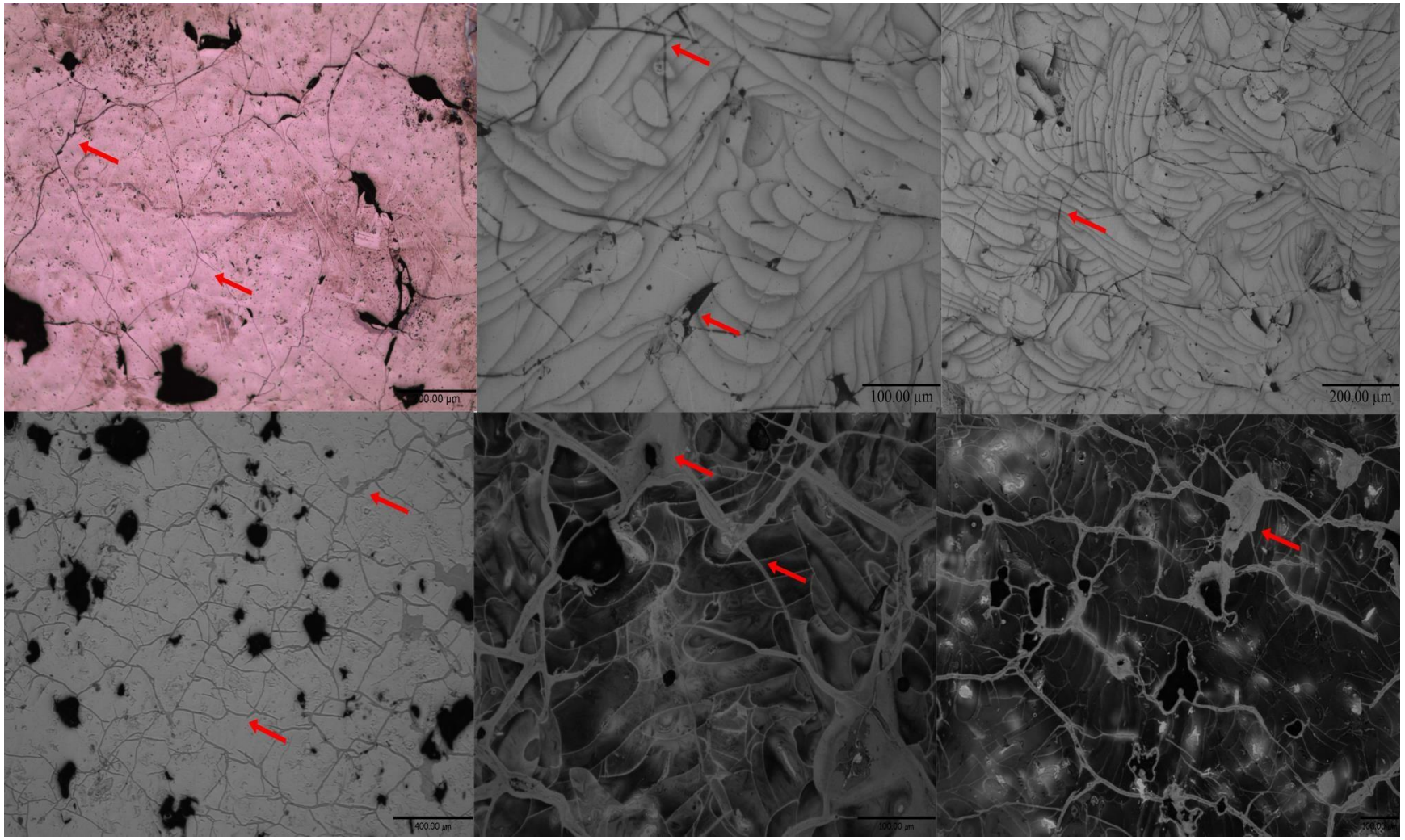

Figure 8-5 Top view of the (a)-(b)-(c) as printed samples and (d)- (e)-(f) hipped sample.

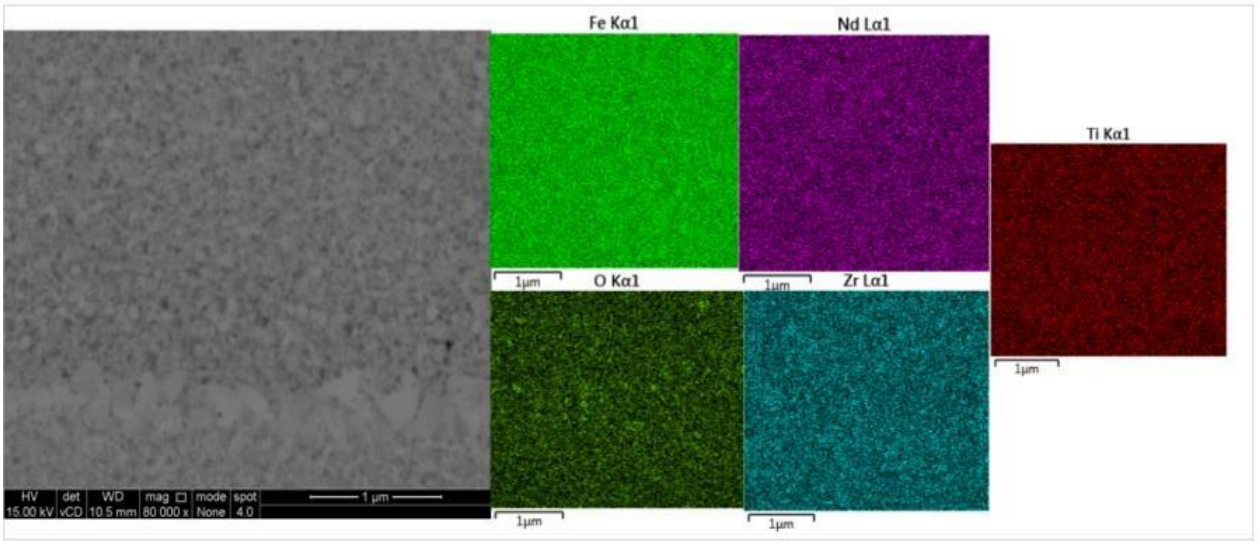

Figure 8-6 EDX elemental mapping of the hipped sample

8.4. Conclusions

The density of the pre-temperature exposed samples, heat treated and heated bed, increases by hipping. By contrast, the density of the room temperature printed samples decreases. That decrease can be explained by the crack propagation as the isostatic pressure applied during hipping. On the other hand, the better sintering in heat treatment and heated bed samples reduces the cracks and porosities which might inhibit or lower the crack propagation that occurs by hipping. Moreover, the lower porosities in these samples keep the low melting point Nd rich phase in the hipped samples.

The magnetic properties tend to decrease after hipping, especially coercivity decreases sharply. Decreases are much more in 900 °C hipped samples. The H_{ci} decrease related to bigger grains in hipped samples in addition to less Nd rich phases in them. On the other hand, B_r reduction relates the magnet density decreases in addition to oxide formations in the hipped samples.

Chapter 9: Conclusions and Future Work

9.1. Conclusions

This thesis investigates the manufacturing of NdFeB magnets using Selective Laser Melting, at room temperature and with preheated beds, in addition to studying post processing techniques, and heat treatment-Ni infiltration-HIPping, in order to improve magnetic properties. The NdFeB magnet is a common strong magnet which has various application areas. It has the strongest energy density compared to other types of magnets. However, the conventional manufacturing methods of NdFeB magnets has design limitations. Moreover, the brittle structure of the material makes it difficult to machine them. In addition, the cost of NdFeB magnets is high due to the limited rare earth element reserve. Hence, SLM is a promising method which can be a solution for complex design magnets with low material wastage. By designing amagnet with cooling channels or by altering the shape of the magnets, the magnetic properties of the magnets can be improved without using more rare earth elements. However, SLM has its challenges. First, the high cooling rates of SLM causes high thermal gradients and residual stresses within the processed material. The combination of residual stresses and the brittle structure of the hard phase results in cracks and layer delamination. Moreover, the brittleness of the material causes post processing challenges. It was very challenging to prepare a sample without cracks andoxidation layers on the surface, which is extremely important since the quality of the sample surface affects SEM/EDX, XRD and magnetic test results. It was difficult to identify the phases in the samples due to the noisy XRD patterns. The reason of this was due to the not 100% flat surfaces of the samples even after grinding polishing. On the other hand, the highly magnetic structure in some of the samples made it difficult to obtain SEM images as the magnetic field would cause shifting during the imaging. Regarding the magnetic tests, they were run mostly using Arnold magnetic technologies. It has beenstated that testing accuracy is dependent upon the accuracy of the surface finish. The samples were ground and polished to improve the surface quality; however, the optic images would prove the height differences on the surfaces due to the extraction of pieces from the surfaces. In addition, if the surfaces are not flat and parallel and/or

the integrity of the sample is not good, the sample under test conditions results in its disintegration. Some of the samples could not survive during the test and crumbled. The results of these samples might be deflected due to the crumbling.

Chapter 4

The first experimental chapter investigated the parameter effects on density and the magnetic properties of the samples. The effect of laser power, laser speed, energy density, hatch distance, layer thickness and energy line were investigated, in addition to performing an investigation on the relationship between the density and magnetic properties. This study investigated the grain morphology and the grain growths in the melt pool, which was not reported previously. The conclusions are asfollows:

- High *ED* causes high residual stresses during the cooling of the samples, causing cracks, material delamination and possible keyholes due to the entrapped air bubbles in the sample. All cause sample failure during or after the printing due to the brittle nature of the material.
- The density of the samples starts to reduce after *LP* 120-130 W (*ED* and *EL* are kept in the safe *ED* range). The combination of very high laser speed and high laser power generates unstable melt pools that result in low- density samples. Laser speed should be sufficiently low to allow sufficient melting and powder consolidation. The very high *LP/LS* (200 W/5500 mm/s) combinations also reduce the integrity of the sample. Because they create very unstable melt pool. In addition, no successful sample was obtained using an *ED* above 125 kJ/mm^3 since high *ED* cause excessive energy input which possibly causing keyhole porosities in the sample. In summary, The *ED* is not the only parameter should be considered. The laser power should be high enough and the laser speed should be slow enough to absorb the *ED* fully by powder layered.
- The decreasing *LT* and *HD* increase the density of thesamples. It was found that the effect of *HD* on sample density is higher than that of *LT*on sample density.
- Regarding density and the magnetic properties, there was a linear relationship that is not entirely found between them. However, it can be said that all highly magnetic samples are highly dense while not all highly dense samples have highly magnetic properties.

- It was concluded that the magnetic properties are related to phase and the microstructure, the former affecting B_r and the latter affecting H_{ci}. Hence, the coolingrates need to be considered. It was found that the higher *Br* samples were obtained by having the *EL* between 0.03 Ws/mm and 0.04 Ws/mm with the *ED* between75 J/mm^3 and 100 J/mm^3, while the B_r values decrease with an increasing *EL* to 0.05 Ws/mm and *ED* to 125 J/mm^3. It is also concluded that the high B_r samples are a result of faster scans.

- The high *LP*/high *LS* combinations (up to 100 W *LP*/3000 mm/s *LS)* give higher sample density and remanence values than the low *LP*/low *LS* combinations (below 60 W *LP*/1250 mm/s *LS*). The printing quality is more likely depending on the laser power however the increasing *ED* also increases the density of the samples.

- The results of the XRD analyses show that there are two main phases in the $Nd_2Fe_{14}B$ samples, which is the strong magnetic phase and the α-Fe phase. It was found that the magnetic properties are highly dependent on these phases. The higher magnetic phase ($Nd_2Fe_{14}B$) was detected in the samples with higher B_r and H_{ci} values and the lower *α-Fe* phase found in the samples has higher B_r and H_{ci} values.

- The maximum properties obtained by parameter optimization are BH_{max}, 0.72 T and 81 kJ/mm^3 respectively. They are the highest properties obtained with *MQP-S-11-9-20001* by SLM without post processing or element doping.

Chapter 5

- Influences of heated bed on sample density, magnetic properties and microstructure were investigated.

- The density percentage of the samples are improved with the heated bed from 90% to 96%; however, no linear relationship was observed between the bed temperature and density increase. This means that heated bed reduces the thermal stresses originated cracks, hence higher density.

- There is difference seen on the integrity of the samples in addition to fluctuations seen in the density results. Some of the samples were tilted forward. This meant that the heated bed build platform is not stable and it needs

to fix tight for repeatability of the experiments. It was the biggest challenge of the heated bed experiments.

- The surface quality of the samples improved. Smoother surfaces were obtained with the heated bed; however, delamination was seen in the layers near the top of the samples. This delamination is related to the faster cooling rates on the top of the samples with the combination of excessive energy input originated by laser source and heated bed.
- The energy product of the magnets was improved by improving the remanence; in contrast, there is a decrease in coercivity. The decrease can be related to the change in microstructure in the heated bed-printed samples. The lower cooling rates cause larger and more dendritic grains in the direction of building, which might reduce the coercivity. The increase in B_r is related to increasing density meaning that higher magnetic structure in the sample.
- In addition, the influences of hatch distance, laser speed in combination of bed temperature was investigated. Coercivity can be improved by lowering the *HD* more than setting the bed temperature or lowering the laser speed. On the other hand, bed temperature highly affects B_r, while the change in *HD* and *LS* does not affect it too much. The densities of the samples are more affected by *HD* than by bed temperatureand laser speed. However, the density and magnetic properties of the samples do not have a strong relationship; hence, it was concluded that the focus should be on the printing parameters that give higher H_{ci} and B_r rather than the higher sample density.

Chapter 6

- The influences of heat treatment on density, magnetic properties and microstructure were investigated. The density of the samples had improved with heat treatment, confirmed with the Archimedes density test and optic images.
- Regarding the magnetic properties, the aim was to increase coercivity by defining the grain boundaries consequently inhibiting the coupling between the magnetic grains, not to improve the B_r. However, samples annealed at 580℃ and 680℃ show relatively high increase in remanence from 0.61 T to 0.68 T

and 0.75 T, respectively, rather than the coercivity increase. The increase might be related to increase in the density since high dense samples include higher magnetic phase.

- SEM images of the heat-treated samples shows a correlation between the magnet microstructure and the coercivity. The main finding is the presence of well-defined grain boundary controls the resistance to demagnetization. Coercivity increased from 1000 kA/m to 1027 kA/m under 580°C treatment and start to decrease to 15kA/m as the heat treatment temperature increased to 980°C. Grain boundaries (GB) are defined well and continious in 580°C annealed samples hence they inhibit the magnetic exchange coupling between the grains and increase the coercivity. While clearly isolated grains are not observed in the samples annealed at 680 °C, which explains the reduction in coercivity.

Chapter 7

- Nickel can be infiltrated into samples by wrapping the thin Nickel foil around them, then treat them together in the furnace at melting temperature of Nickel. Both the increasing Archimedes density results after the infiltration and EDX map results showing the Nickel from top to the bottom of the sample proves it.

- The aim was to improve coercivity through Ni infiltration; however, the magnetic properties decreased dramatically after the infiltration. Because the high temperature treatment destroys the desired microstructure. The very large dendritic grains compared to the room-temperature printed samples, (nanograins are in the room-temperature printed sample) decreases the coercivity to very low values.

- In addition, the Ni content reduces the magnetic content in the samples, consequently reducing the B_r. The *Br* drops more inhalf-size samples due to the higher Ni content in it.

- The phase structure of the infiltrated samples is different from the room-temperature printed sample, which consists of of Nd_2Fe_{17}, less or no hard phases, FeNi/Fe and FeB phases, in addition toNd-oxides. All reduces the *Br*.

- Regarding to magnetic properties, both Br and Hc_i decreases by infiltration. Hc_i values dramatically drops, from 1000kA/m to 11kA/m and10.6kA/m- while the Br reduction is, from 0.61T to 0.41T and 0.20T, from as printed sample to full size and half size infiltrated samples, respectively.

Chapter 8

- HIPping improves the density of the heat-treated and heated bed printed samples while reducing the density of the room-temperature printed samples.
- The decrease inthe room-temperature printed samples can be explained by the crack propagation in the samples as pressure is applied. On the other hand, heat treatment and the heated bed reduces cracks and porosities, which inhibits crack propagation by applying pressure during the hipping. In addition, the lower porosities keep the melting point of the Nd-rich phases low in the HIPped samples, thereby increasing the density of thesamples.
- The magnetic properties decrease after hipping, especially the coercivity decreases remarkably as assumed the high HIPping temperature cause grain coarsening. The theory of loss of Nd phase at the grain boundaries is the other possible reason for the coercivity drops.
- On the other hand, Br reduction relates the magnet density decreases in addition to oxide formations in the HIPped samples. The decreases are more in 900°C HIPped samples than 800°C HIPped samples.

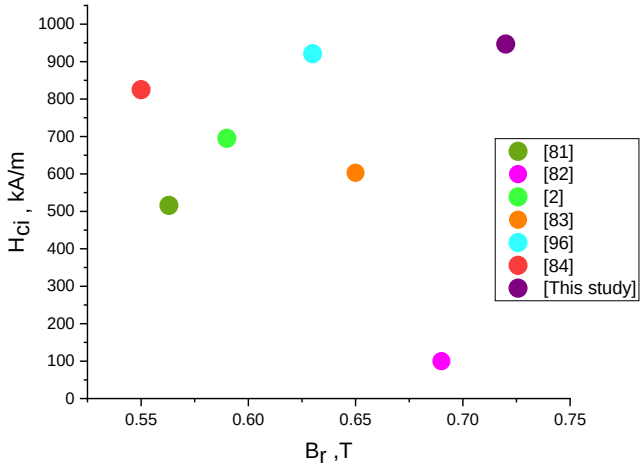

Figure 9-1 State of Art and comparison to literature.

In this study, B_r and BH_{max}, are the highest properties that have improved so far, by parameter optimisation, without any post-processing or element doping, 0.72 T and 81 kJ/mm3, respectively. They are the highest properties obtained by SLM without post-processing or element doping. The coercivity value is 947 ka/M, which is much better than most of the works in the literature. The comparison of this study with literature is shown in Figure X. However, magnetic properties are still lower than their sintered counterparts in the industry, which are around B_r 1.2 T, H_{ci} 1592 kA/m and BH_{max} 310 kJ/m3. On the other hand, using of heated bed and heat treatment after printing has a potential to improve B_r and BH_{max} with compromising the coercivity. Figure 9.2 shows the maximum magnetic properties obtained by heated bed and heat treatment.

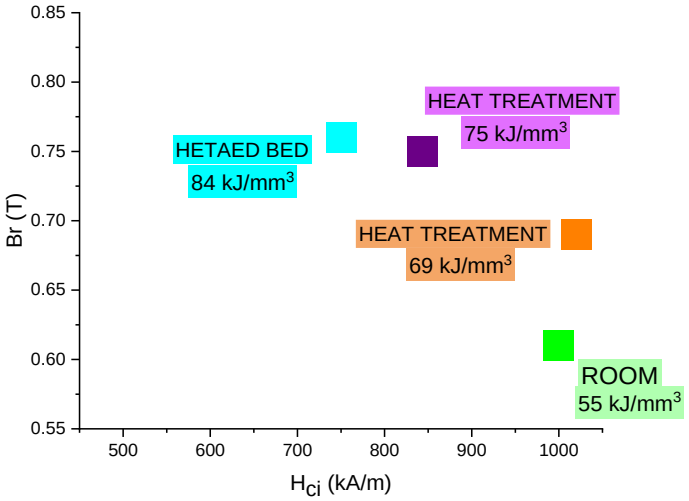

Figure 9-2 The magnetic properties- comparison of the heated bed printed, room temperature printed and heat treated samples. Printing parameters are the same for all samples here. Therefore, effect of technique to magnetic properties can be compared here.

The main conclusion from this work is that selective laser melting of NdFeB magnets is highly sensitive process due to the material`s challenges and fast cooling rates of SLM. The magnetic properties can be improved by optimizing the printing parameters and by using of the heated bed. However, they still need to be improved to use them in electrical motor applications. In addition, this study could be a potential base for the future improvements on heated bed- SLM NdFeB magnets since it is the first study investigating the use of heated bed.

9.2. Recommendations for Future Work

From the finding in chapter 5, heated bed has a great potential to improve SLM-NdFeB magnet properties. And it becomes apparent that there is a need to investigate heated bed capabilities more. The next step on the heated bed would be working on to improve stability of the heated bed. Then conduct more detailed investigations on bed temperature and print parameters, which would provide a better understanding of the benefits and limitations of the heated bed.

Nickel infiltration did not work to improve the magnetic properties since the infiltration was conducted under high temperature and it destroyed the desired microstructure. The next step would be to mix the nickel powder to the magnetic powder feedstock intergranularly before the printing of the sample, instead of performing the post-processing of Ni infiltration at high temperature. In addition, low melting point alloys are highly recommended for infiltration, which reduces the infiltration temperature, which inhibits any grain growth. The possible recommendations are NdCuCo and PrCuCo. Moreover, the Dy doping would be a solution to improve the coercivity of the printed magnets since it works for the sintered magnets very well.

HIPping risks the Nd-rich phases in the samples. The Nd-rich phase would run off with the high pressure in HIPping, which is detrimental to coercivity. Therefore, it is recommended to do HIPping at around 600°C, near the melting point of Nd-rich phases to prevent the loss of the Nd-rich phase. On the other hand, using protective glass sheaths around the samples [95] is the other option to stop the running off of Nd-rich phases by pressure for sintered magnets. This may also work for SLM-printed NdFeB magnets hence it needs to be explored.

The microstructure of the printed samples still needs to be examined. The TEM/EDX analysis would be the next step to analyse the nanograins in SLM-NdFeB magnets.

In that study, the mechanical properties of the SLM printed magnets were not one of the main concerns like density and their magnetic properties since they don't expose the dynamic load during the working of the motor. However, it is suggested to examine the mechanical properties of the magnet since they still need to be strong enough to fit in the rotor core. In addition, the complex-shaped magnets/ magnets with cooling

channels were not studied due to the limited time of the project, and it needed to be investigated.

References

[1] K. Yamazaki and Y. Fukushima, “Effect of eddy-current loss reduction by magnet segmentation in synchronous motors with concentrated windings,” *IEEE Trans Ind Appl*, vol. 47, no. 2, pp. 779–788, 2011, doi: 10.1109/TIA.2010.2103915.

[2] J. Jaćimović *et al.*, “Net Shape 3D Printed NdFeB Permanent Magnet,” *Adv Eng Mater*, vol. 19, no. 8, pp. 1–7, 2017, doi: 10.1002/adem.201700098.

[3] S. Amin, S. Madanzadeh, S. Khan, S. S. H. Bukhari, F. Akhtar, and J. S. Ro, “Effect of the magnet shape on the performance of coreless axial flux permanent magnet synchronous generator,” *Electrical Engineering*, vol. 104, no. 2, pp. 959–968, 2022, doi: 10.1007/s00202-021-01338-x.

[4] J. Du, X. Wang, and H. Lv, “Optimization of Magnet Shape Based on Efficiency Map of IPMSM for EVs,” *IEEE Transactions on Applied Superconductivity*, vol. 26, no. 7, 2016, doi: 10.1109/TASC.2016.2594834.

[5] M. Shokri, N. Rostami, V. Behjat, J. Pyrhonen, and M. Rostami, “Comparison of Performance Characteristics of Axial-Flux Permanent-Magnet Synchronous Machine with Different Magnet Shapes,” *IEEE Trans Magn*, vol. 51, no. 12, 2015, doi: 10.1109/TMAG.2015.2460217.

[6] N. A. Spaldin, “Review of basic magnetostatics,” *Magnetic Materials*, pp. 3–13, 2012, doi: 10.1017/cbo9780511781599.001.

[7] C. All, “_Units_and_Terminology_-_Magnetic_Materials_Group.pdf,” vol. 3, pp. 51–65.

[8] N. A. Spaldin, “Magnetization and magnetic materials,” *Magnetic Materials*, pp. 14–21, 2012, doi: 10.1017/cbo9780511781599.002.

[9] E. Wyslocka and R. Ulewicz, “Magnets: History, the Current State and the Future,” *Metal 2015: 24Th International Conference on Metallurgy and Materials*, no. July 2016, pp. 1680–1686, 2015.

[10] M. J. Kramer, R. W. McCallum, I. A. Anderson, and S. Constantinides, “Prospects for non-rare earth permanent magnets for traction motors and generators,” *Jom*, vol. 64, no. 7, pp. 752–763, 2012, doi: 10.1007/s11837-012-0351-z.

[11] H. Ferrites, S. Type, and N. Type, “Magnetic Materials : Hard Magnets,” pp. 1–8, 2010.

[12] A. Williams, “Classification of Magnetic Materials,” *Classification of Magnetic Materials*, pp. 2–5, 2014, [Online]. Available:

http://www.birmingham.ac.uk/research/activity/metallurgy-materials/magnets/Magnetic-Materials-Background-Information.aspx

[13] S. et al. Kazawa, "'Trends and Problems in Research of Permanent Magnets for Motors — Addressing Scarcity Problem of Rare Earth Elements —,'" *Science & Technology Trends*, no. 38, pp. 40–54, 2011.

[14] I. S. Moosa, "History and Development of Permanent Magnets," vol. 2, no. 1, pp. 18–26, 2014.

[15] G. Bai, R. W. Gao, Y. Sun, G. B. Han, and B. Wang, "Study of high-coercivity sintered NdFeB magnets," *J Magn Magn Mater*, vol. 308, no. 1, pp. 20–23, 2007, doi: 10.1016/j.jmmm.2006.04.029.

[16] X. T. Tang, Z. W. Lu, and A. Z. Sun, "The effect of sintered Nd-Fe-B with Dy infiltration to the plating crafts," *J Magn Magn Mater*, vol. 475, no. November 2018, pp. 10–13, 2019, doi: 10.1016/j.jmmm.2018.11.080.

[17] X. G. Cui *et al.*, "Magnetic properties and microstructure of sintered Nd–Fe–B magnets with intergranular addition of Ni powders," *J Alloys Compd*, vol. 726, pp. 846–851, 2017, doi: 10.1016/j.jallcom.2017.08.061.

[18] P. Zhang, L. Liang, J. Jin, Y. Zhang, X. Liu, and M. Yan, "Magnetic properties and corrosion resistance of Nd-Fe-B magnets with Nd64Co36intergranular addition," *J Alloys Compd*, vol. 616, pp. 345–349, 2014, doi: 10.1016/j.jallcom.2014.07.085.

[19] C. Jin *et al.*, "Magnetic properties and phase evolution of sintered Nd-Fe-B magnets with intergranular addition of Pr–Co alloy," *J Alloys Compd*, vol. 670, pp. 72–77, 2016, doi: 10.1016/j.jallcom.2016.02.006.

[20] P. Zhang, T. Ma, L. Liang, and M. Yan, "Influence of Ta intergranular addition on microstructure and corrosion resistance of Nd-Dy-Fe-B sintered magnets," *J Alloys Compd*, vol. 593, pp. 137–140, 2014, doi: 10.1016/j.jallcom.2014.01.055.

[21] L. Li *et al.*, "A novel method combining additive manufacturing and alloy infiltration for NdFeB bonded magnet fabrication," *J Magn Magn Mater*, vol. 438, pp. 163–167, 2017, doi: 10.1016/j.jmmm.2017.04.066.

[22] T. Sato, N. Oka, T. Ohsuna, Y. Kaneko, S. Suzuki, and T. Shima, "Enhancement of coercivity for Nd-Fe-B thin films by the infiltration of Nd-Cu alloy cap layer," *J Appl Phys*, vol. 110, no. 2, pp. 1–5, 2011, doi: 10.1063/1.3608244.

[23] W. Francis, "Definitions and Units," *Fuels and Fuel Technology*, pp. 3–8, 2013, doi: 10.1016/b978-0-08-025250-6.50006-7.

[24] T. Magnetic, “1 . 1 . 2 BASIC OPERATING PRINCIPLE OF ELECTRIC MOTORS,” no. 2017, pp. 56–58, 2023.

[25] A. Hughes, *Electric motors and drives [electronic resource] : fundamentals, types and applications*, 3rd ed. Amsterdam ; Boston ; London: Elsevier Newnes, 2006.

[26] A. E. Fitzgerald and S. D. Umans, *Electric machinery*, 6th ed. Boston, Mass. ; London: McGraw-Hill, 2003.

[27] T. J. E. Miller, *Brushless permanent-magnet and reluctance motor drives*, 2nd (Corr.)impression. Oxford: Clarendon, 1993.

[28] M. Šustek, M. Marcaník, P. Tomášek, and Z. Úředníček, “DC motors and servo-motors controlled by Raspberry Pi 2B,” *MATEC Web of Conferences*, vol. 125, pp. 1–6, 2017, doi: 10.1051/matecconf/201712502025.

[29] J. R. Hendershot and T. J. E. Miller, *Design of brushless permanent-magnet motors*. Hillsboro, OH : Oxford: Magna Pysics Pub. ; Clarendon Press, 1994.

[30] B. K. Bose, *Modern power electronics and AC drives*. Upper Saddle River, NJ: Prentice Hall PTR, 2002.

[31] C. J. Fraser, “Electrical machines,” *The Mechatronics Handbook*, pp. 20-33-20–51, 2002, doi: 10.1201/9781420037043-13.

[32] U. of LaSalle, “Magnetic Susceptibility,” *Notes*, no. May, pp. 4–7, 2014.

[33] J. M. D. Coey, “Ferromagnetism and exchange,” in *Magnetism and Magnetic Materials*, 2010, pp. 128–129. doi: https://doi.org/10.1017/CBO9780511845000.006.

[34] J. M. D. Coey, “Antiferromagnetism and other magnetic order,” in *Magnetism and Magnetic Materials*, 2010, pp. 195–230. doi: https://doi.org/10.1017/CBO9780511845000.007.

[35] O. Fabiyi, “Chapter 3. Methodology,” *Gated Neighbourhoods and privatisation of urban security in Ibadan Metropolis*, pp. 27–29, 2016, doi: 10.4000/books.ifra.475.

[36] E. P. Wohlfarth, “Hard magnetic materials,” *Adv Phys*, vol. 8, no. 30, pp. 87–224, 1959, doi: 10.1080/00018735900101178.

[37] “6.9: Hard and Soft Magnets - Chemistry LibreTexts,” vol. 310, p. 189204, [Online]. Available: https://chem.libretexts.org/Bookshelves/Inorganic_Chemistry/Book%3A_Introduction_to_Inorganic_Chemistry/06%3A_Metals_and_Alloys-

_Structure_Bonding_Electronic_and_Magnetic_Properties/6.09%3A_Hard_and_Soft_Magnets

[38] H. R.Kirchmayr, “REVIEW ARTICLE Permanent magnets and hard magnetic materials,” *J Appl Phys*, vol. 29, pp. 2763–2778, 1996.

[39] J. Karlsson and O. Söderström, “Review of Magnetic Materials Along With a Study of the Magnetic Stability and Solidity of Y40,” no. June, 2012, [Online]. Available: https://www.diva-portal.org/smash/get/diva2:534040/FULLTEXT01.pdf

[40] L. H. Lewis and F. Jiménez-Villacorta, “Perspectives on permanent magnetic materials for energy conversion and power generation,” *Metall Mater Trans A Phys Metall Mater Sci*, vol. 44, no. SUPPL. 1, 2013, doi: 10.1007/s11661-012-1278-2.

[41] eclipsemagnetics, “Magnet Materials & Assemblies - Sector Expertise - Power Generation.” https://www.eclipsemagnetics.com/row/magnet-materials-and-assemblies/?gclid=EAIaIQobChMI3q3V8ami4QIVGLLtCh2Klw_LEAAYASAAEgI_1_D_BwE

[42] Sas.usace.army.mil., “Savannah District > About > Divisions and Offices > Operations Division > Richard B. Russell Dam and Lake > Hydropower > How Hydropower Works.” https://www.sas.usace.army.mil/About/Divisions-and-Offices/Operations-Division/Richard-B-Russell-Dam-and-Lake/Hydropower/

[43] H. Shokrollahi and K. Janghorban, “Soft magnetic composite materials (SMCs),” *J Mater Process Technol*, vol. 189, no. 1–3, pp. 1–12, 2007, doi: 10.1016/j.jmatprotec.2007.02.034.

[44] J. E. Lenz, “A review of magnetic sensors,” *Proceedings of the IEEE*, vol. 78, no. 6, pp. 973–989, 1990.

[45] McLaren Applied Technologies, “Permanent Magnet Alternator.” https://www.mclaren.com/appliedtechnologies/products/item/alternator-permanent-magnet/

[46] Adams Magnetic Products, “Magnets for Motor Applications.” https://www.adamsmagnetic.com/markets/magnets-motor-applications

[47] Goudsmit, “Permanent Magnets and Precision Machined Parts for Medical Devices.” https://www.goudsmit.co.uk/sectors/medical/

[48] Q. A. Pankhurst, J. Connolly, S. K. Jones, and J. Dobson, “1110.J.Phys.D Appl.Phys.2003,36,R167.pdf,” vol. 36, 2003, doi: 10.1088/0022-3727/36/13/201.

[49] M. A. Riley, A. D. Walmsley, J. D. Speight, and I. R. Harris, “Magnets in medicine,” *Materials Science and Technology*, vol. 18, no. 1, pp. 1–12, 2003, doi: 10.1179/026708301125000140.

[50] A. du Plessis *et al.*, “Standard method for microCT-based additive manufacturing quality control 2: Density measurement,” *MethodsX*, vol. 5, no. September, pp. 1117–1123, 2018, doi: 10.1016/j.mex.2018.09.006.

[51] C. Rong and B. Shen, “Nanocrystalline and nanocomposite permanent magnets by melt spinning technique,” *Chinese Physics B*, vol. 27, no. 11, p. 117502, 2018, doi: 10.1088/1674-1056/27/11/117502.

[52] B. J. F. Herbst, J. J. Croat, and F. E. Pinkerton, “Relationships Between Crystal Structure and Magnetic Properties in Nd 2 Fe 14 B,” no. April, 1984, doi: 10.1103/PhysRevB.29.4176.

[53] K. Hono, “Strategy for high-coercivity Nd – Fe – B magnets,” *Scr Mater*, vol. 67, no. 6, pp. 530–535, 2012, doi: 10.1016/j.scriptamat.2012.06.038.

[54] N. Magnets, “Mikrochimica Acta Metallurgical Factors Determining the Coercivity of,” pp. 115–124, 1987.

[55] T. Shujian, L. Qingfan, L. Shixiang, and Z. Chaogui, “Phase diagram of the ternary system CeCl3-KCl-LiCl,” *J Alloys Compd*, vol. 274, no. 1–2, pp. 142–147, 1998, doi: 10.1016/S0925-8388(98)00551-9.

[56] C. V. Mikler, V. Chaudhary, V. Soni, B. Gwalani, R. V. Ramanujan, and R. Banerjee, “Tuning the phase stability and magnetic properties of laser additively processed Fe-30at%Ni soft magnetic alloys,” *Mater Lett*, vol. 199, pp. 88–92, 2017, doi: 10.1016/j.matlet.2017.04.054.

[57] X. Chen *et al.*, “Laser additive processing of Fe-Si-B-Cu-Nb magnetic alloys,” *J Manuf Process*, vol. 29, pp. 175–181, 2017, doi: 10.1016/j.jmapro.2017.07.029.

[58] C. V. Mikler *et al.*, “Laser Additive Manufacturing of Magnetic Materials,” *Jom*, vol. 69, no. 3, pp. 532–543, 2017, doi: 10.1007/s11837-017-2257-2.

[59] C. V. Mikler *et al.*, “Laser additive processing of Ni-Fe-V and Ni-Fe-Mo Permalloys: Microstructure and magnetic properties,” *Mater Lett*, vol. 192, pp. 9–11, 2017, doi: 10.1016/j.matlet.2017.01.059.

[60] B. Heer and A. Bandyopadhyay, “Compositionally graded magnetic-nonmagnetic bimetallic structure using laser engineered net shaping,” *Mater Lett*, vol. 216, pp. 16–19, 2018, doi: 10.1016/j.matlet.2017.12.129.

[61] E. M. H. White, A. G. Kassen, E. Simsek, W. Tang, R. T. Ott, and I. E. Anderson, “Net Shape Processing of Alnico Magnets by Additive Manufacturing,” *IEEE Trans Magn*, vol. 53, no. 11, 2017, doi: 10.1109/TMAG.2017.2711965.

[62] L. M. Bollig, P. J. Hilpisch, G. S. Mowry, and B. B. Nelson-Cheeseman, “3D printed magnetic polymer composite transformers,” *J Magn Magn Mater*, vol. 442, pp. 97–101, 2017, doi: 10.1016/j.jmmm.2017.06.070.

[63] C. Huber *et al.*, “3D print of polymer bonded rare-earth magnets, and 3D magnetic field scanning with an end-user 3D printer,” *Appl Phys Lett*, vol. 109, no. 16, 2016, doi: 10.1063/1.4964856.

[64] S. J. Leigh, C. P. Purssell, D. R. Billson, and D. A. Hutchins, “Using a magnetite/thermoplastic composite in 3D printing of direct replacements for commercially available flow sensors,” *Smart Mater Struct*, vol. 23, no. 9, 2014, doi: 10.1088/0964-1726/23/9/095039.

[65] L. Lu, P. Guo, and Y. Pan, “Magnetic-Field-Assisted Projection Stereolithography for Three-Dimensional Printing of Smart Structures,” *J Manuf Sci Eng*, vol. 139, no. 7, p. 071008, 2017, doi: 10.1115/1.4035964.

[66] V. Popov, A. Koptyug, I. Radulov, F. Maccari, and G. Muller, “Prospects of additive manufacturing of rare-earth and non-rare-earth permanent magnets,” *Procedia Manuf*, vol. 21, no. 2017, pp. 100–108, 2018, doi: 10.1016/j.promfg.2018.02.199.

[67] L. Li *et al.*, “Big Area Additive Manufacturing of High Performance Bonded NdFeB Magnets,” *Sci Rep*, vol. 6, no. October, pp. 1–7, 2016, doi: 10.1038/srep36212.

[68] L. Li, B. Post, V. Kunc, A. M. Elliott, and M. P. Paranthaman, “Additive manufacturing of near-net-shape bonded magnets: Prospects and challenges,” *Scr Mater*, vol. 135, pp. 100–104, 2017, doi: 10.1016/j.scriptamat.2016.12.035.

[69] M. P. Paranthaman *et al.*, “Binder Jetting : A Novel NdFeB Bonded Magnet Fabrication Process,” vol. 68, no. 7, pp. 1978–1982, 2016, doi: 10.1007/s11837-016-1883-4.

[70] C. Vyas, G. Poologasundarampillai, J. Hoyland, and P. Bartolo, “12 - 3D printing of biocomposites for osteochondral tissue engineering,” in *Biomedical Composites*, 2017, pp. 261–302. doi: https://doi.org/10.1016/B978-0-08-100752-5.00013-5.

[71] K. Anderson, C. Skelly, K. L. Martinson, K. L. Waite, P. M. Auwerda, and G. Heyboer, “Simultaneous multi-state equine business education program,” *J Equine Vet Sci*, vol. 33, no. 5, p. 389, 2013, doi: 10.1016/j.jevs.2013.03.154.

[72] D. Herzog, V. Seyda, E. Wycisk, and C. Emmelmann, “Additive manufacturing of metals,” *Acta Mater*, vol. 117, pp. 371–392, 2016, doi: 10.1016/j.actamat.2016.07.019.

[73] B. Zhang, N. E. Fenineche, L. Zhu, H. Liao, and C. Coddet, “Studies of magnetic properties of permalloy (Fe30%Ni) prepared by SLM technology,” *J Magn Magn Mater*, vol. 324, no. 4, pp. 495–500, 2012, doi: 10.1016/j.jmmm.2011.08.030.

[74] B. Zhang, N. E. Fenineche, H. Liao, and C. Coddet, “Microstructure and magnetic properties of Fe-Ni alloy fabricated by selective laser melting Fe/Ni mixed powders,” *J Mater Sci Technol*, vol. 29, no. 8, pp. 757–760, 2013, doi: 10.1016/j.jmst.2013.05.001.

[75] B. Zhang, N. E. Fenineche, H. Liao, and C. Coddet, “Magnetic properties of in-situ synthesized FeNi3 by selective laser melting Fe-80%Ni powders,” *J Magn Magn Mater*, vol. 336, pp. 49–54, 2013, doi: 10.1016/j.jmmm.2013.02.014.

[76] T. Bauer, A. B. Spierings, and K. Wegener, “Microstructure and Electro-Magnetic Properties of a Nickel-Based Anti-Magnetic Shielding Alloy,” *Proceedings of the 27th Annual International Solid Freeform Fabrication Symposium 2016*, pp. 1856–1867, 2016.

[77] K. J. Jhong, W. C. Huang, and W. H. Lee, “Microstructure and magnetic properties of magnetic material fabricated by selective laser melting,” *Phys Procedia*, vol. 83, pp. 818–824, 2016, doi: 10.1016/j.phpro.2016.08.084.

[78] T. Kolb *et al.*, “Laser Beam Melting of NdFeB for the production of rare-earth magnets,” *2016 6th International Electric Drives Production Conference, EDPC 2016 - Proceedings*, pp. 34–40, 2016, doi: 10.1109/EDPC.2016.7851311.

[79] N. Urban, F. Huber, and J. Franke, “Influences of process parameters on rare earth magnets produced by laser beam melting,” *2017 7th International Electric Drives Production Conference, EDPC 2017 - Proceedings*, vol. 2017-Decem, pp. 1–5, 2018, doi: 10.1109/EDPC.2017.8328149.

[80] D. Goll *et al.*, “Refining the Microstructure of Fe-Nd-B by Selective Laser Melting,” *Physica Status Solidi - Rapid Research Letters*, vol. 13, no. 3, pp. 1–5, 2019, doi: 10.1002/pssr.201800536.

[81] M. Skalon *et al.*, “Influence of Melt-Pool Stability in 3D Printing of NdFeB Magnets on Density and Magnetic Properties,” *Materials*, vol. 13, no. 1, p. 139, 2019, doi: 10.3390/ma13010139.

[82] D. Goll, F. Trauter, T. Bernthaler, J. Schanz, H. Riegel, and G. Schneider, “Additive manufacturing of bulk nanocrystalline fendb based permanent magnets,” *Micromachines (Basel)*, vol. 12, no. 5, 2021, doi: 10.3390/mi12050538.

[83] J. Wu, N. T. Aboulkhair, M. Degano, I. Ashcroft, and R. J. M. Hague, "Process-structure-property relationships in laser powder bed fusion of permanent magnetic Nd-Fe-B," *Mater Des*, vol. 209, p. 109992, 2021, doi: 10.1016/j.matdes.2021.109992.

[84] N. Urban, A. Meyer, S. Kreitlein, F. Leicht, and J. Franke, "Efficient near Net-Shape Production of High Energy Rare Earth Magnets by Laser Beam Melting," *Applied Mechanics and Materials*, vol. 871, pp. 137–144, 2017, doi: 10.4028/www.scientific.net/amm.871.137.

[85] F. Bittner, J. Thielsch, and W. G. Drossel, "Laser powder bed fusion of Nd–Fe–B permanent magnets," *Progress in Additive Manufacturing*, vol. 5, no. 1, pp. 3–9, 2020, doi: 10.1007/s40964-020-00117-7.

[86] F. Vial, F. Joly, E. Nevalainen, M. Sagawa, K. Hiraga, and K. T. Park, "Improvement of coercivity of sintered NdFeB permanent magnets by heat treatment," *J Magn Magn Mater*, vol. 242–245, pp. 1329–1334, 2002, doi: 10.1016/S0304-8853(01)00967-2.

[87] Y. Zhang *et al.*, "Post-sinter annealing influences on coercivity of multi-main-phase Nd-Ce-Fe-B magnets," *Acta Mater*, vol. 146, pp. 97–105, 2018, doi: 10.1016/j.actamat.2017.12.027.

[88] N. Emminghaus, C. Hoff, J. Hermsdorf, and S. Kaierle, "Laser Powder Bed Fusion of NdFeB and influence of heat treatment on microstructure and crack development," *Procedia CIRP*, vol. 94, pp. 211–216, 2020, doi: 10.1016/j.procir.2020.09.040.

[89] H. R. Cha, K. W. Jeon, J. H. Yu, H. W. Kwon, Y. Do Kim, and J. G. Lee, "Coercivity enhancement of hot-deformed Nd-Fe-B magnet by grain boundary diffusion process using the reaction of NdHxand Cu nanopowders," *J Alloys Compd*, vol. 693, pp. 744–748, 2017, doi: 10.1016/j.jallcom.2016.09.167.

[90] M. Tang *et al.*, "Microstructure modification and coercivity enhancement of Nd-Ce-Fe-B sintered magnets by grain boundary diffusing Nd-Dy-Al alloy," *J Magn Magn Mater*, vol. 442, pp. 338–342, 2017, doi: 10.1016/j.jmmm.2017.06.116.

[91] S. Guo, X. Zhang, G. Ding, R. Chen, D. Lee, and A. Yan, "Coercivity enhancement of sintered Nd-Fe-B magnets by chemical bath deposition of TbCl3," *J Appl Phys*, vol. 115, no. 17, pp. 23–26, 2014, doi: 10.1063/1.4867962.

[92] W. F. Li, T. Ohkubo, K. Hono, and M. Sagawa, "The origin of coercivity decrease in fine grained Nd-Fe-B sintered magnets," *J Magn Magn Mater*, vol. 321, no. 8, pp. 1100–1105, 2009, doi: 10.1016/j.jmmm.2008.10.032.

[93] H. W. Chang, Y. I. Lee, P. H. Liao, and W. C. Chang, "Significant coercivity enhancement of hot deformed NdFeB magnets by doping Ce-containing (PrNdCe)70Cu30 alloys

powders," *Scr Mater*, vol. 146, pp. 222–225, 2018, doi: 10.1016/j.scriptamat.2017.11.052.

[94] X. Zheng *et al.*, "Coercivity enhancement by inhibiting the formation of coarse grains region in hot-deformed Nd-Fe-B magnets with WC nano-particles addition," *Scr Mater*, vol. 132, pp. 49–52, 2017, doi: 10.1016/j.scriptamat.2017.01.024.

[95] X. Zhang *et al.*, "Improvement of the thermal stability of sintered Nd-Fe-B magnets by intergranular addition of Dy82.3Co17.7," *J Appl Phys*, vol. 115, no. 17, pp. 3–6, 2014, doi: 10.1063/1.4868491.

[96] F. Bittner, J. Thielsch, and W. G. Drossel, "Microstructure and magnetic properties of Nd-Fe-B permanent magnets produced by laser powder bed fusion," *Scr Mater*, vol. 201, p. 113921, 2021, doi: 10.1016/j.scriptamat.2021.113921.

[97] S. Godavarthi, J. Porcayo-Calderon, E. Vazquez-Velez, M. Casales-Diaz, D. M. Ortega-Toledo, and L. Martinez-Gomez, "Influence of the chemical composition in the electrochemical response of permanent magnets," *Journal of Spectroscopy*, vol. 2015, 2015, doi: 10.1155/2015/356027.

[98] X. Y. Fang, D. Q. Yi, J. F. Nie, X. J. Zhang, B. Wang, and L. R. Xiao, "Effect of Zr, Mn and Sc additions on the grain size of Mg-Gd alloy," *J Alloys Compd*, vol. 470, no. 1–2, pp. 311–316, 2009, doi: 10.1016/j.jallcom.2008.02.069.

[99] H. W. Chang, C. H. Chiu, C. W. Chang, W. C. Chang, A. C. Sun, and Y. D. Yao, "Effect of Ti substitution on the magnetic properties, microstructure, and aftereffect of melt spun PrFeB nanocomposites," *Scr Mater*, vol. 55, no. 6, pp. 529–532, 2006, doi: 10.1016/j.scriptamat.2006.05.032.

[100] T. H. Coil, "Helmholtz coils Helmholtz coils," no. 5.

[101] LakeShore, "Measuring Permanent Magnet Characteristics with a Fluxmeter and Helmholtz Coil," no. 614, 2010, [Online]. Available: www.lakeshore.com

[102] T. Eb, "Chapter 4 Magnetic properties of the layer systems measured by SQUID magnetometry," *Measurement*, pp. 27–40.

[103] H. Gong, K. Rafi, H. Gu, T. Starr, and B. Stucker, "Analysis of defect generation in Ti-6Al-4V parts made using powder bed fusion additive manufacturing processes," *Addit Manuf*, vol. 1, pp. 87–98, 2014, doi: 10.1016/j.addma.2014.08.002.

[104] C. Chen, S. Chang, J. Zhu, Z. Xiao, H. Zhu, and X. Zeng, "Residual stress of typical parts in laser powder bed fusion," *J Manuf Process*, vol. 59, no. October, pp. 621–628, 2020, doi: 10.1016/j.jmapro.2020.10.009.

[105] E. Toyserkani *et al.*, "Experimental and numerical investigation on the effect of layer thickness during laser powder-bed fusion of stainless steel 17-4PH," *International Journal of Rapid Manufacturing*, vol. 9, no. 2/3, p. 1, 2020, doi: 10.1504/ijrapidm.2020.10029113.

[106] X. Shi, C. Yan, W. Feng, Y. Zhang, and Z. Leng, "Effect of high layer thickness on surface quality and defect behavior of Ti-6Al-4V fabricated by selective laser melting," *Opt Laser Technol*, vol. 132, no. June, p. 106471, 2020, doi: 10.1016/j.optlastec.2020.106471.

[107] "White-paper1-EN".

[108] N. T. Oster, "Generation and characterization of anisotropic microstructures in rare earth-iron-boron alloys," p. 134, 2012.

[109] N. Sridharan *et al.*, "Rationalization of solidification mechanism of Nd–Fe–B magnets during laser directed-energy deposition," *J Mater Sci*, vol. 53, no. 11, pp. 8619–8626, 2018, doi: 10.1007/s10853-018-2178-7.

[110] R. Li, Y. Shi, Z. Wang, L. Wang, J. Liu, and W. Jiang, "Densification behavior of gas and water atomized 316L stainless steel powder during selective laser melting," *Appl Surf Sci*, vol. 256, no. 13, pp. 4350–4356, 2010, doi: 10.1016/j.apsusc.2010.02.030.

[111] S. Waqar, K. Guo, and J. Sun, "Evolution of residual stress behavior in selective laser melting (SLM) of 316L stainless steel through preheating and in-situ re-scanning techniques," *Opt Laser Technol*, vol. 149, no. June 2021, p. 107806, 2022, doi: 10.1016/j.optlastec.2021.107806.

[112] M. M. Savalani and J. M. Pizarro, "Effect of preheat and layer thickness on selective laser melting (SLM) of magnesium," *Rapid Prototyp J*, vol. 22, no. 1, pp. 115–122, 2016, doi: 10.1108/RPJ-07-2013-0076.

[113] A. Mazilkin *et al.*, "Grain boundary oxide layers in NdFeB-based permanent magnets," *Mater Des*, vol. 199, p. 109417, 2021, doi: 10.1016/j.matdes.2020.109417.

[114] T. de Terris *et al.*, "Optimization and comparison of porosity rate measurement methods of Selective Laser Melted metallic parts," *Addit Manuf*, vol. 28, no. May, pp. 802–813, 2019, doi: 10.1016/j.addma.2019.05.035.

[115] M. Heydarzadeh Sohi, M. Ebrahimi, A. Honarbakhsh Raouf, and F. Mahboubi, "Comparative study of the corrosion behaviour of plasma nitrocarburised AISI4140 steel before and after post-oxidation," *Mater Des*, vol. 31, no. 9, pp. 4432–4437, 2010, doi: 10.1016/j.matdes.2010.04.017.

[116] C. Huber *et al.*, “Coercivity enhancement of selective laser sintered NdFeB magnets by grain boundary infiltration,” *Acta Mater*, vol. 172, pp. 66–71, 2019, doi: 10.1016/j.actamat.2019.04.037.

[117] A. S. Volegov *et al.*, “Additive manufacturing of heavy rare earth free high-coercivity permanent magnets,” *Acta Mater*, vol. 188, pp. 733–739, 2020, doi: 10.1016/j.actamat.2020.02.058.

[118] K. Essa, P. Jamshidi, J. Zou, M. M. Attallah, and H. Hassanin, “Porosity control in 316L stainless steel using cold and hot isostatic pressing,” *Mater Des*, vol. 138, pp. 21–29, 2018, doi: 10.1016/j.matdes.2017.10.025.

[119] H. V. Atkinson and S. Davies, “Fundamental aspects of hot isostatic pressing: An overview,” *Metall Mater Trans A Phys Metall Mater Sci*, vol. 31, no. 12, pp. 2981–3000, 2000, doi: 10.1007/s11661-000-0078-2.

[120] F. Yang *et al.*, “Performance of Nd-Fe-B Magnets Fabricated by Hot Isostatic Pressing and Low-Temperature Sintering,” *J Mater Eng Perform*, vol. 28, no. 1, pp. 273–277, 2019, doi: 10.1007/s11665-018-3832-6.

[121] Z. Q. Liao, F. Xu, W. J. Yan, Q. J. Huang, G. Chen, and S. D. Li, “Influence of cladless hot isostatic pressing on magnetic properties and corrosion resistance of sintered NdFeB magnets,” *Key Eng Mater*, vol. 538, pp. 211–214, 2013, doi: 10.4028/www.scientific.net/KEM.538.211.

[122] J. Liu *et al.*, “Grain size dependence of coercivity of hot-deformed Nd-Fe-B anisotropic magnets,” *Acta Mater*, vol. 82, pp. 336–343, 2015, doi: 10.1016/j.actamat.2014.09.021.

APPENDICES

Appendix 1 The relationship between some magnetic properties in Gaussian and S.I system G= Gauss, Oe= Oersted ,T= Tesla [2].

Quantitiy	**Gaussian-cgs**	**S.I Units - mks**	**Conversion factor, cgs to mks**
Magnetic Induction (B)	G	T	10^{-4}
Applied Field (H)	Oe	A m^{-1}	$10^3/4\pi$
Magnetisation (M)	Emu/cm^3	A m^{-1}	10^3
Magnetisation (4π m)	G	--	10^3
Magnetic Polarisation (J)	--	T	--
Permeability (μ)	Dimensionless	H m^{-1}	$4\pi\ 10^{-7}$
Susceptibility (χ)	Emu cm^{-3} Oe^{-1}	Dimensionless	4π

Appendix 2 EDX Results of the heat-treated samples at 480°C,580°C,680°C and 880°C

- **EDX point analyses of the annealed sample at 480°C**

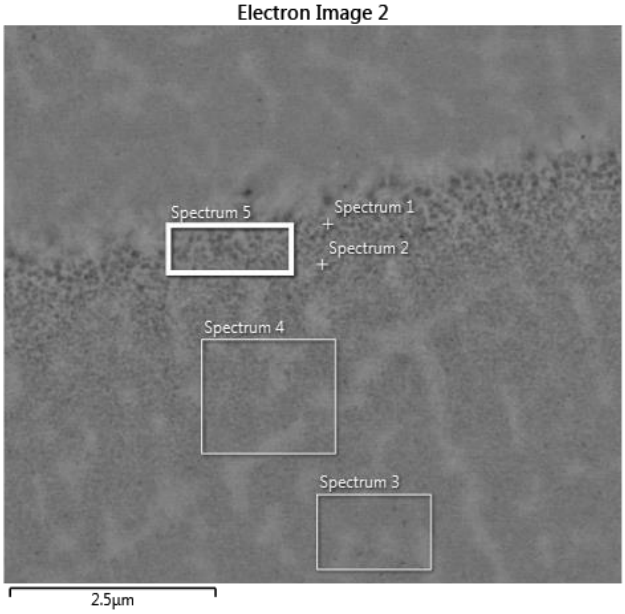

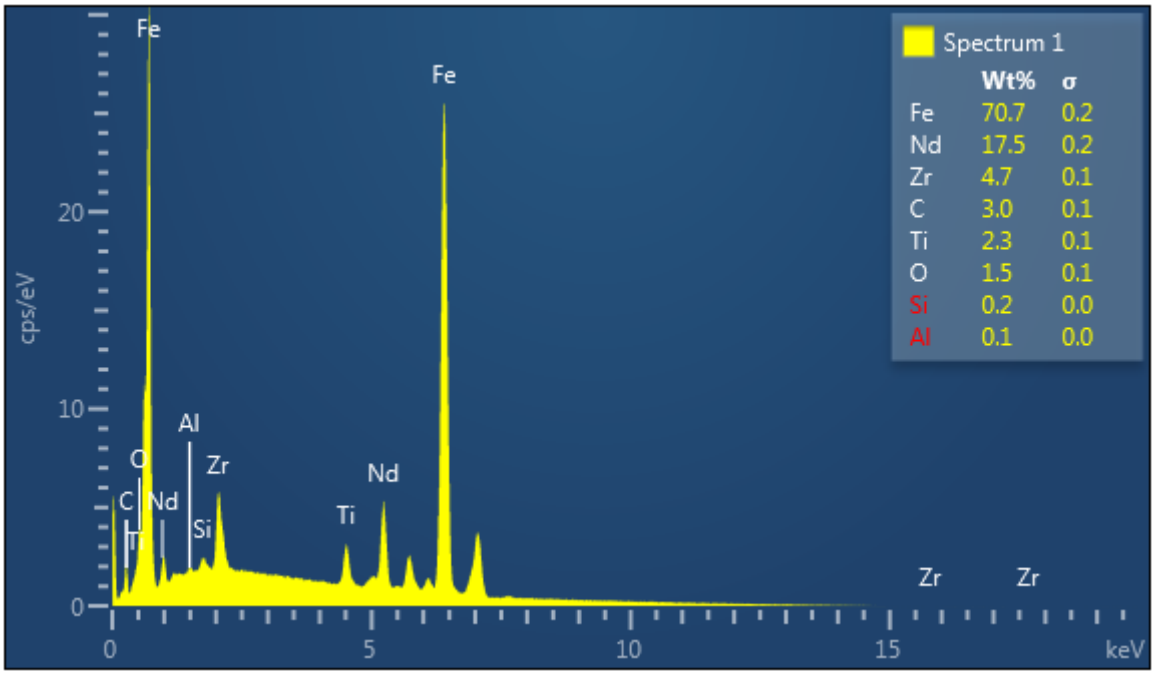

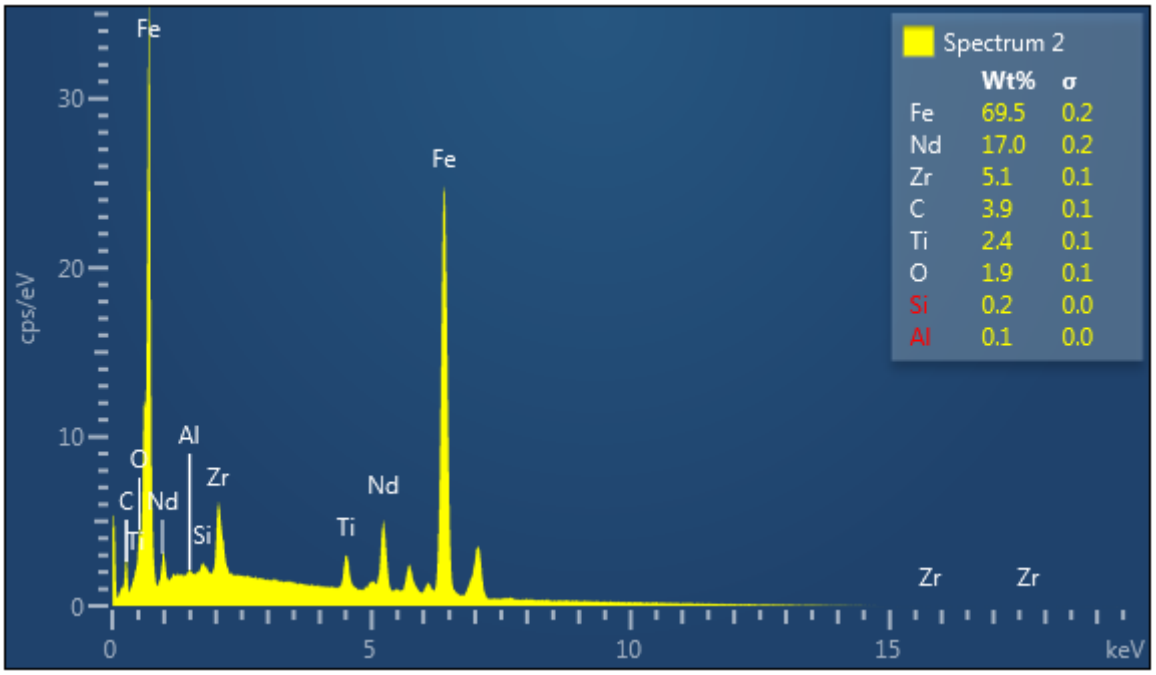
Spectrum 2
Wt% σ
Fe 69.5 0.2
Nd 17.0 0.2
Zr 5.1 0.1
C 3.9 0.1
Ti 2.4 0.1
O 1.9 0.1
Si 0.2 0.0
Al 0.1 0.0
cps/eV
keV
Fe
Al
O
C
Nd
Zr
Si
Ti
Zr
Zr

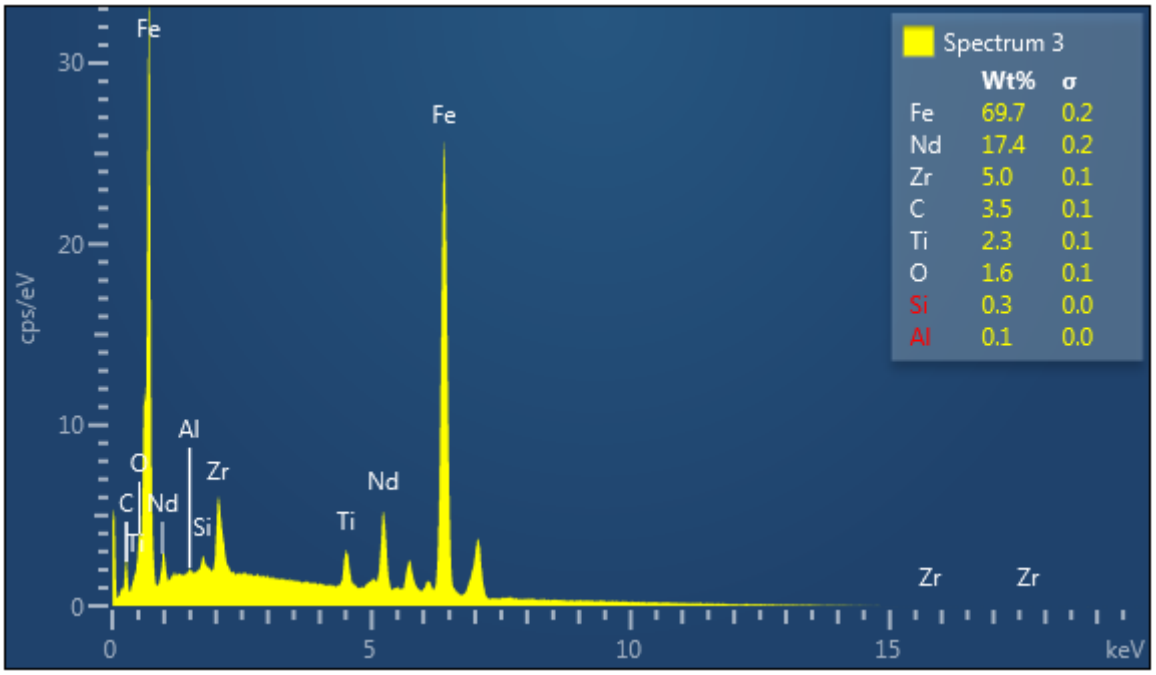
Spectrum 3
Wt% σ
Fe 69.7 0.2
Nd 17.4 0.2
Zr 5.0 0.1
C 3.5 0.1
Ti 2.3 0.1
O 1.6 0.1
Si 0.3 0.0
Al 0.1 0.0
cps/eV
keV
Fe
Al
O
C
Nd
Zr
Si
Ti
Zr
Zr

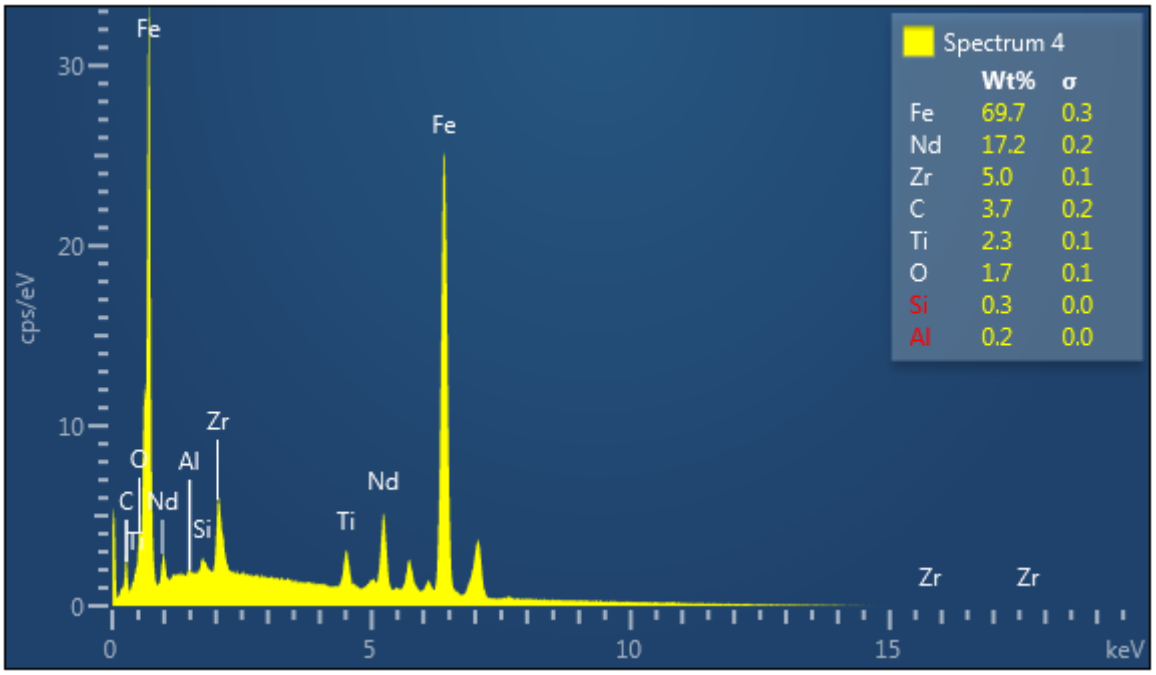
Spectrum 4
Wt% σ
Fe 69.7 0.3
Nd 17.2 0.2
Zr 5.0 0.1
C 3.7 0.2
Ti 2.3 0.1
O 1.7 0.1
Si 0.3 0.0
Al 0.2 0.0
cps/eV
keV
Fe
Zr
O
Al
C
Nd
Si
Ti

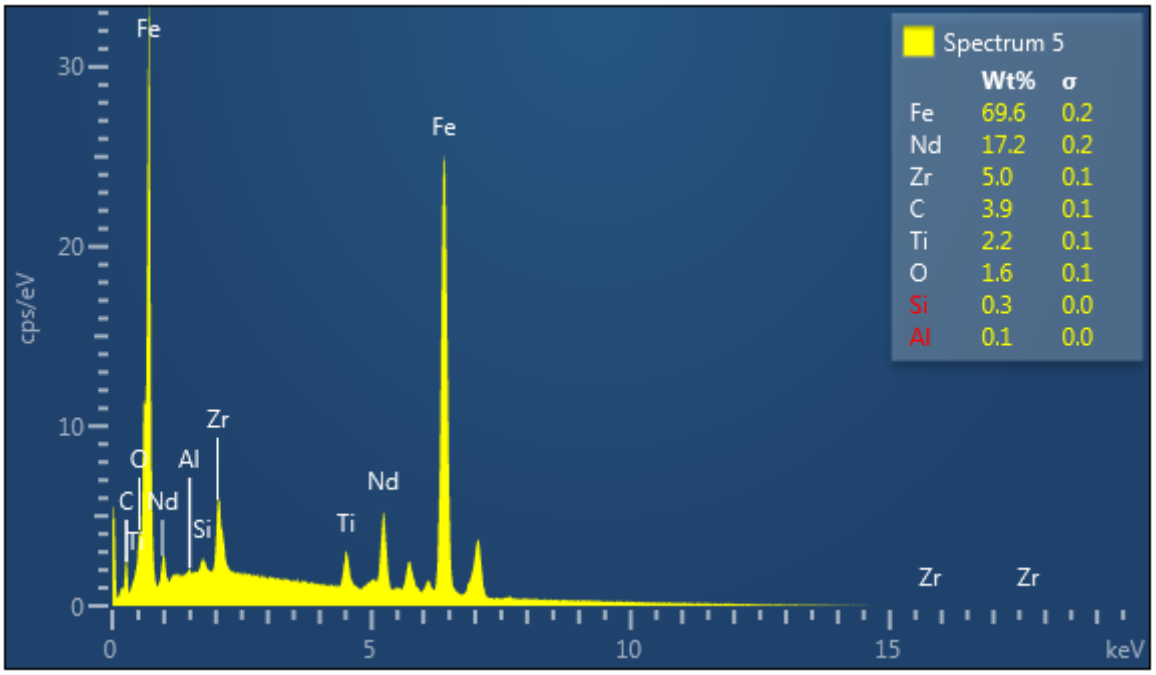
Spectrum 5
Wt% σ
Fe 69.6 0.2
Nd 17.2 0.2
Zr 5.0 0.1
C 3.9 0.1
Ti 2.2 0.1
O 1.6 0.1
Si 0.3 0.0
Al 0.1 0.0
cps/eV
keV
Fe
Zr
O
Al
C
Nd
Si
Ti

- **EDX box analysis of annealed sample at 580°C**

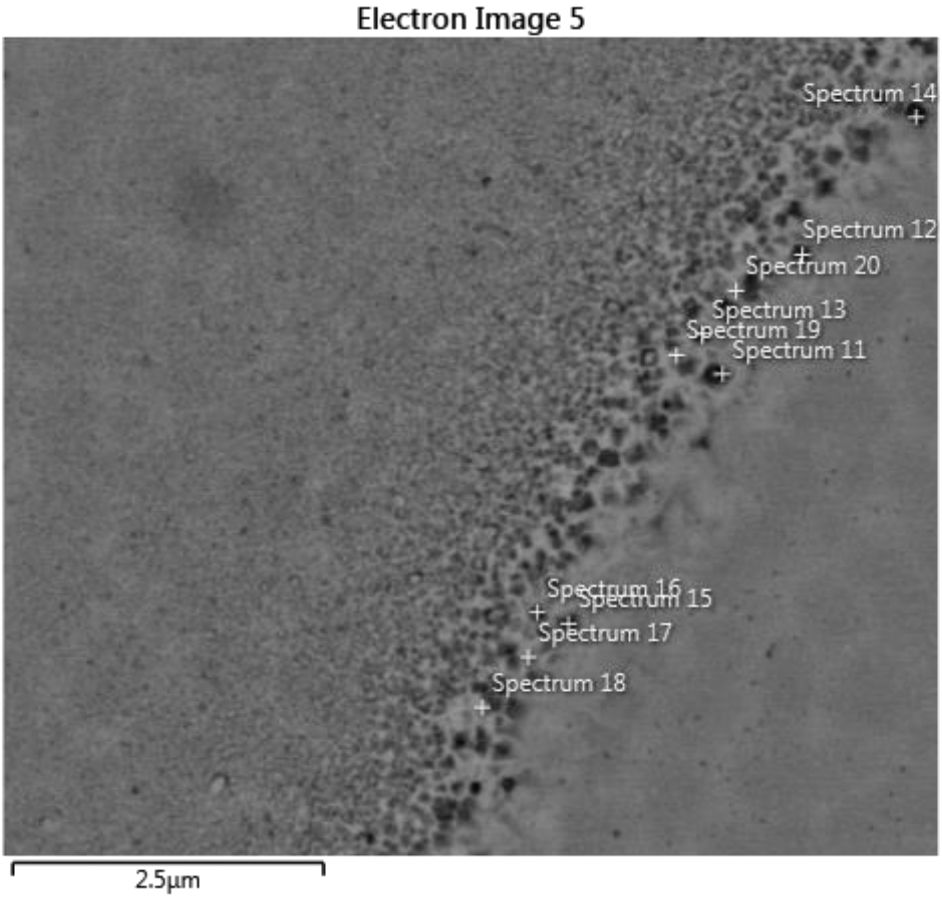

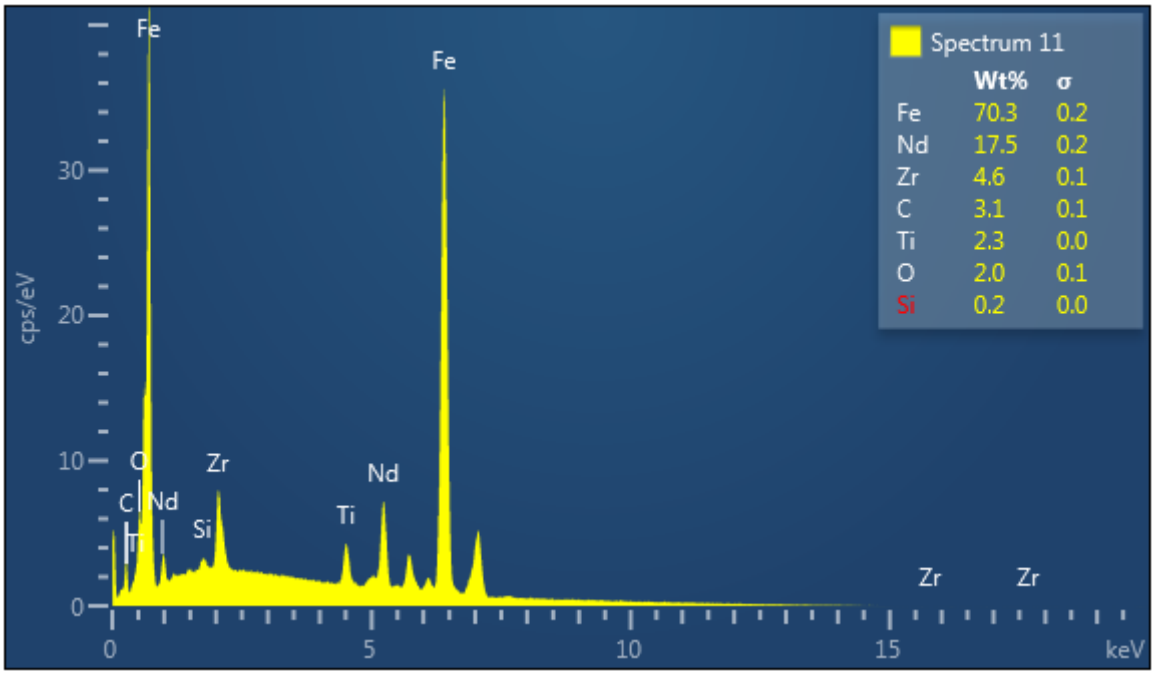

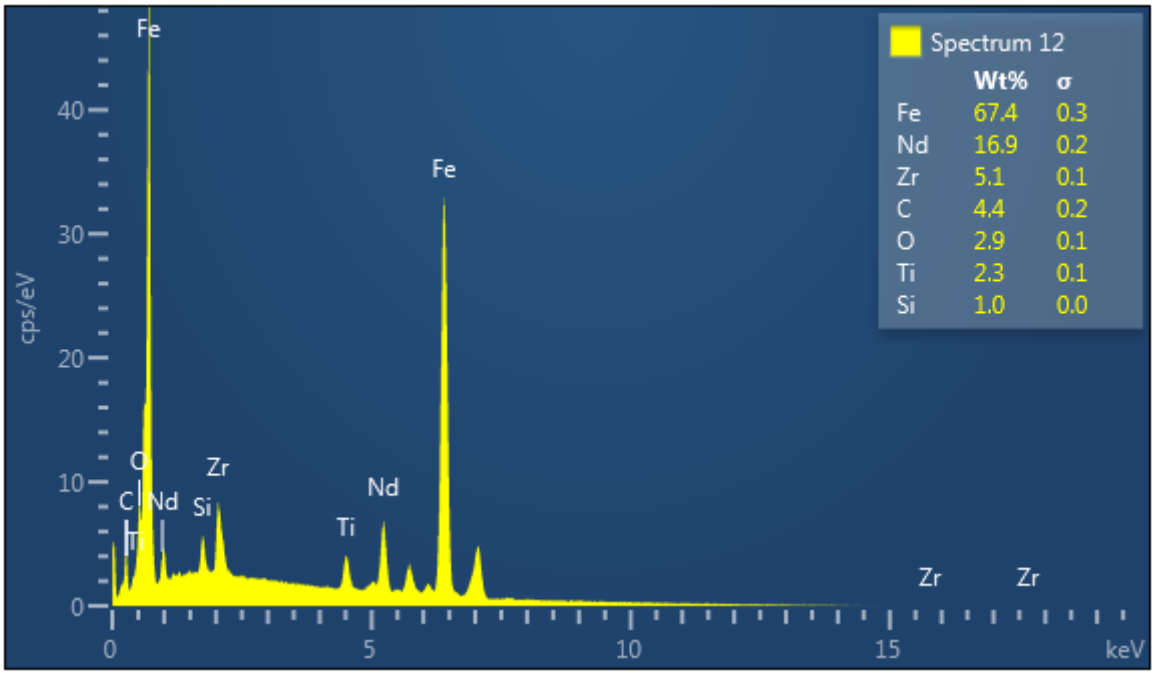
Spectrum 12
Wt% σ
Fe 67.4 0.3
Nd 16.9 0.2
Zr 5.1 0.1
C 4.4 0.2
O 2.9 0.1
Ti 2.3 0.1
Si 1.0 0.0
cps/eV
keV
Fe
O
C
Nd
Zr
Si
Ti
Nd
Fe
Zr
Zr

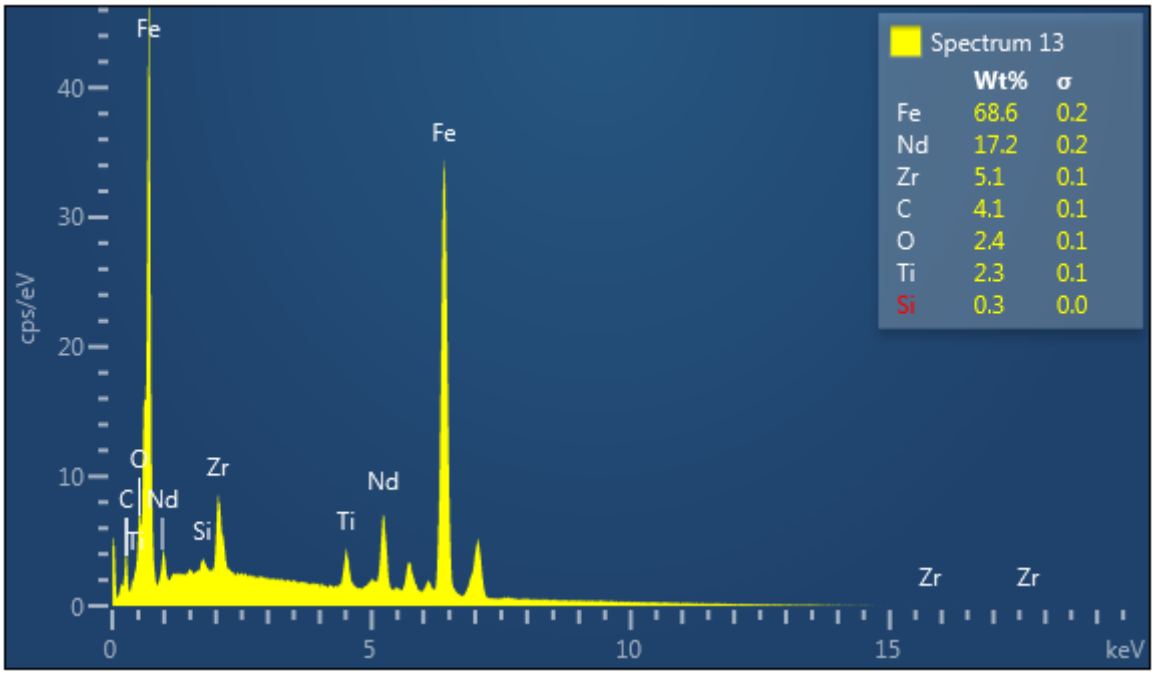
Spectrum 13
Wt% σ
Fe 68.6 0.2
Nd 17.2 0.2
Zr 5.1 0.1
C 4.1 0.1
O 2.4 0.1
Ti 2.3 0.1
Si 0.3 0.0
cps/eV
keV
Fe
O
C
Nd
Zr
Si
Ti
Nd
Fe
Zr
Zr

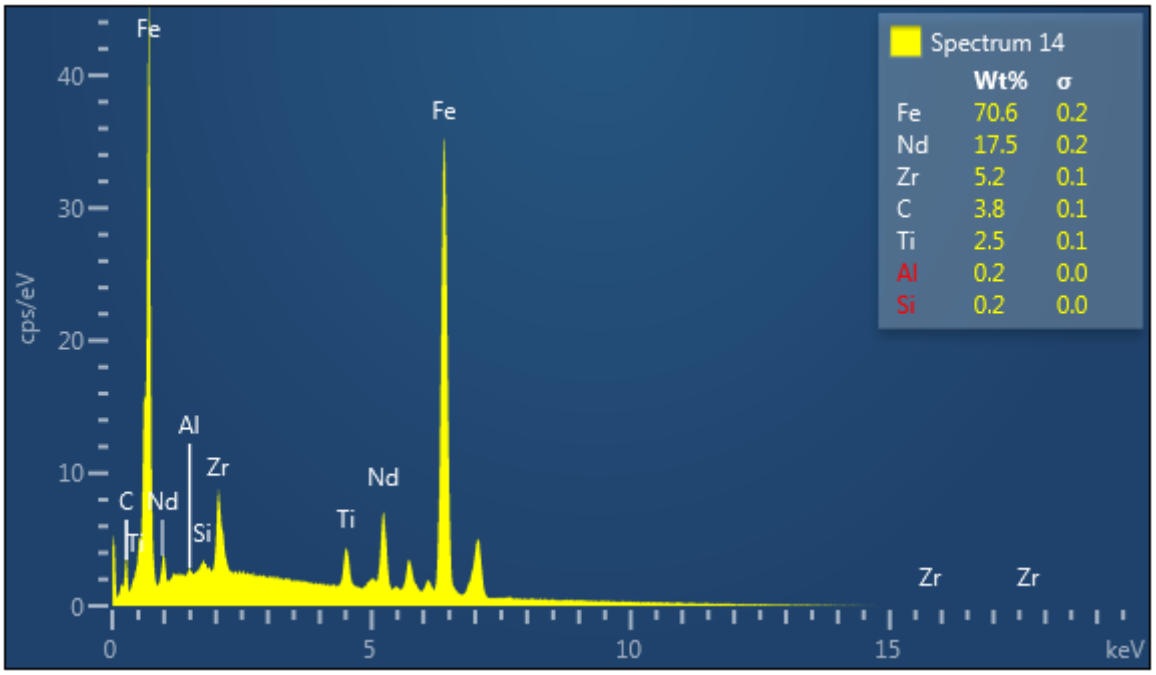
Spectrum 14
Wt% σ
Fe 70.6 0.2
Nd 17.5 0.2
Zr 5.2 0.1
C 3.8 0.1
Ti 2.5 0.1
Al 0.2 0.0
Si 0.2 0.0
cps/eV
keV
Fe
Al
Zr
C
Nd
Ti
Si

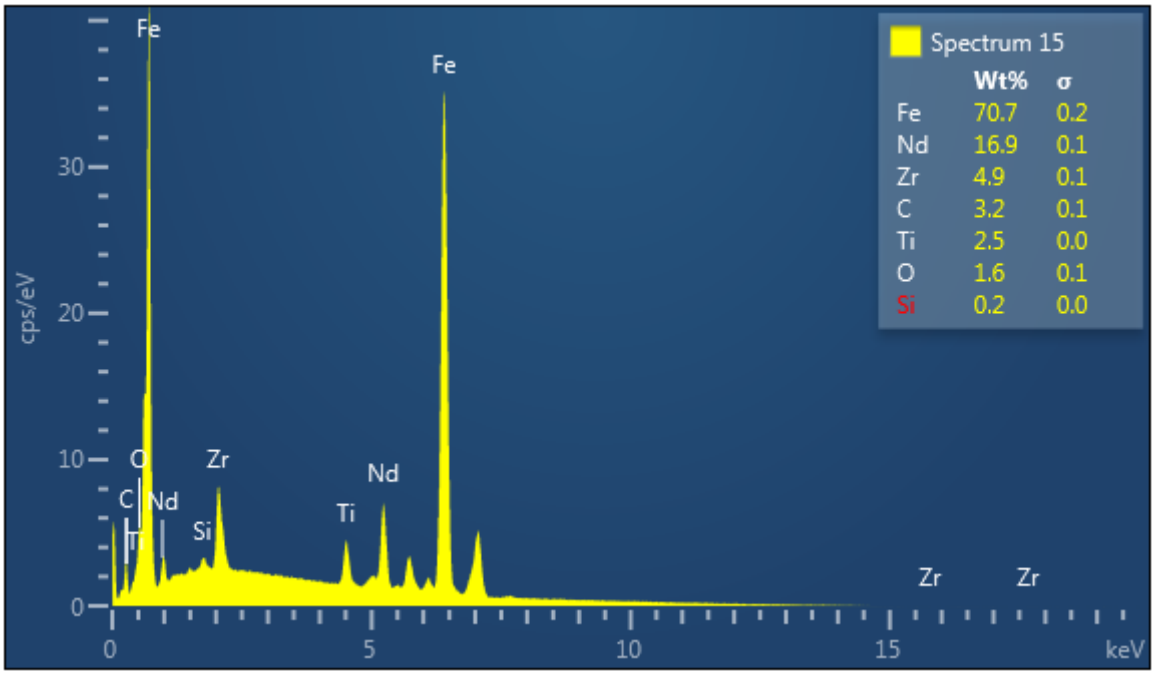
Spectrum 15
Wt% σ
Fe 70.7 0.2
Nd 16.9 0.1
Zr 4.9 0.1
C 3.2 0.1
Ti 2.5 0.0
O 1.6 0.1
Si 0.2 0.0
cps/eV
keV
Fe
O
Zr
C
Nd
Ti
Si

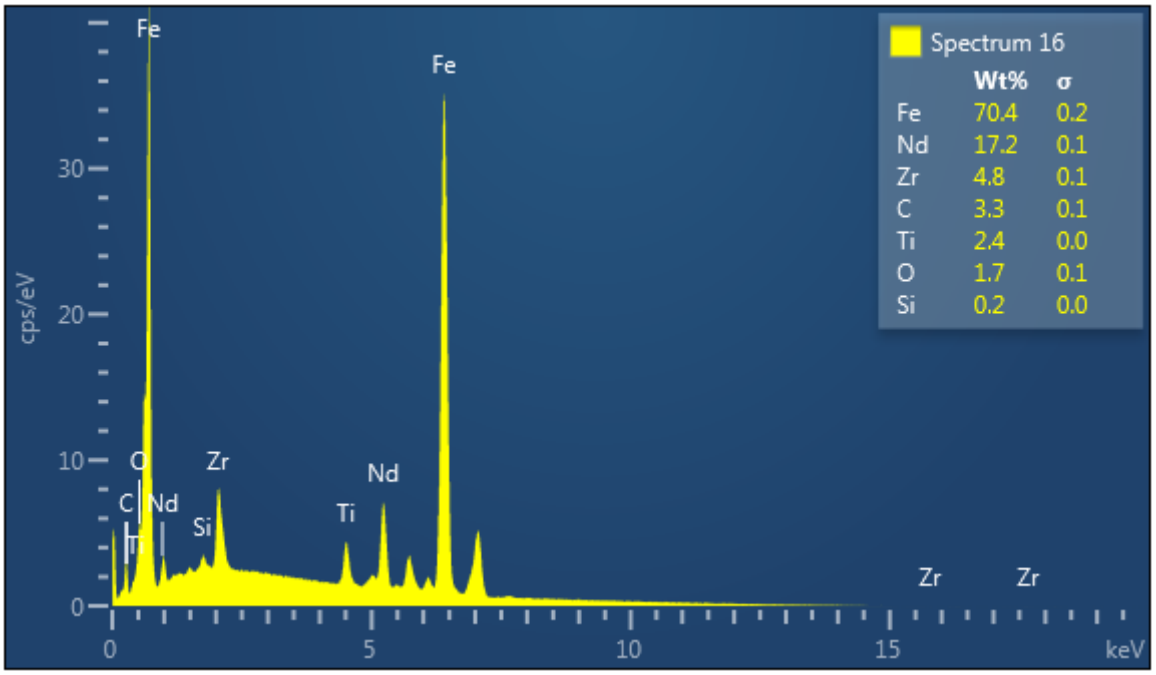
Spectrum 16
Wt% σ
Fe 70.4 0.2
Nd 17.2 0.1
Zr 4.8 0.1
C 3.3 0.1
Ti 2.4 0.0
O 1.7 0.1
Si 0.2 0.0
Fe
Fe
O
C
Nd
Ti
Zr
Si
Ti
Nd
Zr
Zr
cps/eV
keV
0
5
10
15
20
30

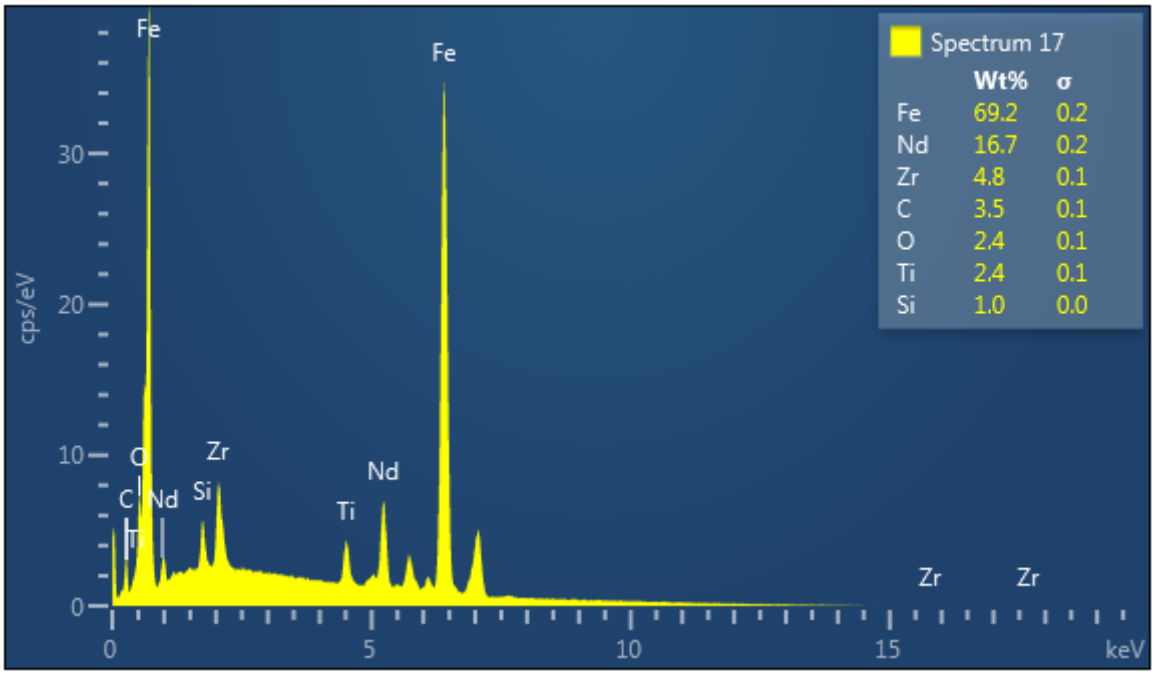
Spectrum 17
Wt% σ
Fe 69.2 0.2
Nd 16.7 0.2
Zr 4.8 0.1
C 3.5 0.1
O 2.4 0.1
Ti 2.4 0.1
Si 1.0 0.0
Fe
Fe
O
C
Nd
Ti
Zr
Si
Ti
Nd
Zr
Zr
cps/eV
keV
0
5
10
15
20
30

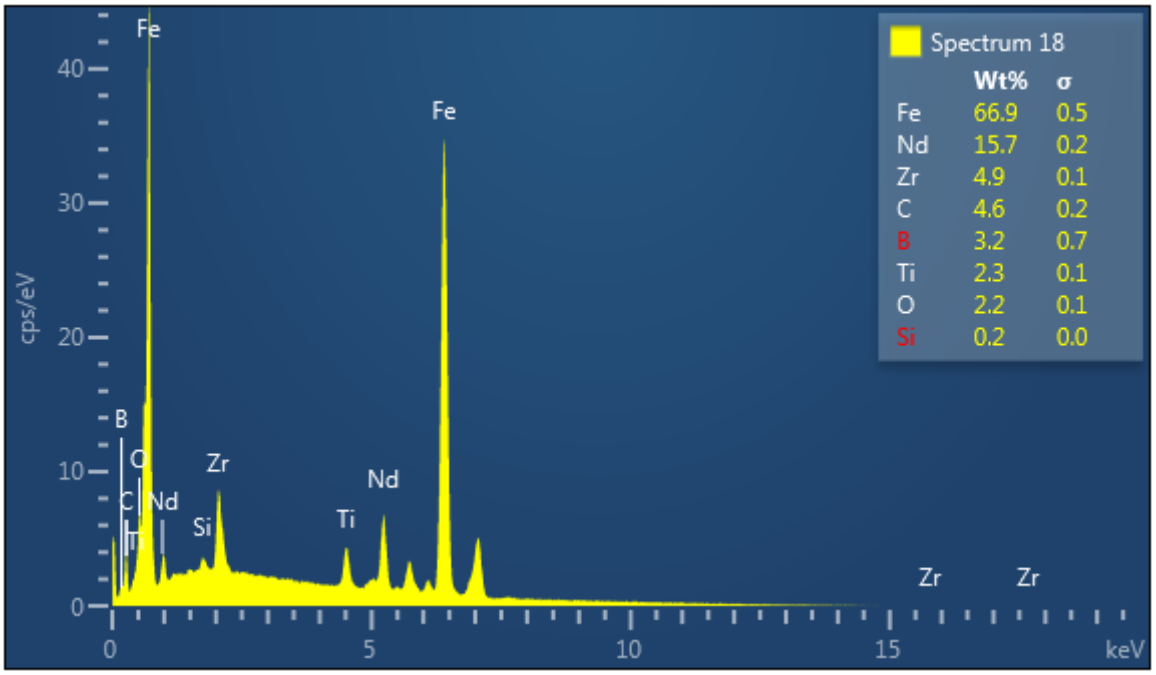
Spectrum 18
Wt% σ
Fe 66.9 0.5
Nd 15.7 0.2
Zr 4.9 0.1
C 4.6 0.2
B 3.2 0.7
Ti 2.3 0.1
O 2.2 0.1
Si 0.2 0.0
cps/eV
keV
Fe
B
O
C
Nd
Ti
Zr
Si
Ti
Nd
Fe
Zr
Zr

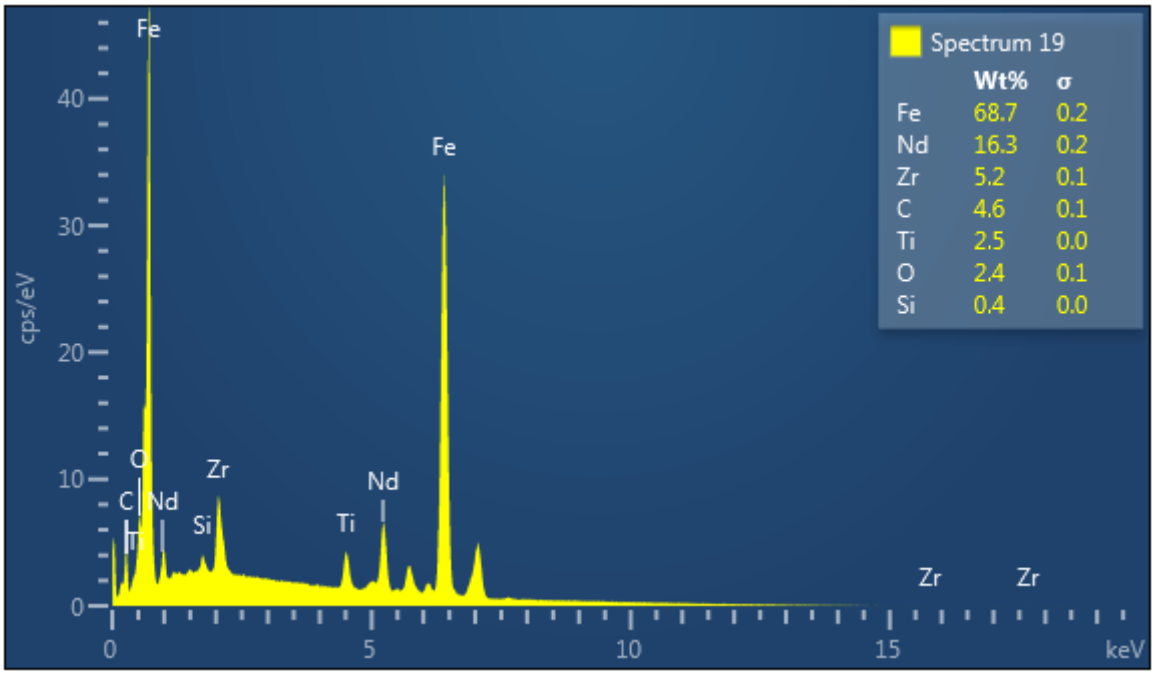
Spectrum 19
Wt% σ
Fe 68.7 0.2
Nd 16.3 0.2
Zr 5.2 0.1
C 4.6 0.1
Ti 2.5 0.0
O 2.4 0.1
Si 0.4 0.0
cps/eV
keV
Fe
O
C
Nd
Ti
Zr
Si
Ti
Nd
Fe
Zr
Zr

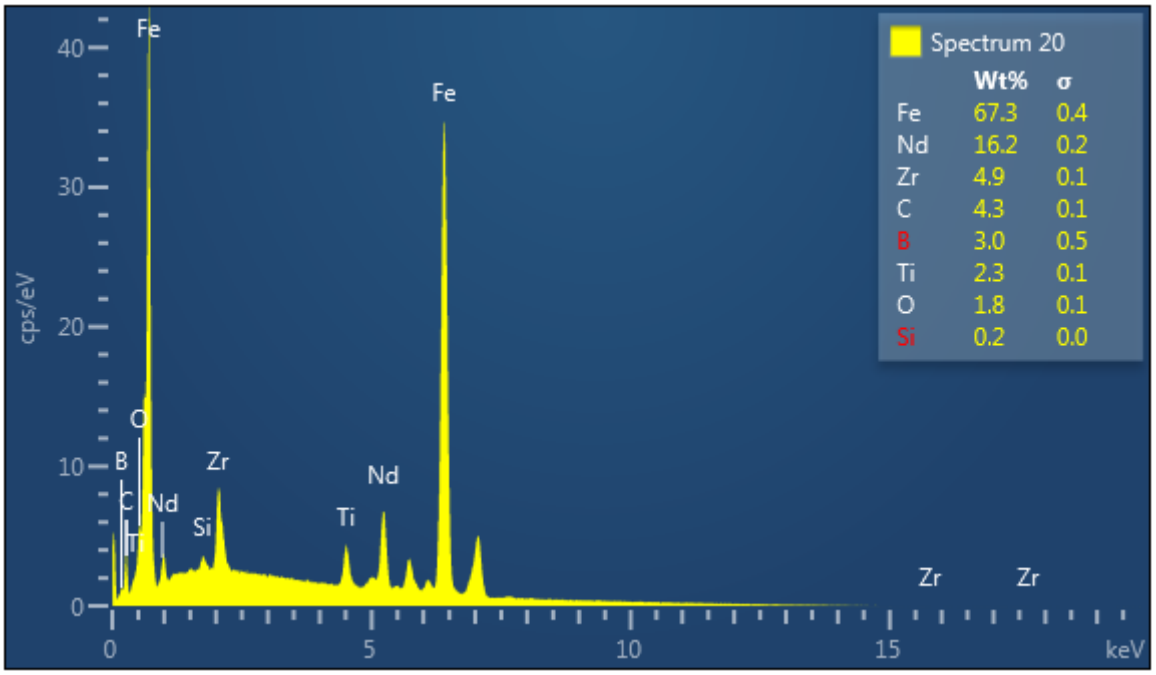

- **EDX box analyses of the annealed sample at 680°C**

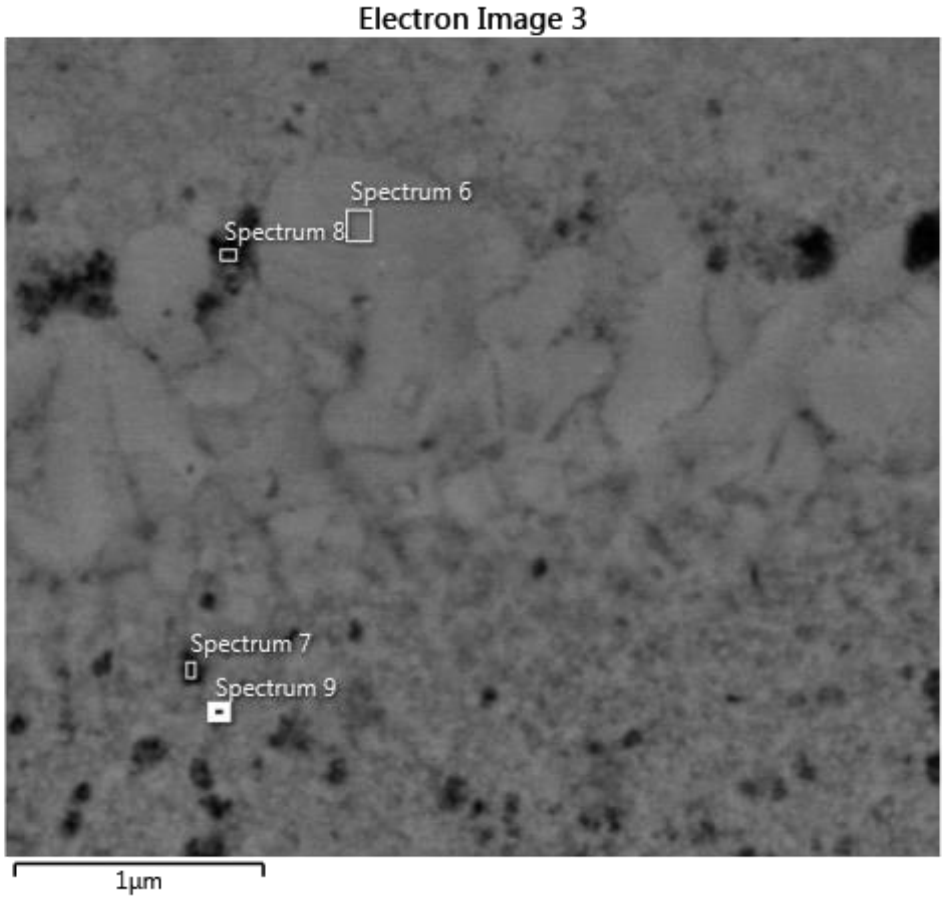

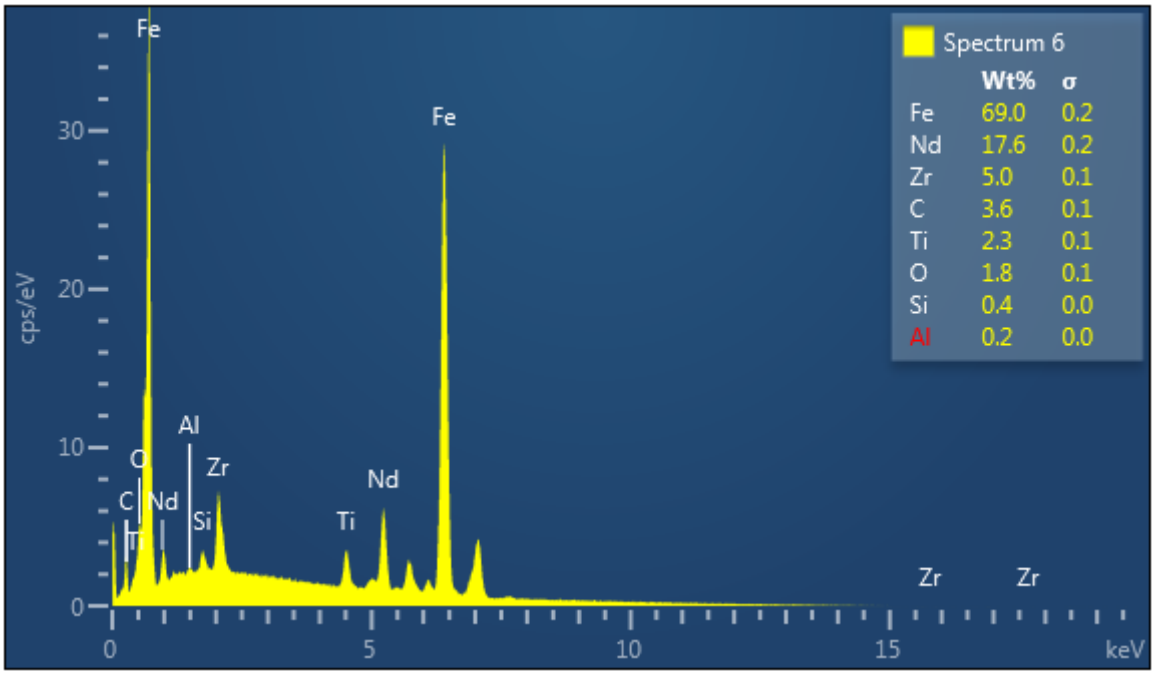
Spectrum 6
Wt% σ
Fe 69.0 0.2
Nd 17.6 0.2
Zr 5.0 0.1
C 3.6 0.1
Ti 2.3 0.1
O 1.8 0.1
Si 0.4 0.0
Al 0.2 0.0
cps/eV
keV
Fe
Al
O
Zr
C
Nd
Si
Ti
Zr
Zr

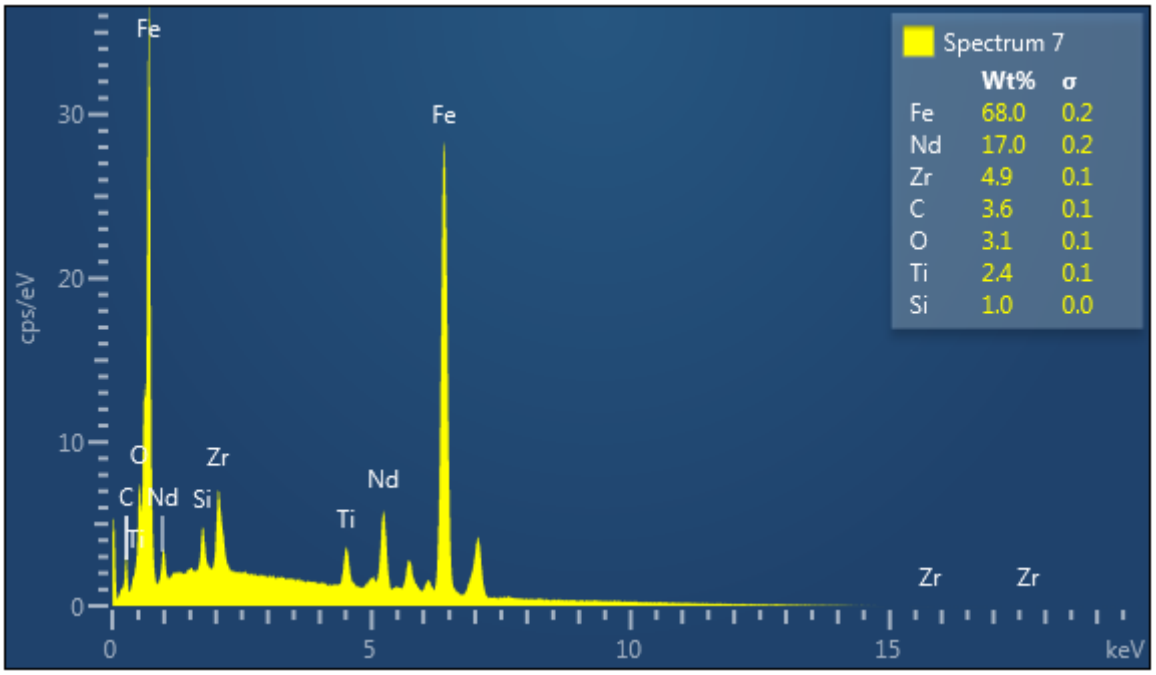
Spectrum 7
Wt% σ
Fe 68.0 0.2
Nd 17.0 0.2
Zr 4.9 0.1
C 3.6 0.1
O 3.1 0.1
Ti 2.4 0.1
Si 1.0 0.0
cps/eV
keV
Fe
O
Zr
C
Nd
Si
Ti
Zr
Zr

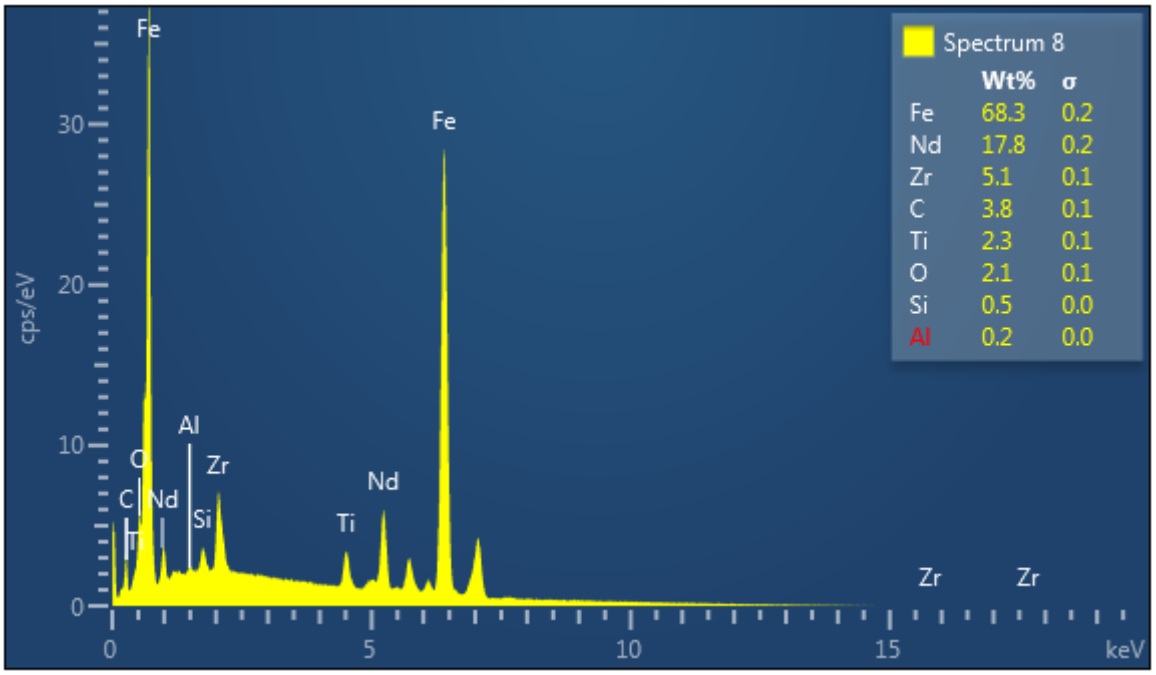
Spectrum 8
Wt% σ
Fe 68.3 0.2
Nd 17.8 0.2
Zr 5.1 0.1
C 3.8 0.1
Ti 2.3 0.1
O 2.1 0.1
Si 0.5 0.0
Al 0.2 0.0
cps/eV
keV
Fe
Al
O
C
Nd
Zr
Si
Ti
Zr
Zr

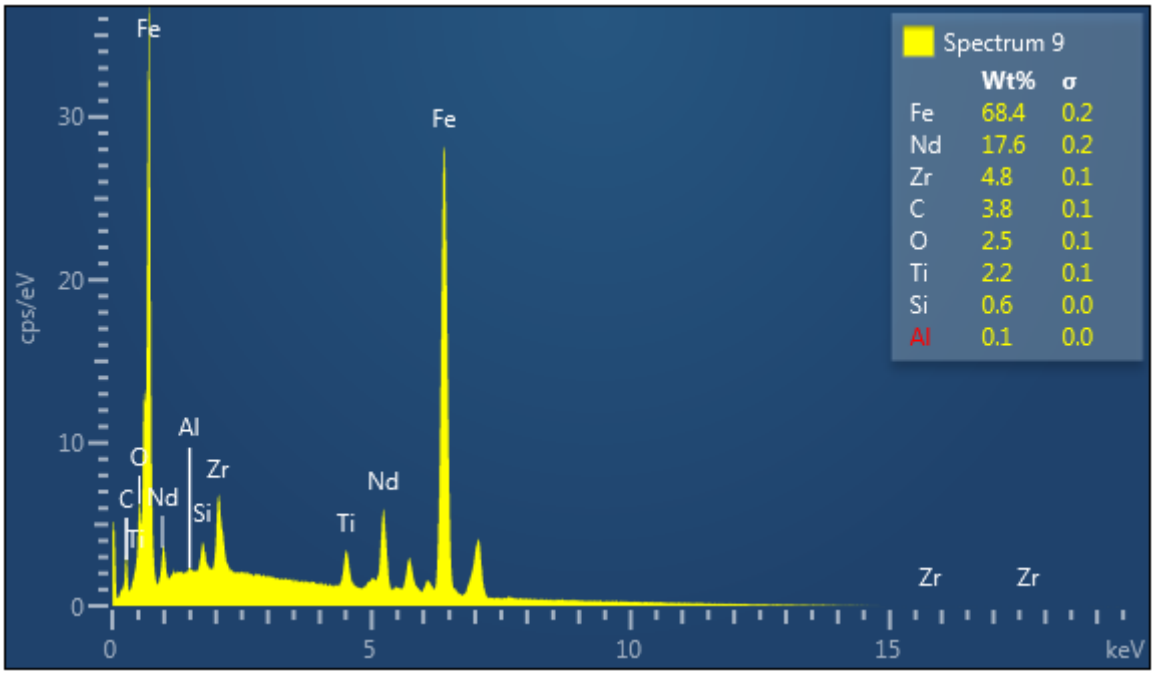
Spectrum 9
Wt% σ
Fe 68.4 0.2
Nd 17.6 0.2
Zr 4.8 0.1
C 3.8 0.1
O 2.5 0.1
Ti 2.2 0.1
Si 0.6 0.0
Al 0.1 0.0
cps/eV
keV
Fe
Al
O
C
Nd
Zr
Si
Ti
Zr
Zr

- **EDX box analyses of the sample annealed sample at 880°C**

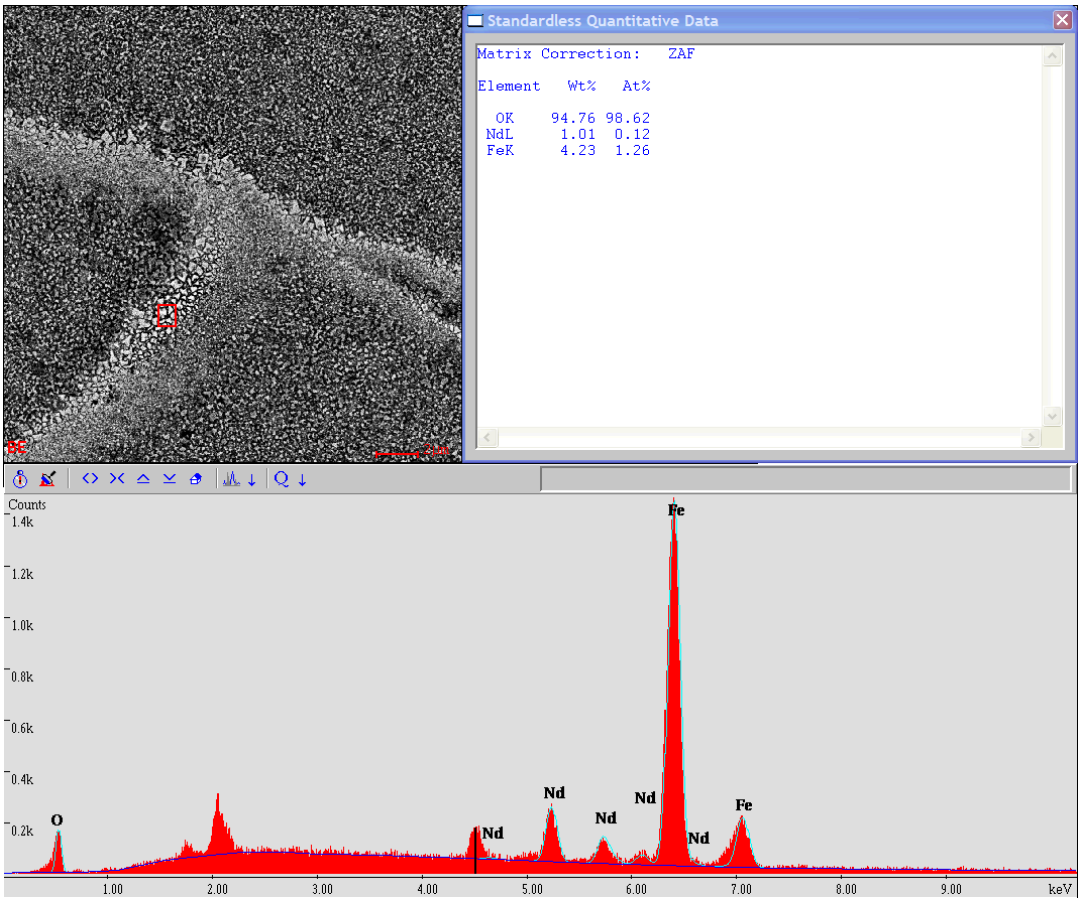

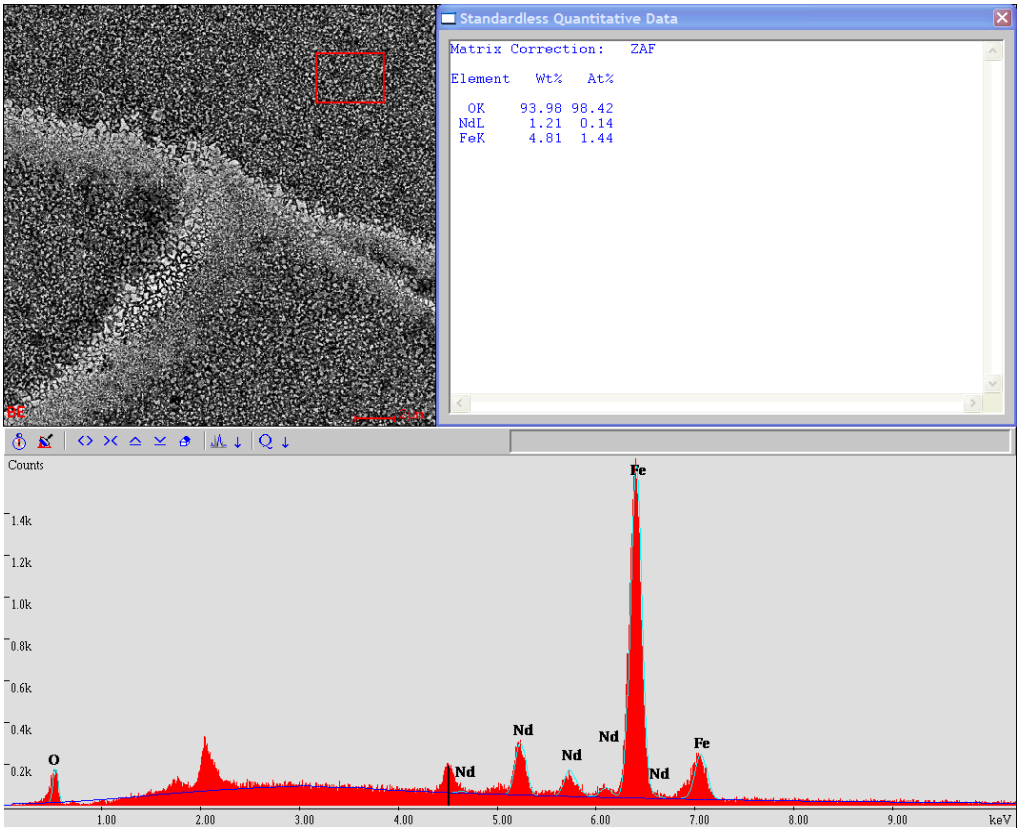

- **EDX box analysis of the annealed sample at 980°C**

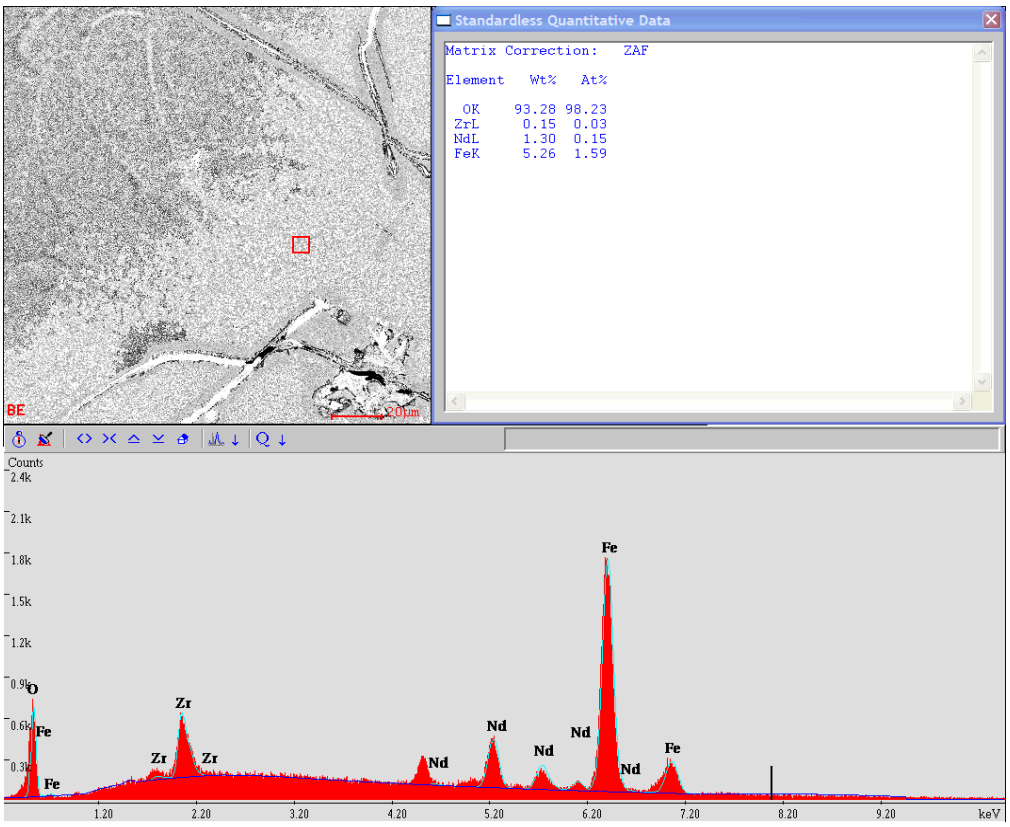

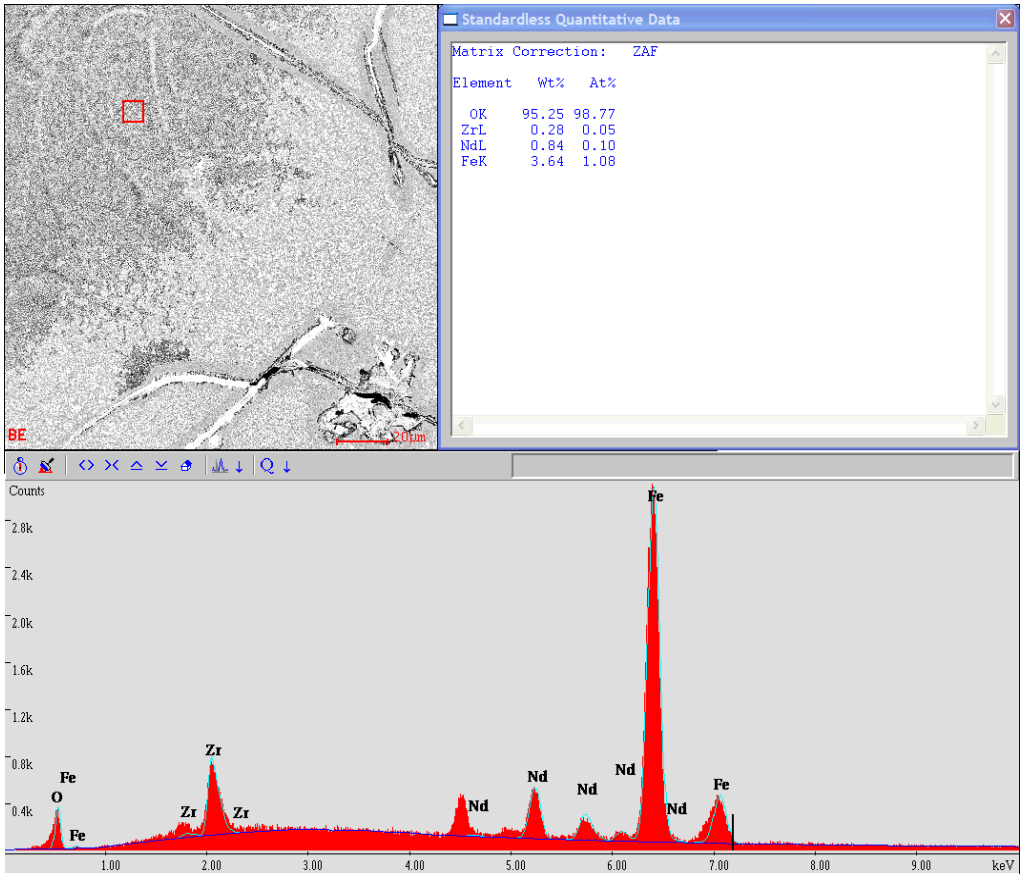
Standardless Quantitative Data
Matrix Correction: ZAF
Element Wt% At%
OK 95.25 98.77
ZrL 0.28 0.05
NdL 0.84 0.10
FeK 3.64 1.08
BE
20µm
Counts
Fe
O
Zr
Nd
keV

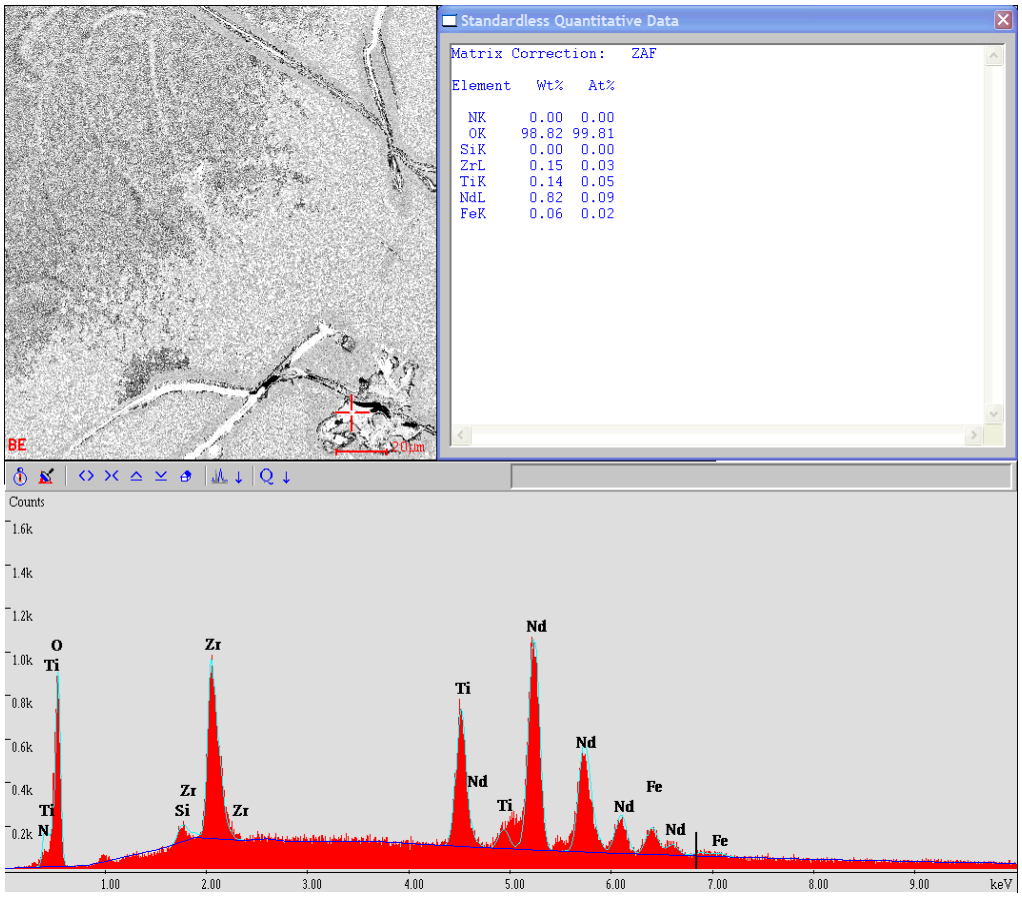
Standardless Quantitative Data
Matrix Correction: ZAF
Element Wt% At%
NK 0.00 0.00
OK 98.82 99.81
SiK 0.00 0.00
ZrL 0.15 0.03
TiK 0.14 0.05
NdL 0.82 0.09
FeK 0.06 0.02
BE
20µm
Counts
O
Ti
Zr
Si
N
Nd
Fe
keV

Appendix 3 EDX Results- Ni Infiltrated sample -Chapter 7

Zr rich- red square

Element	Wt %	At%
ZrL	85.73	78.03
TiK	9.19	15.94
NdL	1.62	0.93
FeK	2.82	4.20
NiK	0.63	0.90
Total	100	100

Needle phase

Element	Wt %	At%
ZrL	29.84	20.61
TiK	5.68	7.47
NdL	0.62	0.27
FeK	56.78	64.05
NiK	7.08	7.60
Total	100	100

Bright phase -NdFeNi

Element	Wt %	At%
ZrL	0.42	0.33
TiK	0.43	0.65
NdL	33.67	16.85
FeK	26.64	34.43
NiK	38.83	47.74
Total	100	100

Dark Phase-Fe rich phase

Element	Wt %	At%
ZrL	23.60	15.96
TiK	2.26	2.91
NdL	0.44	0.19

FeK	64.74	71.52
NiK	8.96	9.42
Total	100	100

Brightest phase- NdNi phase

Element	Wt %	At%
ZrL	0.72	0.62
TiK	0.32	0.53
NdL	42.37	22.80
FeK	18.72	26.01
NiK	37.86	50.05
Total	100	100